MULTI-SCALE STRUCTURE AND DYNAMICS OF VISUAL SIGNALING IN *DROSOPHILA* PHOTORECEPTOR CELLS

APPROVED BY SUPERVISORY COMMITTEE

Rama Ranganathan, M.D. Ph.D.

Paul Sternweis, Ph.D.

Leon Avery, Ph.D.

Steven Altschuler, Ph.D.

Dedication

I would like to thank the members of my graduate committee and lab, my family and friends both near and far, and God, the source of all good things.

Ad maiorem Dei gloriam.

MULTI-SCALE STRUCTURE AND DYNAMICS OF VISUAL SIGNALING IN *DROSOPHILA* PHOTORECEPTOR CELLS

by

STEPHEN JESS HELMS

DISSERTATION

Presented to the Faculty of the Graduate School of Biomedical Sciences

The University of Texas Southwestern Medical Center at Dallas

In Partial Fulfillment of the Requirements

For the Degree of

DOCTOR OF PHILOSOPHY

The University of Texas Southwestern Medical Center at Dallas

Dallas, Texas

May 2012

MULTI-SCALE STRUCTURE AND DYNAMICS OF VISUAL SIGNALING IN *DROSOPHILA* PHOTORECEPTOR CELLS

Stephen Jess Helms, Ph.D.

The University of Texas Southwestern Medical Center at Dallas, 2012

Rama Ranganathan, M.D., Ph.D.

A general problem in science today is how to understand complex systems. An emerging and promising approach makes the bold assumption that complex systems adhere to particular design principles. The power of this is that design principles by definition impose an intuitive nature on a system by presupposing purpose. Existing studies have fruitfully shown the application of engineering principles in biology, but biological systems have many distinct features, particularly due to evolution. In this work, I used *Drosophila* phototransduction, a well-studied sensory system renowned for its high performance, to search for evolutionary design principles. I focused on three

levels of structure in the system: compartmentalization of molecules into microvilli, modularity of dynamic scaffolding by InaD, and functional integration within a single domain of InaD. Using rigorous quantitative measurement and theory with an evolutionary mindset, I uncovered intuitive, simplifying design principles at each level: Microvilli are used to build fast, homogeneous signaling compartments whose dimensions are constrained by these requirements. Dynamic scaffolding is a modular feature of InaD PDZs 4-5 which have been co-inherited in many scaffolds. Within PDZ5, ligand binding and oxidation of the domain are linked through pairwise coupling with a conformational equilibrium—a generic property found in all proteins—and not each other. These results show that this approach can be successful in revealing novel design principles in complex evolved systems.

Table of Contents

Dedication ii
Table of Contents vii
Prior Publications xii
List of Figures xiii
List of Tables xv
List of Equations xvi
List of Appendices xvii
List of Definitions xviii
CHAPTER ONE Evolutionary Design Principles of Signaling 1
The Beauty of Design Principles 2
Complexity as a Symptom of a Lack of Understanding 3
Design Principles as a Mechanism for Making Sense of Complexity 3
Analogous Design Principles from Engineering 4
Information Flow through Network Topologies 4
Feedback 6
Feed-Forward 7
Functional Systems from Dynamical Behaviors 7
Reuse of Modular Parts 9
Optimization of Signaling Performance 11
Distinct Properties of Biological Systems 13
The Inherent Nonlinearity and Functional Diversity of Biological Components 13
Folding 15
Binding 16
Catalysis 18
Allosteric Regulation 19
The Role of Organization in Signaling 22
Limitations of Unorganized Intracellular Signaling 22
Physical Compartmentalization 24
Scaffolding 25
Spatially Inhomogeneous Signaling 27
Noise 29
The Robustness-Adaptability Paradox 30
Robustness of Biological Systems 31
Adaptability 34
Conclusions 39
CHAPTER TWO The *Drosophila* Photoreceptor Cell as a Model of High-Performance Signaling 40

Invertebrate Vision 41
Features of the Eye 41
Microvillar Photoreceptor Cells 42
Electrophysiological Response to Light 43
Impulse Response 44
Steady-State Response 45
Adaptation 46
The *Drosophila* Phototransduction Signaling Network 49
Overview 49
Detection of Light 50
Transduction and Amplification 53
Output 55
Dynamical Behavior 59
Scaffolding by InaD 61
Composition 61
PDZ Domains 62
Interaction with Ligands 63
Domain Classification 64
Regulation of PDZ Domains 65
Altered Properties of Tandem and Extended PDZ Domains 65
Binding Partners 66
Functional Consequences of InaD Localization 68
Dynamic Scaffolding 69
Motivations for this Dissertation 70
CHAPTER THREE The Role of Compartmentalization by Microvilli 72
Introduction 72
Modeling of Ca^{++} Spatiotemporal Dynamics 74
Construction of a Partial Differential Equation Model 74
Estimation of Parameters 77
Somatic Ca^{++} Dynamics 79
Simulations 81
Measurement of Localized Ca^{++} Dynamics 83
Camgaroo-Based Sensors of Localized Ca^{++} 83
Consequences of Uncorrelated Quantum Bumps at Steady-State 86
Steady-State Ca++ Measurements 90
Normalization of the Ca^{++} Response 90
Comparison of Steady-State Responses under Physiological Ca^{++} Conditions 91
Effect of Extracellular Ca^{++} on the Steady-State Ca^{++} Response in the Rhabdomere 92
Comparison of Steady-State Responses under Low Ca^{++} Conditions 94

Estimation of Ca^{++} Signaling Properties from Measurement Fluctuations 95
Consequences for Signaling 97
Physical Analysis of Properties of Signaling Compartments 99
Conclusions 101
Methods 102
Calcium Simulations 102
Flies 102
Immunofluorescence 103
Fluorescent Pseudopupil Imaging 103
Quantum Bump Measurements 104
Camgaroo Fluorescence Measurement 105
Analysis of Ca^{++} Measurements 106
CHAPTER FOUR Modularity of Dynamic Scaffolding by InaD 107
Introduction 107
Identification of NorpA as the Physiological Binding Partner of PDZs 4-5 109
Pull-Down Binding Assay 110
Gel Filtration of a PDZs 4-5 / NorpA Complex 111
Development of a Quantitative Binding Assay 112
Quantitative Binding Measurements 113
Effect of PDZ4 on Binding 114
NorpA, not Trp, is the Ligand 115
Binding Mode between PDZ45 and NorpA 116
Double Mutant Cycles 119
Effect of PDZ4 on the Redox Properties of PDZ5 123
Development of a Quantitative, Precise Redox Assay 124
Redox Titration Theory 124
Issues with the Previous Redox Titration Method 125
Redox Buffering Theory 128
Redox Titration of PDZ5 130
Redox Titration of PDZ45 131
Mutation of the PDZ4 Cysteines to make PDZ45 Δ3C 132
Redox Titration of PDZ45 Δ3C 133
Detection of an Oxidative Dimer in PDZ45 134
Effect of PDZ4 on the Conformation of PDZ5 136
Crystal Structure of PDZ45 136
Evolutionary History of PDZ45 139
Identification of Homologous InaD Fragments 140
Phylogenetic Analysis of PDZ45 Homologs 141
Conclusions 143
Methods 144
Constructs 144

Fluorescence Polarization Binding Assay 145
Protein Expression 145
Pull-Down Binding Assay 146
FRET Binding Assay 146
Redox Titration Assay 147
Crystallization and Structure Determination 148
Bioinformatic Analysis 149
CHAPTER FIVE Functional Integration within InaD PDZ5 151
Introduction 151
Thermodynamic Model of the PDZ5 Redox Switch 153
Coupling and Thermodynamic Boxes 153
Distinction between Macroscopic and Intrinsic Properties 154
Extension to Three Equilibria 155
Thermodynamic Relationship between PDZ5 States 155
Dissection of the Coupling between Binding, Oxidation, and Conformation 157
Detection of Two Redox Conformations in PDZ45 158
Redox Equilibration Kinetics 158
Quasi-Equilibrated Redox Titration 160
Redox-Conformation Coupling 161
Binding-Conformation Coupling 164
Redox-Binding Coupling 165
Energetic Architecture of Redox Switching in PDZ5 168
Comparison with Statistical Correlations in the PDZ Domain Family 169
Physiological Consequences of Dynamic NorpA Localization 172
Analysis of Existing Mutant Fly Phenotypes 172
Simulation of the Effect of NorpA on the Refractory Period 172
Potential Mechanisms for Triggering Oxidation 174
Conformational Control 174
Effect of Acidification on PDZ45 176
Effect of Phosphorylation on PDZ45 179
Biochemical Characterization of Potential Phosphorylation Sites 179
Analysis of Phosphorylation in vivo 184
Conclusions 188
Methods 192
Quantum Bump Simulations 192
Phosphorylation Experiments 193
Generation of Phosphoantibodies 193
Detection of Phosphorylated InaD in vivo 194
CHAPTER SIX Conclusions and Recommendations 196
The Search for Design Principles in Biology 196
Micron Scale: The Role of Compartmentalization by Microvilli 196

Nanometer Scale: Modularity of Dynamic Scaffolding by InaD 197
Angstrom Scale: Functional Integration within InaD PDZ5 199
Future Directions 199
Bibliography 246

Prior Publications

Ybe J. A., Mishra S., **Helms S.**, Nix J. (2007) "Crystal structure at 2.8 A of the DLLRKN-containing coiled-coil domain of huntingtin-interacting protein 1 (HIP1) reveals a surface suitable for clathrin light chain binding." *J. Mol. Biol.* 367(1):8-15.

List of Figures

Figure 1: Network Topology 5
Figure 2: Modularity at Multiple Scales 11
Figure 3: Genetic Variation in Natural Populations 37
Figure 4: Overview of the *Drosophila* Eye 42
Figure 5: The Response to Light 48
Figure 6: Overview of the Phototransduction Pathway 50
Figure 7: Rhodopsin Cycle 52
Figure 8: Transduction and Amplification 55
Figure 9: Activation and Regulation of Trp Channels 59
Figure 10: InaD Gene Family 62
Figure 11: Structural Overview of the PDZ Domain 64
Figure 12: Dynamic Scaffolding by InaD 70
Figure 13: Spatiotemporal Model of Ca^{++} in the Rhabdomere 75
Figure 14: Predicted Spatiotemporal Dynamics of Ca^{++} Following Opening of a Single Channel 82
Figure 15: Predicted Spatiotemporal Dynamics of Ca^{++} During a Quantum Bump 83
Figure 16: Illustration of the Strategy for Measuring Localized Ca^{++} Responses 84
Figure 17: Localization of Camgaroo Sensors 85
Figure 18: Average Quantum Bump Shape of Camgaroo Flies 86
Figure 19: Effect of Uncorrelated Quantum Bumps on the Ca^{++} Measurement 87
Figure 20: Dependency of the Ca^{++} Measurement Distribution on Ca^{++} Response Parameters 89
Figure 21: Normalization of the Ca^{++} Response 91
Figure 22: Ca^{++} Responses with Physiological Extracellular Ca^{++} 92
Figure 23: Dependency of Steady-State Ca^{++} on Extracellular Ca^{++} 93
Figure 24: Ca^{++} Responses with 100 µM Extracellular Ca^{++} 94
Figure 25: Analysis of the Ca^{++} Measurement Distributions 97
Figure 26: Distinct Signaling Modes in the Cell Body and Rhabdomere 99
Figure 27: Physical Constraints on Compartments 101
Figure 28: Fluorescence Polarization Measurement of Binding of PDZ5 C645S to NorpA C-terminal Peptide 110
Figure 29: Measurement of NorpA Binding by Pull Down Assay 111
Figure 30: Co-Purification of NorpA CTD with PDZ45 112
Figure 31: FRET Experiment for Quantitatively Studying PDZ45-NorpA Interaction 113
Figure 32: Effect of PDZ4 on Binding 114
Figure 33: NorpA and Trp Binding 116

Figure 34: Contribution of PDZ4 and PDZ5 to Binding 117
Figure 35: Contribution of the NorpA C-terminus and Internal Loop to Binding 119
Figure 36: Double Mutant Cycle Analysis of PDZ45 Binding Site Mutants and NorpA C-terminal Mutant 120
Figure 37: Double Mutant Cycle Analysis of PDZ45 Binding Site Mutants and NorpA Hypervariable Loop 122
Figure 38: Redox Titration of PDZ45 WT and C645S 132
Figure 39: Binding of PDZ45 Δ3C to NorpA 133
Figure 40: Redox Titration of PDZ5 and PDZ45 Δ3C 134
Figure 41: Structural Analysis of PDZ45 138
Figure 42: Identification of Homologs of the PDZ45 Tandem 140
Figure 43: Phylogenetic Analysis of PDZ45 Homologs 143
Figure 44: Three Equilibria Underlying Redox Switching by InaD PDZ5 153
Figure 45: Sample Thermodynamic Box for Binding and Conformation 154
Figure 46: Thermodynamic Cube Model of PDZ5 155
Figure 47: Oxidation Kinetics of PDZ45 159
Figure 48: Quasi-Equilibrated Redox Titration of PDZ45 Δ3C 161
Figure 49: Thermodynamic Box for Oxidation and Conformation 163
Figure 50: Thermodynamic Box for Binding and Conformation 165
Figure 51: Effect of NorpA Titration on the Redox State 166
Figure 52: Thermodynamic Box for Redox and Conformation in the Presence of Ligand 168
Figure 53: Energetic Architecture of Redox Switching in PDZ5 169
Figure 54: Statistical Coupling between Residues Mediating Binding and Oxidation in the PDZ Domain Family 171
Figure 55: Phenotypes of InaD Mutants 172
Figure 56: Sensitivity of Quantum Bump Properties to NorpA Parameters 174
Figure 57: Dependence of Binding and Redox on the Conformational Equilibrium 175
Figure 58: Effect of Acidification on Binding and Oxidation 178
Figure 59: Structural Consequences of Acidification 178
Figure 60: Characterization of Phosphorylation of PDZ45 by PKC in vitro 182
Figure 61: LC/MS Coverage of PDZ45 Tryptic Fragments 182
Figure 62: Characterization of Potential Phosphorylation Sites 184
Figure 63: Characterization of Anti-Phospho-T661 185
Figure 64: Characterization of Anti-Phospho-T666 186
Figure 65: Detection of Phosphorylated T666 in vivo 187
Figure 66: Binding of PDZ45 Phosphomimic Mutants to NorpA 188

List of Tables

Table 1: InaD Binding Partners 67
Table 2: Parameters of Ca^{++} Model 79
Table 3: Summary of Binding Results 123
Table 4: Redox Buffer Conditions 130
Table 5: Mass Spectrometry of Redox Equilibrated PDZ45 135
Table 6: PDZ45 Crystal Structure Details 139
Table 7: Identification of Homologs of InaD PDZ Domains 141
Table 8: Comparison of InaD Multi-PDZ Domain Homologs 141
Table 9: ESI-MS of PKC-treated PDZ45 182
Table 10: Modified Peptides Detected by LC/MS/MS for PKC-Treated PDZ45 183

List of Equations

Equation 1: Partial Differential Equation Model for Rhabdomeric Ca^{++} 75
Equation 2: Goldman-Hodgkin-Katz Current Equation 75
Equation 3: Simplified Goldman-Hodgkin-Katz Current Equation 76
Equation 4: Constraints for Estimating the Model Parameters 78
Equation 5: Equations Determining the Estimated Model Parameters 78
Equation 6: Ratio of the Light-Induced Current Carried by Ca^{++} 80
Equation 7: Fraction of Ca^{++} that Diffuses into the Soma 80
Equation 8: Somatic Ca^{++} Dynamics 80
Equation 9: Steady-State Solution for Somatic Ca^{++} 81
Equation 10: Analytical Form of the Ca^{++} Steady-State Distribution 88
Equation 11: Nernst Equation 124
Equation 12: General Redox Equilibrium Equation 124
Equation 13: Unbuffered Redox Titration Fitting Equation 125
Equation 14: Buffered Redox Titration Fitting Equation 128
Equation 15: Buffered Redox Titration Curve Fitting 129
Equation 16: Thermodynamic Definition of the Three Equilibria in PDZ5 156
Equation 17: Thermodynamic Definition of the Coupled Equilibria in PDZ5 156
Equation 18: Estimation of the Conformational Equilibrium Constant from Redox Data 162
Equation 19: Estimation of the Oxidation-Binding Coupling from Ligand Saturation Experiments 167

List of Appendices

APPENDIX A Protein Sequences 201
APPENDIX B Matlab Scripts 206

List of Definitions

Arr1/2 – Arrestin 1/2
CaM – Calmodulin
Camga – Camgaroo
CTD – C-terminal domain
DAG – Diacylglycerol
dGq – *Drosophila* G alpha subunit, Q class
DTT – Dithiothreitol
E^0 – Standard redox potential
EGTA – Ethylene glycol tetraacetic acid
FRET – Förster resonance energy transfer
GST – Glutathione S-transferase
GTP – Guanine triphosphate
InaC – Inactivation no afterpotential C (Protein Kinase C)
InaD – Inactivation no afterpotential D (Multi-PDZ scaffolding protein)
IP_3 – Inositol triphosphate
IPTG – Isopropyl-β-D-thiogalactopyranoside
K_{conf} – Conformational equilibrium constant
K_D – Dissociation constant
K_{redox} – Redox equilibrium constant
LIC – Light-induced current
NMR – Nuclear magnetic resonance
NorpA – No receptor potential A (Phospholipase C β)
ODE – Ordinary differential equation
PCR – Polymerase chain reaction
PDE – Partial differential equation
PDZ – Post-synaptic density, Discs-Large, Zona occludens
PDZ45 – PDZs 4-5
PIP_2 – Phosphatidylinositol 4,5-bisphosphate
PKC – Protein Kinase C
PLC – Phospholipase C
PP2A – Protein Phosphatase 2A
QQ – quantile-quantile
SCA – Statistical coupling analysis
TCEP – Tris(2-carboxyethyl)phosphine
Trp(l) – Transient receptor potential (like)
WT – Wild-type

CHAPTER ONE

Evolutionary Design Principles of Signaling

The world is full of systems which appear complex. Complexity can be seen in both human-built systems, such as airplanes, as well as in natural systems, like the protein interaction network of a cell. Furthermore, complex systems occur on many spatial and temporal scales, ranging from atoms to galaxies, picoseconds to billions of years.

Although people frequently refer to systems as complex, the meaning of this term is often more intuitive than rigorous. Complex systems like the examples described above have multiple parts, but not all multi-part systems are thought to be complex. For example, a crystalline solid is composed of many copies of the same molecule, but it is not complex. In contrast, the power grid, composed of many interconnected power stations, is thought to be complex. A possible distinction is that understanding a crystal does not require much more than understanding a single molecule, while the power grid's diverse and variable strength connectivity makes knowledge of the network as important as understanding a single power station. In general, a useful definition is that *complex systems are multi-part systems in which knowledge of the components alone is insufficient to understand the behavior of the system because the interactions between them are non-uniform or not easily predictable.*

How then can we understand complex systems? Two philosophies prevail. In the first, the interactions between the many parts of a complex system are determined through a brute-force approach of experimentation and the behavior analyzed by simulation. In the second, simpler, more tractable model systems are carefully studied to identify underlying principles which are extrapolated to larger systems. While both approaches have their place and can be complementary (Dear 2006), the extrapolation of principles from model systems has particular advantages which will be discussed in detail here.

The Beauty of Design Principles

The rationale behind studying model systems is that in some sense they embody the same principles underlying larger, more complicated systems but are experimentally and theoretically more tractable. One particular area of insight which can be derived from model systems is design principles. These are *principles which correlate the properties of the components of a network or their connections with the function or performance characteristics of the system* (Uri Alon 2007a).

It is not clear that design principles should exist. After all, each complex system may function in a unique manner. Furthermore, in natural systems there is no intelligent designer, further questioning the idea that there should be underlying principles behind their design. Yet, as described below, there are common themes in the design of diverse systems, both human-built and natural.

Fundamentally, the belief that there should be universal principles for complex systems is a deep philosophical assumption that *the world is intelligible and rational* (Dear 2006).

Complexity as a Symptom of a Lack of Understanding

In some sense, complexity is a symptom of a lack of understanding the underlying design principles of a system. As an example, consider an engineered system, the cruise control system in a car. We know that an engineer built this according to a particular design logic, but to non-specialists this system may seem complex because they are unaware of the purpose behind the design of the system. The lesson here is that rather than be enamored or scared of complexity, we must seek to understand the principles underlying the system in order to make sense of it (Uri Alon 2007a).

Design Principles as a Mechanism for Making Sense of Complexity

Design principles, once recognized, provide a preliminary way of understanding complex systems without intense experimentation or detailed simulation. Many complex systems are composed of simpler parts which are combined to perform some function. Understanding the principles with which the system was designed can transform the apparent complexity by annotating systems with purpose (Uri Alon 2007a).

It is important to note here that complex systems have a special property, emergence, which refers to the capacity of these systems to exhibit behaviors that are not predictable from the properties of their individual components. Design principles can explain some of the intended emergent properties of a system, but experimentation and simulation are required to fully understand all the emergent properties of a system. The brute force philosophy of dissecting systems can help here.

Analogous Design Principles from Engineering

We know that human-built systems are created by engineers who use well-established engineering principles in their design. What are the design principles behind biological systems? It is tempting to assume they are the same, but this may not be the case. In biological systems, the "engineer" is evolution, which knows nothing of undergraduate engineering and is not able to plan ahead in its design (Sorger 2005). Despite this, much success has been found in trying to understand biological systems through the lens of traditional engineering (Uri Alon 2003).

Information Flow through Network Topologies

Within a network, subsets of nodes can be thought of as having a particular topology based on identifying patterns in how the nodes are connected (R Milo et al. 2002; S. S. Shen-Orr et al. 2002). This turns out to be a useful

approach because particular network topologies, known as network motifs, have characteristic behaviors in dynamic systems (S. S. Shen-Orr et al. 2002; S Mangan et al. 2003; Brandman et al. 2005; W. Ma et al. 2006; Uri Alon 2007b; T. Y.-C. Tsai et al. 2008; Goentoro et al. 2009; W. Ma et al. 2009; Bleris et al. 2011; N. a Shah et al. 2011). In addition, complicated networks can often be reduced to a simpler subset of nodes which are indirectly connected (W. Ma et al. 2006). This then allows one to predict how a complicated network will behave based on analogy with a simpler model topology. The behavior of two and three node networks can be exhaustively studied computationally, resulting in a rich set of model behaviors from which to draw (W. Ma et al. 2006; N. a Shah et al. 2011; W. Ma et al. 2009). The two major groups of network topologies are feedback and feed-forward loops (Figure 1).

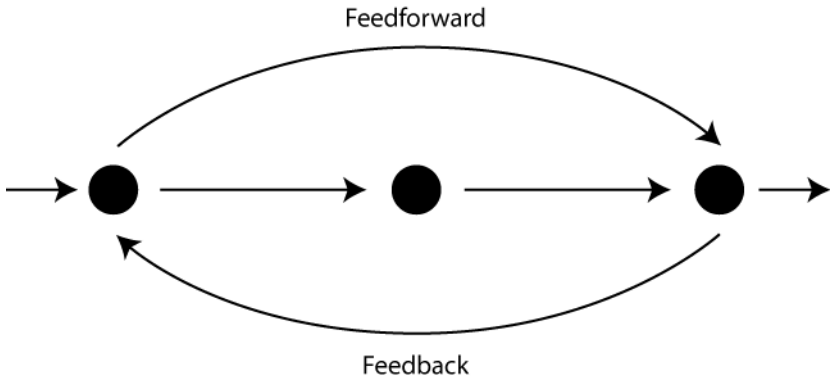

Figure 1: Network Topology

The two main classes of network topologies, feedback and feedforward, are shown. The circles represent nodes in a network and the arrows represent information flow.

Feedback

Feedback topologies are classified based on a signal activating (positive) or inactivating (negative) itself either directly or indirectly.

Negative Feedback

Negative feedback provides a stabilizing force in a system (Brandman et al. 2008). On its own, it is typically used for homeostasis, maintaining a system at a fixed state (Brandman et al. 2008). Typical examples from engineering include cruise-control and thermostats. In biology, negative feedback loops are frequently found in metabolic networks and signaling pathways. As with human-built systems, these loops have been shown to be important in homeostasis when used on their own, acting as a high-pass filter which reduces noise (Austin et al. 2006; Dublanche et al. 2006). In addition to noise suppression, negative feedback can be used to linearize responses, promoting information transfer (R. C. Yu et al. 2008; Nevozhay et al. 2009). When the negative feedback loop is very slow, oscillations can occur (Novák et al. 2008).

Positive Feedback

Positive feedback, in contrast, increases the speed and can destabilize systems (Brandman et al. 2008). As a result, it is important for increasing sensitivity (Hornung et al. 2008) and generating switch-like behavior (Xiong et al.

2003; Angeli et al. 2004; Ferrell 2008; D.-E. Chang et al. 2010; Palani et al. 2011). An example of a system using positive feedback is an amplifier. In biology, many signaling systems which require sensitive detection of inputs use positive feedback. In addition, positive feedback is used to make bistable switches which remain in one state after triggering, such as the commitment of *Xenopus* oocytes to mature following progesterone exposure (Xiong et al. 2003).

Feed-Forward

Feed-forward occurs when a signal is propagated to an output node along both a short and long path (R Milo et al. 2002; S. S. Shen-Orr et al. 2002). Feed-forward loops are then classified by whether the short and long paths stimulate or inhibit the output node and how the output node integrates the two paths (S Mangan et al. 2003). Depending on the details of the connections, feed-forward can filter transient signals, accelerate responses, or generate pulses (S Mangan et al. 2003).

Functional Systems from Dynamical Behaviors

Functional systems often do more than simply linearly relay a signal to an output. The signal can be non-linearly amplified, converted into an all-or-nothing stable switch, or generate oscillations or patterns. While non-linear behaviors are more difficult to predict a priori, dynamical systems theory provides a comprehensive approach to understanding these behaviors.

The dynamic behavior of a system can be predicted by expressing the time-dependence of the parts in the form of differential equations. These equations describe the future state of the system given the initial conditions. In general, this can be expressed as $\frac{d\mathbf{X}(t)}{dt} = f(\mathbf{X}(t), t)$, where $f(\mathbf{X}(t),t)$ is a vector function describing how the system will change as a function of the state vector **X**(t).

The goal of dynamical systems theory is then to use this framework to determine the states in which the system remains indefinitely, known as fixed points or steady-states, or a periodic sequence of states the system follows (Strogatz 1994). These fixed points can be identified by solving $\frac{d\mathbf{X}(t)}{dt} = 0$ for $\mathbf{X}(t) = \mathbf{X}^*$. The sign of the $\frac{d\mathbf{X}(t)}{dt}$ around **X*** determines the stability: If the sign of the derivative is such that the system returns to **X*** following small perturbations, the system is stable (Strogatz 1994).

The power of this approach comes in the realization that dynamic behaviors such as bistability and oscillations each have a common origin in their characteristic dynamical structure (Strogatz 1994) despite occurring in diverse systems. The challenge then is to understand how the topology and parameters of a system produce the dynamical structure. This then allows one to rationally perturb the function and to understand how mutations or regulation alter the behavior of a system.

Reuse of Modular Parts

One of the major advances in modern engineering is the use of modular parts. Instead of designing each system from scratch, engineers can build complex systems by combining pre-existing components with the desired properties. The underlying principle is that modular components should behave in a well-defined manner, independent of the rest of a system, under reasonable conditions (Hartwell et al. 1999; Günter P Wagner et al. 2007).

Nature also uses modular designs (Figure 2). At the organismal level, quantitative traits exhibit heterogeneous covariance, allowing some sets of traits to be independently varied while coupling the variation within phenotypic modules (Cheverud et al. 2004; Günter P Wagner et al. 2007). This phenotypic modularity is molecularly implemented in the functional modularity of the molecular interaction network of the cell (Roguev et al. 2008; Costanzo et al. 2010; Green et al. 2011), which is scale-free with certain nodes acting as hubs either connecting the components of a functional module or mediating the interaction between modules (Barabasi et al. 1999; Han et al. 2004; Maciag et al. 2006; Krogan et al. 2006). These modules represent core processes of the cells as well as the recurring signal transduction machinery (tyrosine kinase signaling, G protein signaling, etc.) which connects diverse receptors and outputs. Modularity is seen even at the level of single proteins, which can contain modular domains which provide common functions such as binding, catalysis, or regulation

(Bhattacharyya et al. 2006), or multiple sectors which allow evolution to independently tune distinct features of the protein (Halabi et al. 2009).

While it is clearly a useful property, the finding of modularity in nature is surprising because evolution might not be expected to build modular systems: Because evolution does not plan ahead, the usefulness of reusing modular parts is unlikely to be directly selected (Günter P Wagner et al. 2007). Several possible explanations for the existence of modularity have been proposed. Under certain conditions, gene duplication and divergence (Sole et al. 2003) or neutral genetic drift (Force et al. 2005) can produce modular networks without invoking any selective advantage. However, theoretical studies have shown that modular designs have a selective advantage in environments which fluctuate since they can more rapidly be used to adapt to a new function (Lipson et al. 2002; Nadav Kashtan et al. 2005).

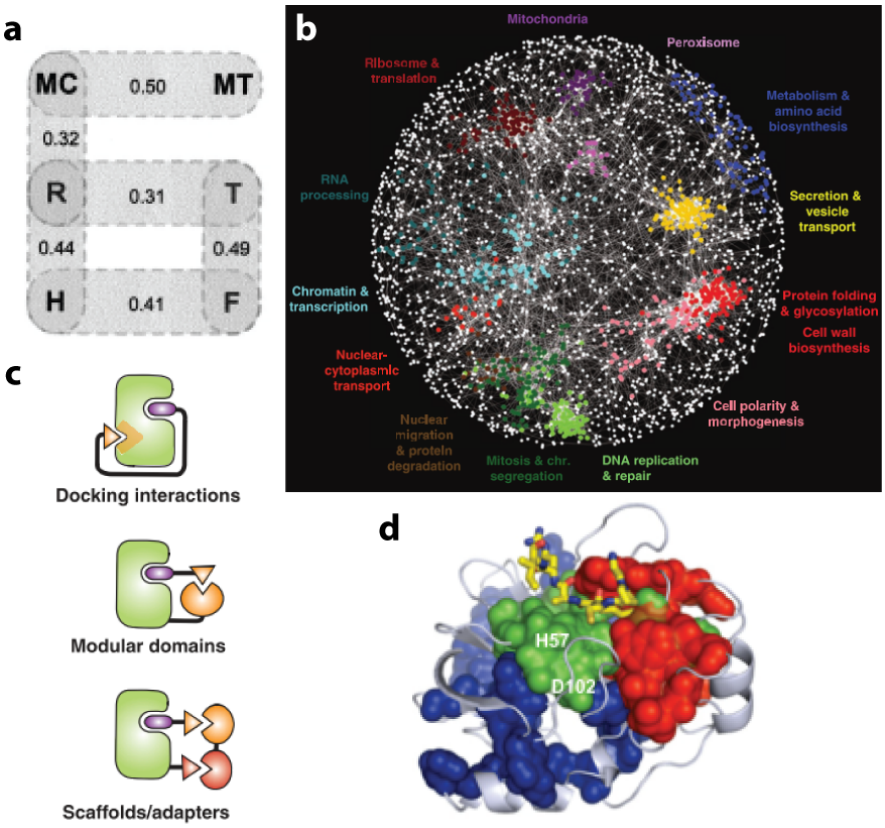

Figure 2: Modularity at Multiple Scales

Modularity is seen at multiple scales in organisms. (a) Correlation between sizes of bones (MC, metacarpal; MT, metatarsal; R, radius; T, tibia; H, humerus; F, femur) in the forelimb (left edge) and hindlimb (right edge) of the macaque, indicating that the correlations break down into modules corresponding to limbs and homologous bones. Reproduced with permission from Figure 8 of (Young et al. 2005). (b) Genetic interaction network of yeast with functional modules labeled in different colors. Reproduced with permission from Figure 1 of (Costanzo et al. 2010). (c) Illustration of the modularity of multi-domain proteins. Reproduced with permission from Figure 1 of (Bhattacharyya et al. 2006). (d) Modularity within a single protein (rat trypsin shown) indicated by the presence of multiple coevolving sectors (specificity in green, catalytic activity in red, fold stability in blue). Reproduced with permission from Figure 4 of (Halabi et al. 2009).

Optimization of Signaling Performance

An obvious goal of human-engineered systems is performance; we want systems to be as good as they can be given a set of constraints. Evolution is no different. By the process of natural selection, any system with improved

performance will be selected if it improves reproductive fitness. The end result is that if a system's performance is under selection for long enough, the system will perform optimally.

However, there are many cases in which one can imagine this limit will not be reached. A system may not need to be very good to maximally improve the reproductive fitness of an organism. Alternatively, it may take infinitely long to tweak a system for optimum performance, a symptom of high dimensionality or simply being very far from the optimum. Finally, if there are many local optima for a system, natural selection may only reach one of these local optima rather than the global optimum.

It is surprising then that there are many cases in which it can be shown that evolution has found the optimal design. For example, kinases in bacteria (Skerker et al. 2005) and binding domains in yeast (Zarrinpar et al. 2003) and mice (Stiffler et al. 2007) appear to have been optimized to minimize cross-talk in their native environment. Laboratory evolution can also find the optimal protein expression (Dekel et al. 2005) or regulatory logic (Poelwijk et al. 2011) given a set of constraints. An unpublished study by Uri Alon's group (conference talk, Q-Bio 2011) suggests that evolution frequently finds the optimal solution given multiple constraints: Many morphological and molecular phenotypes can be shown to be linear combinations of various optimal "specialist" phenotypes. Many biological systems also adapt to their environmental conditions by

optimizing their capacity for information transfer. Furthermore, the information processing strategies used in nature have been shown in several cases to be optimal (T. M. Yi et al. 2000; Kollmann et al. 2005; Andrews et al. 2006, 2007; Kalisky et al. 2007; Tkacik et al. 2009). These examples hint at a surprising simplicity in the evolution of biological systems.

Distinct Properties of Biological Systems

Despite the success of the approach of understanding biological systems through the lens of engineering, biological systems have distinct properties which are not found or typically avoided in traditional engineering (Sorger 2005). Biological components behave nonlinearly, have off-target effects, self-organize, are noisy, and have to withstand mutation while maintaining the ability to adapt. We have a lot to learn about engineering in this sense from nature.

The Inherent Nonlinearity and Functional Diversity of Biological Components

When engineers build complex systems, they often rely on the powerful theory of linear time invariant systems (Nise 2000). This theory allows the output of a system to be predicted from the response of each part to an instantaneous signal. The crux is that each part must respond linearly to the input signal and the response must be independent of the timing of the input. If this is the case, then the part can be used in a complex system and its effect easily predicted.

Of course, the physical laws which govern the function of parts are not always linear or time-invariant. This can be dealt with by designing systems to operate only within the linear range of a component. Nature does not seem to generally take advantage of linear time-invariance, however. Part of this is certainly the inherent non-linearity of the function and regulation of biological molecules, as described here. Another factor may be the evolutionary process of building a system. Regardless, natural systems can teach us much about the design of non-linear systems.

A second problem is the functional diversity of biological molecules. Unlike the components we use in building systems, biological molecules often do not behave only as intended. Proteins have multiple binding partners, enzymes perform side-reactions, and proteins exist in alternative states. Despite this, biological systems function remarkably well.

The fundamental properties of biomolecules—folding, binding, catalysis, and regulation—can be explained in terms of free energy differences. Practically speaking, free energy determines the probability of a protein existing in a particular state or a reaction occurring. This probability is determined from the Boltzmann distribution, which states that the fraction of particles in state i with energy E_i is $\frac{g_i \exp\left(-\frac{E_i}{k_B T}\right)}{Z(T)}$, where g_i is the number of states with that energy level, k_B is the Boltzmann constant, T is the temperature, and Z(T) is the partition function

describing the total ensemble of states. For two states with a free energy difference ΔG, the relative probability of the two states—the familiar equilibrium constant, K—can be calculated by taking the ratio of the Boltmann probability for each state with $E_2 = E_1 + \Delta G$. This gives$K = \exp\left(-\frac{\Delta G}{RT}\right)$, a fundamental nonlinear equation governing the function of biological molecules. The consequences of this are described below.

Folding

Proteins are classically thought to exist in a two-state equilibrium between a folded and unfolded state (Dill et al. 1997), where the folded state is typically the state that is biochemically active. The free energy difference between the two states is known as the stability of the protein, ΔG_{fold}. Post-translational modifications of a protein or mutations can perturb this equilibrium by altering the free energy of folding by ΔΔG. The relative probability of being in the folded state, K_{fold}, is $\exp\left(-\frac{\Delta G_{fold}+\Delta\Delta G}{RT}\right)$, showing that modifications exponentially perturb the folded population.

Conformational Ensemble

The powerful techniques available in modern biophysics have allowed the detection of multiple conformational states in proteins (Baldwin et al. 2009). This can be understood by viewing the conformation of a protein as a large space with

a free energy for each conformational state (Onuchic et al. 1997). The classical view is a limiting case where one conformational state is far more stable than any other (Dill et al. 1997). Classical two-state allosteric conformational transitions, described below, are another limiting case where the landscape has only a few states which are much more stable than the rest.

Protein folding landscapes are often thought of as funnels, with the conformational diversity progressively decreasing as the stability of the fold increases (Onuchic et al. 1997). Experimental studies have revealed that these conformationally diverse high energy states are accessible for many proteins under physiological conditions (Baldwin et al. 2009) and are relevant to processes such as enzymatic catalysis (Buyong Ma et al. 2010) and binding (Boehr et al. 2009). In addition, these high energy states are thought to be important for the promiscuous activity of proteins (Khersonsky et al. 2010).

Binding

A fundamental mechanism by which biomolecules transfer information is by physical interaction, known as binding of a ligand by a receptor (Creighton 1993). This interaction between the receptor (R) and ligand (L) has a free energy of binding, ΔG_{bind}. The relative probability of the bound versus unbound state (K_A, or K_D^{-1}) is again derived from the Boltzmann distribution, resulting in $K_A = \frac{1}{K_D} = \frac{[RL]}{[R][L]} = \exp\left(-\frac{\Delta G_{bind}}{RT}\right)$. Rearranging, we can see that the fraction of

the total that is bound, $\frac{[RL]}{[R]+[RL]}$, is $\frac{[L]}{[L]+K_D}$, the familiar Michaelis-Menten binding equation. As a result, binding is fundamentally a hyperbolic function of ligand. While it is possible for systems to operate under approximately linear conditions by fine-tuning the K_D to match the expected ligand concentration (C. L. Jackson et al. 1990), cells often use elaborate adaptation mechanisms to adjust the signaling dose-response curve to maximize the ability to sense a signal (T. M. Yi et al. 2000; R. C. Yu et al. 2008).

Specificity

Molecules in the cell face the demanding task of interacting with specific partners (often just one) in the context of a crowded environment containing thousands of other types of molecules (Zimmerman 1993). The relative specificity of an interaction is the ratio of the dissociation constants (K_D) for the desired and alternative interaction, $\frac{K_D}{K_{D,nonspecific}} = \exp\left(\frac{\Delta G_{bind}}{\Delta G_{bind,nonspecific}}\right) = \frac{[RL]}{[RL_{nonspecific}]}\frac{[L_{nonspecific}]}{[L]}$. Therefore, the specificity of an interaction, defined by the ratio of the formation of the specific ([RL]) to nonspecific ([$RL_{nonspecific}$]) complex under equal concentration of ligands, increases exponentially with the ratio of the binding free energies. Experimental studies suggest that evolution builds proteins with just enough specificity for their native environment—introduction of novel proteins

(conference talk by Michael Laub, Q-Bio 2011) or transplantation into a new species results in cross-talk (Zarrinpar et al. 2003).

Catalysis

According to transition state theory, the rate of a reaction is limited by the energy barrier associated with the transition state of the reaction (Creighton 1993). The effect of this was initially elucidated in an empirical manner by van't Hoff and Arrhenius and later explicitly tied to the idea of a transition state. This formulation, the Eyring–Polanyi equation, states that the rate of a reaction is $k = \frac{k_B T}{h} \exp\left(-\frac{\Delta G^T}{RT}\right)$, where ΔG^T is the transition state energy, h is Planck's constant, k_B is Boltzmann's constant, R is the ideal gas constant, and T is the temperature. Catalysts speed reactions by lowering the transition state energy.

Enzymes function as catalysts by binding to the transition state of a reaction (Creighton 1993). The classic model of this process is the Michaelis-Menten reaction scheme: $E + S \underset{k_r}{\overset{k_f}{\leftrightarrow}} ES \xrightarrow{k_{cat}} E + P$, where E is the enzyme, S is the substrate, and P is the product. The initial rate of the S → P reaction with enzyme concentrations far less than the substrate concentration is $k_{cat}[E]_0 \frac{[S]}{K_M + [S]}$, where $K_M = \frac{k_r + k_{cat}}{k_f}$. Thus, the enzymatic rate increases hyperbolically with substrate concentration.

Promiscuous Enzymes

As in the case of binding interactions, enzymes often have many substrates—not all of which are obviously productive to the cell. More intriguingly, many enzymes have been shown to be promiscuous, meaning that they perform alternative reaction chemistries (Khersonsky et al. 2010). This promiscuity is thought to result from minor conformations of the enzyme present in the cell (Meier et al. 2007; Nobuhiko Tokuriki et al. 2009). As in the case of binding interactions, evolution appears to only have engineered just enough specificity for the native conditions (Khersonsky et al. 2010)—enzymes often do not discriminate against unnatural ligands (Villiers et al. 2009). High specificity may also limit the performance of the enzyme (Fersht 1999); instead, nature often builds regulatory and proofreading mechanisms (Hopfield 1974; Ninio 1975) to ensure the specificity of enzymatic reactions. These side reactions have an important benefit, however: They provide biological systems with a backup system (Khersonsky et al. 2010) and flexibility in evolving new pathways (Jensen 1976; Jacob 1977; Kurakin 2007), as described in detail later.

Allosteric Regulation

As discussed earlier, proteins can exist in multiple conformational states. These states can differ in their functional activity, such as binding affinity or catalytic rate. The regulation of which state a protein exists in is called allostery.

This regulation can occur through binding of another molecule or modification of the protein. In either case, the preferred state of the protein is perturbed through modulation of the folding free energy landscape of the protein. While this is most often thought of as triggering a change in shape of the protein, the configurational entropy ("dynamics") of the protein can in principle be the sole change in the protein (A. Cooper et al. 1984), as experimentally observed recently (Popovych et al. 2006). The biophysical mechanisms connecting distant sites on a protein are not yet understood, but they can sometimes be predicted by studying co-evolutionary patterns in protein families (Süel et al. 2003; Shulman et al. 2004; Dima et al. 2006; Smock et al. 2010).

Classical Models

The classical models of allostery (Monod et al. 1965; Koshland et al. 1966) were developed as an attempt to explain the observation of cooperative binding in hemoglobin (Bohr et al. 1904). Both models propose that protein subunits exist in either a tense or relaxed state, where the relaxed state has an increased affinity for the ligand. Ligand binding biases a subunit towards the tighter-binding relaxed state, and the conformation of the subunits is coupled. As a result, the apparent binding affinity of the protein oligomer increases as ligand binds, producing a cooperative binding curve which can be fit by the Hill equation: $f_{bound} = \frac{[L]^n}{[L]^n + K_D^n}$ (Hill 1910).

Sequential Koshland-Nemethy-Filmer Induced Fit Model

The Koshland-Nemethy-Filmer (KNF) induced fit model proposes that ligand binding induces the relaxed conformation in a subunit (Koshland et al. 1966). The conformational change in the subunit then induces the neighboring subunits to switch to the relaxed conformation. As a result, a protein oligomer sequentially switches from being fully in the tense-conformation through a series of increasingly relaxed-conformation states to a final fully relaxed-conformation state.

Concerted Monod-Wyman-Changeaux Model

In contrast, the Monod-Wyman-Changeaux (MWC) model proposes that the protein oligomer is in a dynamic equilibrium between an all-tense and all-relaxed state (Monod et al. 1965). Ligand binding selects for the initially minor all-relaxed state, resulting in an increasing proportion of the protein existing in the tight-binding all-relaxed state.

Extension to Protein Ensembles

While the classical models were initially focused on two-state protein oligomers, the same principles apply to monomeric proteins and multi-state ensembles. The key idea is that the allosteric regulator must alter the free energy difference between some of the conformations, leading to a shift in which

conformations are populated (Kumar et al. 2000). Any functional change is mediated by change in the average activity of the ensemble. This is in principle the same as the classical MWC model (Cui et al. 2008). In fact, both classical models can be seen as special cases of a continuum of possible mechanisms coupling changes in conformation with a perturbation (Hammes et al. 2009). Because conformational ensembles are now recognized to be widely important in proteins, it has been proposed that all proteins have the capacity for allosteric regulation (Gunasekaran et al. 2004).

The Role of Organization in Signaling

In contrast with electrical circuits in which similar components can be specifically connected by electrical wiring, the fundamental components underlying biochemical systems—molecules—move and interact by diffusion, a random process. Yet, evolution is also faced with this challenge of creating distinct signaling pathways from the same type of molecules. This creates unique constraints in the design of biological networks.

Limitations of Unorganized Intracellular Signaling

A naïve view of the cell is that it is a bag of freely diffusing molecules, similar to the conditions used in biochemical experiments in test tubes but simply with many additional types of molecules present. Many reactions involve the interaction of two molecules; as a result, the rates of these reactions are limited by

the random diffusional encounter of the molecules. This turns out to be a major limitation for signal processing in cells.

The dimensions of eukaryotic cells range from 10-100 μm, with considerable variation in morphology. The timescale for spatial equilibration of particles diffusing by Brownian motion scales as $\frac{r^2}{6D}$ along the radius (r) of a sphere (Berg 1993), where D is the diffusion coefficient. Proteins and small molecules have diffusion coefficients on the order of 10^1 and 10^2 $\mu m^2/s$, respectively. As a result, equilibration across a spherical cell with a radius of 5-50 μm would take 0.4-40 s and 0.04-4 s for proteins and small molecules, respectively. Diffusion thus sets a lower bound on the timescale on which cells can process signals in the absence of organization.

Diffusion also limits the processing capacity of a cell, since the number of independent signals that can be processed by the same molecular components is limited by their diffusional isolation. For a given timescale, the average radius which a signal diffuses in two dimensions is $\sqrt{4Dt}$ (Berg 1993). We can then approximate the maximum number of diffusion-isolated spots on the cell membrane by dividing the surface area by the diffusion area: $\frac{4\pi r^2}{\pi\left(\sqrt{4Dt}\right)^2}$, which simplifies to $\frac{r^2}{Dt}$. Using the same diffusion coefficients and range of cell sizes as before, the number of distinct second-timescale signals is 2.5-250 and 1-25 for proteins and small molecules, respectively. Thus, cells have a strong pressure to

develop mechanisms to control the diffusion of signals to improve their signal processing capabilities.

Physical Compartmentalization

One mechanism to overcome the limitations imposed by the diffusion of signals is to restrict signals to specific compartments. This can be accomplished physically by enclosing regions of the cell within membranes, as in the case of cellular organelles (Alberts et al. 2002) or cytoskeletal 'fencing' of molecules in the membrane (Sheetz et al. 1980; Sako et al. 1998). The end result of each approach is that the volume accessible to a signal by diffusion is significantly reduced. By placing signals in distinct compartments, cross-talk between pathways can be reduced, improving signaling fidelity. For example, dendritic spines (Shepherd 1996; R Yuste et al. 2000; Murakoshi et al. 2011; Rafael Yuste 2011) and rhabdomeric microvilli (Howard et al. 1987; Hochstrate et al. 1990; S. R. Henderson et al. 2000) implement this strategy to act as independent computational units. Another example is the endocytic compartmentalization of Toll-like receptors, which is thought to limit recognition of self-nucleic acid and generate distinct signaling complexes (Barton et al. 2009).

In addition to improving the specificity of a signal, compartmentalization should also affect signaling dynamics by concentrating molecules into a smaller volume. For first- and second-order reactions, the rate is proportional to the

concentration of the two species; compartmentalization thus increases the rate of reaction by the magnitude of the concentration increase. For zero-order reactions, a constant amount of product is generated independent of the concentration of reactant. In this case, compartmentalization serves to amplify the product concentration, since the volume of the space in which the product is created decreases. This is used to dramatic effect in muscle tissue, where rapid, high amplitude calcium signaling is achieved by restricting signaling to couplons, small regions of the cell where plasma-membrane bound ryanodine receptor clusters are separated from calcium channels on the smooth endoplasmic reticulum by just 12 nm (Cheng et al. 2008). Thus, compartmentalization can dramatically affect the amplitude and kinetics of signaling.

Scaffolding

An alternative to physical compartmentalization by membranes or diffusion barriers is to physically tether signaling molecules together on a scaffolding protein. This mode of organization has been recognized as a fundamental component of physiological signaling pathways for more than two decades (Good et al. 2011). The first scaffolding proteins identified included the non-enzymatic bacterial chemotaxis protein CheW (J. D. Liu et al. 1989) as well as receptor tyrosine kinase adaptor proteins (X. J. Sun et al. 1991), which couple diverse receptors with a shared intracellular downstream pathway. Scaffolds for

MAP kinase pathways were subsequently identified, revealing a role for scaffolding proteins in preventing cross-talk between related pathways (Kranz et al. 1994; K. Y. Choi et al. 1994; Marcus et al. 1994; Printen et al. 1994). The idea of scaffolding proteins as physiologically required connectors of upstream and downstream signaling components has been validated in many additional pathways.

While scaffolding is conceptually similar to physical compartmentalization, it has distinct consequences for signaling. In analogy to the concentration increase by compartmentalization, scaffolding of two molecules reduces rotational entropy and increases their 'local' concentration (Page et al. 1971) to the volume swept by the radius of gyration allowed by the scaffolding protein. This effect can be large: Protein-protein interactions occur on the 10 nm scale; a single molecule restricted to a sphere with a radius of 10 nm would have a concentration of 400 μM. Since most proteins are present in the 0.05-50 μM range in the cell, this results in a large increase in concentration and thus reaction speed.

An important additional consequence is that individual scaffolding molecules and their bound proteins can often be thought of as functionally independent. In many cases, scaffolded molecules only interact with molecules on the same scaffold, as seen by biphasic concentration dependence of signaling output on scaffolding protein concentration (Dickens 1997; Levchenko et al.

2000; Chapman et al. 2009). This can dramatically alter the behavior of biochemical networks (Locasale et al. 2007) as the reactions gain a digital-like nature: scaffolds exist in a discrete set of states, with reactions within them probabilistically occurring as a function of the state of the scaffolding complex and environment. This is in stark contrast with the classical view of enzymatic signaling, in which enzymatic activity increases in an analog manner with increasing enzyme and substrate concentration and proceeds linearly with time.

Scaffolding proteins are composed of modular protein interaction domains, suggesting that the evolutionary wiring of new signaling pathways may simply require the fusion of generic domains which interact with the desired proteins rather than the re-engineering of protein activities or interfaces (Bhattacharyya et al. 2006). Indeed, this modularity of signaling has been successfully employed in the design of synthetic signaling pathways; for example, the yeast growth factor scaffolding protein Ste5 can be functionally replaced *in vivo* with a scaffold composed of alternative protein interaction domains capable of effectively interacting with the appropriate partners (S.-H. Park et al. 2003).

Spatially Inhomogeneous Signaling

Alternatively, it is possible to dynamically compartmentalize signals by specifically localizing either the production or breakdown of a signal while keeping the opposing reaction randomly localized. This results in an

inhomogeneous distribution of the signaling molecule in the cell. There are many examples of the use of this in nature, particularly involving small molecule signals.

The best studied example is Ca^{++} signaling. The concentration of Ca^{++} is ~1.5 mM in the extracellular environment but only 50 nM inside the cell. As a result, when Ca^{++} channels open, there is a large, nearly diffusion-limited influx of Ca^{++} into a highly localized region of the cell. As the Ca^{++} ions diffuse away from the source, the concentration becomes progressively lower, resulting in a substantial signaling gradient ranging from ~100 μM near the channel where it is not in equilibrium with cytosolic buffers to the 50 nM resting state of the cell (Erwin Neher 1998). This provides an opportunity for ensuring specificity by placing molecules, such as calmodulin (Tadross et al. 2008), which only respond to higher Ca^{++} concentrations in the "nanodomain" near the channel, as exemplified by the regulation of K^{+} channels (Berkefeld et al. 2006) and synaptic vesicle release (Heidelberger et al. 1994; Schneggenburger et al. 2000; Beutner et al. 2001; Bollmann et al. 2005).

Another well-studied example involves a family of scaffolding proteins known as A-kinase anchoring proteins (AKAPs), which co-scaffold protein kinase A (PKA) with regulatory molecules in particular locations within the cell (W. Wong et al. 2004). The enzyme adenylyl cyclase produces the diffusible small molecule cyclic adenosine monophosphate (cAMP) which activates PKA. As in

the case of local Ca^{++} signals, this results in a gradient of cAMP originating from the enzyme (Zaccolo et al. 2002), which in some cases is part of the AKAP complex (Dessauer 2009). By anchoring PKA to the zone of high cAMP, AKAPs can restrict PKA phosphorylation to local targets (Carnegie et al. 2003). The best studied example of this is the restriction of PKA activity in muscle cells to the local region of β-adrenergic stimulation (Zaccolo et al. 2002).

All these signaling gradients share a common dynamical origin. These diffusible signals can be modeled by the partial differential equation $\frac{dS(t,x)}{dt} = r^+(x) - r^-(x) + D\nabla^2 S(t,x)$, where S(t,x) is the diffusible signal as a function of time (t) and location (x), $r^+(x)$ and $r^-(x)$ are the influx and efflux rates which may be restricted to particular locations, and D is the diffusion coefficient for the signaling molecule. The shape of the steady-state signaling gradient is a function of the diffusion coefficient and the location of the influx sources and efflux "sinks" (Berg 1993).

Noise

While human-built systems must deal with noise, biological systems are particularly influenced by stochastic fluctuations (Eldar et al. 2010; Balázsi et al. 2011). Noise in biological systems comes from many sources, including gene expression, translational bursts, binomial errors in sorting molecules during cell division, and biochemical reactions involving small numbers of molecules

(McAdams et al. 1999). This noise can be divided into two components: 'intrinsic' noise which corresponds to the fundamental noisiness of the process and 'extrinsic' noise which is a result of cell to cell differences (Elowitz et al. 2002). Elowitz et al. beautifully showed that in bacterial gene expression extrinsic noise dominates (Elowitz et al. 2002). As mentioned earlier, specific network topologies can suppress low or high frequency noise (S Mangan et al. 2003; Austin et al. 2006; Dublanche et al. 2006). Noise suppression is costly, however—the decrease in noise scales with the quartic root of the number of regulator molecules in the optimal case (Lestas et al. 2010).

More interestingly, evolution often uses the noise in these systems to generate phenotypic diversity (Balázsi et al. 2011). For example, *E. coli* randomly switches between antibiotic sensitive and resistant phenotypes (Balaban et al. 2004), *B. subtilis* uses noise to trigger a small fraction of cells to become transiently competent (Süel et al. 2006), and cancer cell subpopulations arise from stochastic cell fate decisions (Gupta et al. 2011). Phenotypic switching is thought to be an important strategy in a fluctuating environment in which the statistics of the environment change slowly (Kussell et al. 2005).

The Robustness-Adaptability Paradox

The final major unique feature of natural systems is that they arise from an evolutionary process (Jacob 1977): they are subject to random mutation and fluctuating selection pressures. This imposes two important design criteria on

biological systems. First, they must be robust to mutation, not easily breaking. Secondly, they must be able to readily adapt to new functional constraints. This creates an apparent paradox in building a system which is robust to most perturbations while at the same time retaining the ability to readily adapt to new requirements.

Robustness of Biological Systems

During each round of DNA synthesis, mutations accumulate at a frequency that varies among organisms but typically ranges from 10^{-10} to 10^{-7} mistakes per nucleotide per generation (Kunkel et al. 2000). One could imagine many designs would not be able to tolerate even a single change; these are non-robust designs. For example, randomly cutting wires inside a television is likely to break the device. In contrast, it is possible to design robust systems such that many random changes have little or no effect.

Mutational Tolerance in Proteins

A naïve reaction to a typical protein structure, with its tightly packed interactions between amino acids with different chemical properties, would be to assume that most mutations would be likely to have a large effect. Surprisingly, this is not the case. A classic series of studies on the interaction of the human growth hormone receptor with growth hormone showed that only a small, non-

obvious fraction of the residues at the interface contributed to binding (B. C. Cunningham et al. 1993; Clackson et al. 1995). These findings have been replicated in many other systems, leading to the view that most mutations in proteins have only a small energetic effect which can be tolerated as long as the overall protein stability is above a threshold (DePristo et al. 2005; Bershtein et al. 2006). Two unpublished studies within the Ranganathan lab have comprehensively investigated the functional and fitness consequences of mutation of every residue of two proteins, finding that indeed, very few positions have a significant effect under conditions of weak to moderate selection (McLaughlin et al.; Stiffler and Ranganathan).

Robustness to Parameter Perturbations in Dynamical Systems

Robustness is also seen at the level of biochemical networks. It has long been recognized that most wild-type alleles are haplosufficient, indicating that reducing gene expression by half has no functional consequence. Using a clever genetic tool, Moriya et al. were able to show that most genes involved in the yeast cell cycle could tolerate a more than 25-fold increase in copy number (Moriya et al. 2006). This robustness to gene dosage can arise from mathematical properties of the reaction network (Shinar et al. 2010) or the use of particular network topologies (Acar et al. 2010; Bleris et al. 2011).

The more general case of parameter robustness is a common feature of models of biological systems (Gutenkunst et al. 2007), first shown theoretically (N Barkai et al. 1997) and experimentally (U Alon et al. 1999) in the bacterial chemotaxis system. Typically, the interesting properties of signaling systems (stable steady-state, bistability, oscillations) are directly related to their dynamical properties. In many systems which have been studied, the dynamical behavior is only sensitive to a small number of 'control' parameters which can trigger bifurcations in the dynamics; robustness can be quantified by the range of parameters that do not perturb the dynamics (L. Ma et al. 2002; Morohashi et al. 2002). An extreme example of robustness is the temperature compensation observed in metabolism (Bullock 1955), circadian clocks (Hogenesch et al. 2011), and bacterial chemotaxis (Oleksiuk et al. 2011). Temperature globally alters reaction rates, and thus the reaction network must be carefully balanced to ensure robustness (Hastings et al. 1957). These findings suggest that robustness is a fundamental design principle of natural biochemical networks. In fact, robustness has been used as an argument for the validity of biological models (Morohashi et al. 2002).

Phenotypic Canalization

Finally, the seemingly complex development of multicellular organisms is surprisingly robust to perturbation. While disruption of individual steps may have

particular consequences, the overall final structure of an organism is often maintained and remarkably reproducible (A. D. Lander 2011). In 1942, Waddington coined the term “canalization” to describe this effect by which a system is seemingly channeled into a particular phenotype despite genetic variation (Waddington 1942). More recent studies have shown that this robustness is in part due to the use of the particular network topologies (Eldar et al. 2002; Melen et al. 2005; W. Ma et al. 2006; Sprinzak et al. 2011), strategies such as spatial filtering (Houchmandzadeh et al. 2002), and the same feedback control mechanisms found in intracellular signaling pathways (A. D. Lander et al. 2009; Lo et al. 2009; Ben-Zvi et al. 2010).

Adaptability

The flip side to robustness is adaptability, the ability of systems to adapt to new functional constraints. Not all systems are adaptable—as explained in the previous section, it is possible to design systems to be highly robust so that perturbations have little functional effect. In many ways, a highly non-robust system can be considered as adaptable, since perturbations to them do lead to large functional effects. The trick is to design systems to be rapidly adaptable while remaining robust to most perturbations. Kirschner and Gerhart have argued that this is accomplished by highly constraining certain core functions while only

weakly constraining regulatory features (M. Kirschner et al. 1998; Gerhart et al. 2007).

Functional Diversity in Proteins

As explained earlier, individual proteins often are functionally diverse, binding alternative targets with a low probability or slowly catalyzing alternative reactions (Khersonsky et al. 2010). These promiscuous reactions have long been recognized as providing a way of rapidly selecting for novel functions (Jensen 1976), but now the molecular mechanisms behind them are becoming clear (Khersonsky et al. 2010). Promiscuity can occur as a result of binding of ligands or substrates to alternative conformations of a protein (L. C. James et al. 2003; C. J. Jackson et al. 2009), or in principle due to altered regulation since some enzymes do not discriminate very well between related substrates (Zhou Songyang et al. 1995; Tremblay et al. 2006). They often do not interfere with the primary function of a protein, so they are not removed by natural selection although neutral drift can alter the spectrum of promiscuous activities (Bloom et al. 2007). However, when a new function is needed, a promiscuous activity of a protein may become useful. While the formerly promiscuous reaction is likely very inefficient, multiple studies have shown that proteins can rapidly adapt to the new constraints through improvement of the reaction by stepwise mutation

(Weinreich et al. 2006; Bloom et al. 2009) as long as the protein is sufficiently stable (DePristo et al. 2005).

Genetic Variation in Populations

Natural selection acts on pre-existing genetic variation. Therefore, when a system adapts to new constraints, the rate of evolution is in part limited by the existence of genetic variation capable of producing the desired phenotype. Extensive studies on traits from multiple organisms governing life history, behavior, physiology, and morphology that quantitatively vary in populations have found that nearly all of them have significant heritability (Figure 3a) (Mousseau et al. 1987; Roff et al. 1987). This indicates that natural populations have significant genetic variability that is also selectable. These quantitative traits are influenced by many loci with small effect sizes that are exponentially distributed (Figure 3b) (Flint et al. 2009). This extensive genetic diversity is not surprising if most mutations are nearly neutral (Kimura 1991), as expected given the general robustness of biological systems.

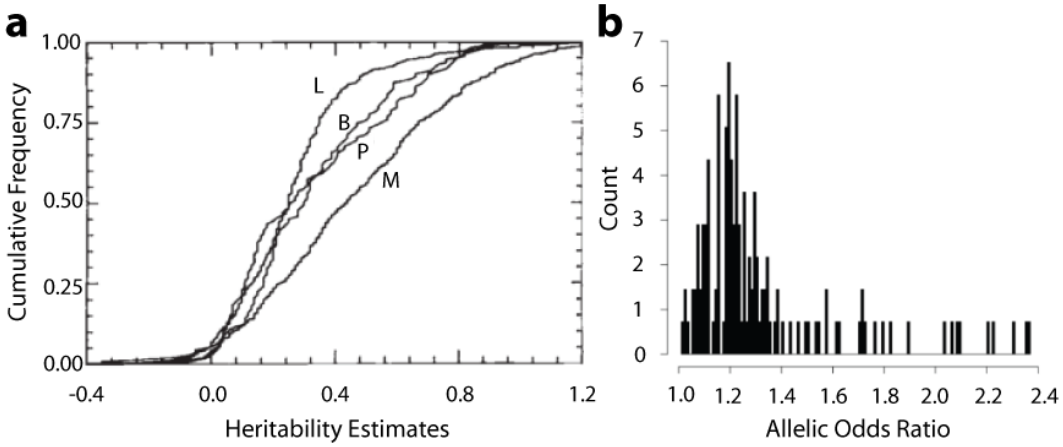

Figure 3: Genetic Variation in Natural Populations

(a) The cumulative probability distribution of the heritability of 1120 quantitative traits from multiple organisms, classified as life history (L), behavior (B), physiology (P), or morphology (M). Adapted from Figure 3 of (Mousseau et al. 1987) with permission. (b) The effect size, measured as allelic odds ratio, of alleles identified in genome-wide association studies in humans. Note that these studies are unlikely to detect alleles with very small effect sizes. Adapted from Figure 1 of (Flint et al. 2009) with permission.

The Role of Epistasis in Shaping Genetic Variation

Because most aspects of an organism are under strong constraints, pre-existing genetic variation often is limited to small phenotypic changes (Kimura 1991; Flint et al. 2009). However, much more phenotypic diversity is seen when genetic variation is combined. For example, mutant alleles in mice frequently have very different phenotypes in different inbred strains (Threadgill et al. 1995). This type of genetic interaction is known as epistasis, which was quantitatively defined by Fisher as a non-additive statistical interaction between two quantitative trait alleles (Fisher 1918). Epistasis can arise from several mechanisms, including

genetic redundancy, mutual participation in a common pathway, and genetic buffering (Lehner 2011).

The intriguing finding is that nature actively uses epistasis to modify phenotypic diversity. A particularly well-studied example is the chaperone protein Hsp90. Under normal conditions, Hsp90 suppresses the effect of mutations in many proteins involved in signaling pathways (Neckers 2007). When an organism encounters stressful conditions, however, Hsp90 no longer buffers the effects of these mutations (Jarosz, Taipale, et al. 2010), revealing the phenotypic diversity that was previous suppressed (Jarosz and Lindquist 2010). If these novel phenotypes are beneficial in the stressful environment, they can now be rapidly selected (Jarosz, Taipale, et al. 2010).

Another fascinating example is the idea of morphological integration. Ideally, the phenotypes of an evolving system should be decomposable into modules which co-vary according to the selection pressures of the environment (G.P. Wagner et al. 1996). Epistasis allows this by coupling the effect of changes at different loci (G.P. Wagner et al. 1996). A mouse study used quantitative trait mapping to look for loci which modify the relationship between morphological characteristics (Cheverud et al. 2004). They found numerous genes which altered the coupling between phenotypes, suggesting that evolution can indeed select for systems with phenotypes which can be varied modularly (Cheverud et al. 2004).

Epistatic interactions have also been shown to be important during laboratory evolution of bacterial populations (H.-H. Chou et al. 2011; Woods et al. 2011).

Conclusions

The pursuit of evolutionary design principles in biological systems has been very fruitful. Like human-built systems, natural systems are characterized by the use of structured networks to achieve particular dynamical behaviors. Furthermore, these systems exhibit features of modular design and optimization. However, biological systems also have unique properties, and the evolutionary process imposes particular constraints in the design of systems. As Dobzhansky stated, “nothing makes sense in biology except in the light of evolution.” (Dobzhansky 1964)

It is clear from the current state of research that the function of particular systems can be well understood within the current theoretical framework given sufficient experimentation and analysis. The danger is that as researchers begin to tackle larger, more complicated systems the clarity of the design principles is lost. The greatest challenge now is to move from applying engineering principles to the function of particular natural systems and instead search for novel design principles unique to biology.

CHAPTER TWO

The *Drosophila* Photoreceptor Cell as a Model of High-Performance Signaling

Drosophila phototransduction is an excellent system for investigating the design principles of signaling. Due to their critical role in organismal fitness, sensory signaling systems such as phototransduction often exemplify the most advanced aspects of signaling, using multiple layers of regulation and performing sophisticated signal processing tasks. For example, *Drosophila* phototransduction is thought to be the fastest G protein signaling system, and it offers single photon sensitivity while retaining the capability to adapt to bright daylight conditions (Roger C. Hardie and P. Raghu 2001). In addition, both the morphology (Land et al. 1992) and physiology (Gonzalez-Bellido et al. 2011) of fly eyes are highly adapted to the ecological niche of the organism. Even within the fly eye, the physiology of photoreceptor cells vary, with cells in the front of the eye responding faster and with better signal to noise (Burton et al. 2011).

From a practical perspective, the *Drosophila* photoreceptor cell offers unparalleled experimental power: *Drosophila* allows for the use of powerful genetic approaches which enable the identification of the genes underlying a process and the precise control and manipulation of the genetic background. It is

also possible to do biochemical experiments either directly from tissue homogenates or using recombinant proteins, as the genome is sequenced. Finally, multiple techniques exist for studying the cellular physiology and behavior of the organism. In this chapter, I will outline some of the details of this powerful system and the principles which enable its high performance.

Invertebrate Vision

Features of the Eye

Each *Drosophila* compound eye (Figure 4) contains 800 ommatidia, the bundles of photoreceptor cells which are the "unit" eyes (D F Ready et al. 1976). In *Drosophila*, each ommatidium contains 8 photoreceptor cells with 6 (R1-R6) arranged radially around two central cells (R7-R8) stacked on top of each other (D F Ready et al. 1976). Each cell sees a different angle of incoming light which varies depending on the relative location in the eye (Borst 2009). Cells which see the same incoming angle of light then connect to the same postsynaptic target in the neural lamina below the retina, an approach known as neural superposition (K Kirschfeld 1967). The end result is that each eye can see 180 degrees with 4.6 degree resolution represented as a 26 x 26 pixel image (Borst 2009). In contrast, human eyes have 60,000 cones, providing 0.01 degree spatial resolution (Borst 2009).

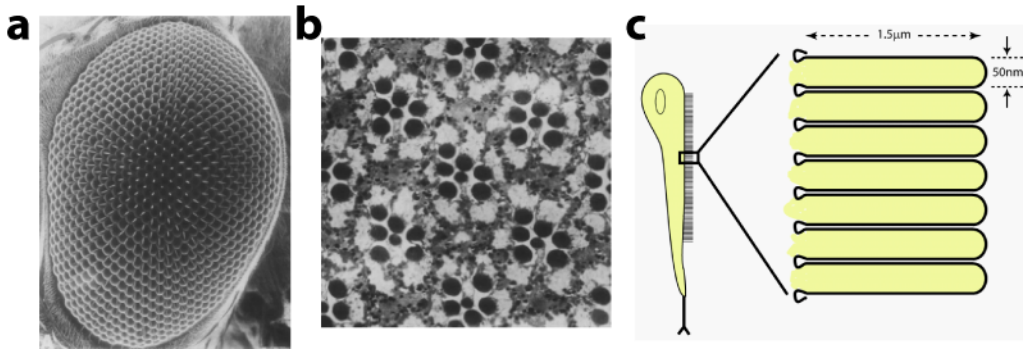

Figure 4: Overview of the *Drosophila* Eye

(a) An scanning electron microscope image of a *Drosophila* eye. (b) A cross section through the eye, revealing ommatidia with prominent rhabdomeres (dark circles). (c) Each ommatidium contains 8 photoreceptor cells, a schematic of which is shown. The rhabdomere contains 30,000 microvilli running down the length of the cell. Panels (a) and (b) reproduced from (D F Ready et al. 1976) with permission.

Microvillar Photoreceptor Cells

During metazoan evolution, two types of photoreceptor cells arose: microvillar and ciliary photoreceptor cells (Fain et al. 2010). Microvillar photoreceptors, which are used in *Drosophila*, contain a specialized light-sensing organelle known as the rhabdomere (Figure 4). Rhabdomeres contain tightly packed microvilli 50-60 nm in diameter and 0.5-2 μm in length (Fain et al. 2010). *Drosophila* rhabdomeres specifically contain 30,000 microvilli which range from 1-1.5 μm in length (Roger C. Hardie 1985). Each microvillus contains the core components of the visual machinery (Roger C. Hardie and P. Raghu 2001) and thus is thought to act as a semi-autonomous light detector (Hochstrate et al. 1990).

Microvillar photoreceptor cells are capable of producing large, rapid responses to single photons while maintaining low noise in the dark. They also

function under bright conditions, with the maximum range determined by the number of transduction units (microvilli, at least in the case of *Drosophila*) and the speed of the response (Fain et al. 2010). *Drosophila* can maximally produce ~4 x 10^5 responses/s (C. F. Wu et al. 1978). This high performance comes at a considerable metabolic cost (Simon B Laughlin et al. 1998).

In contrast, ciliary photoreceptors such as vertebrate cone cells are not capable of detecting single photons and have a far more limited dynamic range (Fain et al. 2010). Rod cells provide single photon sensitivity and low variability, but their responses are an order of magnitude slower and smaller than microvillar photoreceptors and saturate under low light conditions (Fain et al. 2010). However, the dual strategy of using high-sensitivity rods and low-sensitivity cones greatly reduces the metabolic cost in comparison with single purpose microvillar photoreceptor cells (Fain et al. 2010).

Electrophysiological Response to Light

In response to light, *Drosophila* photoreceptor cells produce an inward current (Figure 5) carried primarily by Na^+ and Ca^{++} ions (Rama Ranganathan et al. 1991). There are several experimental paradigms that have been used to study this light-induced current: Electroretinograms (ERGs), which measure the total voltage response of eye to light, are easy to perform and useful for screening flies for visual defects but are difficult to interpret. Intracellular recordings provide single-cell electrical resolution but do not allow the electrical state of the cell or

external environment to be controlled and are difficult to do on small flies. Whole-cell patch-clamped electrophysiological recording from single ommatidia is a very sensitive technique which provides single-cell resolution and the ability to control the chemical composition of both the inside and outside of the cell. It is this technique which has provided the most useful information about the properties of the light response.

Impulse Response

An advantage of studying the visual system is that light is a convenient stimulus. Using a nanosecond-long laser pulse, it is possible to provide an effective delta stimulus to the photoreceptor cells and watch the impulse response (Figure 5a-b). Furthermore, it is possible to detect single-photon responses, known as quantum bumps (C. F. Wu et al. 1975), by recording under low-noise conditions with the light source sufficiently dim to produce responses with Poisson statistics (Figure 5a).

This approach revealed that the quantum bump is characterized by a stochastic latency of ~50 ms followed by a transient current of ~10 pA amplitude and ~20 ms duration (S. R. Henderson et al. 2000). Quantum bumps sum linearly up to at least 1000 effective photons, producing the macroscopic response whose dynamics can be predicted by convolving the quantum bump latency and shape

(S. R. Henderson et al. 2000). Each quantum bump is thought to correspond to activation of a single microvillus (Hochstrate et al. 1990).

Steady-State Response

During prolonged illumination, the light response dramatically adapts, reducing the steady-state current (C. F. Wu et al. 1978) (Figure 5c). As with the macroscopic response, the steady-state current represents the sum of many unsynchronized quantum bumps (Dodge et al. 1968; C. F. Wu et al. 1978). The statistics of the underlying quantum bumps can be estimated using an approach known as fluctuation or 'noise' analysis.

Noise analysis is based on Campbell's theorem, which applied to the light response (Dodge et al. 1968; C. F. Wu et al. 1978) proposes that the observed steady-state current, I(t), is composed of N quantum bumps described by the time-dependent function $I_{QB}(t)$ happening at times t_k: $I(t) = \sum_{k=0}^{N} I_{QB}(t - t_k)$. The mean of this process is $\mu = \langle I(t) \rangle = \lambda \int_{-\infty}^{\infty} I_{QB}(t)dt$, where λ is the frequency of events, and the variance is $\sigma^2 = \lambda \int_{-\infty}^{\infty} I_{QB}^2(t)dt$. Note that the mean can be thought of as the product of the effective amplitude (a) and duration (T) in the case of a rectangular pulse. The effective amplitude of the underlying responses can be estimated by the ratio of the variance to the mean, $\frac{\sigma^2}{\mu} = \frac{\int_{-\infty}^{\infty} I_{QB}^2(t)dt}{\int_{-\infty}^{\infty} I_{QB}(t)dt} = a$, which is independent of the frequency of events. The duration of the quantum

bump can be estimated by fitting the power spectrum of the steady-state response to the Fourier transform of an analytical function that fits the quantum bump shape, $\left|\hat{I}_{QB}(f)\right|^2 = \left|\hat{\Gamma}(f;n,\tau)\right|^2 = \frac{1}{(1+(2\pi\tau f)^2)^{n+1}}$ where the effective duration is $T = \frac{(n!)^2 2^{2n+1}}{(2n)!}\tau$.

This analysis revealed that the rate of quantum bumps increases linearly with light intensity until saturating at ~4 x 10^5 bumps/s (C. F. Wu et al. 1978) (Figure 5d). Since there are ~30,000 microvilli per photoreceptor (Roger C. Hardie 1985), this represents a minimal turnover time of ~150 ms. The large discrepancy between this rate limit and the duration of the quantum bump is due to the refractory period which follows each quantum bump (Hochstrate et al. 1990). The refractory period can be directly observed in *arr2*^{3} flies, in which single photon absorption leads to prolonged activation of the light response and a train of quantum bumps (K. Scott et al. 1997) separated by a highly stochastic ~175 ms delay (C.-H. Liu et al. 2008).

Adaptation

The light response adapts on both fast and slow timescales. Within seconds of constant light exposure, the light response amplitude greatly decreases (Figure 5c). Noise analysis revealed that both the quantum bump amplitude and duration decrease from 9 to ~0.1 pA and 30 ms to 5 ms, respectively, with increasing light intensity during this short period (C. F. Wu et al. 1978; M.

Juusola et al. 2001). After tens of minutes of light exposure, the sensitivity of the cell to light decreases due to a reduced efficiency of generating quantum bumps (Frechter et al. 2007).

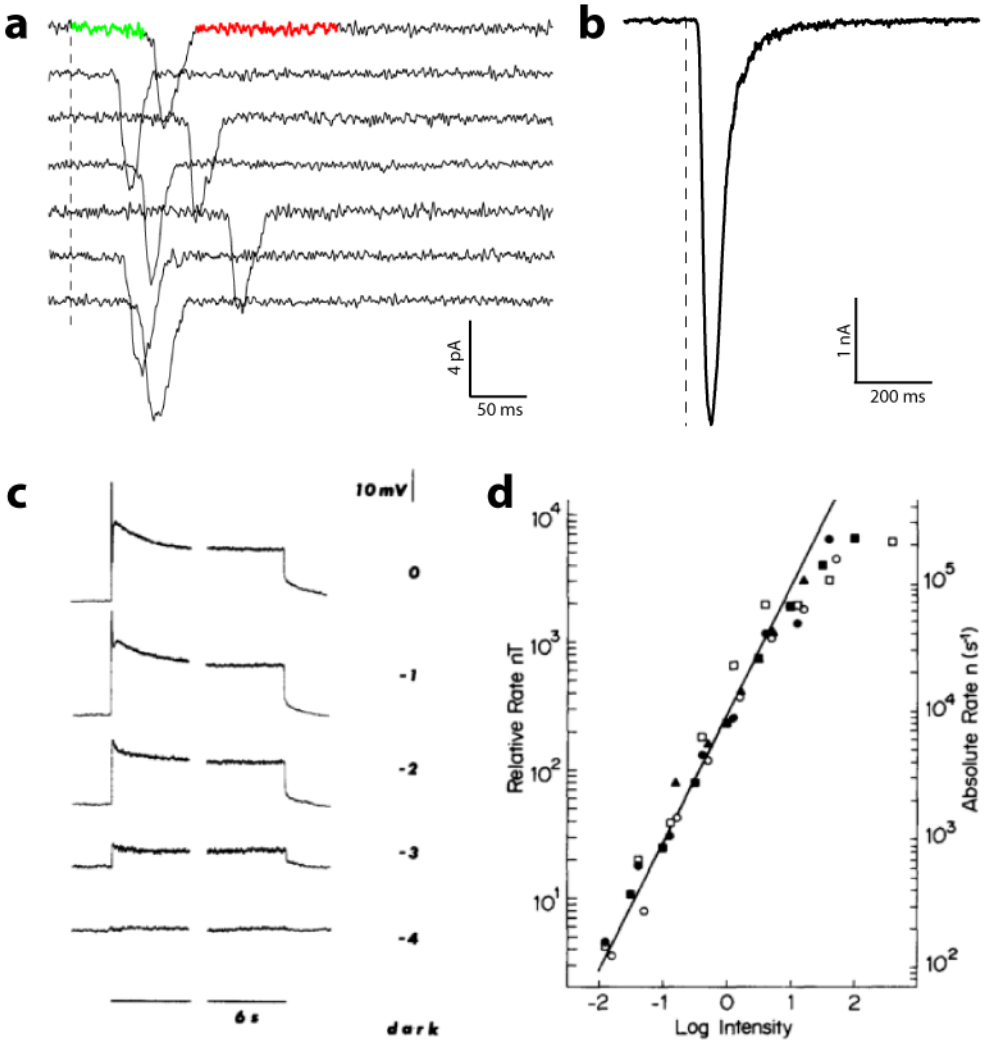

Figure 5: The Response to Light

(a) The stochastic response to single photons, known as quantum bumps. The light stimulus is applied at the dashed line. The latency is highlighted in green and refractory period in red. (b) The macroscopic response to bright stimuli represents the sum of many quantum bumps. The light stimulus is applied at the dashed line. (c) The response to sustained light stimuli with the indicated relative logarithmic light intensity shows ringing and adaptation. (d) The steady-state under constant light stimuli represents the sum of many unsynchronized quantum bumps. The rate of quantum bump generation as a function of light stimulus is shown. Panels (c) and (d) are taken from (C. F. Wu et al. 1978) with permission.

The *Drosophila* Phototransduction Signaling Network

Overview

The biochemical pathway underlying the response to light was primarily worked out in the 1980s and 1990s using the powerful genetic tools available in *Drosophila*. An overview of the pathway is shown in Figure 6. Light is detected by a G-protein coupled receptor, rhodopsin (NinaE), which signals through the G_Q class of heterotrimeric G proteins to activate phospholipase C (PLC, NorpA). Phospholipase C hydrolyzes PIP_2 in the membrane, releasing IP_3, diacylglycerol (DAG), and protons. This causes Trp and Trpl channels to open due to loss of inhibition by PIP_2 and activation by protons. Ca^{++} influx through the Trp channels mediates several feedback pathways: It increases the activation of Trp channels through an unknown mechanism. In conjunction with DAG, Ca^{++} activates protein kinase C (InaC), which inhibits the Trp channels and is required for generating the refractory period. Finally, Ca^{++} activates calmodulin (CaM), which inactivates the channels and activates the myosin NinaC which accelerates the inactivation of rhodopsin by Arr2.

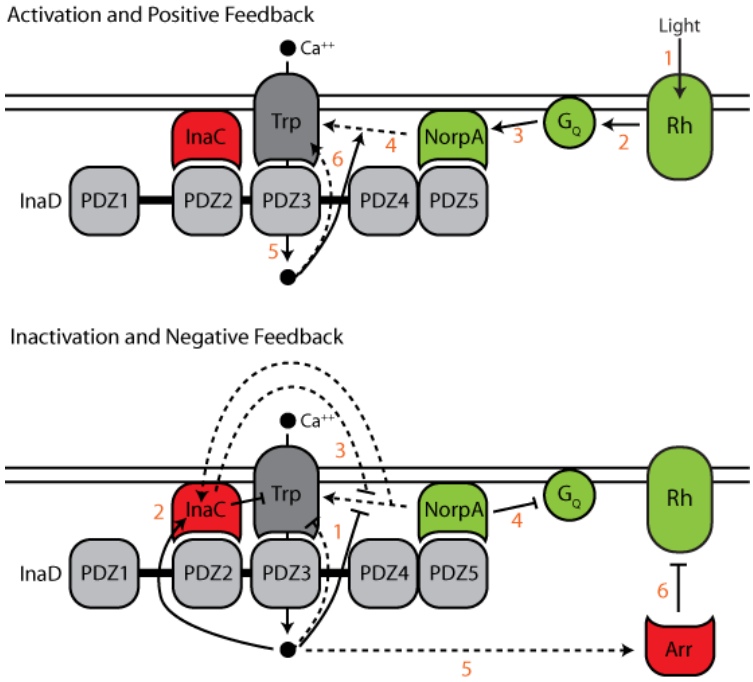

Figure 6: Overview of the Phototransduction Pathway

Arrows indicate the flow of information. Normal arrowheads indicate stimulation; flat arrowheads indicate inhibition. Positive and negative feedback are indicated in green and red (dashed), respectively.

Detection of Light

Rhodopsins

Light is detected by rhodopsin, which in insects converts to a red-shifted active species known as metarhodopsin upon absorption of a photon (William L Pak et al. 1974; Ostroy et al. 1974). There are four rhodopsins in *Drosophila*: The R1-R6 photoreceptors express the blue-light sensitive Rh1 (*ninaE*) which converts between a 480 and 580 nm absorbing species (Ostroy et al. 1974; William L Pak et al. 1974; W. a Harris et al. 1976; Zuker et al. 1985). The R7

photoreceptors express one of two ultraviolet-sensitive rhodopsins, Rh3 and Rh4, which convert from a 370 to 470 nm absorbing species (W. a Harris et al. 1976; Montell et al. 1987; Zuker et al. 1987). Finally, the R8 cells express the blue-light sensitive Rh2 rhodopsin (W. a Harris et al. 1976; A. F. Cowman et al. 1986). Metarhodopsin promotes GTP exchange in a G_Q heterotrimeric G protein (*dgq*) in the photoreceptor cell (Devary et al. 1987; Y. J. Lee et al. 1994).

Inactivation of Metarhodopsin

Metarhodopsin is inactivated by the binding of Arr2, which prevents activation of dGq (Byk et al. 1993) and is the rate-limiting step in termination of signaling (PJ J. Dolph et al. 1993; R Ranganathan et al. 1995). Arr2 is initially localized to the endoplasmic reticulum in the cell body and translocates to the rhabdomere (Kiselev et al. 2000) on a ~90 s timescale, which speeds up by ~10-fold in the presence of Ca^{++} (Satoh et al. 2010). Ca^{++}/calmodulin also provides rapid feedback inhibition on metarhodopsin by regulating the availability of Arr2 through a mechanism which potentially involves NinaC (C.-H. Liu et al. 2008). Metarhodopsin is phosphorylated on its C-terminus by an unidentified rhodopsin kinase (Y N Doza et al. 1992). This phosphorylation is required for internalization of metarhodopsin by Arr1 (Satoh et al. 2005). Camk2 phosphorylates both Arr1 and Arr2 (Hiroyuki Matsumoto et al. 1982, 1984; Yamada et al. 1990; H. Matsumoto et al. 1994), releasing them from rhodopsin (Alloway et al. 1999).

Finally, Ca^{++}/calmodulin stimulates dephosphorylation of rhodopsin by RdgC (Byk et al. 1993; Vinós et al. 1997). Feedback by Ca^{++} plays an important role in controlling the lifetime of metarhodopsin: The presence of Ca^{++} decreases its lifetime from >900 ms to <50 ms (C.-H. Liu et al. 2008).

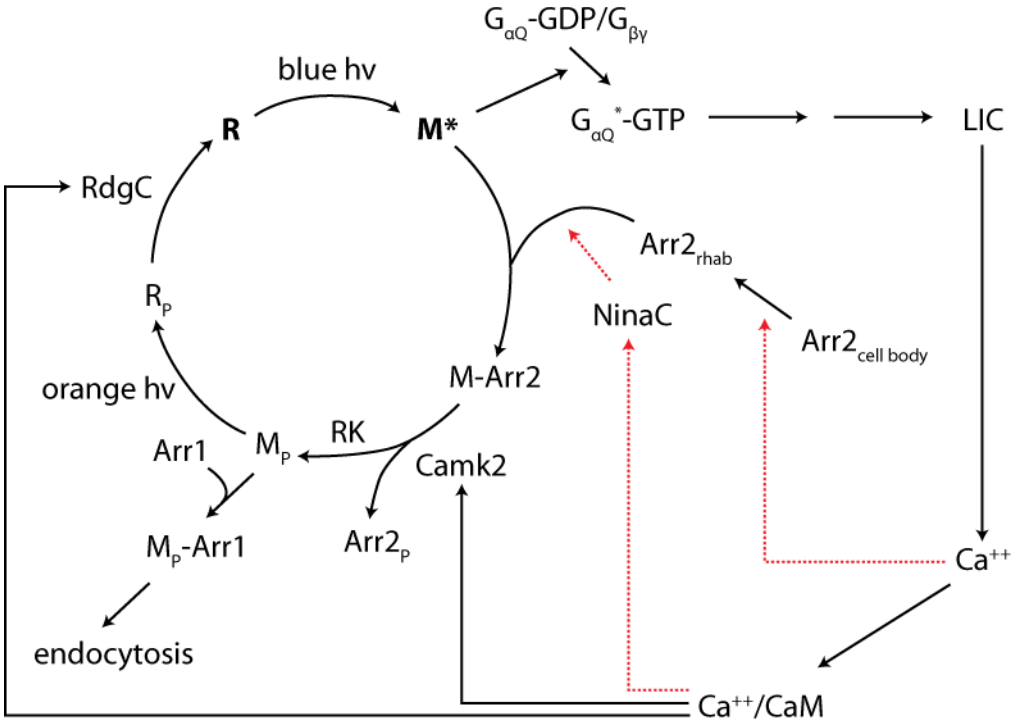

Figure 7: Rhodopsin Cycle

The reactions controlling the activation and inactivation of rhodopsin are shown. Red arrows indicate negative feedback. R: Rhodopsin, M: Metarhodopsin, hv: photon, superscript *: active species, subscript P: phosphorylation, LIC: light-induced current, rhab: rhabdomere.

Transduction and Amplification

Activation and Positive Feedback

Each metarhodopsin activates a few $G_Q\alpha$ subunits (Devary et al. 1987; Y J Lee et al. 1990; Y. J. Lee et al. 1994; K. Scott et al. 1995; Roger C. Hardie et al. 2002), the major source of amplification in the pathway (Roger C. Hardie et al. 2002). The active $G_Q\alpha$-GTP subunits then activate approximately five NorpA proteins by physical association (Devary et al. 1987; Mitchell et al. 1995; Running Deer et al. 1995; M Bähner et al. 2000; Roger C. Hardie et al. 2002). Active NorpA rapidly hydrolyzes PIP_2 in the rhabdomere (Yoshioka et al. 1983, 1985; Devary et al. 1987; Inoue et al. 1988; Toyoshima et al. 1990; Running Deer et al. 1995; Roger C. Hardie et al. 2004), leading to activation of Trp and Trpl channels (Alwai et al. 1972; Paj et al. 1976; J. Huang et al. 2010). Channel activation appears to involve a threshold level of NorpA activity (Pumir et al. 2008), as defects in $G_Q\alpha$ or NorpA activity can be rescued by modulating phosphoinositide metabolism through genetic or biochemical mechanisms (Roger C. Hardie et al. 2002). These steps represent the latency phase of the quantum bump as modulation of them strongly affects the latency distribution. NorpA may also be a target of feedback by Ca^{++}, as it has a bell-shaped dependence on Ca^{++} *in vitro* with peak activity around ~1 μM (Inoue et al. 1988; Toyoshima et al. 1990; Running Deer et al. 1995; Mitchell et al. 1995).

Inactivation and Negative Feedback

The inactivation of these molecules is tightly controlled. In addition to its phospholipase activity, NorpA acts as a GTPase-accelerating protein (GAP) for $G_Q\alpha$ (Chidiac et al. 1999; Cook et al. 2000), an activity which is required for efficient termination of the light response (T. Wang et al. 2008; Waldo et al. 2010). In addition, $G_{\beta e}$ exists in a two-fold excess over $G_Q\alpha$ (Elia et al. 2005), allowing it to suppress dark noise due to spontaneous $G_Q\alpha$ activation and ensure efficient termination of signaling (P. J. Dolph et al. 1994; Elia et al. 2005). Finally, a study which manipulated Ca^{++} levels via the Na^{+}/Ca^{++} exchanger *in vivo* found that NorpA phospholipase activity was suppressed with an IC_{50} of 76 μM in a partly InaC-dependent manner, suggesting that NorpA is a target of negative feedback (Gu et al. 2005). This is important for ensuring that PIP_2 is not depleted (Roger C. Hardie, P. Raghu, et al. 2001), as it is a limiting factor for the quantum bump amplitude (L. Wu et al. 1995) and is resynthesized on a minute timescale (Roger C. Hardie et al. 2004).

Adaptation

In response to prolonged visual signaling from metarhodopsin (Kosloff et al. 2003; Cronin et al. 2004), a fraction of $G_Q\alpha$ proportional to the light stimulus (Cronin et al. 2004) is translocated to the cell body within approximately 5 minutes (Kosloff et al. 2003; Cronin et al. 2004). It returns to the rhabdomere

within 1 hour (Cronin et al. 2004) through a mechanism which requires $G_{\beta e}$ (Frechter et al. 2007) and is sped up by the motor protein NinaC (Cronin et al. 2004; Frechter et al. 2007). This represents a form of adaptation as it decreases the sensitivity of the photoreceptor cells to light (Frechter et al. 2007).

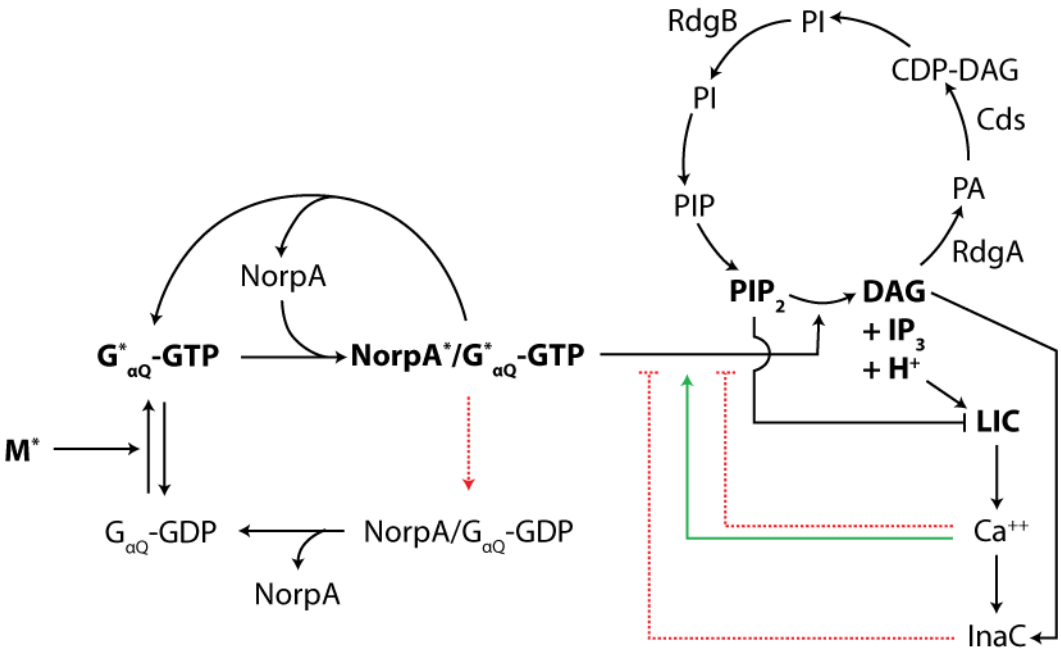

Figure 8: Transduction and Amplification

The reactions which transduce and amplify the signal from metarhodopsin (M*) to the light-induced current (LIC) are shown. Normal arrowheads indicate activation or stimulation, flat arrowheads indicate inhibition. Positive feedback is shown in green, negative feedback in dashed red. Asterisks indicate active species.

Output

Light-Induced Channels

Visual signaling leads to the opening of cation channels (Rama Ranganathan et al. 1991) formed from the Trp and Trpl proteins (Roger C. Hardie

et al. 1992; A. M. Phillips et al. 1992; B. A. Niemeyer et al. 1996). These channels are thought to be composed of non-rectifying Trp homomultimers which are highly permeable to Ca^{++} (Roger C. Hardie et al. 1992), outwardly-rectifying Trp/Trpl heteromultimers which are also highly permeable to Ca^{++} (X. Z. Xu et al. 1997), and outwardly-rectifying Trpl/Trpγ heteromultimers which are not very selective for Ca^{++} (Roger C. Hardie et al. 1992; X. Z. Xu et al. 2000).

Activation of the Trp Channels

Initially the channels were thought to be controlled by a Ca^{++} store-operated mechanism, as is typical for phosphoinositol signaling (Roger C. Hardie 1996a). However, much if not all of the light-induced Ca^{++} increase is carried by extracellular Ca^{++} (Asher Peretz, Sandler, et al. 1994; A Peretz, Suss-Toby, et al. 1994; Rama Ranganathan et al. 1994; Roger C. Hardie 1996b) and deletion of the IP_3 receptor which is required for the canonical store-operated mechanism has no effect on signaling (P. Raghu, N. J. Colley, et al. 2000). Genetic studies indicate the activator of the channel is generated downstream of the phospholipase NorpA (Paj et al. 1976) and upstream of the DAG lipase RdgA (P. Raghu, Usher, et al. 2000; Roger C. Hardie et al. 2003). The current model is that the channels are activated by NorpA-mediated depletion of inhibitory PIP_2 and release of protons (J. Huang et al. 2010).

Light-Induced Ca^{++} Influx

In addition to providing the electrical output of the pathway, channel opening results in a large increase in cytosolic Ca^{++}. The concentration of Ca^{++} rises from hundreds of nanomolar (Roger C. Hardie 1996b) to approximately 600 μM under dark-adapted conditions and 50 μM under light-adapted conditions in the rhabdomere (J. Oberwinkler and Stavenga 2000) and spreads into the cell body (Rama Ranganathan et al. 1994). This large Ca^{++} influx is removed by the Na^{+}/Ca^{++} exchanger CalX (B Minke et al. 1984; Schwarz et al. 1997; T. Wang et al. 2005) which is also in the rhabdomere (Johannes Oberwinkler and Stavenga 2000; T. Wang et al. 2005).

Feedback by Ca++

This influx of Ca^{++} is critical for the rapid kinetics of the response to light as it controls both positive and negative feedback of the macroscopic response (Rama Ranganathan et al. 1991) and quantum bump (S. R. Henderson et al. 2000). Ca^{++} can act directly, as is likely the case for positive feedback on NorpA (Inoue et al. 1988; Toyoshima et al. 1990; Running Deer et al. 1995; Mitchell et al. 1995). There are also two major negative feedback pathways activated by Ca^{++}: the protein kinase C InaC (Rama Ranganathan et al. 1991; Smith et al. 1991) and calmodulin (CaM) (K. Scott et al. 1997). In addition to the feedback targets described earlier, the channels themselves are direct targets of positive and

negative feedback (R C Hardie et al. 1994; Roger C. Hardie 1995) through an InaC-independent mechanism (Gu et al. 2005). At least in the case of Trpl, CaM is responsible for the negative feedback (K. Scott et al. 1997).

Ca^{++}-Mediated Adaptation

Ca^{++} increases in the cell body nearly linearly with the rate of quantum bump generation up to at least 20 μM (Johannes Oberwinkler et al. 1998). This pool of Ca^{++} changes with second-timescale dynamics (Rama Ranganathan et al. 1994), providing a mechanism for integrating signaling activity over long timescales. Adaptation is associated with decreased quantum bump amplitude (C. F. Wu et al. 1978; Johnson et al. 1986), which is likely caused largely by Ca^{++}-mediated decreased channel conductance (Gu et al. 2005). Ca^{++} also mediates light adaptation by triggering the translocation of Trpl out of the rhabdomere on a second timescale (Monika Bähner et al. 2002; Richter et al. 2011).

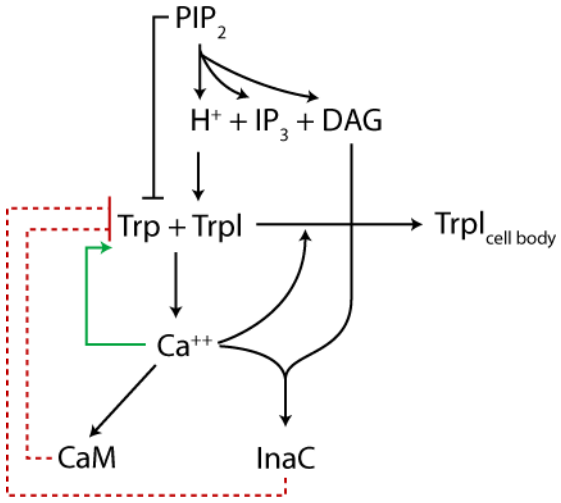

Figure 9: Activation and Regulation of Trp Channels

The reactions which activate and regulate the Trp channels are shown. Normal arrowheads indicate activation or stimulation, flat arrowheads indicate inhibition. Positive feedback is shown in green, negative feedback in dashed red. Asterisks indicate active species.

Dynamical Behavior

Pumir et al. analyzed the quantum bump using an ordinary differential equation model (Pumir et al. 2008). The model included activation of G proteins by rhodopsin, activation of NorpA by G proteins, generation of an unspecified activator molecule by NorpA which cooperatively activates the channels, influx of Ca^{++} ions which cooperatively increases the activation of the channels and is integrated by Ca^{++} buffers which cooperatively increase the inactivation of metarhodopsin, NorpA, the activator molecules, and the channels. The model was simulated using the Gillespie algorithm (Gillespie 1976) to account for the observed stochastic features of the system.

The 18 model parameters were estimated by fitting the statistical properties of simulated quantum bumps to experimentally-determined properties of wild-type quantum bumps. Specifically, the ratio of the half-width of the quantum bump to the time to peak, the average quantum bump shape, coefficient of variation of the amplitude, the number of NorpA molecules activated, and the smaller amplitude in the absence of Ca^{++} feedback were constrained. The model was then tested for the ability to explain the quantum bump properties of *arr2*^{3} and *dgq*^{1} flies.

The model revealed that the phototransduction system acts as a relaxation oscillator which under normal conditions inactivates itself after one oscillation. The refractory period is a result of the slowly-decaying negative feedback by the Ca^{++} buffers whose molecular identity was not specified in the model. The model also explained that quantum bumps are suppressed in the absence of metarhodopsin because there is a dynamic threshold of NorpA activity required to generate quantum bumps. These insights still need to be experimentally tested.

While the use of generic terms to describe the activator of the channels, the channels, and the negative feedback mediators simplified the equations underlying the model, it also means that these parts of the model may not be accurate and do not provide as much insight. For example, the model proposes that Ca^{++} is integrated by a buffer, but this is probably only a good description of negative feedback by calmodulin which exists in high concentrations in the

rhabdomere. InaC, in contrast, is part of the InaD scaffold and thus is probably better thought of as being discretely on or off on each scaffold. Furthermore, several of the feedback reactions, such as the negative feedback on the activator molecules and metarhodopsin, were included in the model out of necessity rather than prior knowledge. This provides useful predictions which can be experimentally tested, but again may represent areas in which the model is incorrect. Subsequent to the publication of this model, however, Roger Hardie's group showed that there is negative feedback on metarhodopsin through calmodulin-mediated release of Arr2 from NinaC (C.-H. Liu et al. 2008).

Scaffolding by InaD

Within the rhabdomere, the scaffolding protein InaD organizes several components of the visual signaling pathway (Figure 6) and plays an important role in facilitating and regulating signaling. Flies lacking InaD display defects in all aspects of visual signaling: latency, activation, inactivation, and deactivation (Susan Tsunoda et al. 1997; Kristin Scott et al. 1998).

Composition

InaD is composed of five PDZ domains in *Drosophila melanogaster* (Susan Tsunoda et al. 1997), although this varies considerably throughout the protein family (Figure 10). For example, PDZ1 is missing in many species, including *D. virilis* and *A. aegypti* (a mosquito). InaD is phosphorylated *in vivo*

(Hiroyuki Matsumoto et al. 1984) and *in vitro* by InaC (Armin Huber, Philipp Sander, and Reinhard Paulsen 1996; A. Huber et al. 1998; Mingya Liu et al. 2000), but no specific functional sites have been identified.

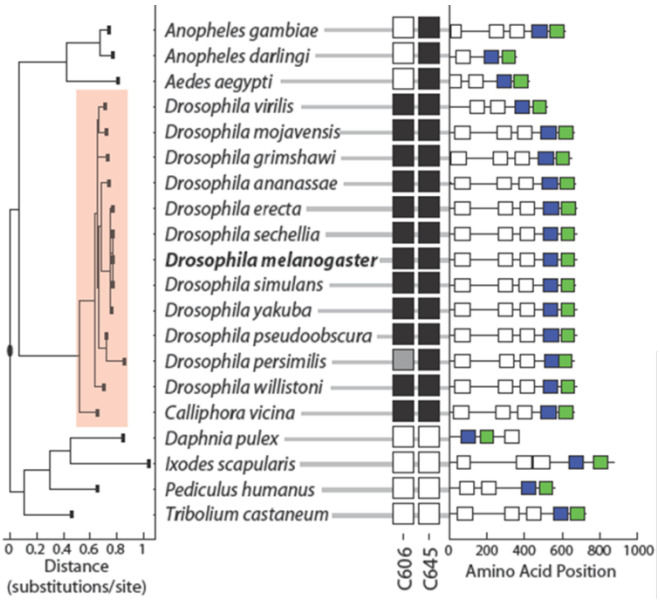

Figure 10: InaD Gene Family

The InaD gene family is shown. For each gene, the presence (black box) or absence (white box) of a cysteine at 606 and 645 is shown (gray box, the domain is unusual and there is a cysteine nearby). On the right, the domain structure of the gene is indicated with boxes representing PDZ domains. The PDZ4 and PDZ5 homologs are colored blue and green, respectively.

PDZ Domains

PDZ domains are small protein-protein interaction domains found in many scaffolding proteins (Nourry et al. 2003), including the Post-Synaptic Density, Discs-Large, and Zona-Occludens proteins for which the domain is named (Kennedy 1995). They occur in bacteria, yeast, plants, and metazoans (Ponting 1997). The domains are 80-90 amino acids in length and contain 5-6 β-strands and two α-helices (Morais Cabral et al. 1996) (Figure 11). They typically bind the

C-termini of proteins (H.-J. Lee and J. J. Zheng 2010), although there are some reports of non-C-terminal "internal" ligands (Hillier et al. 1999; H.-C. Wong et al. 2003; Penkert et al. 2004). In addition, some PDZ domains interact with phosphoinositides (Zimmermann et al. 2002; H. Wu et al. 2007).

Interaction with Ligands

C-terminal ligands bind in a β-strand conformation between the α2-helix and β2-strand with the carboxylate of the ligand coordinated by a loop at the N-terminus of the β2-strand (D. A. Doyle et al. 1996) (Figure 11). In general, the C-terminal ligand position (p0) interacts with β2-1, α2-8, and α2-5 (H.-J. Lee and J. J. Zheng 2010). The second to last position (p-1) was initially thought to not be important as it is often solvent exposed, but in some cases there are preferred residues and the position interacts with β2-2 and β3-5 or the β3-α1 loop (H.-J. Lee and J. J. Zheng 2010). The third to last position (p-2) contributes the most to the binding energy and plays an important role in determining specificity (D. A. Doyle et al. 1996; Z. Songyang et al. 1997; Tonikian et al. 2008). It interacts with α2-1 and α2-5 (H.-J. Lee and J. J. Zheng 2010).

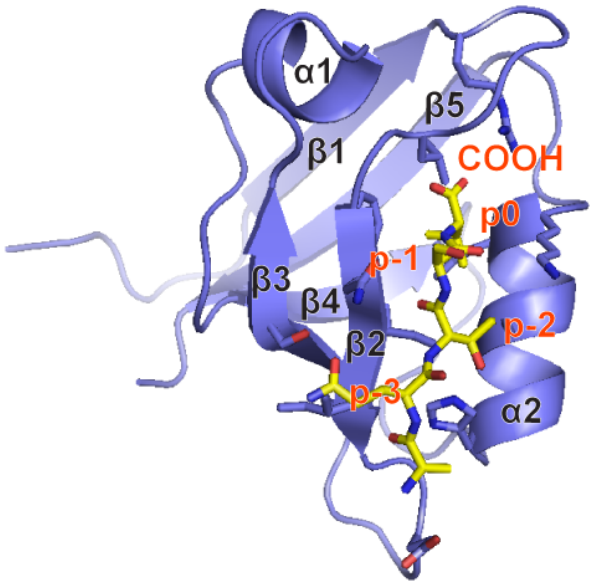

Figure 11: Structural Overview of the PDZ Domain

The third PDZ domain of PSD-95 (blue) bound to ligand (yellow) (PDB 1BE9) is shown. The secondary structural elements are labeled (black) along with the peptide positions (orange).

Domain Classification

PDZ domains were initially classified into three general classes based on their specificity for the C-terminal three residues of target proteins: Class I, S/T-X-ϕ; Class II, ϕ-X-ϕ; and Class III, D/E-X-ϕ , where ϕ is a hydrophobic residue and X is any residue (Z. Songyang et al. 1997). More recently, it has been shown that there are many possible classes (Tonikian et al. 2008) which are evenly distributed in sequence space (Stiffler et al. 2007). These studies have also revealed that specificity often involves more than just the last three residues (Stiffler et al. 2007; Tonikian et al. 2008).

Regulation of PDZ Domains

The interaction of PDZ domains with their ligands has been shown to be regulated in many cases (H.-J. Lee and J. J. Zheng 2010). Sometimes a serine or threonine in the C-terminal motif is phosphorylated, usually disrupting (Matsuda et al. 1999; H J Chung et al. 2000; J. Choi et al. 2002; Hee Jung Chung et al. 2004; Tian et al. 2006; Lin et al. 2007; von Nandelstadh et al. 2009) but sometimes promoting (Adey et al. 2000) binding. Alternatively, the binding pocket of the PDZ domain can be directly phosphorylated, disrupting binding (Raghuram et al. 2003; Mauceri et al. 2007; Voltz et al. 2007; Weinman et al. 2007). More interestingly, PDZ domains can be allosterically regulated. Multiple studies have shown that ligand binding results in propagated changes in protein dynamics out to two distal surfaces (Fuentes et al. 2004; Gianni et al. 2006; Niu et al. 2007; van den Berk, Landi, Walma, Vuister, Dente, and Hendriks 2007a; Petit et al. 2009). In addition, in the Par6 PDZ domain, binding of Cdc42 to the αA helix greatly increases its binding affinity (Garrard et al. 2003; Peterson et al. 2004).

Altered Properties of Tandem and Extended PDZ Domains

Another important aspect of PDZ domains is that they are often found in many copies in proteins. The domains are usually studied in isolation, but in several cases pairs of domains which occur close in primary sequence (“tandem

domains") have been examined. These tandem domains have been shown to have altered binding and folding properties (Grootjans et al. 2000; Q. Zhang et al. 2001; Feng et al. 2003; van den Berk, Landi, Walma, Vuister, Dente, and Hendriks 2007a; Long et al. 2008; W. Wang et al. 2009). In addition, several PDZ domains contain structural extensions on their N- and C-termini (C. K. Wang et al. 2010), which have been shown to alter the binding and folding of the domain (Petit et al. 2009; Bhattacharya et al. 2010).

Binding Partners

It is clear that InaD interacts with many core members of the visual signaling pathway; however, the true physiological binding partners have been difficult to identify due to the lack of quantitative measurements and *in vivo* experiments. The best supported ligands are NorpA, Trp, InaC, and NinaC. The evidence for these interactions is summarized in Table 1. The strongest claims can be made in cases in which the two proteins interact *in vitro*, co-immunoprecipitate *in vivo*, and the interaction can be disrupted by specific mutations in the two proteins, particularly in the C-terminus of the ligand where PDZ domains typically bind. In addition, it appears that localization to the rhabdomere requires InaD in many cases (Susan Tsunoda et al. 1997; H. S. Li et al. 2000; S Tsunoda et al. 2001), so loss of localization and age-dependent degradation in InaD mutants provide supporting evidence for an interaction. Finally, a signaling defect that

occurs due to loss of InaD binding based on additional evidence shows that the interaction with InaD is important.

Table 1: InaD Binding Partners

Protein	**Co-IP with InaD**	**Mislocalization and/or Degradation**	**Signaling Defect**	***In Vitro* Binding**	**References**
NorpA	Yes, disrupted by $inaD^{2}$ (PDZ5 mutant)	Both in $inaD^{1}$, $inaD^{2}$ (PDZ5 mutant), and $norpA^{Y1094S}$	Activation and deactivation in $norpA^{Y1094S}$ and $inaD^{2}$ (PDZ5 mutant)	GST-PDZ5 pull down, PDZ5 binding to NorpA C-terminal domain (no C-terminus) by ELISA binding	(B.-H. H. Shieh et al. 1997; Susan Tsunoda et al. 1997; van Huizen et al. 1998; Kristin Scott et al. 1998)
Trp	Yes, less with $inaD^{215}$ (PDZ3 mutant)	Both in $inaD^{1}$, $inaD^{215}$ (PDZ3 mutant), and $trp^{\Delta 1272}$	Inactivation in $inaD^{215}$	GST-PDZ3 pull-down, interacts with PDZ3 via its last 12 amino acids by overlay assay	(B. H. Shieh et al. 1996; Susan Tsunoda et al. 1997; H. S. Li et al. 2000)
InaC	Yes	Degradation in $inaD^{1}$	Deactivation in $inaC^{I700D}$	GST-PDZ4 pull down, interaction with PDZ2 via InaC C-terminus by Y2H	(Susan Tsunoda et al. 1997; Adamski et al. 1998)

Protein	Co-IP with InaD	Mislocalization and/or Degradation	Signaling Defect	*In Vitro* Binding	References
NinaC	Yes, disrupted by *ninaC*^{I1501E}	Neither, but its C-terminus is sufficient for rhabdomeric localization	Deactivation in *ninaC*^{I1501E}	GST-InaD pull down, interaction with PDZ1 via C-terminus by Y2H	(Wes et al. 1999)
CaM	n/d	n/d	n/d	Ca^{++}-dependent pull down by CaM	(Chevesich et al. 1997)

Functional Consequences of InaD Localization

As can be seen in Table 1, scaffolding of each protein by InaD has important but distinct functional consequences for signaling—and often these consequences are as severe as complete loss of the protein (Adamski et al. 1998; Wes et al. 1999). For example, NorpA must be associated with InaD in order to have rapid activation and deactivation of the light response (B.-H. H. Shieh et al. 1997; Susan Tsunoda et al. 1997; Kristin Scott et al. 1998). Trp, in contrast, must be associated with InaD in order to have rapid inactivation of the light response (B. H. Shieh et al. 1996; Susan Tsunoda et al. 1997; S. R. Henderson et al. 2000; H. S. Li et al. 2000). This may be due to a requirement of InaD for phosphorylation of Trp on S982 by InaC (Popescu et al. 2006). In addition, disruption of the binding of InaC to InaD has a similar phenotype as disrupting

the InaD-Trp interaction (Adamski et al. 1998). The InaD-NinaC interaction appears to be important in deactivation (Wes et al. 1999).

Dynamic Scaffolding

Mishra et al. recently showed that InaD PDZ5 reversibly oxidizes in response to visual signaling (Mishra et al. 2007) (Figure 12). This results in a distorted binding pocket, suggesting that the oxidation should be coupled to unbinding of PDZ5's ligand. The formation of the oxidized state requires InaC, which mediates negative feedback (Rama Ranganathan et al. 1991) and is known to phosphorylate InaD (Armin Huber, Philipp Sander, and Reinhard Paulsen 1996; Hiroyuki Matsumoto et al. 1984; Mingya Liu et al. 2000). Flies in which PDZ5 cannot oxidize lack a refractory period, hyperadapt, and are unable to perceive short periods of darkness.

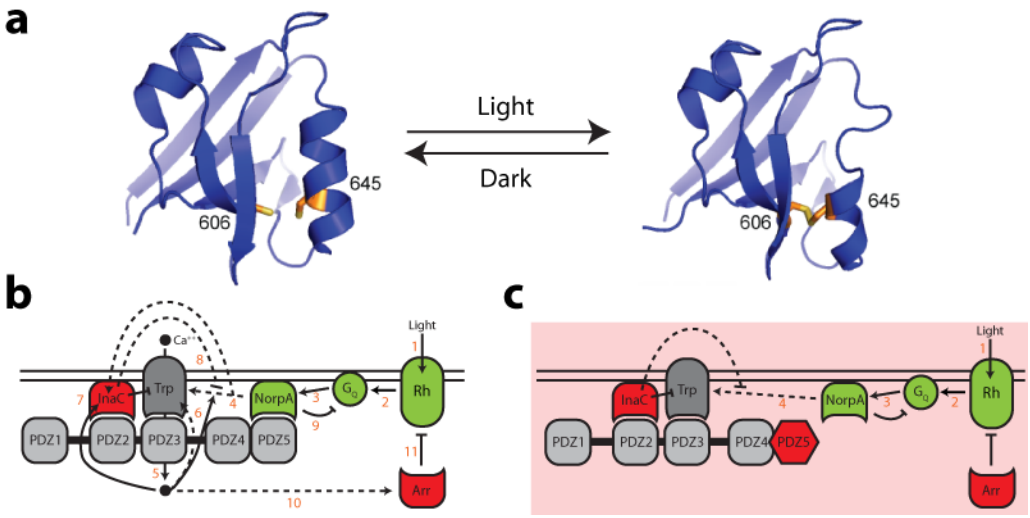

Figure 12: Dynamic Scaffolding by InaD

(a) Cysteines 606 and 645 of InaD PDZ5 reversibly oxidize in response to visual signaling, distorting the binding pocket of the domain. (b) The reduced state is expected to bind its ligand (NorpA), producing the signaling pathway as shown in Figure 6. (c) The oxidized state, in contrast, triggers a refractory period during which signaling is suppressed. This is likely due to loss of scaffolding of NorpA.

Motivations for this Dissertation

I believe the most interesting aspect of biology is its capacity to teach us new design principles that are distinct from engineering. *Drosophila* phototransduction is potentially a rich source of this information, given its clear evolutionary pressure for high performance and exemplification of all the interesting elements of signaling systems: information processing through a relay of multiple proteins and small molecules; a network of highly non-linear interactions with multiple feedback loops; organization by both compartmentalization and a modular scaffold; a clear role for noise as a

fundamental feature and limitation; and evidence of extensive adaptation on organismal and evolutionary timescales.

In my work, I focused on three levels of structure in the *Drosophila* photoreceptor cell: the microvilli which comprise the rhabdomere, the InaD scaffolding protein, and the functional architecture inside a domain of InaD. At each level, I sought to use quantitative approaches with an evolutionary mindset. My hope was that this approach would facilitate the discovery of fundamental design principles of this system.

CHAPTER THREE

The Role of Compartmentalization by Microvilli

Introduction

Intracellular signaling is organized on two spatial scales. On the scale of microns signaling is compartmentalized into organelles or distinct regions of the cell. Interactions with scaffolding proteins or other molecules locally organize signaling on the scale of nanometers. Extensive studies on the role of nanometer-scale signaling organization have revealed its importance in promoting the speed, selectivity, and efficiency of signaling. The role of micron-scale organization is less well studied but is primarily thought to provide specificity by spatially segregating signals.

Phototransduction in the *Drosophila* photoreceptor cell is a classic model of high-performance signaling which exemplifies these two types of organization (Roger C. Hardie and P. Raghu 2001). On the micron scale, Ca^{++}, the central regulator in the pathway, is present both within the cell body as well as the specialized organelle known as the rhabdomere which is composed of 30,000 microvilli (Rama Ranganathan et al. 1994). These microvilli play an important role in facilitating light absorption by increasing the available surface area for

rhodopsin molecules four-fold (Roger C. Hardie et al. 1993). However, microvilli also are the fundamental transduction unit in this system, as the maximal rate of quantum bump generation is approximately equal to the maximum turnover rate of all the microvilli (Hochstrate et al. 1990) and each microvillus contains the same number of channels that are activated during a quantum bump (Roger C. Hardie and P. Raghu 2001).

Many intracellular signals have been shown to be spatially heterogeneous, with high concentrations near the source that dissipate over hundreds of nanometers. These signaling "nanodomains" are thought to provide specificity by restricting the signal response to the region immediately surrounding the source. Within each microvillus of the rhabdomere, there are approximately 60 InaD complexes which co-scaffold the Trp channels with the Ca^{++}-sensitive upstream activator NorpA, the Ca^{++}-dependent negative feedback mediator InaC, and the calmodulin-regulated motor protein NinaC (Rama Ranganathan et al. 1991; Smith et al. 1991; A. Huber, P. Sander, et al. 1996; B. H. Shieh et al. 1996; Chevesich et al. 1997; Susan Tsunoda et al. 1997; Adamski et al. 1998; Wes et al. 1999). While this organization by InaD is similar to that seen in other systems which utilize nanodomains, the small size of a microvillus makes it unclear whether distinct nanodomains could exist within the rhabdomere. Furthermore, heterogeneous signaling within the rhabdomere would seem to conflict with the role of microvilli in concertedly producing quantum bumps.

How does each of these levels of organization contribute to the amazing speed and efficiency of signaling in the photoreceptor cell? A problem in addressing this is the lack of intuitive understanding of the properties of signals in microvilli. In the first part of this chapter, I use theoretical modeling and simulations to gain a quantitative and intuitive understanding of microvillar signaling. In the second part, these predictions are tested experimentally using quantitative measurements of localized Ca^{++} dynamics *in vivo*.

I find that Ca^{++} signaling in the rhabdomere is homogeneously distributed with digital-like fast, high-amplitude dynamics, a characteristic that can be explained by the unique physical properties of microvilli. While organization by InaD is critical for the visual response, Ca^{++} dynamics are no different at InaD than at other locations in the rhabdomere. These findings demonstrate the central importance of micron-scale organization on signaling dynamics.

Modeling of Ca^{++} Spatiotemporal Dynamics

Construction of a Partial Differential Equation Model

To better understand how the unique geometry of microvilli would affect the spatiotemporal dynamics of Ca^{++} signaling, my collaborator Boris Shraiman and I constructed a partial differential equation model inspired by work by (Postma et al. 1999). Our model accounted for localized influx through 15 ($n_{Trp,T}$) randomly-distributed Trp channels ($n_{Trp}(x)$), homogeneous efflux (Johannes

Oberwinkler and Stavenga 2000) (k_{efflux}), and diffusion (D_{Ca}) along the length of a microvillus and into the cell body (Figure 13):

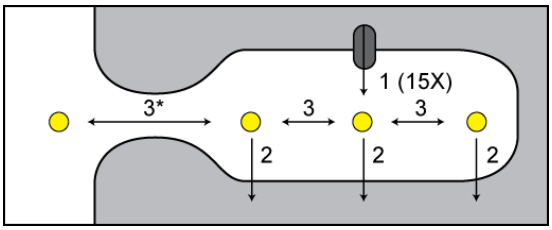

Figure 13: Spatiotemporal Model of Ca^{++} in the Rhabdomere

The model accounts for (1) localized influx through 15 Trp channels, (2) homogeneous efflux by the Na^{+}/Ca^{++} exchanger CalX, and (3) diffusion within and (3*) out of the microvillus.

Equation 1: Partial Differential Equation Model for Rhabdomeric Ca^{++}

$$\frac{\partial[\mathrm{Ca}^{++}](t,x)}{\partial t} = a\frac{n_{\mathrm{Trp}}(x)}{n_{\mathrm{Trp,T}}}\frac{\sigma_{\mathrm{Ca}}}{V_x}I_{\mathrm{QB,norm}}(t) - k_{\mathrm{efflux}}[\mathrm{Ca}^{++}](t,x)$$

$$+ D_{\mathrm{Ca}}\nabla^2[\mathrm{Ca}^{++}](t,x)$$

$$D_{\mathrm{Ca}}\frac{\partial}{\partial \mathrm{x}}[\mathrm{Ca}^{++}](t,x)|_{x=l_{\mathrm{m}}} = 0$$

$$[\mathrm{Ca}^{++}](t,x)|_{x=0} = [\mathrm{Ca}^{++}]_{\mathrm{cell}}$$

The channel mole influx (σ_{Ca}) was modeled using the Goldman-Hodgkin-Katz current equation (Hille 2001), which states that the flux (ϕ, in A/cm^2) through a membrane is:

Equation 2: Goldman-Hodgkin-Katz Current Equation

$$\phi_S = Pp_S z_s^2\left(\frac{EF^2}{RT}\right)\frac{\left([\mathrm{S}] - [\mathrm{S}]_{\mathrm{ext}}\exp\left(-\frac{z_s FE}{RT}\right)\right)}{1-\exp\left(-\frac{z_s FE}{RT}\right)}$$

This model primarily contains physical constants, such as the charge on the ion (z_s); E, the membrane potential; F, Faraday's constant; R, the ideal gas constant; T, the temperature; and [S] and $[S]_{ext}$, the concentrations of the ion on the inside and outside of the membrane (in mM), respectively. The two parameters are P, the total permeability of the membrane, and p_s, the relative permeability of the ion s. Since the extracellular concentration of each ion is much greater than the intracellular concentration and the membrane potential is highly negative, we can simplify this equation by removing the contribution of the outward flux through the channels. To calculate the current, I multiply ϕ_s by the surface area. The surface area (cm^2) and the permeability (m/s) can be combined into one unknown parameter, κ (with units of dL/s). That produces this simplified equation:

Equation 3: Simplified Goldman-Hodgkin-Katz Current Equation

$$\sigma_x = \kappa \alpha \beta_x$$

$$\alpha = \frac{EF}{RT}$$

$$\beta_x = \frac{z_x p_x \mathrm{e}^{-z_x \alpha}}{1 - \mathrm{e}^{-z_x \alpha}} X_{\mathrm{ext}}$$

In the simulations, a discrete number ($n_{\mathrm{Trp,T}}$) of channels are randomly placed ($n_{\mathrm{Trp}}(x)$) along the length of a microvillus. The mole flux through the channels is divided by the local volume (V_x) to obtain the flux in terms of concentration.

Rather than explicitly model the signaling reactions, I scaled the total channel mole influx (σ_{Ca}) by the time-dependent amplitude of a normalized dark-adapted or light-adapted quantum bump ($I_{QB,norm}$). Under light-adapted conditions, the channel influx was linearly decreased (a) to match the observed decrease in quantum bump peak current.

The remaining two terms account for Ca^{++} efflux and diffusion. Efflux by the sodium-calcium exchanger CalX was modeled as a first-order homogeneous process since it is unknown how many exchangers are present in each microvillus. Diffusion was modeled using the standard approach, Fick's law (Berg 1993).

The two boundary conditions indicate that there is no flux at the tip of a microvillus (l_m) and that the concentration of Ca^{++} in the cell body is constant ($[Ca^{++}]_{cell}$). These are good assumptions, as the first corresponds with a physical boundary and the second is known to change on a much slower timescale than the quantum bump.

Estimation of Parameters

The two unknown parameters describing the channel influx and the efflux rate were estimated from (1) the peak amplitude of a quantum bump and (2) the peak Ca^{++} concentration of a dark-adapted photoreceptor cell. These two constraints can be written as:

Equation 4: Constraints for Estimating the Model Parameters

$$\frac{I_{\mathrm{QB}}}{F} \cong \alpha(z_{\mathrm{Ca}}\sigma_{\mathrm{Ca}} + z_{\mathrm{Na}}\sigma_{\mathrm{Na}}) + \frac{V_{\mathrm{m}}}{n_{\mathrm{Ca:CalX}}} k_{\mathrm{efflux}}\mathrm{Ca}_{\mathrm{peak}}$$

$$\mathrm{Ca}_{\mathrm{peak}} = \frac{\frac{\alpha\sigma_{\mathrm{Ca}}}{V_{\mathrm{m}}}}{k_{\mathrm{efflux}} + \frac{D}{l_{\mathrm{m}}^2}}$$

where I_{QB} is the peak amplitude of the quantum bump, V_m is the volume of the microvillus, and $n_{Ca:CalX}$ is the number of Na^+ ions per Ca^{++} ions transported by CalX.

The first equation states that the ion flux at the peak of the quantum bump, in terms of moles, is equal to the Ca^{++} and Na^+ fluxes through the Trp channels plus the net flux through the Na^+/Ca^{++} exchanger. The second equation is the spatially-averaged steady-state solution of the model. Simultaneously solving these two equations for κ, the channel flux parameter, and k_{efflux}, the efflux rate, we get:

Equation 5: Equations Determining the Estimated Model Parameters

$$\kappa = \frac{\frac{I_{\mathrm{QB}}}{F} + \frac{V_{\mathrm{m}}\mathrm{Ca}_{\mathrm{peak}}D}{n_{\mathrm{Ca:CalX}}l_{\mathrm{m}}^2}}{\alpha(z_{\mathrm{Ca}}\beta_{\mathrm{Ca}} + z_{\mathrm{Na}}\beta_{\mathrm{Na}})\left(1 + \frac{\beta_{\mathrm{Ca}}}{n_{\mathrm{Ca:CalX}}(z_{\mathrm{Ca}}\beta_{\mathrm{Ca}} + z_{\mathrm{Na}}\beta_{\mathrm{Na}})}\right)}$$

$$k_{\mathrm{efflux}} = \frac{\kappa\alpha\beta_{\mathrm{Ca}}}{V_{\mathrm{m}}\mathrm{Ca}_{\mathrm{peak}}} - \frac{D}{l_{\mathrm{m}}^2}$$

For a 9 pA quantum bump with a peak Ca^{++} concentration of 700 µM, κ is 5.4×10^{-12} dL/s and k_{efflux} is 10^4 s^{-1}. This permeability results in the Trp channels

passing 2.2 x 10^{-17} moles of Ca^{++} per second, or approximately 8 mM/ms given the volume of a microvillus, when open. The calculated efflux rate is several orders faster than the previous estimate of 1.2 s^{-1} which was probably limited by diffusion from the cell body to the rhabdomere (T. Wang et al. 2005) ($l = \sqrt{\frac{D_{\mathrm{Ca}}}{k}} =$ 13.8 μm assuming a diffusion-limited step).

Table 2: Parameters of Ca^{++} Model

Parameter	Value
$[Ca^{++}]_{ext}$	1.5 mM (Hofstee et al. 1996)
$[Na^{+}]_{ext}$	120 mM (Hofstee et al. 1996)
D_{Ca}	220 $\mu m^2/s$ (Allbritton et al. 1992)
E	-60 mV
k_{efflux}	1.07E4 s^{-1}
l_m	1 μm (Roger C. Hardie 1985)
l_{neck}	0.06 μm (E Suzuki et al. 1993)
n_{Trp}	15 (Roger C. Hardie and P. Raghu 2001)
p_{Ca}	0.85 (H. Reuss et al. 1997)
p_{Na}	0.02 (H. Reuss et al. 1997)
$r_{Ca:CalX}$	3 (Gu et al. 2005)
r_m	0.03 μm (Roger C. Hardie 1985)
r_{neck}	0.0175 μm (Boschek 1971)
V_m	2.8E-18 L
z_{Ca}	2
z_{Na}	1
κ	5.4E-12 dL/s

Somatic Ca^{++} Dynamics

This model can also be used to understand the behavior of the cell soma. For this purpose, it is useful to rewrite the model in terms of the light-induced current. To do this, we must first determine the ratio of the current which is carried by Ca^{++}. This can be found by calculating the fraction of the current

carried by each ion from the Goldman-Hodgkin-Katz equation (Equation 1) and the efflux through the Na^+/Ca^{++} exchanger:

Equation 6: Ratio of the Light-Induced Current Carried by Ca^{++}

$$r_{\mathrm{Ca}} = \frac{z_{\mathrm{Ca}}\sigma_{\mathrm{Ca}}}{\sigma_{\mathrm{Ca}}\left(z_{\mathrm{Ca}} + \frac{k_{\mathrm{efflux}}}{n_{\mathrm{Ca:CalX}}\left(k_{\mathrm{efflux}} + \frac{D}{l_{\mathrm{m}}^2}\right)}\right) + z_{\mathrm{Na}}\sigma_{\mathrm{Na}}}$$

The fraction of rhabdomeric Ca++ that diffuses into the cell body can be determined by realizing Ca^{++} leaves either via efflux (k_{efflux}) or diffusion to the cell body ($\frac{D}{l_{\mathrm{m}}^2}$):

Equation 7: Fraction of Ca^{++} that Diffuses into the Soma

$$f_{\mathrm{soma}} = \frac{\frac{D}{l_{\mathrm{m}}^2}}{k_{\mathrm{efflux}} + \frac{D}{l_{\mathrm{m}}^2}}$$

The dynamics of somatic Ca++ can then be written as:

Equation 8: Somatic Ca^{++} Dynamics

$$\dot{\mathrm{Ca}}_{\mathrm{soma}} = \frac{f_{\mathrm{soma}} r_{\mathrm{Ca}}}{zFV_{\mathrm{c}}} I - \frac{D}{l_{\mathrm{c}}^2}\mathrm{Ca}_{\mathrm{soma}}$$

where I is the light-induced current, l_{c} is the average length of the cell body to the rhabdomere, and V_{c} is the volume of the cell. The dynamics of the cell body are dominated by diffusion from the cell body to the rhabdomere ($\frac{D}{l_c^2}$), which occurs on a timescale of seconds. The steady-state solution for the soma is:

Equation 9: Steady-State Solution for Somatic Ca^{++}

$$\mathrm{Ca}_{\mathrm{soma}} = \frac{f_{\mathrm{soma}} r_{\mathrm{Ca}}}{zFV_{\mathrm{c}}\left(\frac{D}{l_{\mathrm{c}}^2}\right)}\mathrm{I}$$

This shows that somatic Ca^{++} increases linearly with the light-induced current in the absence of buffering, as observed experimentally (Johannes Oberwinkler et al. 1998).

Simulations

I simulated the model using the finite difference method, which converts a partial differential equation into a series of ordinary differential equations in which the spatial locations have become state variables (Fall et al. 2002). Similar to the approach used by Postma et al (Postma et al. 1999), I only considered dynamics along the length of the microvillus as diffusion in that dimension occurs much slower. For the simulations, I used an evenly spaced grid with 50 locations along the length of the microvillus.

The simulations revealed two intriguing features. First, the dynamics were surprisingly fast. As a result, Ca^{++} rapidly equilibrates following single channel opening, reaching a stable distribution in under a millisecond (Figure 14). Ca^{++} dynamics are also not limiting during dark-adapted (Figure 15a) or light-adapted (Figure 15c) responses. Secondly, we do see substantial gradients (~50%) depending on the relative location of the channels despite the small size of a microvillus. If the localization is random, however, then on average there is only a

steep gradient near the base of a microvillus where it contacts the cell body (Figure 15b,d). Thus, the modeling predicts that Ca^{++} should have fast dynamics with high amplitude and a homogeneous distribution on average.

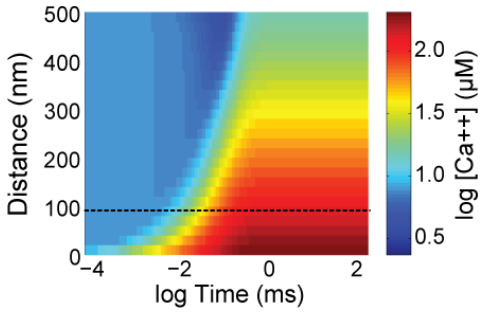

Figure 14: Predicted Spatiotemporal Dynamics of Ca^{++} Following Opening of a Single Channel

The spatiotemporal dynamics of Ca^{++} following opening of a single channel are shown. The distance axis indicates the distance from the pore. The dashed black line indicates the predicted average inter-channel distance in the rhabdomere. Note that a steady-state distribution is reached within 1 ms and that there is a substantial steady-state gradient, consistent with the literature on Ca^{++} nanodomains.

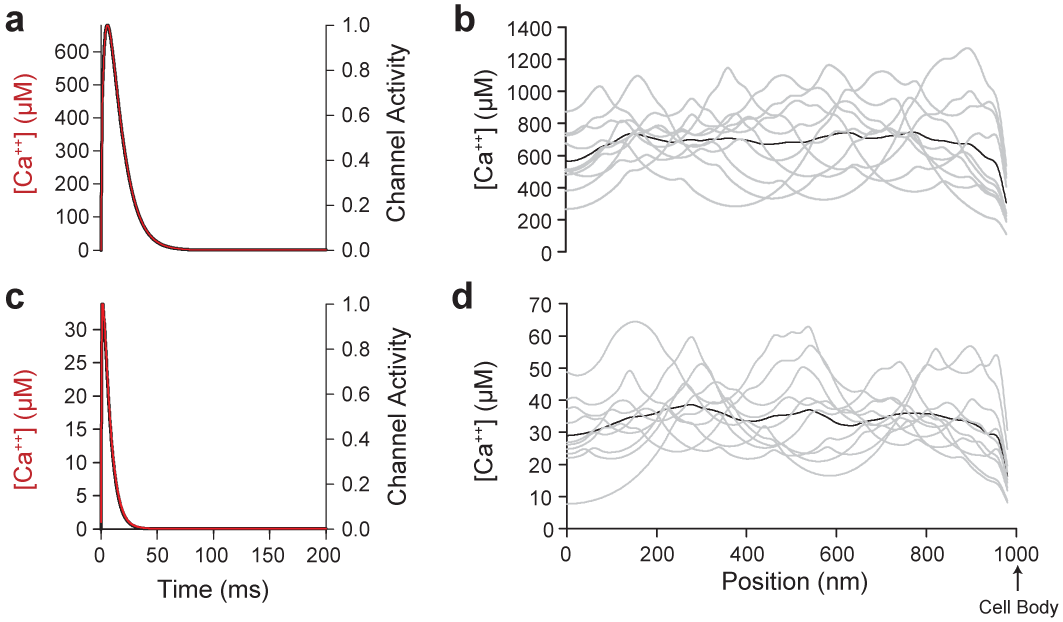

Figure 15: Predicted Spatiotemporal Dynamics of Ca^{++} During a Quantum Bump

The spatiotemporal dynamics of Ca^{++} during a quantum bump are shown for (a-b) dark-adapted and (c-d) light-adapted conditions. (a,c) The spatially-averaged concentration of Ca^{++} (red) is shown as a function of time and is overlaid with the channel dynamics (black). (b,d) The spatial profile at the peak of the quantum bump is shown for individual runs (gray lines) and the average of many runs (black line).

Measurement of Localized Ca^{++} Dynamics

Camgaroo-Based Sensors of Localized Ca^{++}

To test these predictions of homogeneously-distributed, rapid Ca^{++} signaling in the rhabdomere, Adrienne Hahn developed reagents to measure Ca^{++} at specific sites within the photoreceptor cell (Hahn 2004) using the genetically-encodable yellow-fluorescent-protein-based Ca^{++} sensor Camgaroo (Baird et al. 1999). She expressed free Camgaroo (Cyto-Camga) as a sensor for the cell body,

and fused Camgaroo to Arrestin-2 (Camga-Arr2) and InaD (Camga-InaD and InaD-Camga) for sensors of the rhabdomere (Kiselev et al. 2000) and InaD complex, respectively (Figure 16).

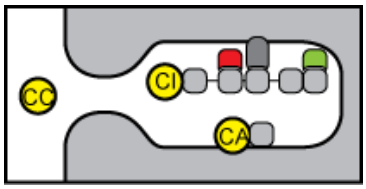

Figure 16: Illustration of the Strategy for Measuring Localized Ca^{++} Responses

The three sensors were designed to measure Ca^{++} in the cell body (CC, Cyto-Camga), rhabdomere (CA, Camga-Arr2), and InaD complex (CI, Camga-InaD/InaD-Camga).

With the help of W. Ryan Williamson, I confirmed the localization of the sensors by immunofluorescence (Figure 17a). In contrast with Cyto-Camga, both Camga-Arr2 and Camga-InaD are detected primarily in the rhabdomere. This can also be seen in images of the fly pseudopupil, which is an image formed from ~20 ommatidia (Franceschini et al. 1971). Both Camga-Arr2 and Camga-InaD have fluorescent pseudopupils, while Cyto-Camga has a fluorescent eye but dark pseudopupil (Figure 17b).

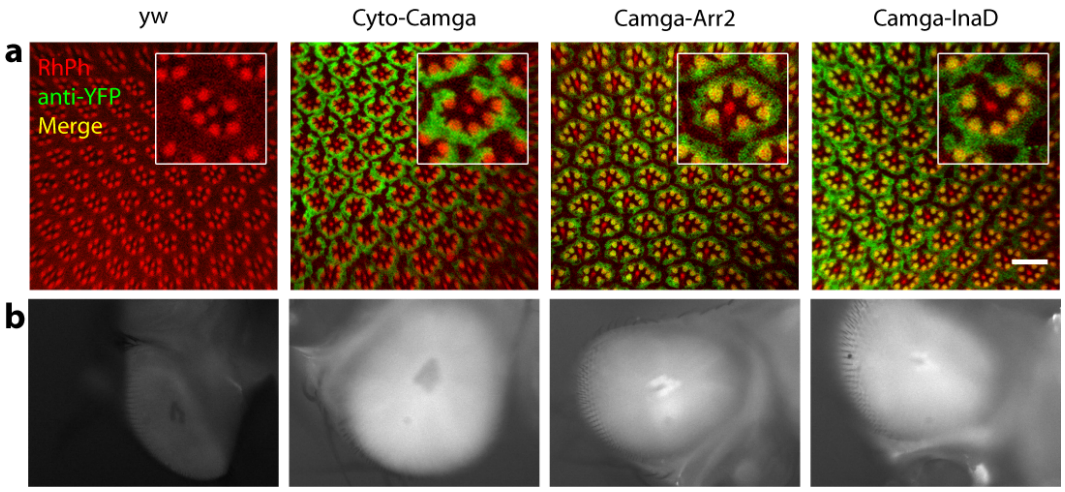

Figure 17: Localization of Camgaroo Sensors

The intracellular localization of the Camgaroo sensors was determined by (a) immunofluorescence using rhodamine-labeled phalloidin to detect actin filaments in the rhabdomere and anti-YFP to detect Camgaroo, and (b) pseudopupil imaging showing YFP fluorescence.

To test whether the sensors perturbed the light response, I measured the statistics of quantum bumps from each and compared them with wild-type flies. I found that they did not disrupt the activation or inactivation of the visual response (Figure 18), suggesting that there is no significant change in the behavior of the tagged proteins.

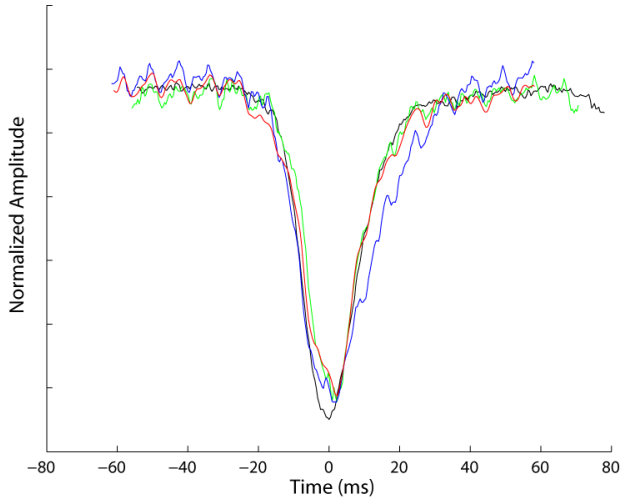

Figure 18: Average Quantum Bump Shape of Camgaroo Flies

Quantum bumps were measured in yw (wild-type, black), Cyto-Camga (green), Camga-Arr2 (blue), and Camga-InaD (red) flies. The average normalized quantum bump shape for each is shown.

Consequences of Uncorrelated Quantum Bumps at Steady-State

An additional experimental challenge to studying Ca^{++} dynamics in the rhabdomere is that the quantum bumps that occur at steady-state are not correlated (Dodge et al. 1968; C. F. Wu et al. 1978) due to the random nature of the refractory period (C.-H. Liu et al. 2008). Because I observe an average over many microvilli at steady-state, direct information about the dynamics of Ca^{++} at steady-state is lost. However, the dynamics of Ca^{++} affect the statistics of the noise, suggesting it may be possible to recover this information (Figure 19).

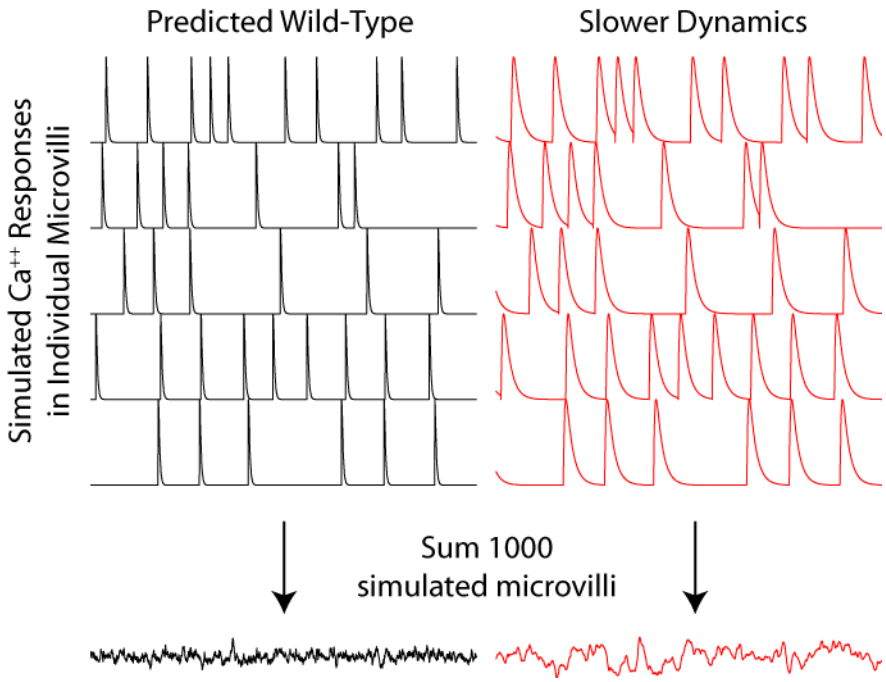

Figure 19: Effect of Uncorrelated Quantum Bumps on the Ca^{++} Measurement

Simulated Ca^{++} responses separated by refractory periods of random length are shown for several independent microvilli with (black) the predicted wild-type properties or (red) slower dynamics. Summing 1000 of these responses leads to a flat response with noise which is related to the quantum bump dynamics.

We can think about the steady-state measurement analytically to understand how the dynamics of Ca^{++} are encoded in the steady-state measurement. In the simplest case in which Ca^{++} switches digitally between two levels, the steady-state observation is the average of these two states, weighted by the time spent in each state. More generally, this can be thought of as the time average of the Ca^{++} response during a typical quantum bump:

Equation 10: Analytical Form of the Ca^{++} Steady-State Distribution

$$\mathbf{Ca_{ss}} = \frac{1}{\boldsymbol{\tau_{ref}}} \int_0^{\boldsymbol{\tau_{ref}}} \mathrm{Ca}(t)dt$$

where τ_{ref} is the refractory period length, which on average is much longer than the duration of an adapted quantum bump (C. F. Wu et al. 1978; M. Juusola et al. 2001).

However, the refractory period is highly stochastic, ranging from 50-1000 ms (C.-H. Liu et al. 2008). As a result, the steady-state Ca^{++} measurements come from a random distribution (Figure 20). When the refractory period is much longer than the quantum bump—which is what occurs on average—the steady-state Ca^{++} concentration is approximately just the basal concentration. However, when the refractory period is short, the average Ca^{++} concentration increases dramatically. Because the refractory period is only rarely short, this introduces a positive skew to the predicted Ca^{++} measurement distribution.

By systematically varying the amplitude, kinetics, and basal level of the quantum bump Ca^{++} response, it is possible to determine how each of these properties affects the measurement distribution (Figure 20). I found that each had a distinct effect: The basal concentration shifts the mean of the distribution, while the peak concentration nearly uniformly changes the variance. The most dramatic effect is seen with decreasing the efflux rate kinetics, which greatly increases the variance and introduces a large positive skew. Because each of these parameters

produces distinct phenotypes, it should be possible to estimate them from real measurements.

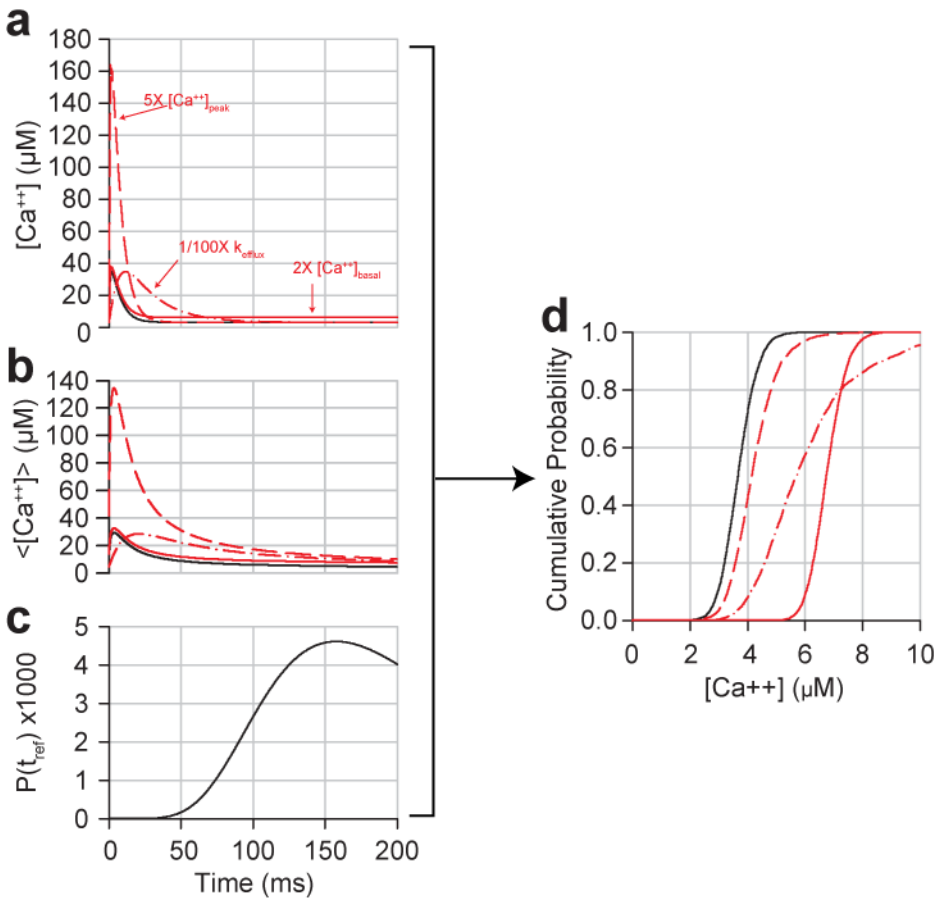

Figure 20: Dependency of the Ca^{++} Measurement Distribution on Ca^{++} Response Parameters

(a) Ca^{++} responses during a simulated quantum bump are shown with the (black) predicted parameters or (red) perturbations to the basal or peak concentration and the efflux rate. (b) The average Ca^{++} concentration over the Ca^{++} responses from (a) is calculated by integrating from 0 to the indicated time. (c) A subset of the refractory period distribution, indicating how it relates to the dynamics of the quantum bump. (d) Using the refractory period distribution from (c) and the average Ca^{++} curve from (b), it is possible to predict a measurement distribution. Note that the rare observation of much higher average Ca^{++} concentrations introduces positive skew.

Steady-State Ca++ Measurements

Next, I measured the localized steady-state calcium concentration by illuminating patch-clamped, dissected photoreceptor cells with blue light. This simultaneously excites Camgaroo and activates rhodopsin, allowing me to monitor each sensor during visual signaling. The fluorescence of all three sensors quickly rose and relaxed to a steady-state under constant blue light (Figure 21). To show that the fluorescence changes were related to Ca^{++} signaling, Adrienne Hahn recorded from blind *norpA*^{P41} flies and wild-type flies in the absence of extracellular Ca^{++}—neither showed any change in fluorescence (Hahn 2004).

Normalization of the Ca^{++} Response

To normalize the fluorescence, I measured the initial fluorescence, which was similar to the fluorescence after treatment with the Ca^{++}-chelator EGTA, and the fluorescence following treatment with the Ca^{++} ionophore ionomycin. The normalized fluorescence was then converted to a concentration using the Camgaroo binding curve (K_D = 7 μM, n = 1.3) measured by Adrienne Hahn (Hahn 2004) (Figure 21).

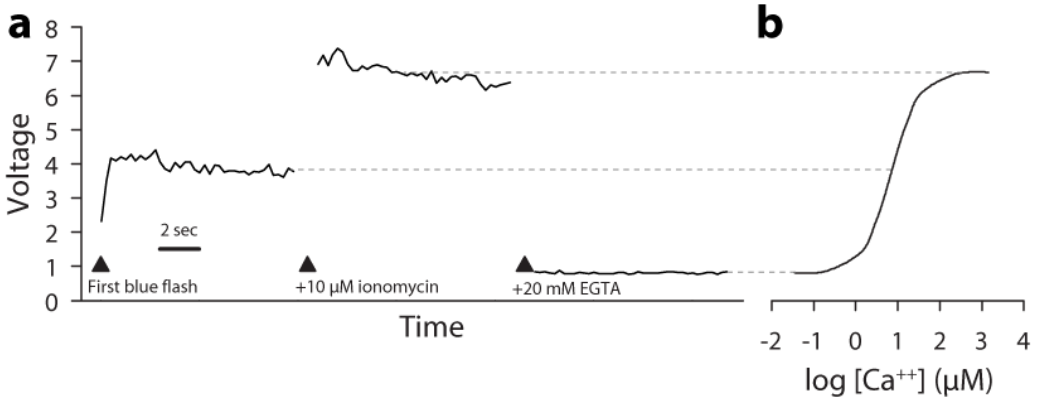

Figure 21: Normalization of the Ca^{++} Response

(a) The raw fluorescence response of an InaD-Camga fly is shown following the initial exposure to blue light, treatment with 10 µM ionomycin to increase intracellular Ca^{++}, and lastly treatment with 20 mM EGTA to decrease Ca^{++}. (b) The fluorescence response was normalized and then converted to Ca^{++} concentration using the dose response curve of Camgaroo.

Comparison of Steady-State Responses under Physiological Ca^{++} Conditions

Under physiological extracellular Ca^{++} conditions, the average intracellular Ca^{++} concentration detected by each of the sensors rose over a few hundred milliseconds to ~8 µM and then decreased over several seconds to a steady-state concentration of ~4 µM (Figure 22). The responses of the three sensors were indistinguishable, which is not surprising since the theory predicted that average of the Ca^{++} measurement distribution is approximately just the basal Ca^{++} concentration which is likely similar to the cytoplasmic concentration.

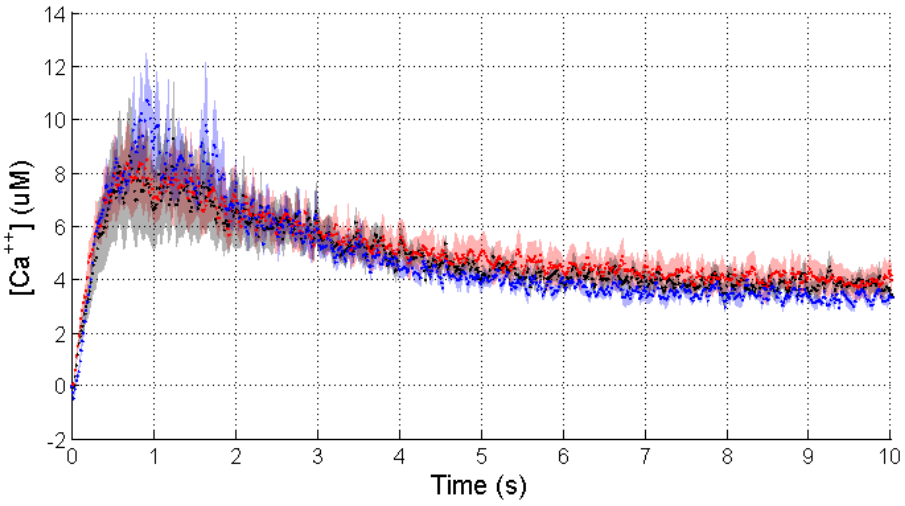

Figure 22: Ca^{++} Responses with Physiological Extracellular Ca^{++}

The Ca^{++} response of Cyto-Camga (black), Camga-Arr2 (blue), and Camga-InaD (red) is shown under physiological extracellular Ca^{++} conditions (1.5 mM). The shaded areas indicate the standard error of the mean.

Effect of Extracellular Ca^{++} on the Steady-State Ca^{++} Response in the Rhabdomere

The properties of the quantum bump are known to be strongly dependent on the extracellular Ca^{++} concentration (S. R. Henderson et al. 2000) due to its role in feedback (Rama Ranganathan et al. 1991). As the extracellular Ca^{++} concentration is decreased, there is a strong transition at 100 µM where the latency peaks, amplitude decreases, and duration increases (S. R. Henderson et al. 2000). If the response of the rhabdomeric sensors matches Cyto-Camga because the quantum bump is much faster than the refractory period, then changing the extracellular Ca^{++} concentration may reveal this effect.

Using another InaD sensor, InaD-Camga, developed by Adrienne Hahn which was shown by her to be properly localized (Hahn 2004), I tested the steady-state response under various extracellular Ca^{++} conditions (Figure 23). I found that the steady-state Ca^{++} concentration when there was greater than ~200 µM extracellular Ca^{++} matched the results measured with the three sensors described in the previous section. However, at 100 µM there was a large and highly cell-to-cell variable increase in the steady-state Ca^{++} concentration. Below 90 µM, there was very little increase in Ca^{++} upon illumination. This suggests that the rhabdomeric response does indeed strongly relate to quantum bump dynamics.

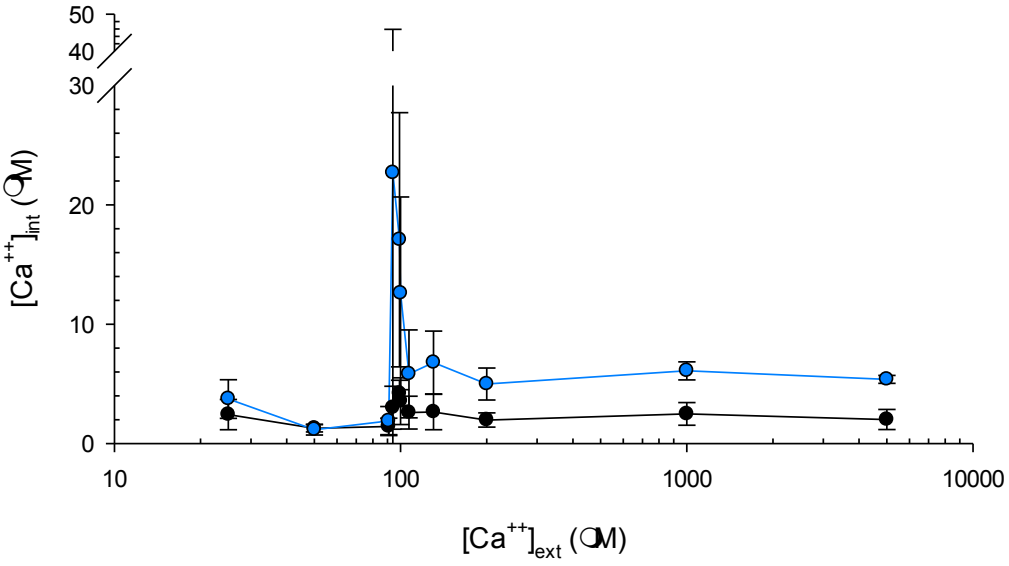

Figure 23: Dependency of Steady-State Ca^{++} on Extracellular Ca^{++}

The initial (black) and steady-state (blue) Ca^{++} measured by InaD-Camga is plotted as a function of extracellular Ca^{++}.

Comparison of Steady-State Responses under Low Ca^{++} Conditions

Given the strong extracellular Ca^{++} dependency, I repeated the steady-state measurements at 100 µM extracellular Ca^{++} under patch-clamped conditions with the Cyto-Camga and Camga-InaD sensors (Figure 24). Cyto-Camga detected an increase of ~2 µM Ca^{++} that lacked the initial peak observed previously and there was less noise at steady-state. Camga-InaD, in contrast, varied highly between cells, ranging from a small increase with low noise as observed in Cyto-Camga to a large, continuously increasing Ca^{++} response with high noise. This indicated that the rhabdomeric sensors are indeed detecting something distinct from Cyto-Camga and pointed to the measurement noise as the primary location of this information.

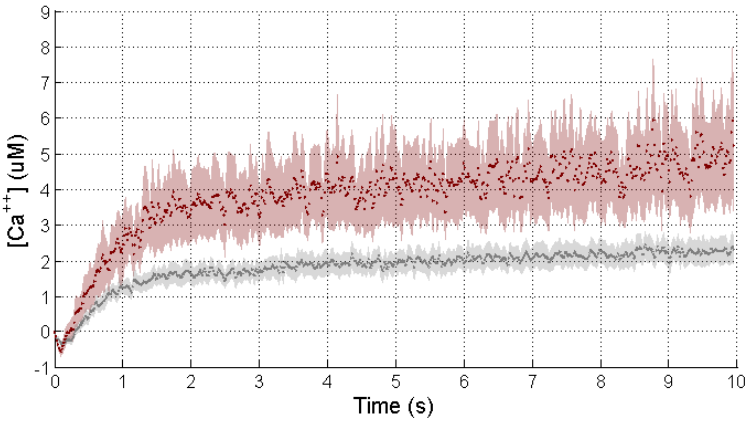

Figure 24: Ca^{++} Responses with 100 µM Extracellular Ca^{++}

The average Ca^{++} response of Cyto-Camga (gray) and Camga-InaD (red) with 100 µM extracellular Ca^{++} is shown. The shaded area indicates the standard error of the mean.

Estimation of Ca^{++} Signaling Properties from Measurement Fluctuations

If Ca^{++} is indeed spiking much faster than the quantum bump at steady-state, then it should be possible to see this in the shape of the measurement distribution, as I predicted. A convenient way to compare the shapes of distributions is to plot the distributions in what is known as a QQ plot (Wilk et al. 1968). In this plot, the percentiles of each distribution are plotted against each other. The power of this is that linearly related distributions fall on a straight line. Deviations from a linear relationship indicate differences in the shape of the distribution, such as the positive skew we expect the rhabdomeric sensors to have. Comparing the normalized distributions of the measurements (Figure 25a), I found that both Camga-Arr2 and Camga-InaD on average have more positive skew than is observed in Cyto-Camga, as predicted (two-way ANOVA comparing the deviations to a random model, P=1.5e-10 and 1.7e-23, respectively). In addition, Camga-Arr2 and Camga-InaD approximately come from linearly related distributions (two-way ANOVA comparing the deviations to a random model, P=0.04, deviations are smaller in magnitude), suggesting that they sense the same Ca^{++} fluctuations at steady-state.

Next, I used simulated annealing to estimate the properties of the Ca^{++} dynamics from the single-cell measurement distributions of Camga-Arr2 and Camga-InaD (Figure 25b-e). The estimates were strikingly similar between the

two sensors, indicating that the basal Ca^{++} concentration is similar to that found in the cell body and that Ca^{++} spikes to tens of micromolar, decaying with rapid kinetics. The estimated efflux rate is similar to the value I calculated for the model, and the basal and peak Ca^{++} concentrations are similar to previous estimates for the adapted response (J. Oberwinkler and Stavenga 2000).

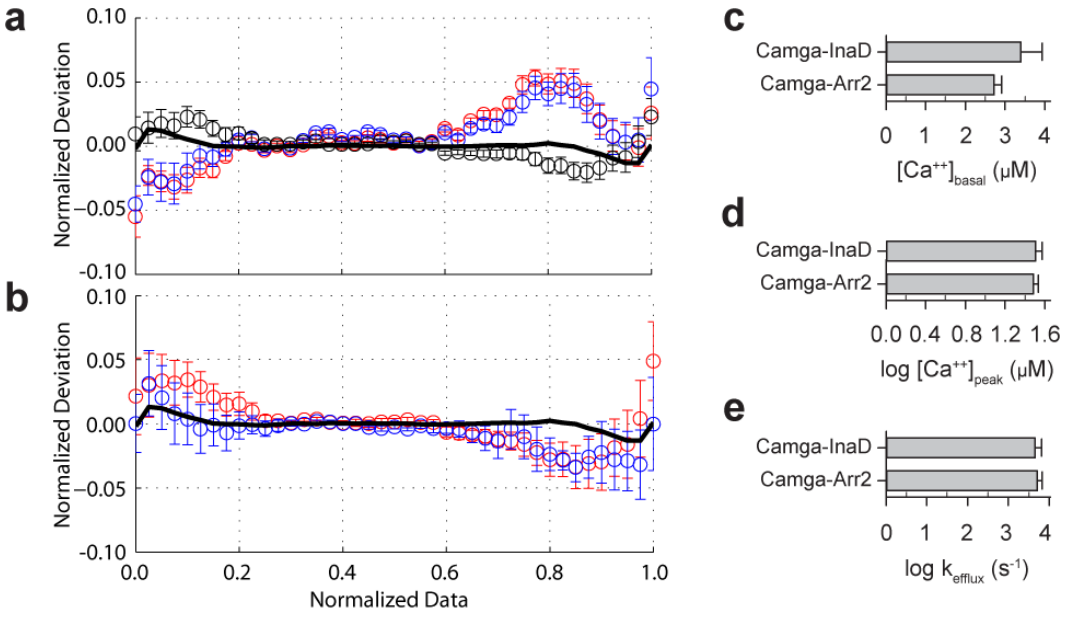

Figure 25: Analysis of the Ca^{++} Measurement Distributions

(a) The steady-state Ca^{++} measurement distributions were normalized and compared to each other using a quantile-quantile (QQ) deviation plot. A linear relationship in the quantiles indicates that the distributions have the same shape. For each pair of distributions, the quantile of one distribution is plotted against the difference in the quantiles of the two distributions in order to emphasize the difference in distribution shape. The average of these comparisons is shown for (y vs x) (blue) Camga-Arr2 vs Cyto-Camga, (red) Camga-InaD vs Cyto-Camga, and (black) Camga-InaD vs Camga-Arr2. The solid black line is a random model comparing normalized finite sampled normal distributions. The deviations from the line in the y axis for the two comparisons with Cyto-Camga indicate that the rhabdomeric sensors experience slightly more positive skew than Cyto-Camga. (b) A QQ deviation plot comparing the measurement distributions for Camga-Arr2 (blue) and Camga-InaD (red) vs. the model fit. The solid black line is the same random model from (a). The deviations are not significant (two-way ANOVA between the deviations and a random model). (c-e) The individual cell measurement distributions were fit by simulated annealing to the theoretical distribution model. The resulting estimates for (c) basal Ca^{++}, (d) peak Ca^{++}, and (e) efflux rate are shown. The error bars indicate the standard error of the mean.

Consequences for Signaling

These results show that compartmentalization enables Ca^{++} signaling to happen on two timescales. Somatic Ca^{++} integrates the average rate of signaling on the timescale of seconds (Figure 26a). It also influences the basal Ca^{++}

concentration in the rhabdomere (Figure 26b) and thus may slowly titrate feedback processes (Gu et al. 2005). In contrast, rhabdomeric Ca^{++} dynamically changes on the millisecond timescale (Figure 26b). These millisecond changes in Ca^{++} occur uniformly across the compartment and reach much higher concentrations than observed in typical nano- or microdomains. As a result, Ca^{++}-dependent positive and negative feedback should be kinetically limited during the quantum bump (Figure 26c), activating nearly instantaneously across a microvillus as Ca^{++} binds following the opening of the first channel. After the channels close, the feedback should inactivate nearly at the rate of unbinding of Ca^{++}, as this is slower or on the same timescale (~10^2-10^4 s^{-1}) as efflux for a low micromolar affinity diffusion-limited binder. In addition, the peak Ca^{++} concentration is sufficiently high to activate most of the Ca^{++} feedback processes (Gu et al. 2005), even under light-adapted conditions. Thus, proteins mediating Ca^{++}-feedback likely signal in a digital manner during the quantum bump, rapidly switching on and off as fast as they can bind and unbind Ca^{++}.

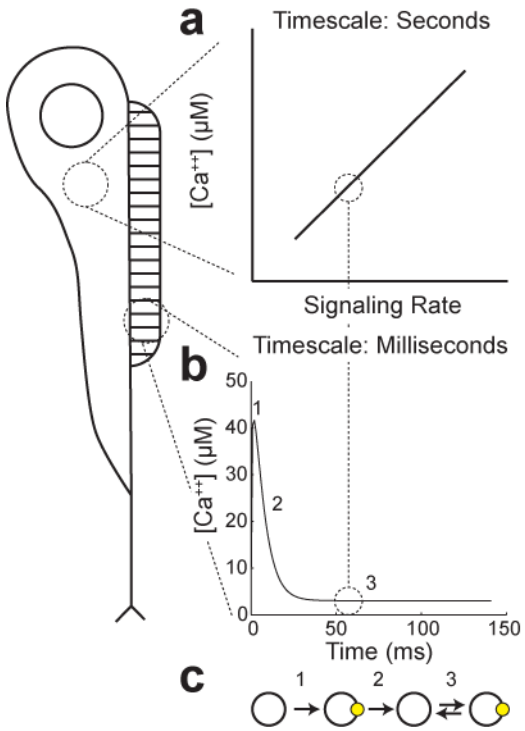

Figure 26: Distinct Signaling Modes in the Cell Body and Rhabdomere

(a) In the soma, Ca^{++} changes with second-timescale dynamics proportionally with the signaling rate. (b) Rhabdomeric Ca^{++}, in contrast, changes with millisecond timescale dynamics. (c) Ca^{++} is sufficiently high amplitude and rapid in the rhabdomere that it may act digitally. (1) The initial peak may activate Ca^{++} feedback in a kinetically-limited manner, followed by (2) kinetically-limited unbinding. (3) During the refractory period, the basal concentration is coupled to the cell soma, providing a mechanism to slowly titrate feedback processes.

Physical Analysis of Properties of Signaling Compartments

Microvilli are uniquely suited to achieve these properties. The equilibration timescale of a compartment is $\frac{l}{2nD}$, where l is the length, D is the diffusion coefficient, and n is the number of dimensions. Since the equilibration timescale of a compartment increases with the length of its longest axis, a larger compartment would result in a slower equilibration time (Figure 27a). Similarly,

the peak amplitude (C_{peak}) of a compartmentalized signal at steady-state originating from a source of rate r_{influx} with surface density ρ is a function of the surface area (A) to volume (V) ratio: $0 = \frac{r_{influx}\rho A}{V} - k_{efflux}C_{peak}$, which simplifies to $C_{peak} = \frac{r_{influx}}{k_{efflux}}\rho\frac{A}{V}$. Since the surface area to volume ratio is always a function of $\frac{1}{l}$, the relative density of channels or the activity level of each channel must increase linearly with the radius of a spherical or cylindrical compartment to achieve the same peak Ca^{++} concentration (Figure 27b). This may be physically impossible as the rhabdomeric membrane is already thought to be exceptionally densely packed.

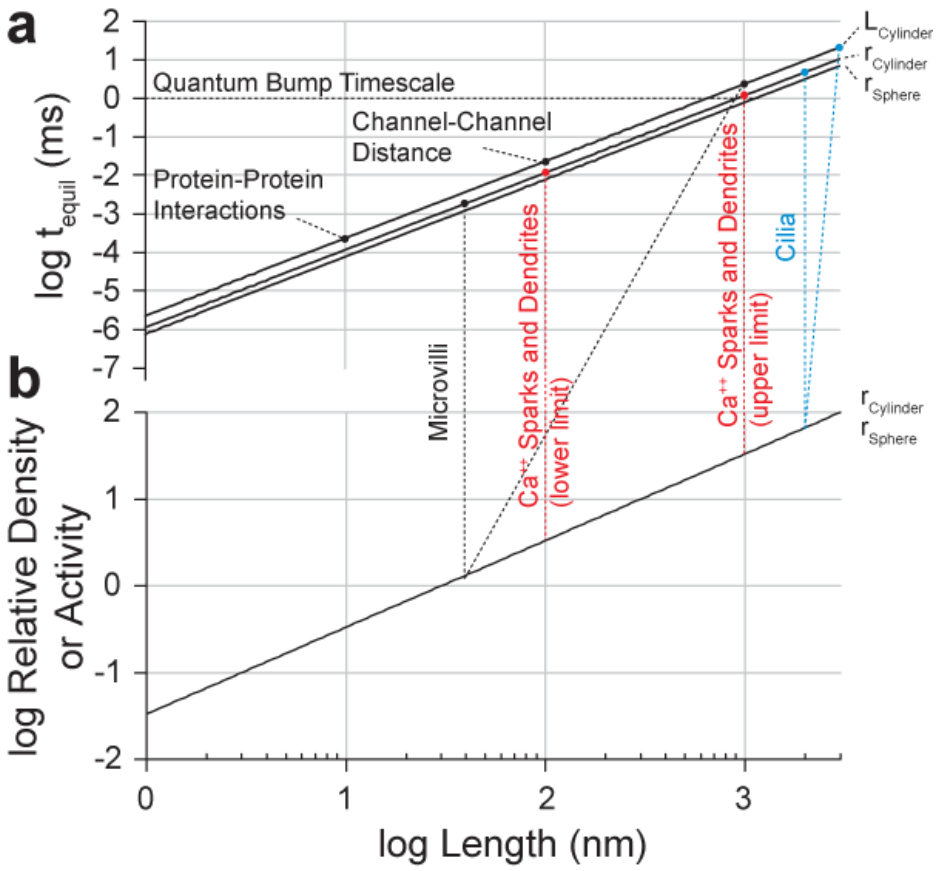

Figure 27: Physical Constraints on Compartments

Various physical compartments found in cells are shown with their typical dimensions plotted against the (a) equilibration time of the compartment along the length or radius and (b) the relative density or activity of the signal source that is needed to maintain the same peak amplitude.

Conclusions

In closing, these results indicate a role for micron-scale organization in shaping the dynamics of signaling. *Drosophila* phototransduction is widely renowned for its exceptional speed and sensitivity. These results show that these features can partially be explained as the physical consequence of signaling in microvilli independently of the role of the scaffolding protein InaD or

specializations of visual proteins. Microvilli on their own impart rapid equilibration and high amplitude to diffusible signals due to their short length and small volume. This allows them to act as digital compartments, rapidly switching between low and high signaling states. Micron-scale organization of signaling proteins may be an important influence on the dynamics of many other physiological systems.

Methods

Calcium Simulations

The Ca^{++} PDE model was discretized onto a one-dimensional equally-spaced 50 point grid spanning 1 μm in length corresponding to a cylinder with a 30 nm radius. The flux term between the microvillus and the cell body was adjusted to account for the narrow neck (cylinder of 60 nm length and 17.5 nm radius). Calcium simulations of the set of ODEs were then performed in MATLAB (MathWorks) by the ode15s stiff multistep solver which uses the numerical differentiation formulas algorithm. The full MATLAB script can be seen in Appendix B.

Flies

y w (yellow-bodied, white-eyed) flies were used as the "wild-type" strain. Flies expressing the Camgaroo fusions under the Rh1 promoter were generated by P-element transformation by Adrienne Hahn (Hahn 2004). The lines used here are

y w;;P[y^{+}, Cyto-Camga]#15 (“Cyto-Camga”), *y w P[y^{+},Camga-Arr2]#38* (“Camga-Arr2”), *y w;P[y^{+},Camga-InaD]#25* (“Camga-InaD”), and *y w;;P[y^{+},InaD-Camga]#6* (“InaD-Camga”).

Immunofluorescence

Retinal tissue from virgin flies was prepared with assistance from W. Ryan Williamson (Robin Heisinger lab) according to the method described in (Williamson et al. 2010). Following fixation, the samples were incubated overnight in PBS + 0.3% Triton-X 100 with 1:200 monoclonal anti-GFP (MMS-118P from Covance) to detect Camgaroo and 1:1000 rhodamine-labeled phalloidin (Invitrogen) to detect actin. The samples were washed two times with PBS + 0.3% Triton-X 100 and then incubated for 2 hours with PBS + 0.3% Triton-X 100 with 1:1000 Alexa488-conjugated goat anti-mouse secondary antibody (Invitrogen, kindly provided by Steven Altschuler and Lani Wu). Finally, the samples were washed 4X for 10 minutes with PBS + 0.3% Triton-X 100 and mounted by gluing the retinas on a Sylgard-coated slide in VectaShield mouting media (Vector Labs). The samples were imaged on a Zeiss confocal microscope in the lab of Robin Heisinger.

Fluorescent Pseudopupil Imaging

Fluorescent pseudopupil imaging was performed on a Zeiss fluorescence stereomicroscope. Flies were immobilized by inserting them head-first into a

snipped 10 μL pipette tip, allowing just the eyes to pass through. Yellow fluorescence imaging (Zeiss filter set 46, excitation filter: 500 ± 25 nm bandpass, emission filter: 535 ± 30 nm) was then performed with mercury lamp illumination. The microscope was focused slightly below the surface of the eye in order to visualize the pseudopupil.

Quantum Bump Measurements

Ommatidia were prepared according to the method described in (Rama Ranganathan et al. 1991) by dissecting the retina in Ringer's solution (125 mM $CsCl_2$, 10 mM HEPES, 30 mM sucrose pH 7.1) under dim red light, tearing the retina several times, and then triturating ~5X through a 10 μL pipette tip. The cells were added to bath solution (120 mM NaCl, 5 mM KCl, 10 mM HEPES, 4 mM $MgCl_2$, 24 mM proline, 5 mM alanine, 1.5 mM $CaCl_2$ pH 7.1 or as otherwise indicated). Ommatidia were then subjected to whole cell patch clamp using series resistance compensation. The patch pipette contained 95 mM K-gluconate, 40 mM KCl, 10 mM HEPES, 2 mM $MgCl_2$, 4 mM Mg-ATP, 0.5 mM Na-GTP, 1 mM NAD^+, adjusted to pH 7.15 with KOH. Cells with reversal potentials between -40 and -70 mV were used. The signal was amplified through an Axopatch 200B (Axon Instruments), filtered at 200 Hz (LPF-8, Warner Instrument), and digitized at 10 kHz (PCI-6052E DAQ Board, National Instruments). Quantum bumps were measured by dim laser flashes which successfully produced responses less than 50% of the time. Quantum bumps were detected and fit in MATLAB

(MathWorks) by processing with a 25 ms moving average filter and detecting deviations of more than 2 standard deviation with amplitude greater than 3 pA, duration greater than 9 ms, peak time greater than 6 nm, half-rise time of less than 50 ms, and total duration less than 150 ms. The average shape was calculated by normalizing by the amplitude and aligning the midpoint between the half-rise and half-inactivation times. The MATLAB analysis scripts are in Appendix B.

Camgaroo Fluorescence Measurement

Camgaroo fluorescence was measured using a photodiode in patch-clamped cells (except for the InaD-Camga data in Figure 23) by illuminating with 30 Hz pulsed 488 nm light from a dye laser that was filtered through a blue-violet narrow neutral band filter (NBV, Olympus). Following measurement of the light response, the cells were treated with 10 μM ionomycin (+ 10 mM Ca^{++} if the bath solution had less than 1 mM) for a few minutes to measure the fluorescence under high Ca^{++}, and then 20 mM EGTA to confirm the low Ca^{++} state. Because EGTA treatment distorted the cell morphology, the initial fluorescence measurement was typically used for the low Ca^{++} state. A small amount of photobleaching was detected in the ionomycin fluorescence recordings; this was fit in each cell by a biexponential curve and used to correct for photobleaching in all recordings. The normalized fluorescence measurements were converted to Ca^{++} concentrations using the Camgaroo Ca^{++} binding curve, as described in the text. The full MATLAB analysis script is in Appendix B.

Analysis of Ca^{++} Measurements

The Ca^{++} measurements were analyzed in MATLAB (MathWorks). The Ca^{++} response curves were processed with a 20-point (600 ms) moving average filter to remove slow components. The noise characteristics of the processed response became stable after approximately 5 s; this was considered steady-state. The steady-state measurement samples were fit by simulated annealing to Equation 10. The Ca^{++} response used was an analytical fit of the light-adapted quantum bump ($\frac{1}{\Gamma(n)\tau\left(\frac{t}{\tau}\right)^{n}\exp\left(-\frac{t}{\tau}\right)}$, $\tau = 0.0054$, $n = 0.2834$), convolved with a single exponential decay of rate $k_{efflux,}$ scaled by $[Ca^{++}]_{peak}$ and shifted by $[Ca^{++}]_{basal}$. The refractory period times measured in (C.-H. Liu et al. 2008) were fit to a general generalized extreme value distribution ($\mu = 175$ ms, $\sigma = 82$ ms, $k = 0.24$) and used to sample Equation 10. The quality of the fit was scored by measuring the deviation of the measured and experimental distributions from a unity relationship on a QQ plot, as in Figure 25, which involves calculating the summed squared error in the difference of the percentiles of the two distributions. The full MATLAB analysis script is in Appendix B.

CHAPTER FOUR

Modularity of Dynamic Scaffolding by InaD

Introduction

Scaffolding proteins are thought to promote the evolvability of signaling pathways by decomposing the regulatory and catalytic activities of proteins into modular elements which can then be easily replaced (Bhattacharyya et al. 2006). These modular elements are generally thought to be individual protein domains, structural units which have homologs in many proteins (Creighton 1993). Consistent with this view, the yeast mating scaffold Ste5 is unaffected when its protein interaction domains are replaced with other domains which are capable of recruiting the same binding partners (S.-H. Park et al. 2003). In addition, recruitment of novel interaction partners to the scaffold changes the signaling dynamics (Bashor et al. 2008). However, recent work has shown that many structural domains are not independent (C. K. Wang et al. 2010), provoking the question of whether this view may be too simplistic.

Intriguingly, the InaD scaffold shows signs of phenotypic modularity. InaD promotes the sensitivity, activation, and inactivation of the light response by coordinating many of the core reactions of the signaling pathway (see chapter 2). In addition to a null allele, two InaD mutants occurring in the PDZ3 and PDZ5 domains were previously identified in genetic screens (B. H. Shieh et al. 1996;

Susan Tsunoda et al. 1997). These mutations specifically disrupt inactivation and activation, respectively, suggesting that the effects of InaD on vision can be modularly decomposed.

The potentially modular role for InaD PDZ5 is particularly interesting as the Ranganathan lab recently found it is dynamically regulated during the visual signaling cycle (Mishra et al. 2007). In response to visual signaling, cysteines 606 and 645 of PDZ5 oxidize, distorting the binding pocket of the domain (Figure 12). The oxidized state is required for generation of a refractory period following channel opening. Intriguingly, the two cysteines are a recent evolutionary innovation found only in fast-flying flies (Figure 10), suggesting that this dynamic scaffolding system was easy to engineer into PDZ5.

Isolated from the rest of InaD, however, PDZ5 does not recapitulate the behavior seen *in vivo*. PDZ5 *in vitro* does not bind its physiological partner NorpA and has a disulfide bond that is too strong to be reduced under physiological conditions (Mishra et al. 2007). While this may be due to unidentified regulatory factors, it is also possible that PDZ5 is not independent from the rest of InaD.

In this chapter, I identify PDZ4 as a necessary component for the binding of PDZ5 to its physiological ligand, NorpA. In addition, PDZ4 acts as an allosteric inhibitor of disulfide bond formation in PDZ5. While PDZ5 is therefore not an independent module, bioinformatic techniques suggest that PDZs 4-5 have

coevolved together in many proteins independently from the rest of InaD and likely represent a true module.

Identification of NorpA as the Physiological Binding Partner of PDZs 4-5

InaD PDZ5 is thought to bind to NorpA, a phospholipase C β involved in activation of the visual response (Alwai et al. 1972; Paj et al. 1976; J. Huang et al. 2010). The best evidence for this comes from studies on two mutants in flies. The first, *inaD*^{2} (G605E), is a mutation in PDZ5 which causes mislocalization of NorpA *in vivo*, reduced sensitivity, a long, highly stochastic latency, and slow activation and inactivation of the visual response (Susan Tsunoda et al. 1997). Later it was shown that a C-terminal mutation in NorpA, Y1094S, also disrupted NorpA localization and resulted in similar effects on the visual response (B.-H. H. Shieh et al. 1997). While reports of qualitative pull-down binding assays and other experiments have supported the claim that NorpA binds to PDZ5 (B.-H. H. Shieh et al. 1997; Susan Tsunoda et al. 1997; van Huizen et al. 1998), these studies did not use highly purified proteins and I and other members of the Ranganathan lab have not been able to reproduce these findings (Figure 28, Figure 29).

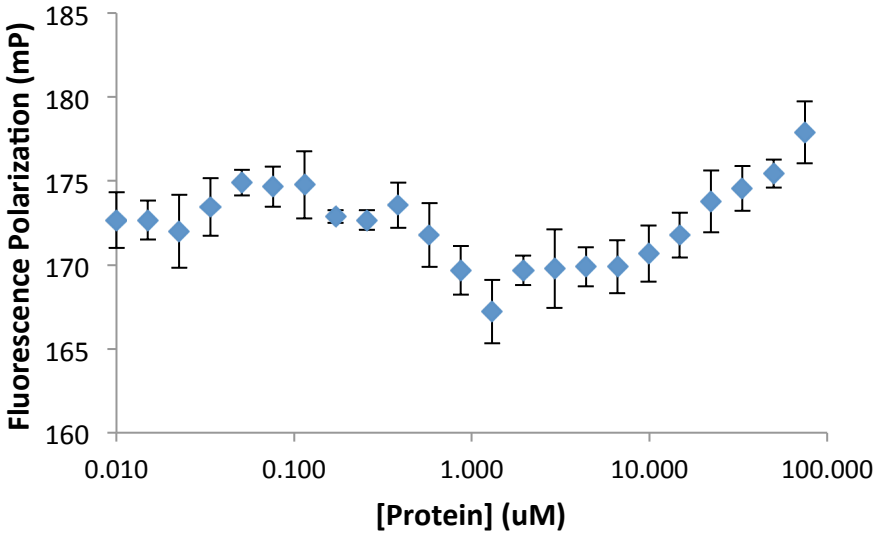

Figure 28: Fluorescence Polarization Measurement of Binding of PDZ5 C645S to NorpA C-terminal Peptide

The binding of PDZ5 C645S to a rhodamine-labeled C-terminal peptide of NorpA was measured by fluorescence polarization. There was no significant titration up to 100 μM as indicated by the lack of a significant change in polarization.

Several recent reports have indicated that the folding and binding properties of some PDZ domains are sensitive to N- and C-terminal extensions, which are often other PDZ domains (C. K. Wang et al. 2010). InaD PDZ4 is separated from PDZ5 by a short linker (six amino acids in *Drosophila melanogaster*) throughout the InaD gene family (Figure 10, Appendix A). Thus, we hypothesized that PDZ4 may alter the properties of PDZ5.

Pull-Down Binding Assay

I first screened the binding properties of PDZ5 and PDZs 4-5 (PDZ45) with the C-terminal domain (CTD) of NorpA (869-1095) using a pull-down assay

(Figure 29). The CTD is a coiled-coil structural domain of phospholipase C β proteins which also contains the C-terminus of the protein (Singer et al. 2002), the putative ligand for PDZ5. I incubated purified PDZ5 and PDZ45 under reducing conditions with the His-tagged NorpA CTD at micromolar concentrations, washed to remove unbound protein, and then eluted the bound protein. I found that PDZ45 but not PDZ5 interacted with the NorpA C-terminal domain (CTD).

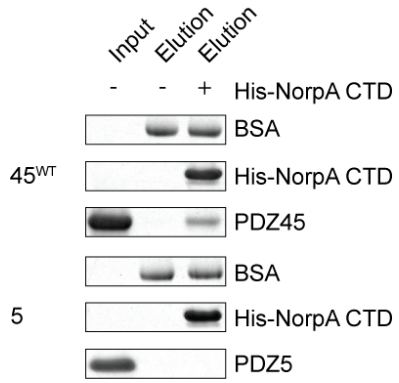

Figure 29: Measurement of NorpA Binding by Pull Down Assay

The binding of PDZ45 and PDZ5 to His-NorpA CTD was tested by pull down assay under reducing conditions. Bovine serum albumin (BSA) was added to the elution buffer as a loading control.

Gel Filtration of a PDZs 4-5 / NorpA Complex

Mike Socolich tested whether it was possible to purify a PDZ45/NorpA CTD complex. He co-expressed NorpA with His-tagged PDZ45 and then co-purified the proteins by Ni-affinity purification (Figure 30a) followed by size-exclusion chromatography ((Figure 30b-c). The co-purification of the two proteins to near homogeneity indicates that the two proteins directly interact and form a stable complex.

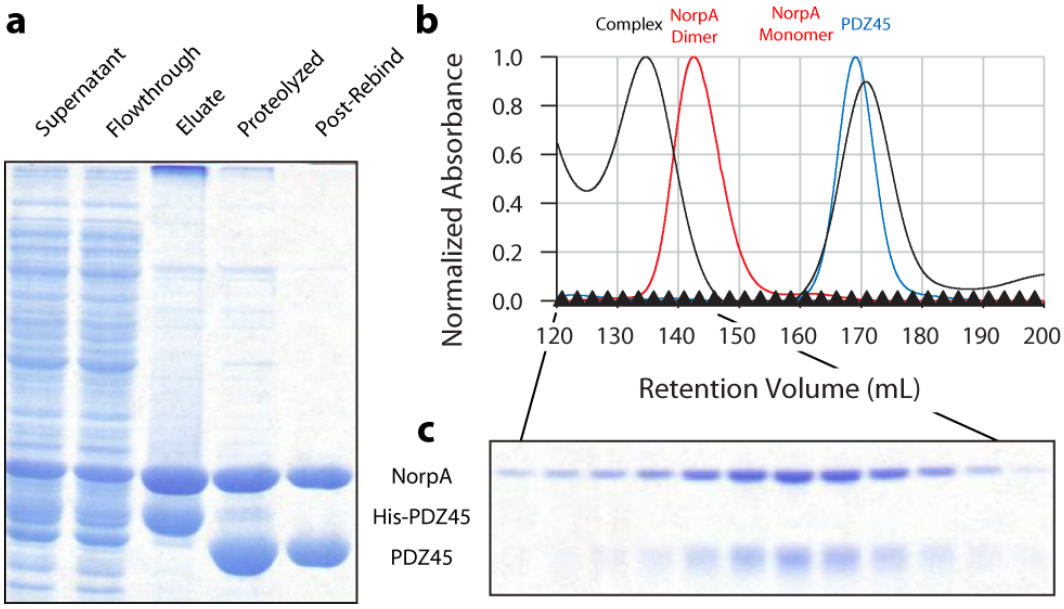

Figure 30: Co-Purification of NorpA CTD with PDZ45

(a) NorpA CTD was co-expressed with His-tagged PDZ45. The soluble protein (supernatant) was bound to Ni-NTA, unbound proteins were removed (flowthrough), and the bound complex was eluted (eluate). The His tag was removed by proteolysis with PreScission Protease (proteolyzed) followed by rebinding to Ni-NTA (post-rebind). (b) The complex (black) was then subjected to size-exclusion chromatography. For comparison, the elution profiles of NorpA (red) and PDZ45 (blue) alone are also shown. (c) Fractions (black triangles) from the peak containing the PDZ45-NorpA complex are shown.

Development of a Quantitative Binding Assay

Based on these results, Rama Ranganathan, Mike Socolich, and I then designed a quantitative Förster Resonance Energy Transfer (FRET) binding assay using Cerulean-tagged (Rizzo et al. 2004) PDZ45 and Venus-tagged (Nagai et al. 2002) NorpA CTD (Figure 31a). Mike Socolich designed and cloned the constructs and I developed the assay. I found that Cerulean-PDZ45 fluorescence was quenched with the addition of nanomolar concentrations of Venus-NorpA CTD in a dose-dependent manner with a maximal decrease of ~10% (Figure

31b). Both the quenching of Cerulean and increased fluorescence by Venus were reversed by the addition of untagged PDZ45 (Figure 31c), indicating that the effect was indeed due to FRET.

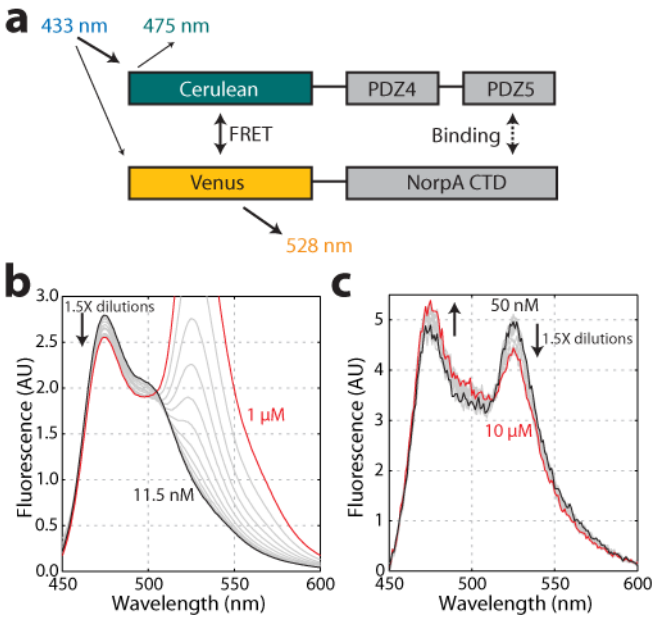

Figure 31: FRET Experiment for Quantitatively Studying PDZ45-NorpA Interaction

(a) PDZ45 and NorpA were fused to Cerulean and Venus, respectively, to generate proteins which would undergo FRET upon binding. (b) As Venus-NorpA was titrated up to 1 µM against a fixed concentration of Cerulean-PDZ45, the fluorescence from Cerulean (475 nm) decreased. (c) Addition of low micromolar concentrations of PDZ45 restored the Cerulean-PDZ45 and decreased the Venus-NorpA fluorescence, indicating the presence of FRET.

Quantitative Binding Measurements

I quantitatively measured binding by monitoring FRET inhibition while competing the wild-type interaction with unlabeled proteins. There were two questions to address: How much does PDZ4 influence binding, and secondly, what is the binding mode between PDZ45 and NorpA?

Effect of PDZ4 on Binding

I confirmed the qualitative pull-down results, finding that PDZ45 interacted tightly with a K_D of 0.6 ± 0.1 μM while PDZ5 C645S did not inhibit FRET even at 100 μM (Figure 32). This loss of binding in PDZ5 is not due to oxidation or the C645S mutation—this mutant is locked in the reduced state, has a typical conformation in the binding pocket, functions normally *in vivo* under conditions in which the refractory period is unimportant (Mishra et al. 2007), and has little effect on binding in PDZ45.

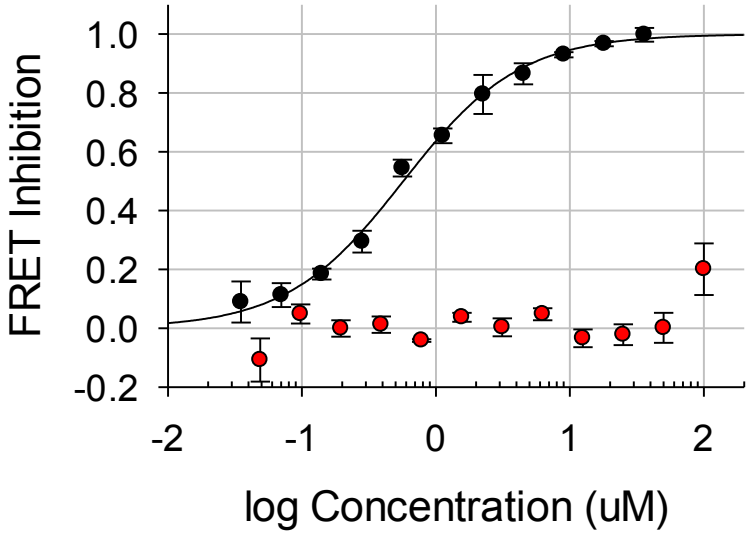

Figure 32: Effect of PDZ4 on Binding

The competition binding curves of PDZ45 (black) and PDZ5 C645S (red) are shown.

NorpA, not Trp, is the Ligand

I expected PDZ5 to bind to the C-terminus of NorpA, as this is the typical mode of binding in PDZ domains (Hung et al. 2002) and as already mentioned, a C-terminal mutation in NorpA, Y1094S, is known to be important (B.-H. H. Shieh et al. 1997). However, a recent study argued that PDZ5 binds to Trp based on similarity of PDZ5's preferred ligand residues with the Trp C-terminus (W. Liu et al. 2011). This contradicts the genetic evidence, and the authors were only able to observe tight binding in the presence of PDZ3, which genetic and biochemical evidence indicates binds Trp (B. H. Shieh et al. 1996; Susan Tsunoda et al. 1997). I found that the Trp peptide used by Liu et al. was unable to compete with the PDZ45-NorpA interaction even at 1 mM. In contrast, full length wild-type NorpA CTD bound tightly with a K_D of 0.8 ± 0.1 μM (Figure 33).

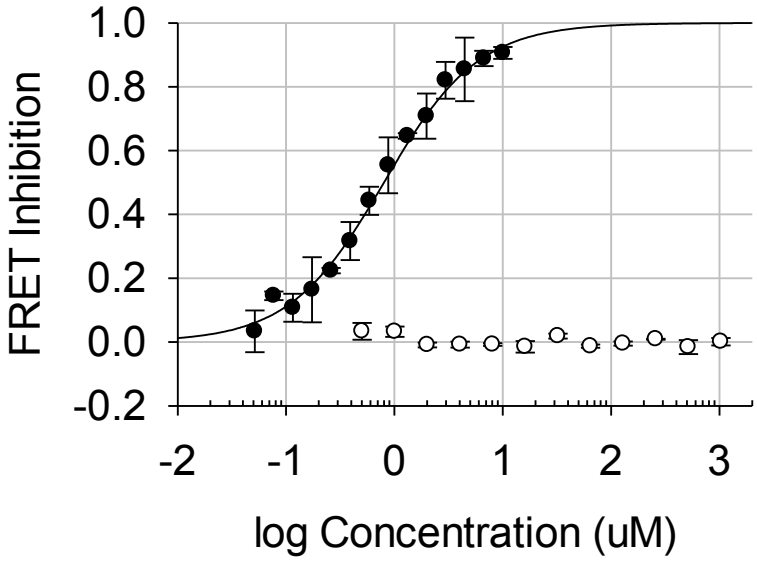

Figure 33: NorpA and Trp Binding

The competition binding curves for NorpA CTD (black) and Trp C-terminal peptide (white) are shown.

Binding Mode between PDZ45 and NorpA

Individual Contribution of PDZ4 and PDZ5

To test whether PDZ5 was responsible for binding in PDZ45, I made mutations in the α_2-1 position of each domain (PDZ4: T553A, PDZ5: F642A), a site known to contribute most to the binding energy in other PDZ domains (Tonikian et al. 2008; Z. Songyang et al. 1997) . I found that PDZ45 T553A had a small effect on binding (1.6 ± 0.2 μM), while F642A strongly reduced the K_D to 50 ± 10 μM (Figure 34). This suggests that PDZ5 is primarily responsible for binding in PDZ45.

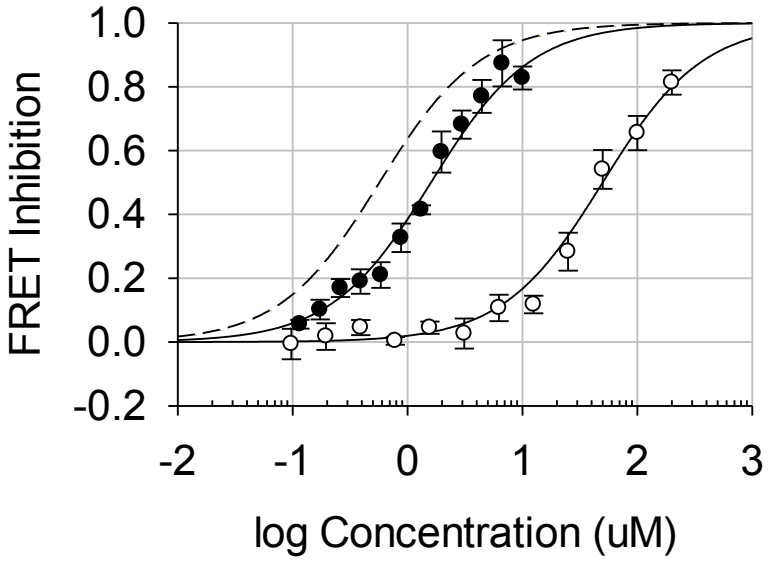

Figure 34: Contribution of PDZ4 and PDZ5 to Binding

The competition binding curves for PDZ45 T553A (black, PDZ4 binding site mutant) and F642A (white, PDZ5 binding site mutant) are shown. The dashed line is the PDZ45 WT binding curve fit.

Contribution of the NorpA C-terminus

PDZ domains typically interact primarily with the last three amino acids of a protein with limited additional interaction sites (D. A. Doyle et al. 1996; H. H. Lee, Molla, et al. 2010). Therefore, it was surprising to find that a peptide containing the last seven amino acids of NorpA bound very weakly with a K_D of 260 ± 50 μM. The Y1094S mutation, however, decreased binding of the CTD 15-fold to 12 ± 2 μM, indicating that the C-terminus of NorpA is important for binding (Figure 35).

A Potential Internal Binding Site on NorpA

While these results indicate that PDZ45 does indeed bind the C-terminus of NorpA, the inability of the C-terminal peptide to bind as tightly as the full domain suggests there are additional binding determinants beyond the -7 position. In agreement with this, Liu et al. found that a C-terminal peptide from NorpA with three additional residues bound considerably better than the peptide I used, but still failed to bind with low micromolar affinity (W. Liu et al. 2011).

In an attempt to generate a better construct of NorpA for crystallization, Mike Socolich tried removing a hypervariable loop (NorpA 924-928) that was removed from the homologous turkey phospholipase C β when it was crystallized (Singer et al. 2002). He found that this construct (NorpA CTD Δ5) no longer co-purified with PDZ45, so I tested its binding quantitatively. I found that this construct bound much more weakly with a K_D of 56 ± 4 μM (Figure 35). The protein migrated as a dimer like the wild-type construct and showed no signs of aggregation, suggesting this deletion did not structurally compromise the protein. Intriguingly, this loop is coupled to G protein binding in the turkey protein (Singer et al. 2002).

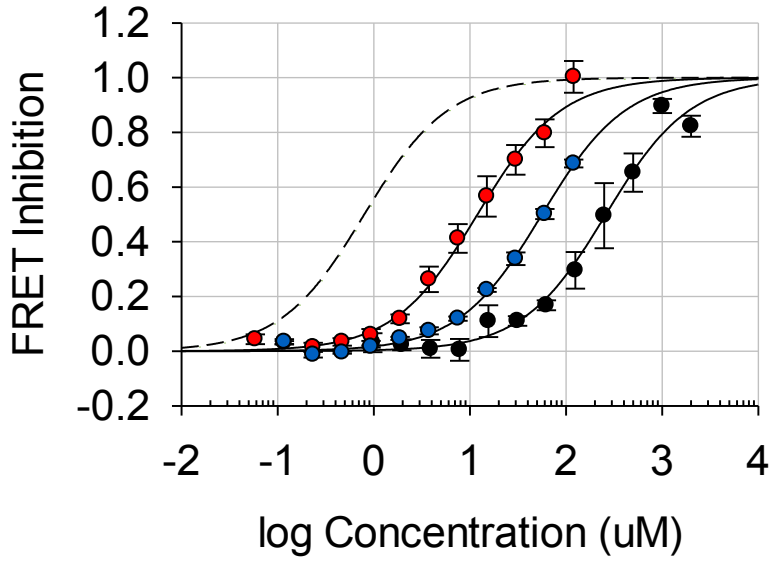

Figure 35: Contribution of the NorpA C-terminus and Internal Loop to Binding

The competition binding curves for the NorpA C-terminal peptide (black), NorpA CTD Y1094S (red), and NorpA CTD Δ5 (blue) are shown. The dashed curve is the NorpA CTD (WT) fit.

Double Mutant Cycles

In order to determine whether PDZ5 interacted with the C-terminus, I re-assayed NorpA Y1094S using Cerulean-PDZ45 T553A or F642A instead of WT (Figure 36a). Both mutations had less severe effects in combination with the NorpA C-terminal mutation, indicating that both sites are energetically coupled with the NorpA C-terminus. The magnitude of the coupling was much stronger with PDZ5 (3.4 ± 0.4 kT) (Figure 36c) than PDZ4 (1.5 ± 0.4 kT) (Figure 36b).

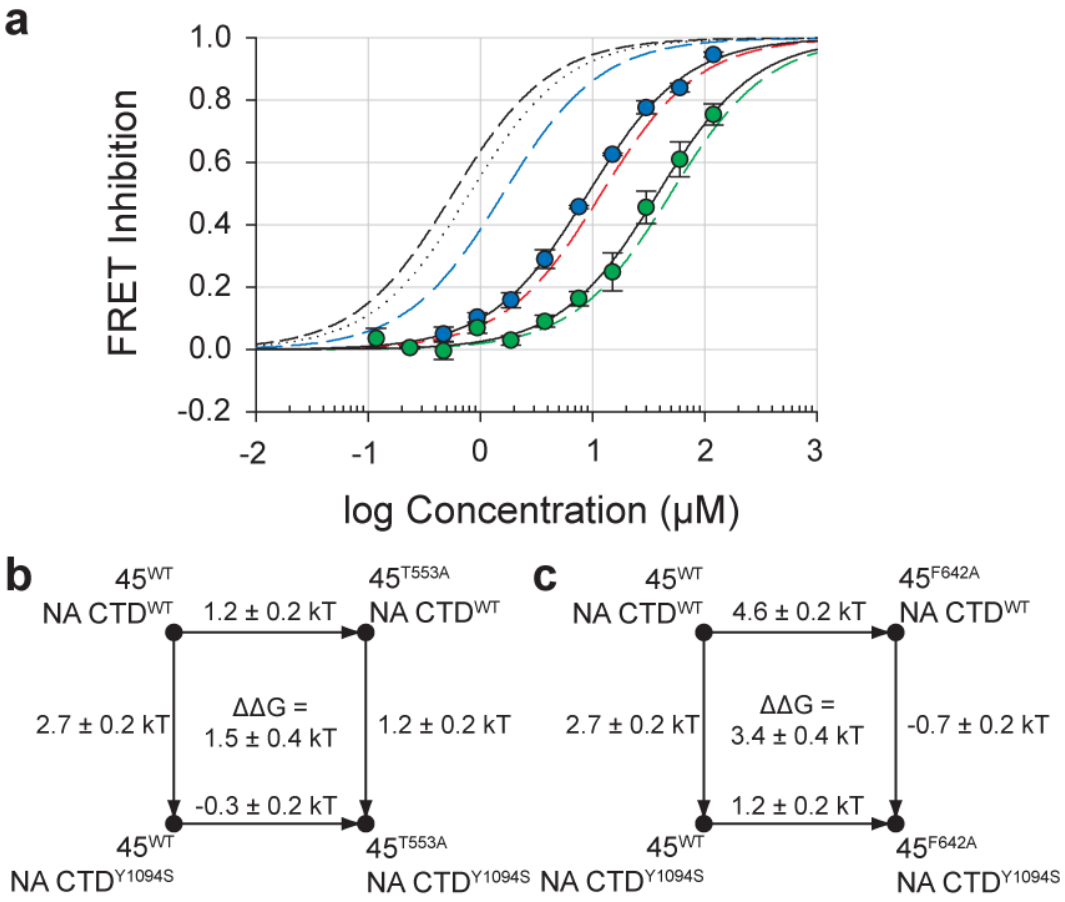

Figure 36: Double Mutant Cycle Analysis of PDZ45 Binding Site Mutants and NorpA C-terminal Mutant

(a) The competition binding curves for NorpA CTD Y1094S in the background of Cerulean-PDZ45 T553A (PDZ4 binding site, blue) or F642A (PDZ5 binding site, green) are shown. The black dashed and dotted curves are the titration fits for PDZ45 WT and NorpA CTD WT, respectively. The red dashed curve is the titration fit for NorpA CTD Y1094S, and the titration fits for PDZ45 T553A and F642A are shown in blue and green dashed lines, respectively. (b-c) Thermodynamic double mutant cycles are shown for the interaction of NorpA Y1094S and (b) PDZ45 T553A and (c) F642A.

Similarly, I tested the interaction of PDZ4 and PDZ5 with the deletion of the hypervariable loop of NorpA (Figure 37a). Again, both mutations had less severe effects in combination with the NorpA C-terminal mutation, indicating that

both sites are energetically coupled with the hypervariable loop in NorpA. Like the C-terminus, the magnitude of the coupling was much stronger with PDZ5 (4.7 ± 0.4 kT) (Figure 37c) than PDZ4 (1.6 ± 0.5 kT) (Figure 37b).

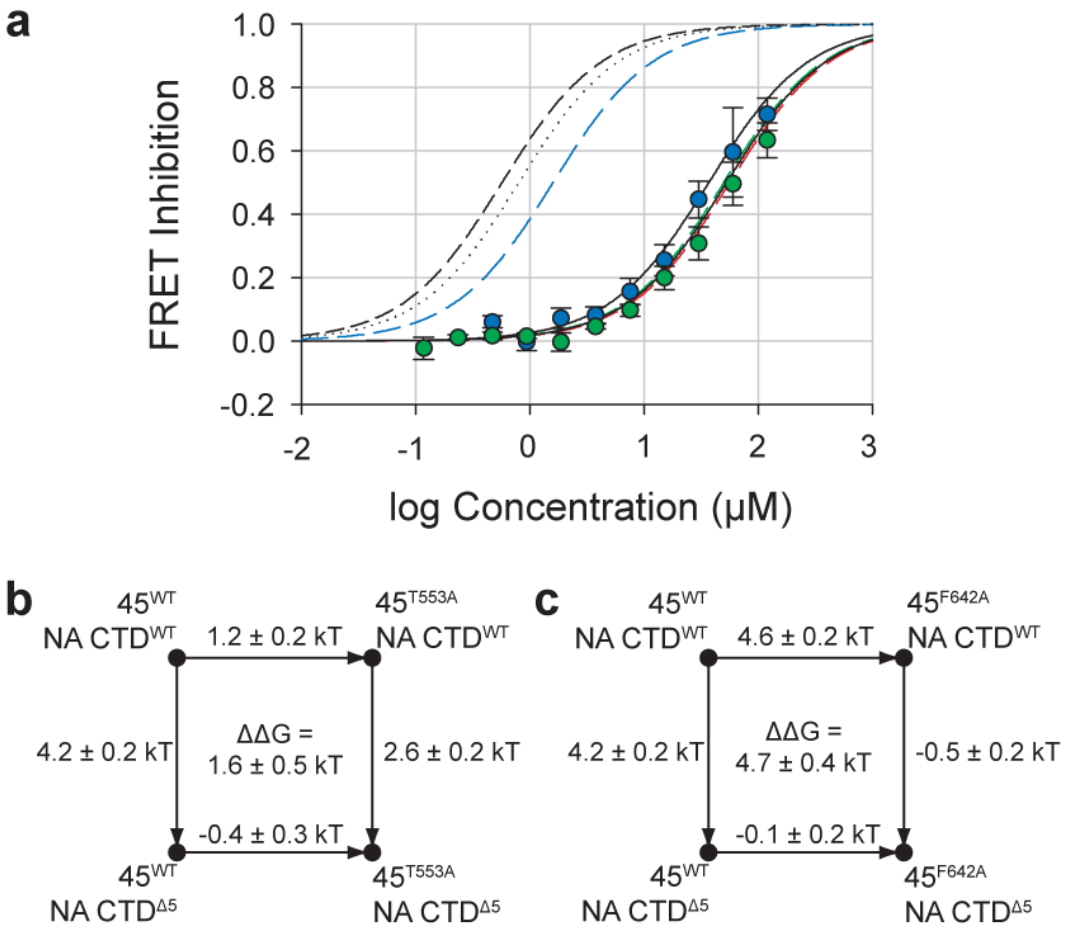

Figure 37: Double Mutant Cycle Analysis of PDZ45 Binding Site Mutants and NorpA Hypervariable Loop

(a) The competition binding curves for NorpA CTD Δ5 in the background of Cerulean-PDZ45 T553A (PDZ4 binding site, blue) or F642A (PDZ5 binding site, green) are shown. The black dashed and dotted curves are the titration fits for PDZ45 WT and NorpA CTD WT, respectively. The red dashed curve is the titration fit for NorpA CTD Δ5, and the titration fits for PDZ45 T553A and F642A are shown in blue and green dashed lines, respectively. (b-c) Thermodynamic double mutant cycles are shown for the interaction of NorpA Δ5 and (b) PDZ45 T553A and (c) F642A.

Table 3: Summary of Binding Results

Competitor (Double Mutant)	Binding Affinity (μM)
PDZ45 WT	0.6 ± 0.1
PDZ45 C645S	3.3 ± 0.5
PDZ45 Δ3C	1.5 ± 0.2
PDZ45 T553A	1.6 ± 0.2
PDZ45 F642A	50 ± 10
PDZ5 C645S	>1000
NorpA CTD	0.8 ± 0.1
NorpA C-terminal peptide	260 ± 50
NorpA CTD Y1094S	12 ± 2
NorpA CTD Y1094S (PDZ45 T553A)	9.1 ± 0.7
NorpA CTD Y1094S (PDZ45 F642A)	38 ± 6
NorpA CTD Δ5	56 ± 4
NorpA CTD Δ5 (PDZ45 T553A)	37 ± 7
NorpA CTD Δ5 (PDZ45 F642A)	53 ± 4
Trp C-terminal peptide	>10000

Effect of PDZ4 on the Redox Properties of PDZ5

In addition to its inability to bind NorpA, free PDZ5 readily oxidizes under physiological conditions *in vitro* (Mishra et al. 2007). Oxidation results in a conformational change which distorts the α_2 helix of the binding pocket (Mishra et al. 2007). Although the C645S mutation prevents oxidation, it is possible that this conformational change occurs in the absence of the disulfide bond. I hypothesized that the large effect of PDZ4 on the binding affinity of PDZ5 may be a result of a shift in this conformational equilibrium and would thus also alter the redox properties of PDZ5.

Development of a Quantitative, Precise Redox Assay

Redox Titration Theory

In a redox titration, an oxidizable protein is mixed with a reducing and/or oxidizing agent (the redox buffer, usually DTT or glutathione). The redox reaction of each component is characterized by its standard redox potential (E^0) and the Nernst equation:

Equation 11: Nernst Equation

$$E = E^0 - \frac{RT}{nF}\ln\left(\frac{[\text{Reduced}]^{\chi_\text{r}}}{[\text{Oxidized}]^{\chi_\text{o}}}\right)$$

where *R* is the ideal gas constant, *T* is the temperature, *n* is the number of electrons transferred (2 for disulfide exchange reactions), *F* is Faraday's constant (96,485.3365 C/mol), and *x* is the stoichiometry of reduced (r) and oxidized (o) species in the reaction (usually 1, but the oxidation of glutathione forms a dimer and so it has $x_\text{r} = 2$).

At equilibrium, the redox potential of each reaction (*E*) is the same:

Equation 12: General Redox Equilibrium Equation

$$E_B = E_P = E_B^0 - \frac{RT}{nF}\ln\left(\frac{[\text{B}_\text{r}]^{\chi_r}}{[\text{B}_\text{o}]^{\chi_o}}\right) = E_P^0 - \frac{RT}{nF}\ln\left(\frac{[\text{P}_\text{r}]}{[\text{P}_\text{o}]}\right)$$

where B is the redox buffer, and P is the protein. In general, we can see by rearranging that:

$$E_P^0 = E_B^0 + \frac{RT}{nF}\ln\left(\frac{[\mathrm{P_r}][\mathrm{B_o}]^{\chi_o}}{[\mathrm{P_o}][\mathrm{B_r}]^{\chi_r}}\right)$$

Issues with the Previous Redox Titration Method

The Ranganathan lab's previous study (Mishra et al. 2007) and Liu et al. 2011 performed unbuffered redox titrations by adding in what was assumed to be fully reduced DTT or oxidized glutathione to fully oxidized PDZ5 or reduced PDZ45. The fraction of the protein that was reduced ($\%_{red}$) was then measured. Since the initial concentrations (indicated with a 0 subscript) and total protein ($[\mathrm{P}]_{tot}$) were assumed to be known, the equilibrium concentrations are the following:

$$\Delta[\mathrm{P_r}] = \left(\%_{red} - \%_{red,0}\right)[\mathrm{P}]_{\mathrm{tot}}$$

$$[\mathrm{B_r}] = [\mathrm{B_r}]_0 - \Delta[\mathrm{P_r}]$$

$$[\mathrm{B_o}] = [\mathrm{B_o}]_0 + \Delta[\mathrm{P_r}]$$

Subtituting these expressions into the general equation for the standard redox potential of the protein and rewriting the ratio of reduced to oxidized protein in terms of $\%_{red}$, we get:

Equation 13: Unbuffered Redox Titration Fitting Equation

$$E_P^0 = E_B^0 + \frac{RT}{nF}\ln\left(\left(\frac{\%_{red}}{1-\%_{red}}\right)\left(\frac{[\mathrm{B_o}]_0 + \left(\%_{red} - \%_{red,0}\right)[\mathrm{P}]_{\mathrm{tot}}}{[\mathrm{B_r}]_0 - \left(\%_{red} - \%_{red,0}\right)[\mathrm{P}]_{\mathrm{tot}}}\right)\right)$$

The problem with this approach is that it is susceptible to many errors due to the numerous variables in the fit and the typical assumption that the initial materials are purely in one state. One can see the magnitude of these errors (ε) by taking the difference in the equation above for the case of reducing a protein with ($\%_{red,0}$=0, $[B_o]_0$=0) and without the assumption of fully oxidized protein and reduced buffer:

$$\epsilon = \frac{RT}{nF}\left(\ln\left(\frac{\%_{red}\left([B_o]_0 + [P]_{tot}\left(\%_{red} - \%_{red,0}\right)\right)}{\left([B_r]_0 - [P]_{tot}\left(\%_{red} - \%_{red,0}\right)\right)(1 - \%_{red})}\right) - \ln\left(\frac{\%_{red}^2[P]_{tot}}{([B_r]_0 - \%_{red}[P]_{tot})(1 - \%_{red})}\right)\right)$$

Note that $\frac{RT}{nF}$ is ~13 mV. The individual errors from the assumptions of starting with completely oxidized protein and completely reduced buffer can be estimated by calculating the second-order Taylor series expansion of ε around ($\%_{red,0}$=0, $[B_o]_0$=0):

$$\epsilon\left(\%_{red,0}\right) = -\frac{RT}{nF}(\ln(\%_{red}) - \ln([B_o]_0 + \%_{red}[P]_{tot}) + \ln([P]_{tot})) - \frac{RT}{nF}\left(\frac{\%_{red,0}[P]_{tot}([B_o]_0 + [B_r]_0)}{([B_o]_0 + \%_{red}[P]_{tot})([B_r]_0 - \%_{red}[P]_{tot})}\right) + O\left(\%_{red,0}^2\right)$$

$$\epsilon([B_o]_0) = \frac{RT}{nF}\left(\ln\left(\frac{\%_{red} - \%_{red,0}}{[B_r]_0 - [P]_{tot}\left(\%_{red} - \%_{red,0}\right)}\right) - \ln\left(\frac{\%_{red}}{[B_r]_0 - \%_{red}[P]_{tot}}\right) + \frac{[B_o]_0}{[P]_{tot}\left(\%_{red} - \%_{red,0}\right)}\right) + O([B_o]_0^2)$$

By inspection, we can see that the effect of unaccounted partially reduced protein at most contributes an error of approximately $-\frac{RT}{nF}\frac{4[\mathrm{B_r}]_0}{2[\mathrm{B_r}]_0-[\mathrm{P}]_{\mathrm{tot}}}\%_{red,0}$ at the midpoint of the titration when the buffer is initially all reduced. For buffer concentrations of ~10X the protein concentration or more and with at most 10% initial reduction of the protein, this error is on the order of a few millivolts.

The effect of unaccounted oxidation of the reduced buffer is $\frac{RT}{nF}\frac{[\mathrm{B_o}]_0}{[\mathrm{P}]_{\mathrm{tot}}(\%_{\mathrm{red}}-\%_{\mathrm{red},0})}$. Unless the protein concentration is much greater than the oxidized buffer concentration, this effect is large, approximately 26 mV times the ratio of oxidized buffer and protein concentrations. Given that the experiments are typically done with protein concentrations more than an order of magnitude less than the buffer concentration, this effect can be significant even with only 1-10% oxidation of the buffer. In addition, commercially available reducing agents are only guaranteed to <0.1-1% oxidation and improper storage can further increase this fraction.

The converse experiment of oxidizing a protein suffers from the same errors. The effect of partial oxidation is even smaller than the effect of partial reduction, occuring only in higher order terms of the Taylor series. The error due to partial reduction of the buffer is equivalent to the error in reducing a protein:

$\frac{RT}{nF}\frac{[\mathrm{B_r}]_0}{[\mathrm{P}]_{\mathrm{tot}}(\%_{\mathrm{red}}-\%_{\mathrm{red},0})}$. With glutathione as the oxidant, the error increases two fold due to the square dependence on the concentration of reduced glutathione.

Redox Buffering Theory

An alternative approach used in this study is to buffer the redox condition by keeping the concentration of oxidized and reduced buffer much greater than the concentration of protein that reacts at equilibrium. Under these conditions, the concentrations of reduced and oxidized buffer do not change significantly at equilibrium, and thus the redox potential is fixed to the initial redox potential of the buffer. With this simplification, the redox potential of the protein can be calculated as:

Equation 14: Buffered Redox Titration Fitting Equation

$$E_P^0 = E_B + \frac{RT}{nF}\ln\left(\frac{\%_{red}}{1-\%_{red}}\right)$$

This has several advantages. Since a large, known amount of both reduced and oxidized buffer are added, impurities in the chemicals are less important as long as the concentrations are not vastly different. In addition, the initial state of the protein is no longer important, removing another source of error. Finally, because the exact same buffer conditions can be used to both oxidize and reduce proteins, the errors become systematic rather than idiosyncratic and thus comparisons become much less error prone.

Fitting of Buffered Redox Titrations

As described in the previous section, the equilibrium condition for a buffered redox titration is solely dependent on the redox potential of the buffer (E_B) and the fraction of the protein that is reduced ($\%_{red}$) along with a set of physical constants (R, T, n, F). The titrations are plotted as $\%_{red}$ vs. E_B, and thus we can rewrite the titration equation in this form for fitting:

Equation 15: Buffered Redox Titration Curve Fitting

$$\%_{red} = a\frac{\exp\left(\frac{nF}{RT}(E_P^0 - E_B)\right)}{1 + \exp\left(\frac{nF}{RT}(E_P^0 - E_B)\right)}$$

Because of the limitations of identifying the distinct reduced and oxidized bands by densitometry, the real titrations do not always saturate at 100% reduced. As a result, I scaled the titration by *a*, the maximum fraction reduced. In some other cases, the protein did not completely oxidized and a term was added to adjust the baseline.

Redox Buffer Conditions

Redox buffers were prepared with 25 mM DTT_{ox} and two-fold dilutions of DTT_{red}. The redox potential is calculated from the Nernst equation (Equation 11) with a standard redox potential of -323 mV for DTT (Szajewski et al. 1980). The

redox potential of a titration sample will be approximately equal to the redox potential of the DTT solution if the concentration of the protein that reacts with the buffer does not significantly change the ratio of DTT_{red} to DTT_{ox}.

Table 4: Redox Buffer Conditions

E (V)	DTT_{red} (mM)	DTT_{ox} (mM)	DTT_{red}/DTT_{ox}
-0.335	6.3E+01	25	2.5E+00
-0.326	3.1E+01	25	1.3E+00
-0.317	1.6E+01	25	6.3E-01
-0.308	7.8E+00	25	3.1E-01
-0.299	3.9E+00	25	1.6E-01
-0.290	2.0E+00	25	7.8E-02
-0.280	9.8E-01	25	3.9E-02
-0.271	4.9E-01	25	2.0E-02
-0.262	2.4E-01	25	9.8E-03
-0.253	1.2E-01	25	4.9E-03
-0.244	6.1E-02	25	2.4E-03
-0.235	3.1E-02	25	1.2E-03
-0.226	1.5E-02	25	6.1E-04
-0.217	7.6E-03	25	3.1E-04
-0.208	3.8E-03	25	1.5E-04
-0.199	1.9E-03	25	7.6E-05
-0.190	9.5E-04	25	3.8E-05
-0.180	4.8E-04	25	1.9E-05
-0.171	2.4E-04	25	9.5E-06

Redox Titration of PDZ5

I performed redox titrations by equilibrating each protein under a particular redox potential using the dithiothreitol redox buffer listed in Table 4 and then assayed the oxidation state of the two cysteines. Oxidation was monitored by labeling free thiols with a ~500 Da maleimide, producing a 1 kD

shift on a SDS-PAGE gel (Figure 40a). In this assay, free PDZ5 titrates with a standard redox potential (E^0) of -284.6 ± 0.8 mV (Figure 40b-c). The cytoplasmic redox conditions in the *Drosophila* photoreceptor cell are unknown, but measurements of the glutathione redox state in other cell types range from -200 to -260 mV (Kemp et al. 2008), and I observed non-physiological oxidation of cysteines above -220 mV (Figure 38). This suggests that free PDZ5 would indeed be oxidized *in vivo*.

Redox Titration of PDZ45

PDZ4 contains three cysteines, two of which are located on the surface. Initially I tried measuring the redox potential of WT PDZ45 (Figure 38a), but under very oxidizing conditions the additional cysteines oxidize even in PDZ45 C645S (Figure 38b). This makes it difficult to specifically follow the oxidation of the PDZ5 cysteines. However, it was clear that the titration occurred in the -220 to -240 mV region. Shan Mishra previously showed that the C645S mutation eliminates all oxidized InaD species *in vivo* (Mishra et al. 2007), indicating that species which titrate like PDZ45 C645S will not be oxidized *in vivo*.

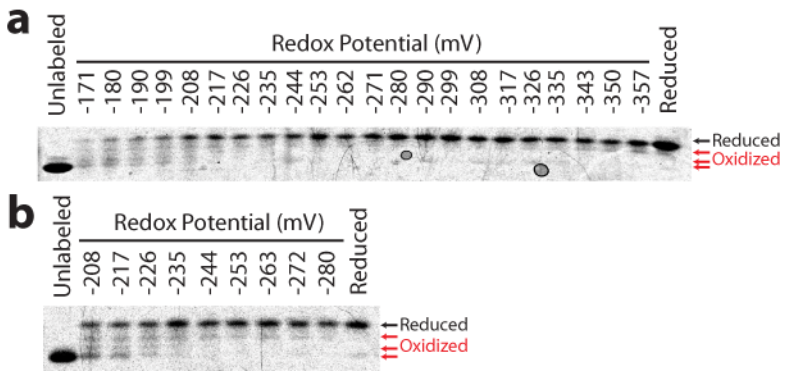

Figure 38: Redox Titration of PDZ45 WT and C645S

Redox titrations of (a) PDZ45 WT and (b) C645S were performed using a 1-2 hour equilibration. In both cases, multiple oxidized species are present, preventing a focused analysis on the C606-C645 disulfide. We previously demonstrated that the C645S mutation eliminates all physiological disulfide bond formation in InaD, indicating that the oxidized species we observe below -226 mV are not relevant in vivo.

Mutation of the PDZ4 Cysteines to make PDZ45 Δ3C

To specifically follow oxidation of PDZ5, I mutated the three cysteines in PDZ4 to alternative amino acids found in the InaD gene family (C504T/C515A/C539T) (Appendix A). This construct, PDZ45 Δ3C, binds to the NorpA CTD with a similar affinity as WT PDZ45 (Figure 39), indicating that the mutations are at least not severe enough to disrupt NorpA binding.

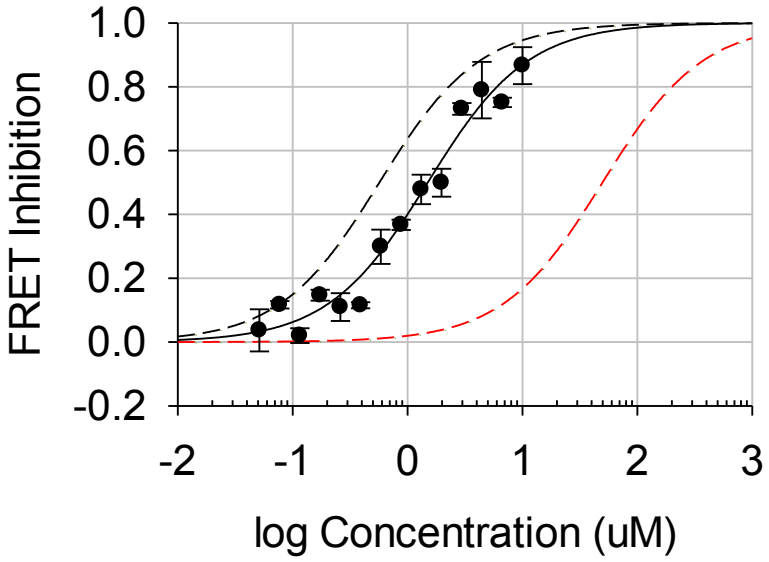

Figure 39: Binding of PDZ45 Δ3C to NorpA

The competition binding curve of PDZ45 Δ3C is shown. For comparison, the titration fits for PDZ45 WT (black dashed line) and F642A (red dashed line, PDZ5 binding site mutant) are shown.

Redox Titration of PDZ45 Δ3C

I then measured the redox potential of PDZ45 Δ3C. PDZ45 Δ3C titrated with an E^0 of -242 ± 2 mV (Figure 40), a 42 mV (3.3 ± 0.2 kT) destabilization of the disulfide bond by PDZ4 relative to free PDZ5. Liu et al. independently observed inhibition of oxidation of PDZ5 by PDZ4 (W. Liu et al. 2011), but their results are quantitatively different than mine. This is probably due to their use of unbuffered redox titrations with different redox reagents for PDZ45 and PDZ5, which can produce substantial errors. It may also be due to differences in the construct used, as the exact N- and C-termini of the PDZ domains seems to

influence their function (C. K. Wang et al. 2010), an effect we have also observed with the redox properties of PDZ5 (data not shown).

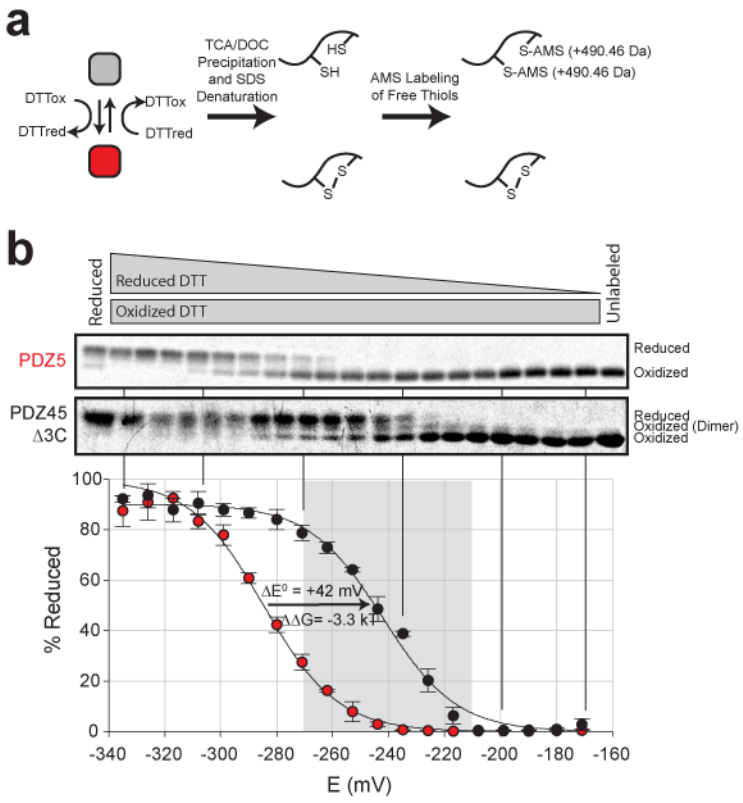

Figure 40: Redox Titration of PDZ5 and PDZ45 Δ3C

(a) Proteins were equilibrated in a DTT-based redox buffer, precipitated, denatured, and then free thiols were labeled with AMS, a ~500 Da maleimide. (b) Gels of the redox titration of PDZ5 and PDZ45 Δ3C are shown with the titration plotted below.

Detection of an Oxidative Dimer in PDZ45

Near the midpoint of the titration, a singly-oxidized species was observed in PDZ45 but never in PDZ5 (Figure 40b). One explanation for this could be that the protein forms an oxidative dimer. To test this, I prepared samples of PDZ45 Δ3C by equilibrating for 26 hours at -244 mV or in 10 mM TCEP (reducing

conditions), precipitated, washed, and resuspended in detergent-free denaturing buffer (80 mM HEPES pH 7, 6.7M urea, 6.7M guanidine HCl) containing 50 mM iodoacetamide and incubated for 30 minutes at room temperature to block free cysteines. The samples were then desalted and submitted to the UT Southwestern Protein Technology core facility for electrospray mass spectrometry analysis. The identified masses are listed in Table 5 along with the expected masses for the assigned species.

Table 5: Mass Spectrometry of Redox Equilibrated PDZ45

Observed Mass (Da)	Assignment	Expected Mass (Da)	Present Under…	
			Reducing Conditions	-240 mV Conditions
22421 ± 3	Oxidized (-2H)	22420	-	Y
22537 ± 3	+2 Cam	22536	Y	Y
22594 ± 3	+3 Cam	22593	Y	Y
22651 ± 3	+4 Cam	22650	Y	Y
44843 ± 5	Oxidative Dimer (-2H)	44842	-	Y
44958 ± 5	Oxidative Dimer (-1H) +1 Cam	44957	-	Y
45015 ± 5	Oxidative Dimer (-1H) +2 Cam	45014	-	Y
45073 ± 5	Oxidative Dimer (-1H) +3 Cam	45071	-	Y

Cam: Carboxamidomethyl (+57 Da), from reaction with iodoacetamide

Disulfide exchange reactions occur via two steps. In the case of oxidizing PDZ45, a thiolate anion from PDZ45 performs a nucleophilic attack of oxidized DTT, the donor disulfide, forming a PDZ45-DTT mixed disulfide. Then, a second thiolate anion from PDZ45 performs a nucleophilic attack of the mixed disulfide, resulting in disulfide bond formation in PDZ45 and release of reduced DTT. Normally, intramolecular disulfide bonds are strongly preferred

thermodynamically due to entropy and kinetically due to the proximity of the second attacking intramolecular thiolate anion. The observation that there is a significant increase in intermolecular disulfide bond formation in PDZ45 suggests that one of the cysteines in PDZ45 but not PDZ5 is particularly unreactive at pH 7, which is consistent with the significant increase in the redox potential.

Effect of PDZ4 on the Conformation of PDZ5

Crystal Structure of PDZ45

The previous study indicated that PDZ5 switched from an open to closed conformation in the binding pocket upon oxidation (Mishra et al. 2007). The finding that PDZ4 promotes binding of NorpA and inhibits disulfide bond formation suggested that PDZ5 is in the open conformation in PDZ45. Shan Mishra therefore crystallized PDZ45 and solved the structure to 2.4Å. Despite being crystallized under non-reducing conditions in which free PDZ5 is completely oxidized (Mishra et al. 2007), the protein was observed in the reduced form (Figure 41a). The asymmetric unit contained four PDZ45 molecules with very similar conformation to each other and reduced free PDZ5 (Figure 41b). This conformation is typical of PDZ domains apart from the α_1 helix and thus would be expected to bind ligand.

Given its inability to bind NorpA, it is likely that the open state is not the major conformation of reduced free PDZ5 in solution. In agreement with this, the interaction with PDZ4 substantially alters the chemical environment of much of

PDZ5 beyond the immediate interface, including the binding pocket (W. Liu et al. 2011). The interface with PDZ4 buries 2683Å^2 (21% of the total surface) and contains many polar contacts, including one between H510 of PDZ4 and S621 of PDZ5 on the α_1 helix, a known allosteric region in PDZ domains (Garrard et al. 2003). In addition, the C-terminal tail forms interactions with both the interdomain linker as well as PDZ4. The lack of direct contact between PDZ4 and either cysteine of PDZ5 indicates that the observed functional effects must be transmitted through some allosteric pathway, although the details of this pathway are not obvious from either the structure or the biochemical experiments presented here.

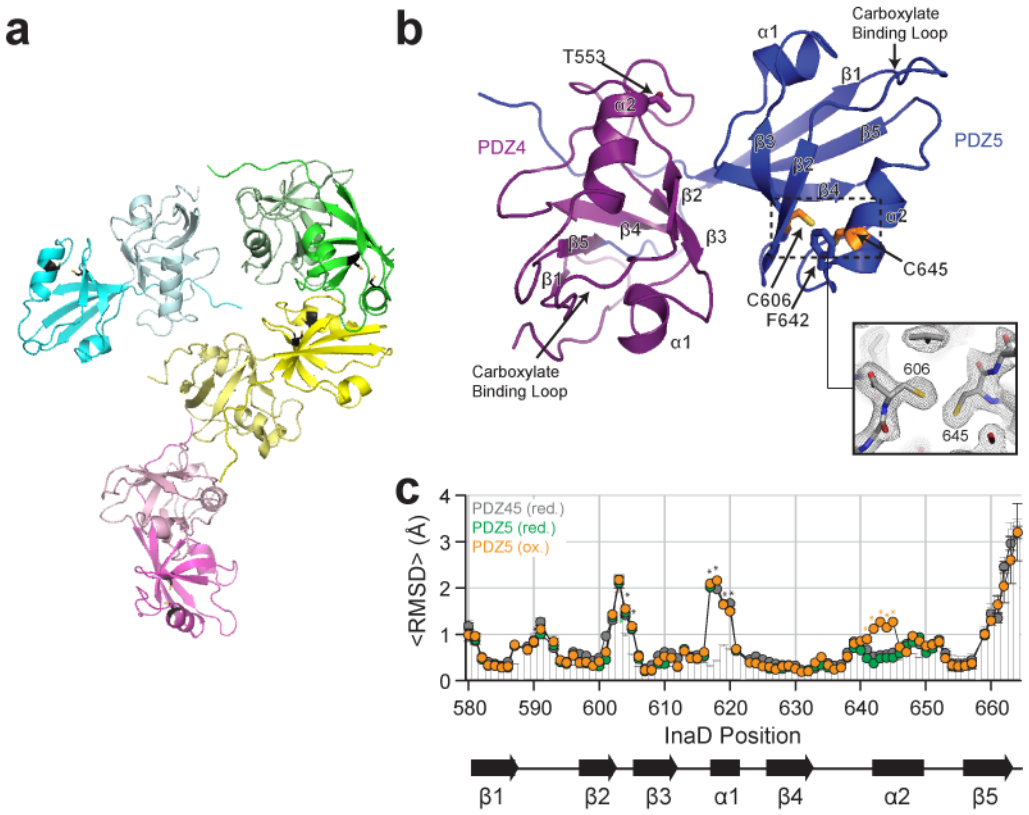

Figure 41: Structural Analysis of PDZ45

(a) The asymmetric unit of the crystal structure is shown with different hues for each molecule. PDZ5 is shown in a darker shade with C606 and C645 in black sticks. (b) The structure of one of the PDZ45 molecules in the asymmetric unit is shown with various structural elements highlighted. The inset shows the electron density around the PDZ5 cysteines, demonstrating that they are reduced. (c) The average RMSD deviation of the various PDZ5 structures is shown in comparison with a large number of reference domains. The average RMSD between the reference domains is shown in the gray bars.

Table 6: PDZ45 Crystal Structure Details

Data Collection and Phasing	
Space Group	$P2_12_12_1$
Cell Dimensions	a=88.34 Å, b=106.38 Å, c=108.64 Å, α=β=γ=90°
Source	APS 19-BM
Wavelength (Å)	0.97945 (peak)
Resolution Range (Å)	20-2.4
Reflections	38201
Completeness	
All/Outer Shell	99.0/97.8
I/σ	
All/Outer Shell	15.5/2.7
Refinement	
Resolution Limit (Å)	2.4
Reflections	
Working/Test	38201/2019
R (R_{free})	0.23 (0.29)
No. of atoms	
Protein	6103
Water	298
Mean B factor ($Å^2$)	20.9
RMSD Bond Length (Å)	0.021
RMSD Bond Angle	2.1

Evolutionary History of PDZ45

The data presented so far show that the function of PDZ5 is intimately influenced by the presence of PDZ4, discrediting the view of PDZ5 as an independent module. The PDZ45 tandem, however, seems to recapitulate the physiological properties of PDZ5 and therefore may qualify as a module. In the traditional view of modularity in scaffolding proteins, modules are swapped out over evolutionary time to introduce new functionality to the scaffold

(Bhattacharyya et al. 2006). Is there evidence of this type of modularity in the evolutionary record of PDZ45?

Identification of Homologous InaD Fragments

To test this, I searched for homologs of PDZ45 outside of the InaD gene family using PSI-BLAST (Altschul et al. 1997). To prevent the selection of generic PDZ domain matches, I performed only three rounds of PSI-BLAST and chose cutoff values that typically resulted in a single hit per gene. I identified 140 tandem hits found in searches of PDZ4, PDZ5, and PDZ45 with stringent cutoffs as the list of homologous tandem PDZ domains (Figure 42). This approach is relatively conservative as it only includes approximately 30% of the PDZ45 hits; in addition, many of the subthreshold hits are also tandem domains found in all three searches and may represent additional homologs.

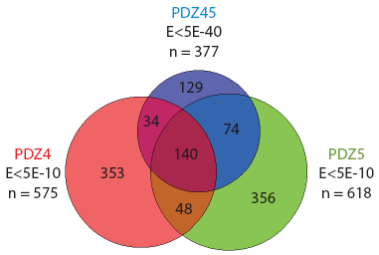

Figure 42: Identification of Homologs of the PDZ45 Tandem

Venn diagram showing the overlap in hits from three rounds of conservative PSI-BLAST searches using InaD PDZ4, PDZ5, or PDZs 4-5 against the NCBI non-redundant database. The expectation value cutoffs were heuristically chosen to exclude generic PDZ domain matches.

This result for PDZ45 is unique within InaD. I performed a similar analysis for other sets of PDZ domains from InaD. The results are shown below in

Table 7. The off-diagonal numbers indicate the number of unique NCBI gene identifier numbers shared between each group. Note that in Figure 42, PDZ45 was subjected to a stricter comparison in which only overlapping hits between PDZ4, PDZ5, and PDZ45 were counted as homologs. As shown in Table 8, only the PDZ45 tandem has homologs outside of the strict InaD gene family.

Table 7: Identification of Homologs of InaD PDZ Domains

Dataset	PDZ2	PDZ3	PDZ4	PDZ5	PDZ23	PDZ34	PDZ45	PDZ345
PDZ2	149							
PDZ3	24	961						
PDZ4	138	61	575					
PDZ5	130	171	188	618				
PDZ23	76	23	75	72	76			
PDZ34	61	65	63	60	61	106		
PDZ45	106	206	174	262	73	61	377	
PDZ345	65	22	67	67	61	61	68	68

Table 8: Comparison of InaD Multi-PDZ Domain Homologs

Datasets	# of Homologs	Included Gene Families
PDZ2 & PDZ3 & PDZ23	23	InaD (fly, mosquito, bee, beetle, ant, louse)
PDZ3 & PDZ4 & PDZ34	24	InaD (fly, mosquito, bee, beetle, ant)
PDZ4 & PDZ5 & PDZ45	142	See Figure 43a
PDZ3 & PDZ4 & PDZ5 & PDZ345	21	InaD (fly, mosquito, beetle)

Phylogenetic Analysis of PDZ45 Homologs

Next, I examined the evolutionary history of PDZ45 by constructing a neighbor-joining phylogenetic tree from an alignment of these tandem domains (Figure 43a-b). The sequences were relatively equally spaced on the tree, indicating that no one sequence was highly dissimilar from the rest. In addition to InaD and isolated multi-PDZ domains scaffolds from distant organisms, I found

four other major clusters on the tree corresponding with PDZs 1-2 of the Lnx E3 ubiquitin ligase family, PDZs 7-8 of the nematode Mpz-1 family, PDZs 8-9 of InaD-like, and PDZs 10-11 of MPDZ. The sequences within each gene family clustered in a similar manner as the species tree, suggesting the alignment quality was sufficiently good to estimate the phylogeny of the genes. These proteins are found in diverse taxa spanning the metazoan lineage (Figure 43c). This suggests that PDZs 4-5 have indeed been coevolving for a long time and that the interdomain coupling we observe in InaD may be present in the other gene families as well.

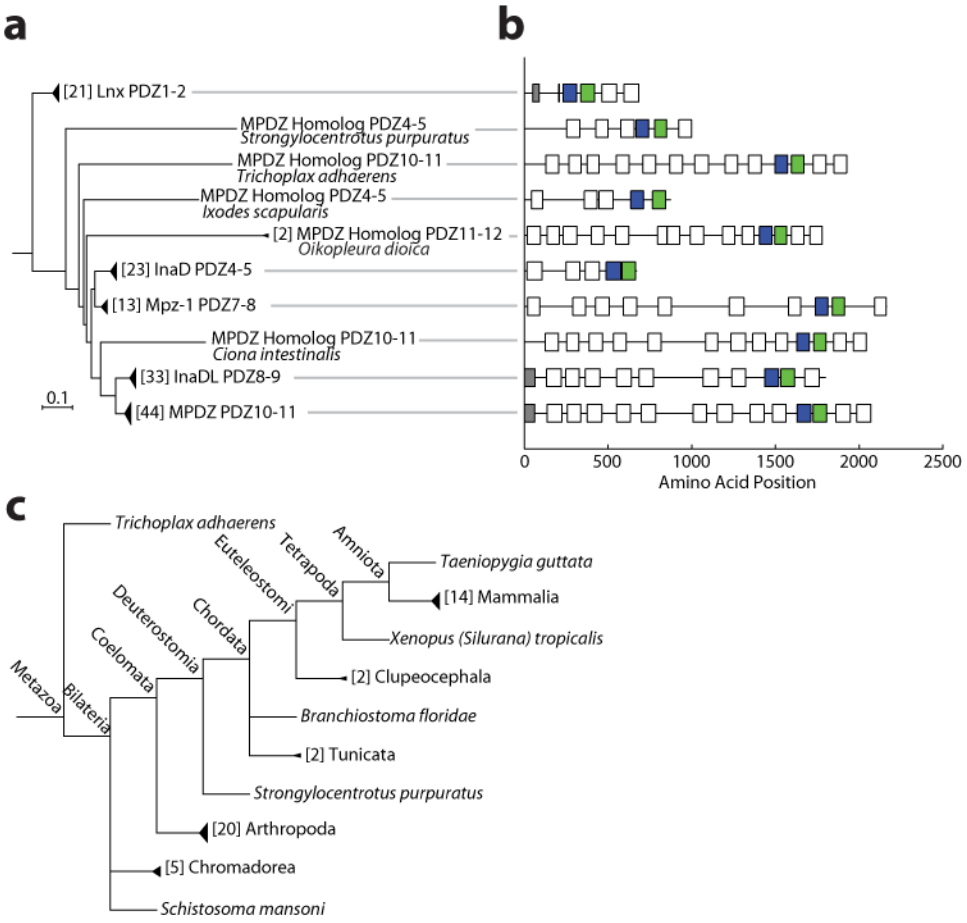

Figure 43: Phylogenetic Analysis of PDZ45 Homologs

(a) The neighbor-joining distance tree is shown for the 140 tandem domain homologs of PDZ45 aligned using Promals3D. The scale bar indicates the number of substitutions/site. Bracketed numbers indicate the number of genes within that clade. (b) Domain structures of representative family members from the tree. PDZ4 homologs are shown in blue, PDZ5 in green. (c) NCBI taxonomy tree of the species included in the 140 tandem domain homologs. Bracketed numbers indicate the number of species contained in the indicated lineage.

Conclusions

The results presented here demonstrate that PDZ5 is not a module. On its own, PDZ5 fails to bind NorpA and oxidizes under physiological conditions. Instead, PDZ4 and PDZ5 form an intimate structural module which binds NorpA

and is reduced under physiological conditions. Additionally, the evidence presented here suggests that the binding mode with NorpA involves both domains and an internal site in NorpA, an unusual phenomenon in PDZ domains. Furthermore, the domains appear to have co-evolved in many distinct scaffolding protein families apart from the rest of InaD, indicating true modularity. While this challenges the common assumption that single protein domains are the evolutionary unit of scaffolding proteins, the long coevolution of the two domains provides time for them to become coupled. This may explain how complex regulatory features such as dynamic scaffolding can rapidly arise in evolution.

Methods

Constructs

InaD PDZ5 (residues 580-674) was cloned into pRSETB His-GFP using SphI and XhoI with a thrombin site between GFP and PDZ5 using standard methods. The PDZ5 C645S construct was described previously (Mishra et al. 2007). InaD PDZs 4-5 (residues 474-674) was cloned into pET28a+ with an N-terminal His-tag followed by a PreScission Protease site. NorpA CTD (residues 869-1095) was cloned into pET28a+ using NdeI/NotI with an N-terminal His-tag followed by a thrombin site. Cerulean and Venus constructs were made by first cloning the fluorescent proteins followed by a GGSGG linker into pET28b(+) using NheI/SacI or NheI/BamHI, respectively. InaD PDZ45 (residues 474-674) and the NorpA CTD (residues 869-1095) were then inserted at SacI/XhoI or

BamHI/XhoI, respectively. All point mutations were introduced by either QuikChange site-directed mutagenesis (Stratagene) or overlap extension PCR. The NorpA C-terminal peptide (acetyl-NH-GKTEFYA-COOH, MW 856.9 Da) and Trp C-terminal peptide (acetyl-G-RGKSTVTGRMISGWL-COOH, MW 1706.02 Da) were synthesized by the UT Southwestern Protein Technology core facility.

Fluorescence Polarization Binding Assay

A titration of PDZ5 C645S was made by setting up 50 µL 1.5X serial dilutions of 75 µM protein in 50 mM Tris pH 8, 100 mM NaCl, 10% glycerol, 0.02% bovine serum albumin, 1 mM DTT, with 20 nM tetramethylrhodamine (TMR)-conjugated NorpA C-terminal peptide (TMR-GKTEFYA-COOH) in a 384-well plate. The samples were centrifuged to pellet dust and aggregated materials, incubated for 45 minutes, and then the fluorescence was measured in a Victor fluorescence plate reader using rhodamine filters (Perkin Elmer).

Protein Expression

Proteins were expressed in BL21-DE3 cells (Stratagene) at 18°C overnight following IPTG induction and then purified by either nickel or glutathione affinity chromatography. The purification tag was proteolyzed overnight by the addition of 1:50 w/w thrombin (NorpA constructs, PDZ5), 1:50 w/w Factor Xa (PDZ5 C645S), or 10 units/mg PreScission Protease (GE; PDZ45 constructs) and then

removed by re-binding to affinity resin. The proteins were then further purified by size exclusion chromatography on either a Superdex 75 or Superdex 200 column in 50 mM HEPES pH 7, 100 mM NaCl, 10% glycerol, and 1 mM DTT or 50 mM Tris pH 7.5, 100 mM NaCl (PDZ5 C645S).

Pull-Down Binding Assay

His-NorpA CTD was pre-incubated for 1 hour with Ni-NTA (Qiagen) in binding buffer (50 mM Tris pH 8, 100 mM NaCl, 50 mM imidazole) at 4°C. During this time, 50 µL of 10 µM InaD PDZ45 WT, T553A, F642A, and PDZ5 were also pre-incubated under reducing conditions (1 mM TCEP) in the binding buffer for 30 minutes on ice. The beads with or without pre-incubated NorpA were washed 1X and then resuspended with the 10 µM InaD solutions. The NorpA CTD concentration was also 10 µM after resuspension. The samples were equilibrated for 30 minutes at room temperature with mixing and then washed 2X. Finally, the bound sample was eluted with binding buffer containing 250 mM imidazole + 1 mg/ml BSA as a loading control and run on an SDS-PAGE gel.

FRET Binding Assay

Competitor proteins were co-incubated with 50 nM Cerulean-PDZ45 and 300 nM Venus-NorpA in 50 mM HEPES pH 7, 100 mM NaCl, 10% glycerol, 5% bovine serum albumin, 1 mM TCEP. For the NorpA CTD Δ5 and PDZ45 F642A double mutant experiments, 100 nM Cerulean-PDZ45 F642A and 1 µM Venus-

NorpA was used to increase the amount of FRET. The fluorescence emission spectra from 450 to 600 nm were measured in a Photon Technology International fluorimeter using 433 nm illumination. FRET inhibition was measured as the change in the FRET ratio (528 nm/475 nm), normalized in each experiment to a Michaelis-Menten fit. For PDZ5 C645S and Trp C-terminal peptide, the amplitude was normalized to the average maximal FRET ratio change of all the PDZ45 constructs. Curve fitting was performed in MATLAB (Mathworks).

Redox Titration Assay

Proteins (400 µL of 0.4 µM, 40 µL of 4 µM was used when NorpA was co-incubated) were incubated at 30°C in a dithiothreitol (DTT, E^0 = -323 mV (Szajewski et al. 1980)) redox buffer containing 10 mM HEPES pH 7, 50 mM NaCl, 1% glycerol, 25 mM oxidized DTT (Sigma), and the necessary amount of reduced DTT (Sigma) calculated using the Nernst equation (see Supplemental Info for details). Equimolar or 10 mM HEPES pH 7.0 was added to the reduced DTT to ensure the solution was exactly at pH 7.0. After 26 hours (unless otherwise indicated), 0.1% sodium deoxycholate and 30% trichloroacetic acid were added. The proteins were precipitated on ice for at least 30 minutes and centrifuged at 15,000 x g for 15 minutes to pellet. The pellet was rinsed three times with cold acetone and then air dried for 5 min. The pellets were resuspended in 200 mM Na_2HPO_4 pH 7.0, 1% (w/v) SDS with 10 mM 4-acetamido-4'-maleimidystilbene-2,2'-disulfonic acid (AMS; MW, 536.44 Da;

Molecular Probes). After approximately 1 min at room temperature, labeling was quenched by adding 10 mM reduced DTT. 10 mM tris(2-carboxyethyl)phosphine (TCEP) pH 7.0 was then added and the solution was incubated for 10 min to reduce any oxidized cysteines. The remaining reduced cysteines were then blocked by incubation with 50 mM iodoacetamide for 30 min. Finally, non-reducing Laemmli buffer was added and the samples were run on either Bio-rad 16.5% Tris-Tricine Criterion precast gels (PDZ5) or hand-poured large-format 12% Tris-Glycine gels for a GE SE600 gel apparatus.

Crystallization and Structure Determination

Selenomethionyl protein was produced by Shan Mishra by growing cells in M9 minimal media at 37°C to OD600 of 1.0, then incubating with amino acids (lysine, phenylalanine, threonine at 100mg/L; isoleucine, leucine, valine at 50mg/L, Se-methionine at 60mg/L) for 15 minutes, and finally inducing with 1mM IPTG overnight at 16°C. Protein purification was carried out as above. Mass spectrometry analysis of the purified selenomethionyl protein indicated complete (100%) incorporation of Se-Met at all 4 methionine sites.

Crystal trials were conducted by Shan Mishra at 4°C using the hanging drop vapor diffusion method at 0.4mM protein concentration. Small crystals grew spontaneously within 1 day with well solution containing 26-30% PEG 8000, 0.1-0.6M NaCacodylate, pH 5.4-6.0. Larger crystals were obtained by microseeding into equilibrated drops at lower protein concentration (0.1-0.2 mM).

Single crystals were cryoprotected by serial equilibration into well solutions containing increasing amounts of glycerol (up to 15%) and flash frozen in liquid nitrogen.

Data were collected at 100K at beamline 19-BM at the Advanced Photon Source, Argonne National Laboratory. Indexing, scaling and phasing were carried out by Shan Mishra with the HKL-3000 package and model refinement was carried out with the CCP4 suite. The statistics are summarized in Table 6. The structure was solved using SAD methods and a single dataset collected at the peak of the selenium excitation scan. Automated Patterson search methods using ShelX (in HKL-3000) identified all 16 selenium sites. After solvent flattening and phase extension to 2.4Å, the experimental electron density map was easily traceable. A randomly selected set of reflections (5%) was flagged for cross-validation. Manual model building was performed in Coot, and computational refinement was performed in CCP4 utilizing the program Refmac5. No non-crystallographic symmetry restraints were used during phasing or refinement.

Bioinformatic Analysis

Homologs of PDZ45 were identified using three rounds of PSI-BLAST searches for PDZ4, PDZ5, or PDZ45 against the NCBI non-redundant database. For PDZ4 and PDZ5, the PSI-BLAST inclusion cutoff was E<5E-14. This was chosen based on the distribution of E values observed for domains from single multi-PDZ domain proteins. For PDZ45, the cutoff was 5E-20. During the first

round subthreshold sequences corresponding to MPDZ and InaDL isoforms were included. High scoring hits where the sequence length was <70% were excluded to eliminate hits where only one domain of PDZ45 would match. The hitlists were then refiltered in MATLAB (Mathworks) using the indicated cutoff values and PDZ45 hits which overlapped with both a PDZ4 and PDZ5 hit were chosen as tandem homologs.

CHAPTER FIVE

Functional Integration within InaD PDZ5

Introduction

A fundamental problem in signaling is how proteins integrate and process information. Proteins often respond to multiple regulatory inputs by adjusting their catalytic or binding properties (Creighton 1993; Alberts et al. 2002). This allows evolution to build sophisticated information processing circuits using features such as feedback regulation, as discussed in chapter 1. The seemingly complex atomic structure of proteins, however, makes it difficult to intuitively understand how this required functional integration is achieved.

A major breakthrough in the understanding of protein regulation came from Monod, Wyman, and Changeaux (Monod et al. 1965) and Koshland, Nemethy, and Filmer (Koshland et al. 1966) who developed two competing theoretical models for a phenomenon known as allostery. The central idea of each was that proteins exist in multiple conformational states with distinct activities and this conformational equilibrium is influenced by the binding of allosteric regulatory factors. Proteins are now known to generally feature long-range energetic coupling (Gunasekaran et al. 2004) which allows perturbations at the surface, such as binding or modification, to trigger changes at distant sites. The

physical mechanisms underlying this connectivity are not yet generally understood.

InaD PDZ5 provides a powerful model system for investigating how proteins integrate multiple functions. As discussed in the previous chapter, PDZ5 oxidizes in response to visual signaling, altering the conformation of its binding pocket and suppressing further signaling, probably through unbinding of its ligand, NorpA (Mishra et al. 2007) (Figure 12). This indicates that PDZ5 is characterized by at least three equilibria: oxidation, binding, and conformation (Figure 44).

An important question in understanding both the biology of PDZ5 and the general problem of functional integration is to identify how these equilibria are coupled. In this chapter, I demonstrate that PDZ5 has a pairwise energetic architecture in which oxidation and binding are each strongly coupled to the conformational equilibrium but not to each other. As a result, oxidation triggers unbinding of NorpA, which can explain many of the features of the refractory state. The input mechanism triggering oxidation is still unclear but is likely to work by perturbing the conformational equilibrium.

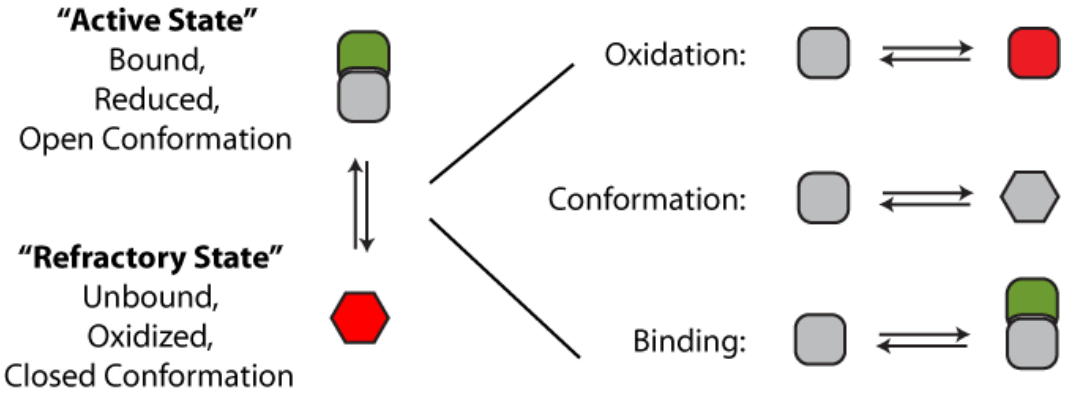

Figure 44: Three Equilibria Underlying Redox Switching by InaD PDZ5

InaD PDZ5 in vivo switches between an active state in which it is bound to NorpA, reduced, and in an open conformation to a refractory state in which it is likely unbound from NorpA, oxidized, and in a closed conformation. Three equilibria underlie this switching process: oxidation, conformation, and binding.

Thermodynamic Model of the PDZ5 Redox Switch

Coupling and Thermodynamic Boxes

Coupling fundamentally means that equilibria have different magnitudes in different backgrounds. As a concrete example, consider the potential coupling between binding and conformation in PDZ5. We can draw a "thermodynamic box" with one of these equilibria on each axis and the remaining corner the combination of the two states (Figure 45). Following the typical terminology, I'll refer to the conformation which binds better as the "open" conformation and the other as the "closed" conformation. If the closed conformation binds worse than the open conformation by a factor β, then the conformational equilibria must also change by a factor β in the bound state due to conservation of energy. The factor β

is known as the allosteric coupling constant, and the free energy of coupling is $\Delta\Delta G = RT\ln(\beta)$.

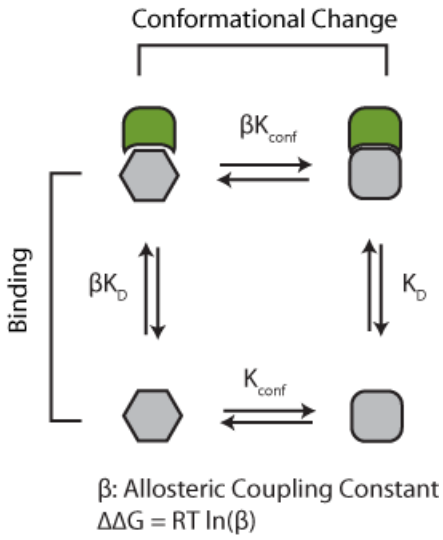

Figure 45: Sample Thermodynamic Box for Binding and Conformation

The thermodynamic box for conformation and binding is shown. Note that the equilibria on each side of the box are related by the same factor β.

Distinction between Macroscopic and Intrinsic Properties

It is important to note that the macroscopic properties of coupled thermodynamic systems are typically not the same as the intrinsic properties of the molecule but instead represent an average of the intrinsic properties of each state biased by the equilibrium constant. For example, in this particular case, the ratio of the apparent binding affinity to the intrinsic binding affinity of the open conformation is $\frac{K_{D\text{app}}}{K_D} = \frac{1+K_{\text{conf}}}{\frac{1}{\beta}+K_{\text{conf}}}$. In the limit of large coupling, this simplifies to $1 + \frac{1}{K_{\text{conf}}}$. Therefore, it is important to either isolate the distinct states of coupled

systems or take into account the effect of the equilibrium constant on the property that is measured.

Extension to Three Equilibria

In analogy to the thermodynamic box, PDZ5 can be formally thought of as a thermodynamic cube with allosteric coupling constants between oxidation and conformation (α), binding and conformation (β), and oxidation and binding (γ) (Figure 46). To understand the energetic structure of this system, it is necessary to measure these three coupling constants.

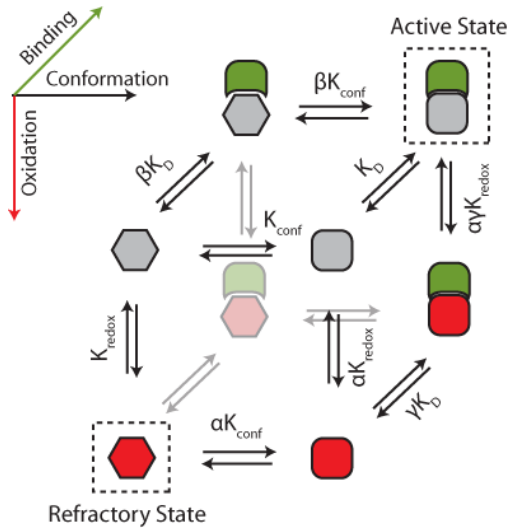

Figure 46: Thermodynamic Cube Model of PDZ5

Since the redox switching of PDZ5 involves three equilibria, it is formally a thermodynamic cube with the three axes being binding, conformation, and oxidation.

Thermodynamic Relationship between PDZ5 States

The fundamental equilibrium equations defining the cube in Figure 46 are

Equation 16: Thermodynamic Definition of the Three Equilibria in PDZ5

$$K_{\mathrm{conf}} = \frac{O}{C}$$

$$K_{\mathrm{D}} = \frac{O * L}{OL}$$

$$K_{\mathrm{redox}} = \exp\left(-\frac{nF}{RT}(E_C^0 - E_{env})\right) = \frac{C_{ox}}{C}$$

where O is the "open" state which binds NorpA and C is the "closed" state which does not bind. K_{conf}, K_{D}, and K_{redox} are the conformational, dissociation, and redox equilibrium constants at a particular environmental redox potential (E_{env}), respectively. L is the concentration of free ligand and OL is the concentration of the ligand-bound "open" state. C_{ox} designates the oxidized "closed" state. The other constants are: n, the number of electrons involved in the redox reaction (2); F, Faraday's constant; R, the ideal gas constant; T, the temperature; E_C^0, the standard redox potential of the "closed" state.

These three processes all potentially interact, giving rise to a series of cooperativities (α, β, γ) in the coupled reactions:

Equation 17: Thermodynamic Definition of the Coupled Equilibria in PDZ5

$$O_{ox} = \alpha K_{\mathrm{redox}} O$$

$$E_O^0 = E_C^0 - \frac{RT}{nF}\ln(\alpha)$$

$$CL = \frac{C * L}{\beta K_D}$$

$$O_{ox}L = \frac{O_{ox} * L}{\gamma K_D}$$

$$C_{ox}L = \frac{C_{ox} * L}{\beta\gamma K_D}$$

There is an additional possible third-order cooperativity corresponding to the reactions leading to the ligand-bound, oxidized, closed state, but this state is very weakly populated under my experimental conditions and I do not have data to constrain it. I assume it is non-cooperative here.

To analyze the model, I need to express all the species in terms of the open state, O, using the thermodynamic relationships listed above. I then solve for the concentration of the open state by substituting the equilibrium equations into the conservation of mass equation:

$$O = P_T - C - OL - CL - O_{ox} - C_{ox} - O_{ox}L - C_{ox}L$$

where P_T is the total protein concentration.

Dissection of the Coupling between Binding, Oxidation, and Conformation

To measure these coupling constants, we must analyze each pair of equilibria in isolation and be able to identify each state. There are obvious ways to study the bound and oxidized states—the protein can be saturated with ligand or placed under very oxidizing conditions. Distinguishing the two conformations is tougher, however. Traditionally spectroscopic methods such as nuclear magnetic

resonance (NMR) spectroscopy are used to quantitatively study the conformational state of proteins. NMR is a powerful approach, but it is very sensitive to any perturbation in the electromagnetic field around an atom (Cavanaugh et al. 2007). This can make it difficult to distinguish distinct effects within a protein, such as the formation of the disulfide bond and a more global conformational change in the protein, in the absence of additional experiments. An alternative approach, successfully applied here, is to kinetically isolate the conformational change from the binding and oxidation reactions, eliminating the allosteric averaging in macroscopic experiments.

Detection of Two Redox Conformations in PDZ45

Redox Equilibration Kinetics

While measuring the oxidation kinetics of PDZ45 (Figure 47), I fortuitously discovered that the conformational equilibrium was kinetically isolated from oxidation. Under very oxidizing conditions (12.5-25 mM oxidized DTT, no reduced DTT added, redox potential greater than -190 mV), PDZ45 completely oxidized at a rate proportional to the oxidized DTT concentration with single-exponential kinetics, as expected for a second-order reaction. Under less oxidizing conditions which were still sufficient to completely oxidize the protein at equilibrium (25 mM oxidized DTT, reduced DTT added to set the redox potential to -208 mV), the oxidation followed biexponential kinetics. The fast rate

matched the rate of oxidation under very oxidizing conditions, while the slow rate was ~4X slower.

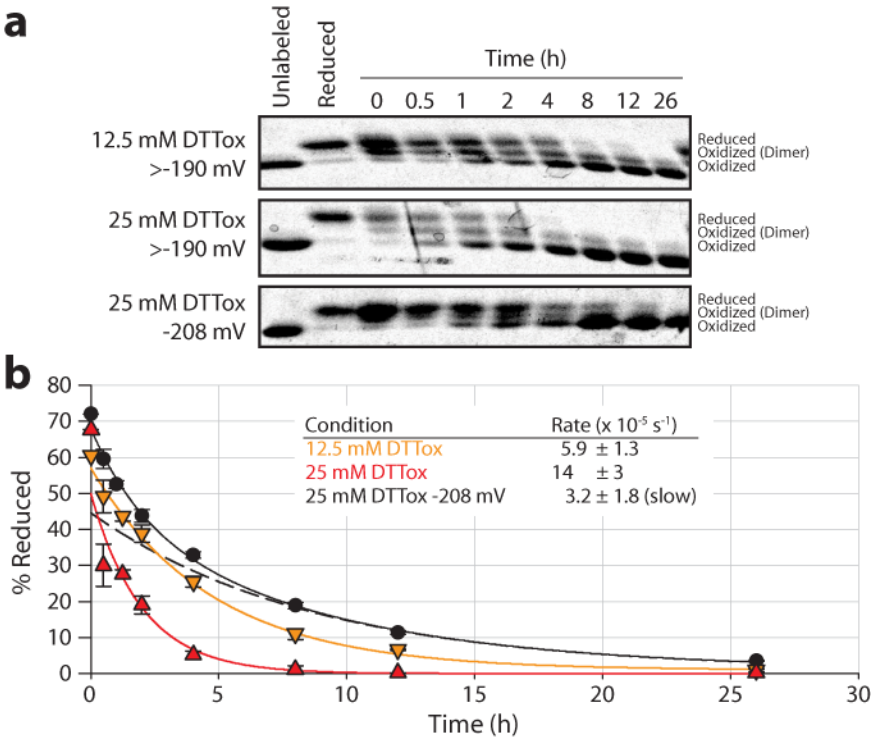

Figure 47: Oxidation Kinetics of PDZ45

(a) Gels showing the oxidation kinetics of PDZ45 Δ3C under very oxidizing (>-190 mV) or mildly oxidizing (-208 mV) conditions with the indicated amount of oxidized DTT measured by AMS labeling. (b) Plots of the oxidation kinetics along with single (red, orange) or double (black solid line) exponential fits. The fitted rates are listed in the inset table. Note that at -208 mV the oxidation followed biexponential kinetics. The slow rate is shown on the plot as the dashed black line.

The apparent redox potential of the oxidation-conformation coupled system is an average between the redox potentials of the open and closed conformations, biased by the conformational equilibrium. As a result, it is possible that the open and closed conformations differentially oxidize under

milder oxidizing conditions which are still sufficient to completely oxidize PDZ45 at equilibrium. If the conformational change was slow, this would result in the emergence of a second kinetic process, rate-limited by the conformational dynamics, as oxidized species interconverted conformation. The observation of this phenomenon suggests that the conformational change is indeed rate-limiting.

A fortunate consequence of the kinetic separation of timescales is the possibility of observing the intrinsic equilibrium constant of each state instead of the allosteric average: If we measure the redox properties after a couple of hours of equilibration, the system will be at a quasi-equilibrium in which the redox state of each conformation in isolation has reached equilibrium while the conformational change has not occurred. This should result in the appearance of two distinct titrations for each conformation.

Quasi-Equilibrated Redox Titration

I performed redox titrations of PDZ45 Δ3C, measuring the redox state after 2 h while the protein was at quasi-equilibrium (Figure 48). The protein titrated in a biphasic manner with inflections at -212 ± 6 mV (open conformation) and -293 ± 7 mV (closed conformation) with the -212 mV population more prevalent. As shown in Figure 40, the two populations are fully equilibrated after 26 hours, and the titration has only a single apparent inflection point with an E^0 of -242 mV. This confirms that there are two distinct conformations in PDZ45 which

slowly interconvert under the experimental conditions. Given the similarity of the redox potentials, it also suggests that free PDZ5 can be used as a proxy for the closed conformation.

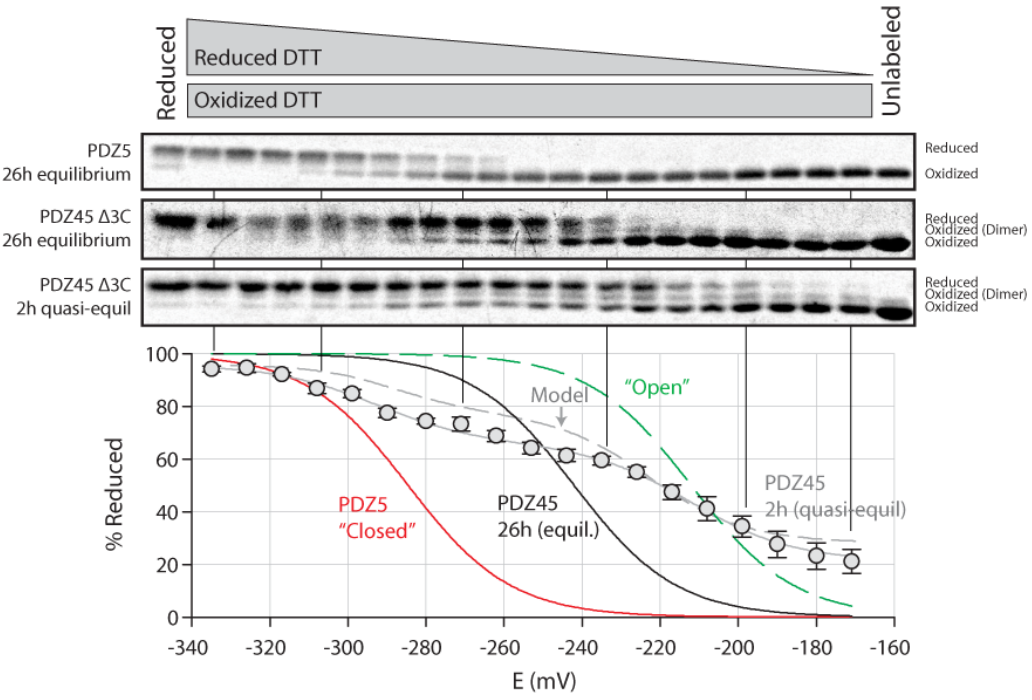

Figure 48: Quasi-Equilibrated Redox Titration of PDZ45 Δ3C

Redox titrations of PDZ5 and PDZ45 Δ3C (26h equilibration) repeated from Figure 40 are shown with a quasi-equilibrated (2h equilibration) titration of PDZ45 Δ3C. The plot shows the quasi-equilibrated titration (gray circles) along with the fits of the PDZ5 (red line) and PDZ45 Δ3C (black line) fully equilibrated titrations. The quasi-equilibrated titration has two inflections, one very similar to PDZ5 and the other occurring under very oxidizing conditions (open state, green dashed line). A kinetic simulation of the titration using the parameters from Figure 49 and Figure 47 is also shown (dashed gray line).

Redox-Conformation Coupling

The observation of the two distinct redox states in PDZ45 allowed me to directly measure the coupling between redox and conformation and also estimate the magnitude of the conformational equilibrium (Figure 49). From the difference

in the redox potentials of the two states, I calculate that α is 1/270 (-5.6 ± 0.2 kT). The conformational equilibrium constant (K_{conf}) can be calculated using α and the equilibrium redox potential using the allosteric model (Equation 16 and Equation 17).

In the experiment there is no ligand so I can simplify the equation for the open state concentration by substituting L = 0:

$$O(L=0) = \frac{K_{\mathrm{conf}} K_{\mathrm{redox}} P_T}{1 + \alpha K_{\mathrm{conf}} + K_{\mathrm{redox}} + K_{\mathrm{conf}} K_{\mathrm{redox}}}$$

I can now solve for the fraction of the total protein that is reduced:

$$f_{red} = \frac{O + C}{P_T}$$

$$f_{red}(L=0) = 1 - \frac{1 + \alpha K_{\mathrm{conf}}}{1 + K_{\mathrm{redox}} + \alpha K_{\mathrm{conf}} + K_{\mathrm{conf}} K_{\mathrm{redox}}}$$

The conformational equilibrium constant that gives 50% reduction at $E_{env,50\%}$ can be found by solving for K_{conf} when $f_{red} = 0.5$ (note that K_{redox} is a function of E_{env}):

$$E_{env,50\%} = E_C^0 - \frac{RT}{nF} \ln\left(\frac{1 + \alpha K_{\mathrm{conf}}}{1 + K_{\mathrm{conf}}}\right)$$

Equation 18: Estimation of the Conformational Equilibrium Constant from Redox Data

$$K_{\mathrm{conf}}(E_{env} = E_{env,50\%}) = \frac{1 - K_{redox}^{-1}}{K_{redox}^{-1} - \alpha}$$

For the observed values of $E_{env,50\%}$ = -242 ± 2 mV, E_O^0 = -212 ± 6 mV, α = -5.6 ± 0.5 kT, K_{conf} is estimated to be 29 ± 2. The conformational equilibrium constant for the oxidized form would then be 0.11 ± 0.07.

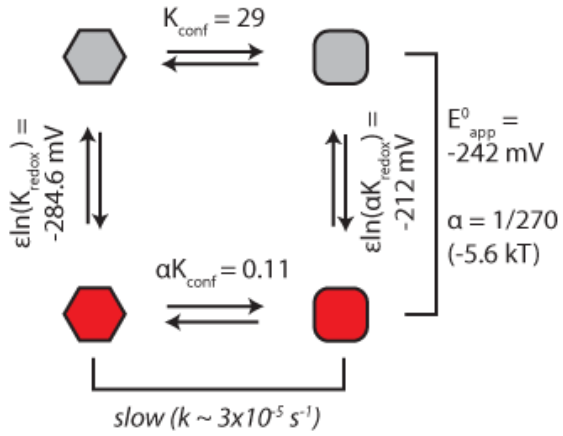

Figure 49: Thermodynamic Box for Oxidation and Conformation

The thermodynamic box for the oxidation and conformational equilibria is shown with the estimated parameters. $\epsilon = \frac{RT}{nF}$.

Using these equilibrium constants and the measured kinetics, I simulated the redox titration at 2h and found that these values recapitulated the observed titration curve (Figure 48). The slight deviation under more reducing conditions is probably due to using the PDZ5 redox potential rather than the observed closed state redox potential.

Because of the large coupling between oxidation and conformation and the small magnitude of K_{conf}, the conformational equilibrium switches from favoring the open to the closed conformation upon oxidation (Figure 49). This is consistent with the structural difference between the oxidized and reduced states. Note that

while the redox data reveals the presence of a non-negligible fraction of the closed conformation in reduced PDZ45, the equilibrium is sufficiently far to the right to not produce a detectable mixture by traditional NMR methods, as 97% of the protein should be in the open state.

Binding-Conformation Coupling

Since free PDZ5 strongly prefers the closed conformation (I estimate $K_{conf,PDZ5} < 1/10$ from the redox and binding data), I can now interpret the earlier binding experiment in the context of the thermodynamic model. Since $K_{conf,PDZ45}$ is greater than 10, the binding affinity of PDZ45 is a good estimate of the K_D of the open conformation. Therefore I can directly estimate β from the difference in the K_D of PDZ5 and PDZ45 to be greater than 1700 (>7.4 kT). This results in binding strongly biasing the conformational equilibrium towards the open conformation (Figure 50).

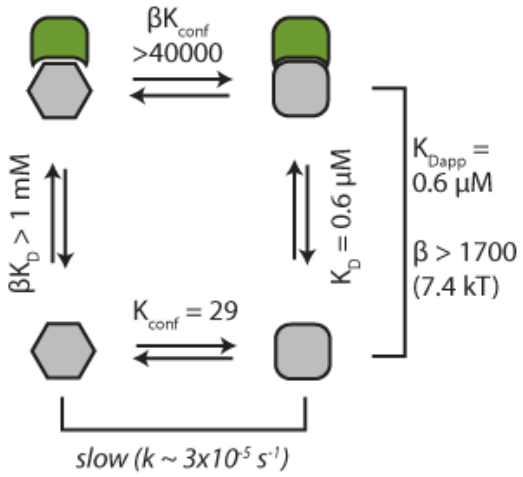

Figure 50: Thermodynamic Box for Binding and Conformation

The thermodynamic box for the binding and conformational equilibria is shown with the estimated parameters.

Redox-Binding Coupling

The serial coupling of oxidation to binding through the conformational equilibrium is on its own enough to result in unbinding of NorpA upon oxidation. In order to determine whether there was any direct coupling between oxidation and binding, I measured the effect of NorpA on the redox potential (Figure 51). I tested this by equilibrating PDZ5 and PDZ45 Δ3C with increasing concentrations of NorpA CTD under conditions in which they are 20–40% reduced in the absence of ligand (-280 and -235 mV, respectively). I found that binding of NorpA shifted the population of PDZ45 Δ3C from 16 ± 4% to 75 ± 5% reduced. The change in redox state occurred with a binding affinity of 0.9 ± 0.4 μM, in agreement with the earlier binding experiments (Figure 33). The redox state of

isolated PDZ5 was unaffected as expected given its weak K_D for the NorpA CTD. This confirms that oxidation of PDZ5 is coupled to unbinding of NorpA.

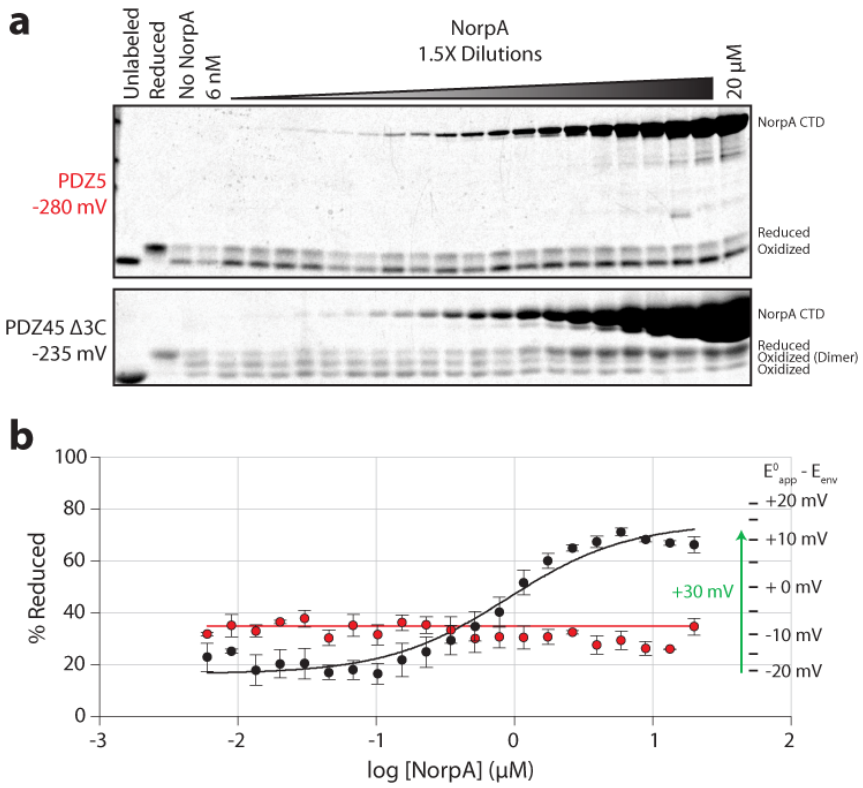

Figure 51: Effect of NorpA Titration on the Redox State

(a) The redox states of PDZ5 and PDZ45 Δ3C were assayed under conditions which partially reduce the protein and then various amounts of NorpA CTD were added. (b) Quantification of the redox state as a function of the concentration of NorpA. PDZ45 is shown in black, PDZ5 in red. On the right, the percent reduced expected for various shifts in the apparent redox potential versus the environment are indicated in 5 mV intervals.

To determine whether this coupling arose from the serial coupling through the conformational equilibrium or instead required additional direct coupling, I returned to the thermodynamic model. In the case of infinite coupling, it is clear that oxidation and binding would be exclusive, resulting in saturating binding

completely reducing the protein. As I repeatedly observed significant oxidation with saturating ligand at -235 mV, this is clearly wrong.

In the non-cooperative case, ligand binding shifts the apparent redox potential towards the open conformation's due to the perturbation of the conformational equilibrium. Using the thermodynamic model, I can model the conditions used in the experiment by calculating the fraction reduced, f_{red}, under conditions of saturating ligand (note that K_{redox} is a function of E_{env}):

$$f_{red,L\to\infty} = \lim_{L\to\infty} f_{red} = \frac{\gamma K_{\mathrm{redox}}(1+\beta K_{\mathrm{conf}})}{1+\gamma K_{\mathrm{redox}}+\alpha\beta K_{\mathrm{conf}}+\beta\gamma K_{\mathrm{conf}}K_{\mathrm{redox}}}$$

To reduce the uncertainty, I can estimate the effective redox potential ($E_{env,eff}$) from the fraction reduced in the absence of ligand. This turns out to be -220 ± 10 mV, slightly more oxidizing than the intended -235 mV. I can then estimate γ from the saturating ligand measurement by solving $f_{red,L->\infty}$ for γ at $E_{env,eff}$ (note that K_{redox} is a function of E_{env}):

Equation 19: Estimation of the Oxidation-Binding Coupling from Ligand Saturation Experiments

$$\gamma\left(E_{env}=E_{env,eff}\right)=\frac{f_{red,L\to\infty}(1+\alpha\beta K_{\mathrm{conf}})K_{\mathrm{redox}}}{\left(1-f_{red,L\to\infty}+\beta K_{\mathrm{conf}}-\beta K_{\mathrm{conf}}f_{red,L\to\infty}\right)}$$

For $E_{env,eff}$ = -220 ± 10 mV and $f_{red,L->\infty}$ = 0.75 ± 0.04, $\gamma \sim 1$ ($\Delta\Delta G = 0.5 \pm 0.9$ kT). Therefore, there is no significant cooperativity between oxidation and binding (Figure 52). This makes sense, as both cysteines are in the core of the protein and are unlikely to directly influence binding.

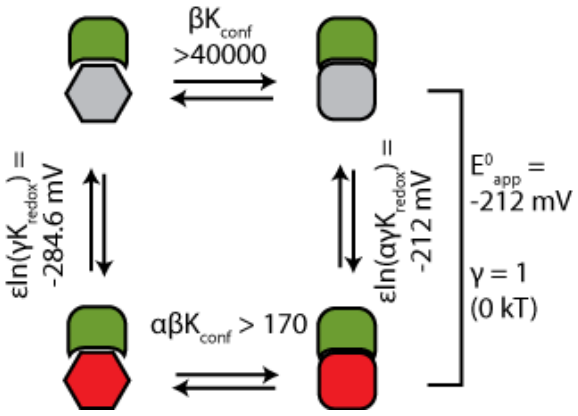

Figure 52: Thermodynamic Box for Redox and Conformation in the Presence of Ligand

The thermodynamic box for the oxidation and conformational equilibria is shown in the ligand-bound state with the estimated parameters. Note that ligand binding shifts the apparent redox potential due to its effect on the conformational equilibrium. If there were additional coupling, the intrinsic redox potentials would also be perturbed. $\epsilon = \frac{RT}{nF}$.

Energetic Architecture of Redox Switching in PDZ5

These results demonstrate that oxidation of PDZ5 triggers unbinding of NorpA through mutual coupling with the conformational equilibrium in PDZ5 and not directly. As a result, what was initially a thermodynamic cube (Figure 46) can instead be viewed as a series of thermodynamic boxes linked by the conformational equilibrium (Figure 53). Changes in the binding of NorpA and redox potential can be interpreted from the change in the conformational equilibrium.

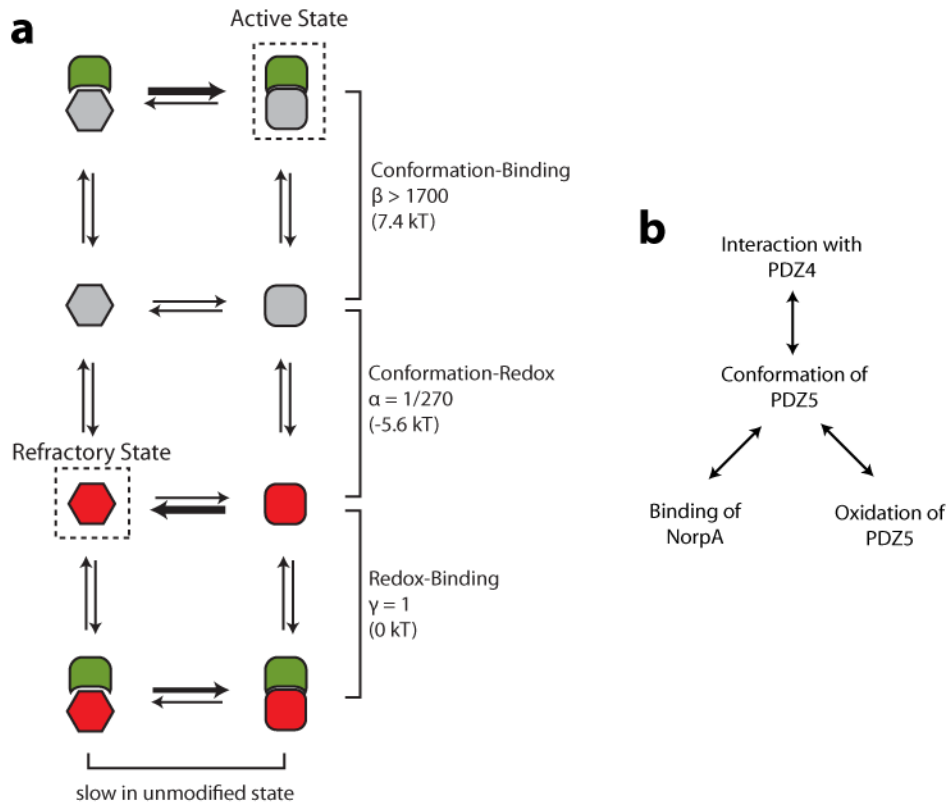

Figure 53: Energetic Architecture of Redox Switching in PDZ5

(a) The energetic architecture of redox switching in PDZ5 can be drawn as a series of linked thermodynamic boxes since there is no energetic coupling between redox and binding. All the effects are mediated through changes in the conformational equilibrium (illustrated by changes in the size of the arrows). (b) The system can also be thought of as a network in which each of the components is connected to the conformational equilibrium.

Comparison with Statistical Correlations in the PDZ Domain Family

The observation that the disulfide bond in PDZ5 is a recent evolutionary innovation (Figure 10) suggests that this regulation was somehow easy to engineer into the protein. A plausible hypothesis for this is that the coupling between the residues mediating disulfide bond formation, the conformational equilibrium, and the binding pocket is an ancient feature of the PDZ domain. The

Ranganathan lab has developed a statistical approach to detect coupling by examining the coevolutionary pattern of residues in protein families. In brief, the conservation-weighted covariation is calculated for residue pairs in a large multiple sequence alignment. For a detailed explanation, see (S. W. Lockless et al. 1999; Halabi et al. 2009).

The PDZ domain, like all the proteins examined so far, features a sparse coupling pattern with 10-20% of the protein highly coevolving and the rest evolving nearly independently (Figure 54a). Using spectral analysis, the independent sets of residues mediating the coupling pattern, known as sectors, can be identified (Halabi et al. 2009). In the case of the PDZ domain, there is one sector which connects the binding pocket with two distal surfaces (Figure 54c). Intriguingly, this sector contains the two residues responsible for disulfide bond formation in PDZ5.

How does the experimental coupling pattern I measure in PDZ5 compare with this analysis? Looking at the matrix of coupling values between residue pairs, there is strong coupling between C606 and C645S but only weak coupling between the binding pocket residue F642 and either cysteine (Figure 54b). Not surprisingly given their co-occurrence in the sector, there are a set of strongly coupled residues in the β2-β3 loop connecting the cysteines to the binding pocket. While this warrants additional investigation, this is a tantalizing suggestion that

the regulatory features of PDZ5 indeed represent a more ancient shared property of PDZ domains.

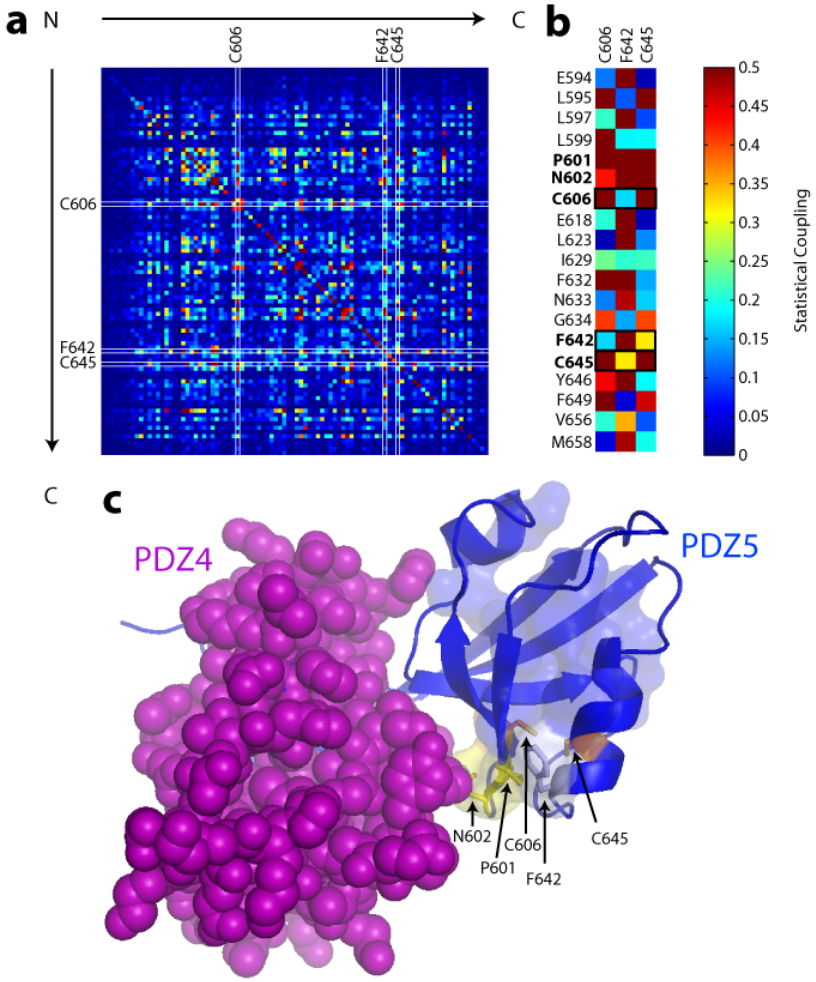

Figure 54: Statistical Coupling between Residues Mediating Binding and Oxidation in the PDZ Domain Family

(a) Matrix of statistical coupling values between pairs of residues in the PDZ domain family. The binding site (F642) and cysteines (C606, C645) are indicated. (b) Matrix showing the coupling between the binding site and cysteines with sector residues. Note that while the cysteines are strongly coupled, the binding site is only weakly coupled to each of them. P601 and N602 mediate coupling between the two sites. (c) Structure of PDZ45 shown with PDZ4 in space filling and the PDZ sector overlaid on PDZ5 as a transparent surface. Note that the sector connects the binding site (light blue) and cysteines (orange) out to the interface. Sector residues mediating high coupling between the two sites are shown in yellow.

Physiological Consequences of Dynamic NorpA Localization

Analysis of Existing Mutant Fly Phenotypes

To effectively generate a refractory period, oxidation of PDZ5 must reduce the probability of successfully responding to light. NorpA is known to be critical for this—mutant flies in which NorpA is less active or mislocalized, including the PDZ5 mutant *inaD*^{2}, are less sensitive to light, have a long, highly stochastic latency, smaller amplitude, and slower response kinetics (Susan Tsunoda et al. 1999) (Figure 55). In contrast, loss of scaffolding of Trp due to the inaD^{215} mutation affects inactivation instead of activation (B. H. Shieh et al. 1996; S. R. Henderson et al. 2000).

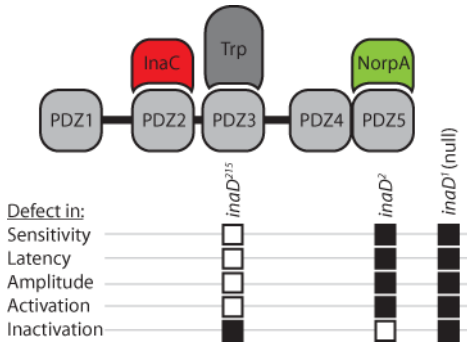

Figure 55: Phenotypes of InaD Mutants

The phenotypes of InaD mutants are shown. *inaD*^{215} and *inaD*^{2} are mutations in PDZ3 and PDZ5, respectively. Filled-in boxes represent defects in the listed property.

Simulation of the Effect of NorpA on the Refractory Period

The Ranganathan lab recently reported a quantitative model of the quantum bump which was able to recapitulate several known phenotypes of

phototransduction mutants (Pumir et al. 2008). NorpA is modeled as performing two activities: indirect activation of the Trp channels through its phospholipase activity (k_A) and inactivation of the G protein through its GTPase-activating function (γ_{PLC}) (Figure 56a).

I tested whether modulation of these properties could mimic a refractory period by analyzing many simulated quantum bump trials with the perturbed parameters. I found that the efficiency (the probability of successfully opening the channels), latency, and amplitude were all strongly dependent on both activities of NorpA (Figure 56b-d). A 10-fold change in either activity would be sufficient to recapitulate the known phenotypes of NorpA mislocalization, suggesting that scaffolding by InaD increases the phospholipase or decreases the GTPase-activating activity of NorpA by at least this amount.

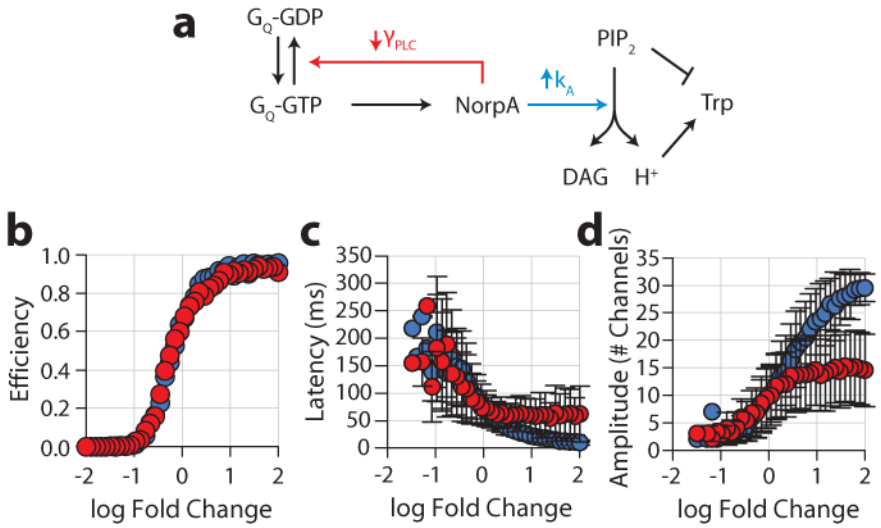

Figure 56: Sensitivity of Quantum Bump Properties to NorpA Parameters

(a) Subset of the phototransduction pathway focusing on the reactions performed by NorpA. I simulated the effects of modulating the GTPase-activating (γ_{PLC}, red) and phospholipase (k_A, blue) activities in the Ranganathan lab's previously published quantitative model of the single photon response. The effects on the (b) efficiency, (c) latency, and (d) amplitude indicate that these parameters have large effects on vision.

Potential Mechanisms for Triggering Oxidation

Conformational Control

The data presented here suggest that the mechanism which triggers oxidation in vivo likely acts by perturbing the conformational equilibrium, potentially by disrupting the interaction between PDZ4 and PDZ5. Because the conformational equilibrium is coupled to binding, oxidation, and the interaction with PDZ4, all of these things would be simultaneously affected (Figure 57).

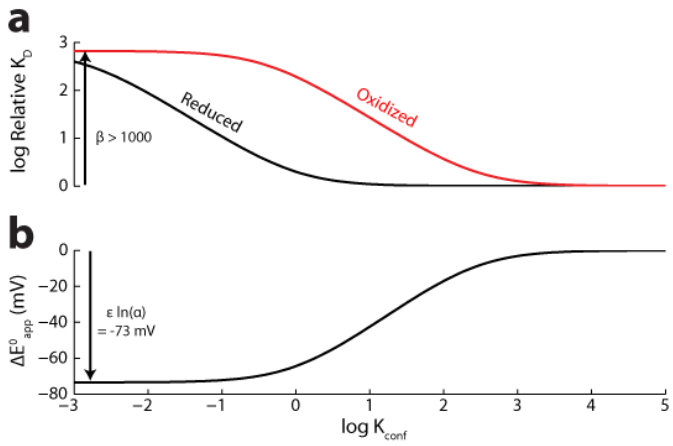

Figure 57: Dependence of Binding and Redox on the Conformational Equilibrium

The effect of the conformational equilibrium on the relative (a) binding affinity and (b) the redox potential is shown. In the case of the binding affinity, oxidation perturbs the conformational equilibrium, further decreasing binding as indicated. $\epsilon = \frac{RT}{nF}$.

What might perturb the conformational equilibrium? Many factors can influence the conformation of proteins—binding, modifications such as phosphorylation, changes in ionic composition of the solvent just to name a few. Indeed, Shan Mishra previously showed that oxidation required the presence of InaC (Mishra et al. 2007), which is known to multiply phosphorylate InaD (Hiroyuki Matsumoto et al. 1984; A. Huber et al. 1996; Mingya Liu et al. 2000). Another potential mechanism came from a paper which emerged during the course of this work: Liu et al. proposed that acidification uncouples PDZ4 from PDZ5 based on interpretation of hydrogen bonding with histidines in a peptide-bound structure of PDZ45 they solved (W. Liu et al. 2011). Some preliminary work investigating these two potential input mechanisms is described here.

Effect of Acidification on PDZ45

Liu et al. proposed that acidic conditions uncoupled PDZs 4-5, triggering oxidation and unbinding (W. Liu et al. 2011). However, it is unclear from data whether this actually occurs as the effects they observed could be kinetic nature. I repeated the redox and binding measurements at pH 5.8 (

Figure 58). At equilibrium, acidic conditions actually bias PDZ45 even more towards the open conformation. Furthermore, the structure of PDZ45 presented here was crystallized under acidic conditions while the one reported in Liu et al. was crystallized under neutral conditions (W. Liu et al. 2011). Despite this, the structures are nearly identical with some minor side chain rearrangements near the PDZ4 binding pocket (Figure 59). However, I did observe subtle changes in the oxidation kinetics (data not shown), suggesting acidic conditions may lower the energy barrier to conformational switching.

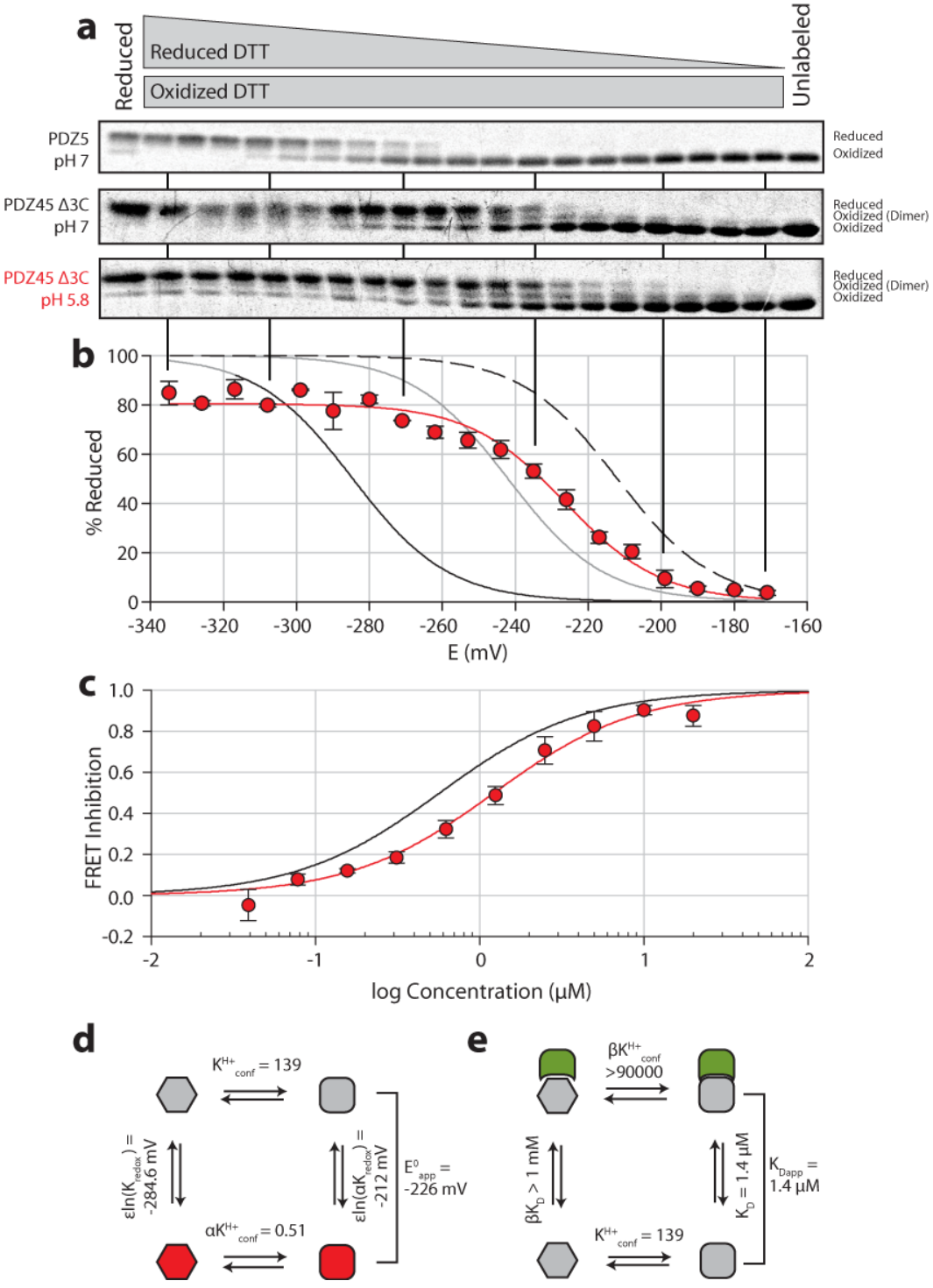
a
Reduced
Reduced DTT
Oxidized DTT
Unlabeled
PDZ5
pH 7
Reduced
Oxidized
PDZ45 Δ3C
pH 7
Reduced
Oxidized (Dimer)
Oxidized
PDZ45 Δ3C
pH 5.8
Reduced
Oxidized (Dimer)
Oxidized
b
% Reduced
E (mV)
c
FRET Inhibition
log Concentration (μM)
d
K^{H+}_{conf} = 139
εln(K_{redox}) = -284.6 mV
εln(αK_{redox}) = -212 mV
E^0_{app} = -226 mV
αK^{H+}_{conf} = 0.51
e
βK^{H+}_{conf} >90000
βK_D > 1 mM
K_D = 1.4 μM
K_{Dapp} = 1.4 μM
K^{H+}_{conf} = 139

Figure 58: Effect of Acidification on Binding and Oxidation

(a) Gels showing redox titrations of PDZ5 and PDZ45 Δ3C at pH 7 (from Figure 40) with PDZ45 Δ3C at pH 5.8. (b) Plot of the redox titration of PDZ45 Δ3C at pH 5.8 (red circles) along with fits to PDZ45 Δ3C at pH 5.8 (red line) and pH 7 (gray line) and the open (black dashed line) and closed (black solid line) conformations. (c) Competition binding curve for PDZ45 at pH 5.8 (red circles) using the FRET binding assay. The binding curve at pH 7 is also shown (black line). (d-e) Interpretation of the redox and binding data in terms of thermodynamic boxes for (d) redox and (e) binding with conformation.

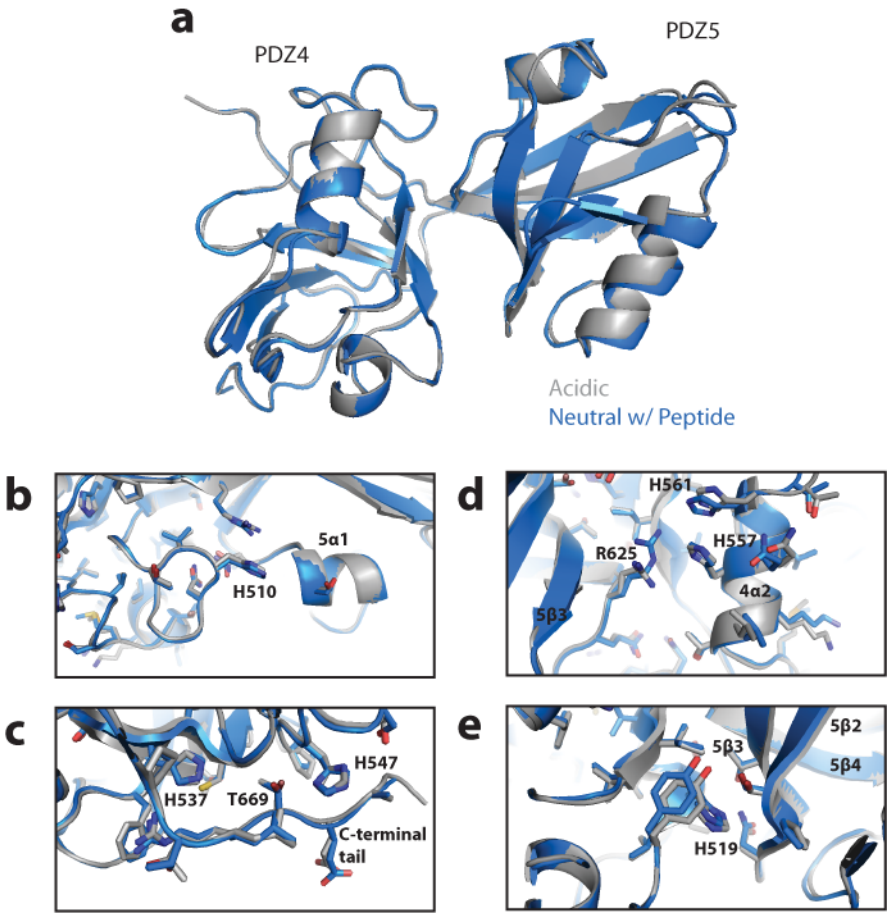

Figure 59: Structural Consequences of Acidification

(a) Comparison of the structure of PDZ45 under neutral conditions with peptide bound (PDB:3R0H) versus the unliganded state under acidic conditions. (b-e) Close-up view of the regions surrounding each of the histidines in PDZ4. (c) Note that T669 and H547 are unchanged. (d) Note that R625 and H561 are perturbed.

Effect of Phosphorylation on PDZ45

Shan Mishra demonstrated that oxidation of PDZ5 does not occur *in vivo* when the protein kinase C (PKC) InaC is knocked out (Mishra et al. 2007). InaC is known to multiply phosphorylate InaD, although functional sites have not yet been identified. I investigated whether PDZ45 was a substrate for PKC *in vitro* and *in vivo* and whether any phosphorylation sites identified affected the binding or redox properties.

Biochemical Characterization of Potential Phosphorylation Sites

Development of a Phosphorylation Assay

I was given Sf9 cells expressing His-tagged human PKCα, a homolog of InaC, by Paul Sternweis and major basic protein (MBP), a nonspecific kinase substrate, by Melanie Cobb. Following the phosphorylation conditions published in (Sando et al. 2003), I tested phosphorylation using MBP, PDZ5, and PDZ45 under reducing conditions (

Figure 60). In agreement with preliminary work done by Shan Mishra, I found that PDZ5 was phosphorylated very slowly with a low molar ratio of phosphate incorporation. In contrast, PDZ45 was a much better substrate, yielding detectable levels of phosphorylated protein although still much lower than MBP. These initial results had very little PKC-specific phosphorylation, so I optimized the conditions, determining the K_M by measuring the phosphorylation rate as a function of substrate concentration (

Figure 60b-c) and the phosphorylation kinetics (

Figure 60d-e). After these optimizations, I was able to get a substantial amount of PKC-dependent phosphorylation of PDZ45.

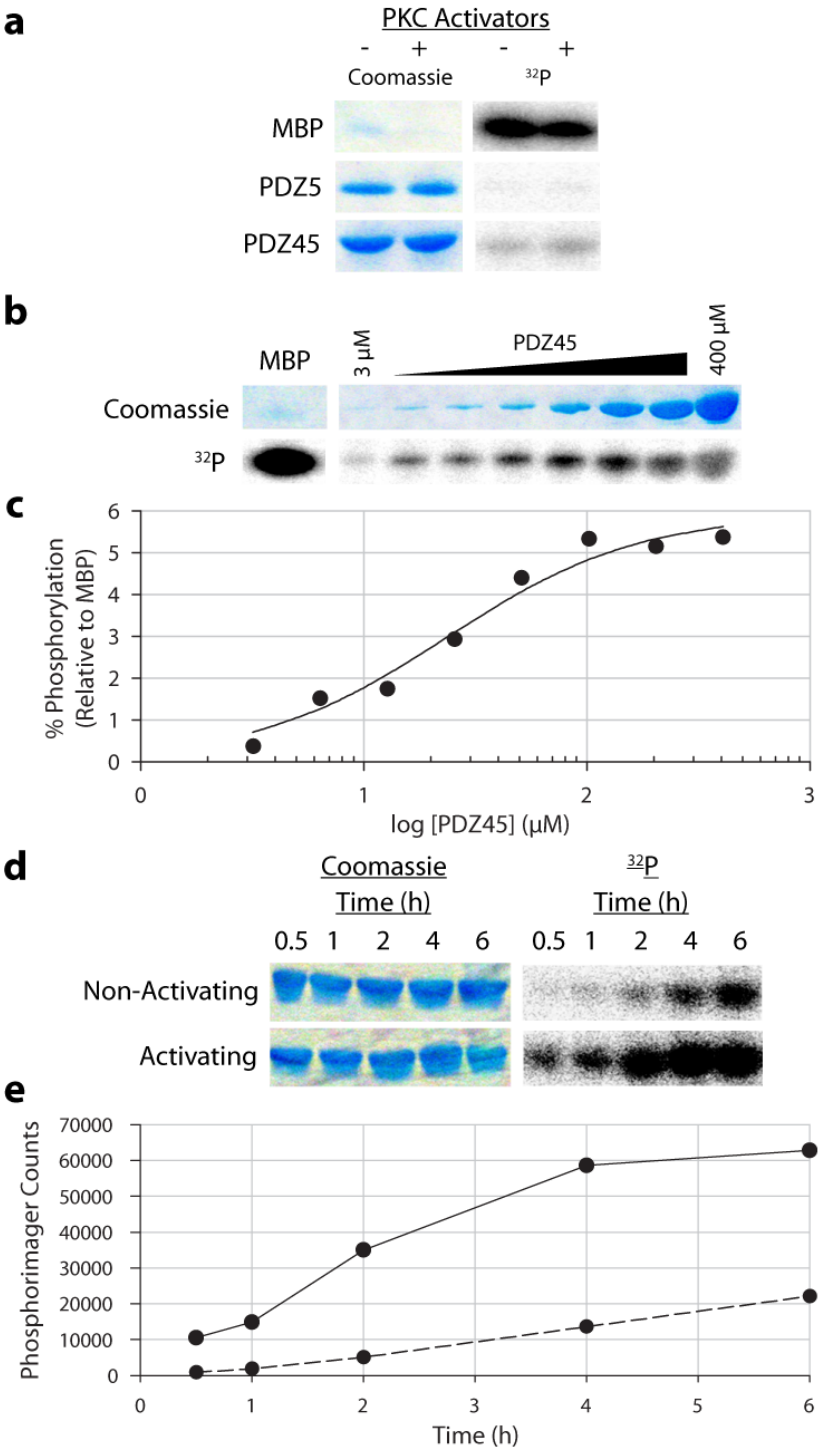
a
PKC Activators
- + - +
Coomassie
32P
MBP
PDZ5
PDZ45
b
MBP
3 µM
PDZ45
400 µM
Coomassie
32P
c
% Phosphorylation (Relative to MBP)
log [PDZ45] (µM)
d
Coomassie
Time (h)
32P
Time (h)
0.5 1 2 4 6
0.5 1 2 4 6
Non-Activating
Activating
e
Phosphorimager Counts
Time (h)

Figure 60: Characterization of Phosphorylation of PDZ45 by PKC in vitro

(a) Treatment of MBP, PDZ5, and PDZ45 with human PKCα under non-activating or activating conditions. Only weak PKC-dependent activity was detected in these initial experiments. (b-c) Determination of the K_M of PKC for PDZ45. (b) Gel showing the phosphorylation level of different concentrations of PDZ45 and (c) plot of the relative phosphorylation level along with a sigmoidal fit to determine the K_M. (d-e) (d) Gel and (e) plot showing phosphorylation kinetics of PDZ45 under activating (solid line) and non-activating (dashed line) conditions.

Identification of Phosphorylation Sites

Mass Spectrometric Analysis

I submitted *in vitro* phosphorylated protein to the Protein Chemistry core facility at UT Southwestern for identification of the phosphorylation sites by tandem mass spectrometry. They detected singly and doubly phosphorylated species (Table 9) corresponding to phospho-T661 and phospho-T661/T666 in PDZ45 (Table 10) based on 72% coverage of PDZ45 (Figure 61).

Table 9: ESI-MS of PKC-treated PDZ45

Sample	Masses Detected
Non-PKC-Treated	22459
PKC-Treated	22459, 22539 (+1 PO_4), 22619 (+2PO_4)

```
  1 GPLGSPEFTA EIKPNKKILI ELKVEKKPMG VIVCGGKNNH VTTGCVITHV
 51 YPEGQVAADK RLKIFDHICD INGTPIHVGS MTTLKVHQLF HTTYEKAVTL
101 TVFRADPPEL EKFNVDLMKK AGKELGLSLS PNEIGCTIAD LIQGQYPEID
151 SKLQRGDIIT KFNGDALEGL PFQVCYALFK GANGKVSMEV TRPKPTLRTE
201 APKA
```

Figure 61: LC/MS Coverage of PDZ45 Tryptic Fragments

The sequence of recombinant PDZ45 is shown. The tryptic fragments detected by ESI-MS following liquid chromatography are shown in bold red text. This represents 72% coverage of the protein.

Table 10: Modified Peptides Detected by LC/MS/MS for PKC-Treated PDZ45

Tryptic Fragment Mass	MS/MS Assignment
1512.8 (m/z 505.3)	VSMEVTRPKPTLR (WT)
1592.8 (m/z 531.9)	VSMEV**T**RPKPTLR (phospho-T661), could not rule out possible VSMEVTRPKP**T**LR (phospho-T666) too
1672.8 (m/z 558.6)	VSMEV**T**RPKP**T**LR (phospho-T661/T666)

Mutational Analysis

I mutated T661 and T666 alone and in combination and tested their phosphorylation by PKC (Figure 62). T661A substantially reduced the phosphate incorporation while T666A had little to no effect, indicating that T661 is indeed being phosphorylated *in vitro*. Mutating both sites did not completely eliminate the phosphate incorporation, however. Much of the remaining phosphorylation occurs under non-activating conditions as well, suggesting that this phosphorylation is not likely to be relevant.

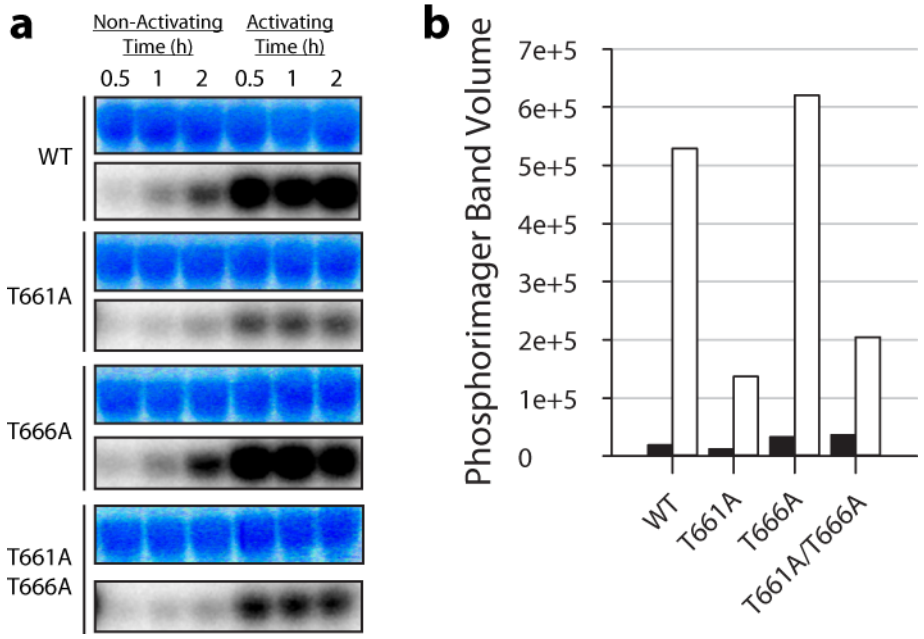

Figure 62: Characterization of Potential Phosphorylation Sites

(a) Gels showing phosphorylation of PDZ45 phosphomutants by PKC under non-activating or activating conditions. For each mutant, the top gel is the Coomassie stained gel and the bottom is ^{32}P detected by a phosphorimager. (b) Quantification of the level of phosphorylation after 30 minutes under non-activating (black) or activating (white) conditions for the mutants.

Analysis of Phosphorylation in vivo

Development and Characterization of Phospho-Specific Antibodies for PDZ45

Shan Mishra had already developed a phospho-T666 antibody based on his results with PDZ5, although he had not determined the optimal conditions for using the antibody. Since I detected T661 as the primary site in PDZ45, I had Covance develop a phospho-T661 antibody using a phospho-peptide followed by positive and negative selection for recognition of the phospho- and non-phospho

peptides, respectively. I then determined the optimal concentrations for both antibodies and their relative specificity for the phosphorylated form (Figure 63 and Figure 64). The T661 and T666 phosphoantibodies had optimal discrimination of phosphopeptide or wild-type flies treated with PKC activators versus InaC-null flies at antibody dilutions between 1:500 and 1:1000. The T666 antibody was ~1000-fold selective for the phosphorylated form of the antigen (Figure 64).

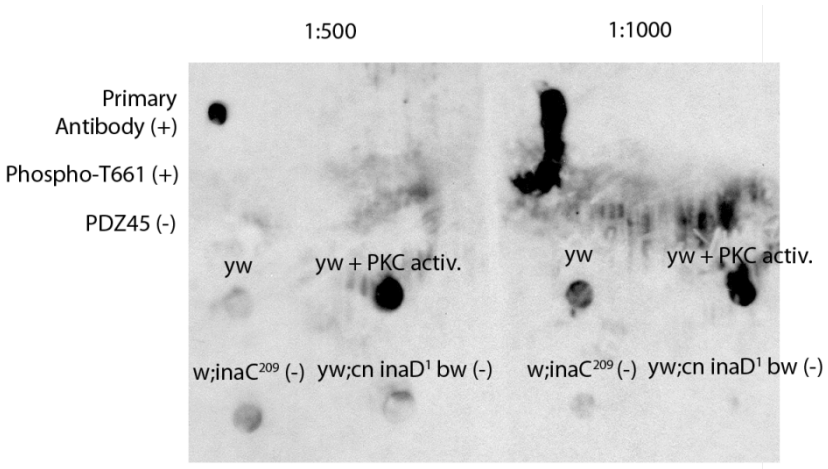

Figure 63: Characterization of Anti-Phospho-T661

Two dot blots processed using 1:500 or 1:1000 anti-phospho-T661 antibody are shown. The primary antibody was spotted as a positive control. In addition, phospho-T661 peptide and unphosphorylated PDZ45 were spotted as positive and negative controls, respectively, at 10, 1, and 0.1 fmol (none were detected). The bottom set of four spots are fly head extracts from wild-type (*yw*), PKC-null (*w;inaC*^{209}), or inaD-null (*yw;cn inaD*^{1} *bw*) flies. Wild-type flies were also tested in the presence of PKC activators (+ PKC activ.).

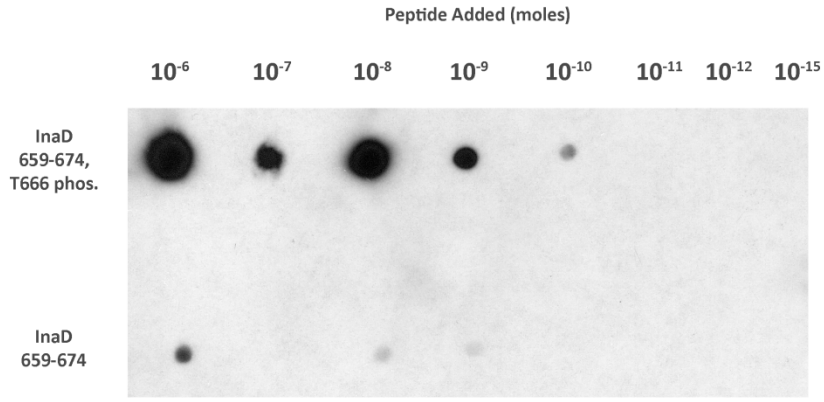

Figure 64: Characterization of Anti-Phospho-T666

A dot blot processed using anti-phospho-T666 antibody is shown. Serial dilutions of an InaD peptide containing phosphorylated or non-phosphorylated T666 are spotted.

Detection of Phosphorylation in vivo

I then tested whether these antibodies could detect phosphorylation at these sites *in vivo*. Both antibodies recognized some antigen in wild-type flies which could be increased by activation of PKC and was in both cases greatly reduced in InaC-null flies (Figure 63 and Figure 65). In the case of T666, I tested dark and light conditions but was unable to reproducibly detect a difference. Interestingly, *dgq* flies, which have 100-fold less G protein, reproducibly had much higher phospho-T666 antigen (Figure 65). Similar levels could be obtained from wild-type flies following treatment with PKC activators (Figure 65). These results suggest that T661 and T666 are phosphorylated in vivo, although the conditions under which they are preferentially phosphorylated and their functional role, if any, are far from clear.

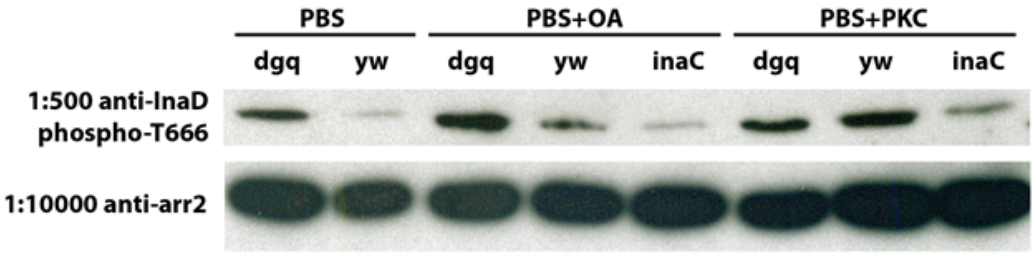

Figure 65: Detection of Phosphorylated T666 in vivo

Western blots of G protein hypomorphic (*dgq*), wild-type (*yw*), and PKC-null (*w;inaC*^{209}) fly head extracts incubated in PBS either alone, with protein phosphatase 2A inhibitor okadaic acid (+OA), or okadaic acid with PKC activators (PBS+PKC) are shown.

Functional Characterization of Phosphomimic Mutations in PDZ45

As a preliminary investigation into the functional consequences of phosphorylation, I tested the effect of glutamate phosphomimic mutations at T661 and T666 in PDZ45 on binding of NorpA using the pull-down assay (Figure 66). I found that T661E reduced binding, although less severely than the binding site mutant F642A, while T666E had no effect on binding. Mutation of both sites had no additional effect.

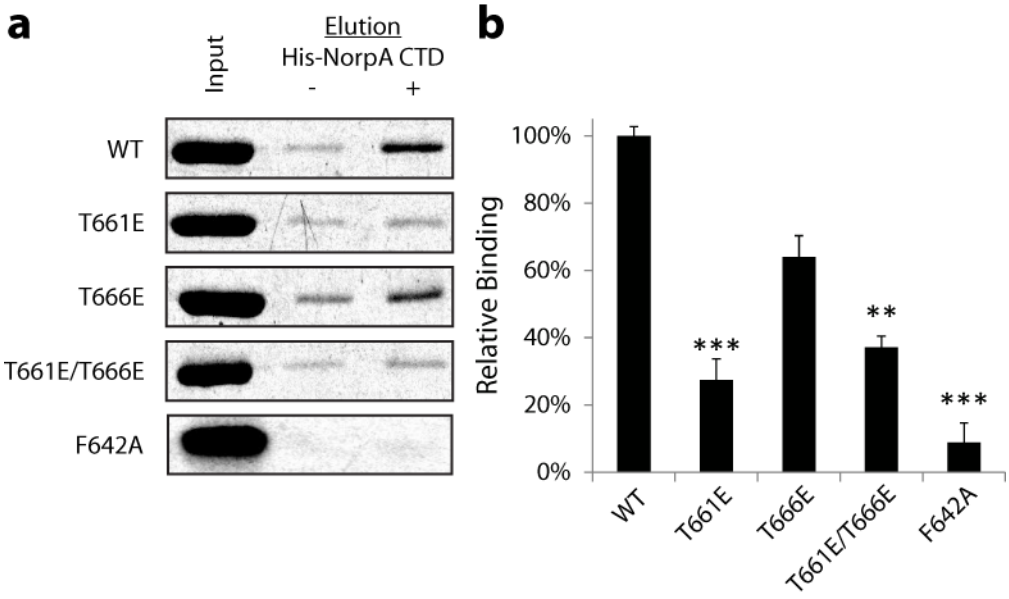

Figure 66: Binding of PDZ45 Phosphomimic Mutants to NorpA

(a) Gels showing PDZ45 protein pulled down in a Ni-NTA binding assay with or without His-NorpA CTD at low micromolar concentrations. (b) Quantification of the binding results with non-specific binding (lane with no His-NorpA CTD) subtracted. Significance vs wild-type: **, P<0.01 (ANOVA), ***, P<0.001 (ANOVA).

Conclusions

In summary, I have now shown that oxidation of PDZ5 triggers unbinding of NorpA indirectly through coupling of each process to a conformational equilibrium. This provides a mechanism by which oxidation of PDZ5 can cause a refractory state. The *Drosophila* phototransduction pathway is highly stochastic with the initial steps each involving only a few molecules. As a result, the probability of successfully responding to receptor activation, known as the visual efficiency, is steeply dependent on the activity of each of the steps upstream of channel opening. NorpA is particularly important as it mediates the first step of

vision at which there is significant amplification. Not surprisingly, mutations in which NorpA is not localized to InaD or in which the activity or expression is decreased have severe effects on the efficiency, latency, activation, and inactivation of the visual response.

It remains to be seen how the redox switch in PDZ5 is activated by visual signaling, but the thermodynamic model provided here provides a hypothesis as to how this may occur. I found that oxidation is coupled to NorpA binding through the conformational equilibrium in PDZ5. In addition, I showed in the previous chapter that PDZ4 structurally interacts with PDZ5 and strongly biases the conformational equilibria towards the open state. The redox environment in the photoreceptor cell is not known to fluctuate with signaling, which suggests that oxidation of PDZ5 likely happens instead by a change in the redox potential of PDZ45. This could be triggered by either perturbing the intrinsic redox potential of the open or closed state or the conformational equilibrium via the interaction between PDZs 4 and 5.

Many mechanisms could be employed to perturb PDZ45. Liu et al. recently proposed that NorpA-mediated acidification would uncouple PDZs 4-5 (W. Liu et al. 2011), but I now show that acidic conditions actually stabilize the open conformation. Alternatively, the Ranganathan lab previously showed that a loss of function mutant in InaC, the *Drosophila* eye PKC, prevents formation of the disulfide bond in vivo (Mishra et al. 2007). InaC is known to multiply

phosphorylate InaD (Matsumoto et al. 1984; Huber, P. Sander, and Paulsen 1996; Mingya Liu et al. 2000) but no functional sites have been identified.

I showed here that PDZ45 is a substrate of PKC both *in vitro* and *in vivo*. While the K_M of PKC for PDZ45 is reasonable, the maximal phosphate incorporation is quite low. This may be due to the slow conformational change I observed in PDZ45. Liu et al. reported that mutation of T669, which forms a salt bridge with a histidine in PDZ4, dramatically increased phosphorylation. It may be possible that phosphorylation is only efficient under acidic conditions, either due to conformational differences or a lower energy barrier for conformational switching. Phosphorylation of T661 may be relevant, as the T661E mutation appears to disrupt binding. There is much work left to fully determine the functional role and relevance of these sites.

It has been proposed that proteins may generally display long-range energetic couplings which represent sites at which allosteric regulation may emerge (Gunasekaran et al. 2004). In agreement with this, at least some PDZ domains display propagated changes in protein dynamics upon ligand binding (Gianni et al. 2006; Niu et al. 2007; Jun Zhang et al. 2010; Fuentes et al. 2004; Petit et al. 2009), and the Ranganathan lab has identified a set of coevolving residues in the PDZ domain family which connect the ligand binding pocket with two distant surface sites (S. W. Lockless et al. 1999). Intriguingly, one of these surface sites, the α_1 helix, is involved in allosteric activation of the Par6 PDZ

domain by Cdc42 (Garrard et al. 2003). In PDZ45, C606 and C645 are part of this coevolving network and there is a contact between the α_1 helix of PDZ5 and a histidine of PDZ4. In addition, tandem PDZ domains are a common feature of scaffolding proteins, and there are a few studies which report structural coupling between tandem domains without a clear physiological role (W. Wang et al. 2009; van den Berk, Landi, Walma, Vuister, Dente, and Hendriks 2007b; Long et al. 2008; Feng et al. 2003; Q. Zhang et al. 2001; Grootjans et al. 2000) . These results suggest that many PDZ domains may have the latent capacity for the emergence of allosteric behavior.

More generally, the design principles underlying the stepwise evolution of regulatory networks in nature are not well understood. Since the oxidation of PDZ5 arose recently in fast-flying flies (Figure 10), the mechanisms presented here provide insight into this problem. We find that the oxidation of PDZ5 is "wired" in a modular fashion, affecting binding of NorpA indirectly through the conformational equilibrium. One can imagine a potential two-step evolutionary path: First, the unidentified activation mechanism was coupled to the conformational equilibrium, resulting in some regulatory control over NorpA. Subsequently, the coupling between the disulfide bond and the conformation evolved, providing a larger magnitude effect on NorpA and a way of locking the protein into the closed conformation for a longer period of time, creating a

refractory period. An important question to address now is how each of these processes is physically connected to the conformational equilibrium.

In addition, the finding that the target of dynamic scaffolding is NorpA, a point of the signaling network which is not robust to perturbation, is intriguing. The general robustness of evolved signaling networks is thought to be a design principle by which nature deals with mutation. A trade-off of making a network generally robust is that some parts become more sensitive to perturbation. This work suggests that rather than a negative byproduct of robust design, these sensitive nodes may represent natural targets of the regulatory innovation that is required to build sophisticated systems.

Methods

Quantum Bump Simulations

Quantum bump stochastic simulations of the Pumir model (Pumir et al. 2008) were performed in MATLAB (MathWorks) using the Gillespie algorithm (Gillespie 1976). The sensitivity analysis was performed at 40 parameter values spaced logarithmically from 2 log orders below to 2 log orders above the published value. At each condition, 500 quantum bump simulations were executed and the results were fit to determine the distribution of quantum bump properties. The two parameters which were varied were k_A (the phospholipase activity) and γ_{PLC} (the GTPase activity).

Phosphorylation Experiments

One liter of Sf9 cells expressing His-tagged human PKCα (provided by Paul Sternweis) were pelleted, and resuspended in 20 mM HEPES pH 7.5, 150 mM NaCl, 20 mM imidazole, 2.5 mM EGTA, 2.5 mM betamercaptoethanol with PMSF, pepstatin, and leupeptin. The cells were freeze thawed, sonicated briefly, and then centrifuged at high speed to pellet cellular debris and insoluble protein. The supernatant was bound to 1 mL of Ni-NTA (Qiagen) and then batch washed with buffer containing 20 mM imidazole. Finally, >95% pure protein was eluted with 100 mM imidazole-containing buffer.

Phosphorylation was carried out in 20 mM MOPS pH 7.4, 5 mM MgCl2, 40 μM ATP (spiked with γ-^{32}P-ATP to a final specific activity of 0.3-3 Ci/mmol), 1% glycerol, 1 mM TCEP, 1 μM okadaic acid. For activating conditions, 100 μM $CaCl_2$, 140 μM brain phosphatidylserine (Avanti Polar Lipids), and 3.8 μM 18:1 dioleoylglycerol pyrophosphate (diacylglycerol, Avanti Polar Lipids) were added. For non-activating conditions, 0.5 mM EGTA was added. The enzyme concentration was typically 10 μM. Reactions were carried out at 30°C, and gels were imaged on a STORM phosphorimager (GE).

Generation of Phosphoantibodies

Phospho-T666 antibody was previously produced by Shan Mishra by immunizing rabbits against a peptide containing phospho-T666 and then purifying antibodies recognizing the phosphopeptide. A phosphospecific antibody to T661

was generated by Covance by immunizing two rabbits with 500 μg NH_2-NGKVSMEV-pT-RPKPTLRTEAPKAC-COOH, conjugated with KLH, four times over two months. The blood from the rabbits was combined and antibodies were purified for recognition of phosphopeptide and lack of recognition of non-phosphorylated peptide.

Detection of Phosphorylated InaD in vivo

Samples for Western blotting with the phosphoantibodies were prepared by sonicating 5 fly heads in 50 μL of fly head buffer (30 mM Tris pH 6.8, 10% SDS, 0.02% bromophenol blue, 10% glycerol, and 5% betamercaptoethanol). For Figure 65, flies were homogenized into PBS alone or with either 1 nM okadaic acid to inhibit the PP2A phosphatase or 1 mM MgATP, 1 μM phorbol myristic acid (PMA), and 1 mM $CaCl_2$ to activate endogenous InaC. Fly head buffer was then added prior to SDS-PAGE.

Western blotting was performed by directly spotting antigen or transferring antigen from a SDS-PAGE gel to PVDF membrane. The blot was then blocked with PBS or Tris-buffered saline (TBS) with 0.02% Tween-20 containing 5% milk for 1 hour at room temperature and then incubated with a small volume of buffer containing 5% milk and primary antibody overnight. The blot was then washed 2X with buffer containing 0.02% Tween-20, incubated with a small volume of buffer containing 5% milk and horseradish peroxidase-conjugated secondary antibody for 1 hour at room temperature. The blot was then

washed vigorously at least 4X with buffer containing 0.02% Tween-20, and finally, the blot was developed with ECL or ECL Plus (GE).

CHAPTER SIX

Conclusions and Recommendations

The Search for Design Principles in Biology

A central problem in science today is how to understand complex systems. At the beginning of this dissertation, I described the strategy of assuming the existence of design principles—characteristics of a system which can predict and explain its function. Existing work has successfully focused on finding analogous design principles from engineering. However, biological systems have many distinct features, in particular their creation by evolution, which may utilize novel design principles which have not yet been identified. I sought to identify design principles at three structural levels in the *Drosophila* photoreceptor cell, a well-studied model which is renowned for its signaling performance. To facilitate this search, I devised an approach of quantitative experimentation and theoretical investigation from an evolutionary perspective.

Micron Scale: The Role of Compartmentalization by Microvilli

The first level of structure I investigated was the dramatic compartmentalization of signaling by microvilli in the photoreceptor cell. Previous studies had suggested a role for this structure in promoting light absorption or potentially creating high-amplitude signals. I used theoretical

modeling and quantitative measurements of localized Ca^{++} signaling to investigate how this organization alters spatiotemporal signaling dynamics. I found that microvilli enable fast, high amplitude, homogeneous Ca^{++} signaling due to their unique physical properties. This enables cells to build semi-autonomous signaling units which signal in a digital manner. It also eliminates the need to invoke specialized signaling proteins or spatial signaling gradients to explain the remarkable signaling dynamics of this system.

Compartmentalization is a common feature of signaling systems. This work suggests that specialized dynamical features can be created by placing molecules in compartments with particular physical constraints. I think it is important to examine the dynamical properties of other compartments, such as dendrites and cilia, to see how their physical properties relate to their functional constraints. The end goal should be a general theory for signaling compartments explaining how constraints on functional properties of systems relate to the dynamic and physical properties of compartments.

Nanometer Scale: Modularity of Dynamic Scaffolding by InaD

Next, I focused on the other prominent form of organization in this system: the scaffolding protein InaD which coordinates many of the core reactions mediating vision. Scaffolding proteins are thought to facilitate evolution by decomposing signaling regulation into protein domain modules which can be

swapped out over evolutionary time scales. I investigated whether a novel feature the Ranganathan lab recently discovered, dynamic regulation of vision by InaD PDZ5, could be explained by the features of PDZ5 alone. I found that PDZ5 was unable to recapitulate the physiological features of dynamic scaffolding by InaD. Instead, the inclusion of PDZ4, which is close to PDZ5 in primary structure throughout the gene family, was required to explain the physiological features. InaD PDZs 4-5 have tandem homologs in many other multi-PDZ scaffolds, suggesting that they have indeed evolved as a modular unit. This confirms that modularity does exist within InaD, but the modules are not always single protein domains as is commonly thought. Instead, more complex modules can be built over long periods of co-evolution.

This issue of defining modules is an important question both for the practical investigation of biological systems as well as a complete understanding of their design. I think two major problems need to be addressed. First, is there a way to reliably predict modules given the evolutionary history of proteins? Second, are there general features of or constraints on the way evolution builds coupled modules from initially independent components? Answering these questions demands a large-scale investigation into coupling in systems and their evolutionary history.

Angstrom Scale: Functional Integration within InaD PDZ5

Finally, I examined functional integration within InaD PDZ5, which regulates signaling dynamics during vision by undergoing a conformational change due to oxidation. I measured the allosteric coupling between the oxidation, conformational change, and binding reactions performed by PDZ5. I found that binding and oxidation were linked through pairwise coupling with the conformational change, not directly to each other.

This is a nice design from an evolutionary perspective, as proteins are generally thought to have some capacity for conformational change and it is easier to imagine a stepwise path to building a system this way. However, this is an anecdotal story. Additional work needs to be done in other multi-functional proteins to see if this design is general. Another aspect that remains to be understood is the mechanism by which these properties become coupled to the conformational equilibrium.

Future Directions

There is much left to learn about evolutionary design principles. In this study, I focused on three structural levels of the *Drosophila* photoreceptor cell. While each level is quite different in appearance, similar features and problems arose at each level. In all three levels, much of the design related to achieving particular patterns of coupling and independence—coupling the activity of

molecules in one microvilli while keeping them independent from others, coupling some domains of a protein while making others independent, and coupling independent functions of a protein domain through a conformational equilibrium. While this hints at a general design strategy, each case was an anecdotal story. In the future, I think it will be important to develop experimental approaches and theoretical tools capable of analyzing coupling in many systems. In addition, the ties to evolution in this work came purely from inductive reasoning rather than experimental observations. Therefore, future studies should explicitly study either the natural variation evolution acts on or compare evolutionarily related instances of a system.

APPENDIX A
Protein Sequences

Constructs

Underlined sequence is non-native and mutations are shown in bold.

"PDZ5" from pRSET His-GFP-PDZ5:

GSPEGLEKFNVDLMKKAGKELGLSLSPNEIGCTIADLIQGQYPEIDSKLQRGDI
ITKFNGDALEGLPFQVCYALFKGANGKVSMEVTRPKPTLRTEAPKA

"PDZ5-AAAS" (used in Figure 29) from pGEX-3X PDZ5

GIPRNSLEKFNVDLMKKAGKELGLSLSPNEIGCTIADLIQGQYPEIDSKL
QRGDIITKFNGDALEGLPFQVCYALFKGANGKVSMEVTRPKPAAAS

"PDZ5 C645S" from pGEX-3X PDZ5 C645S

GIPRNSLEKFNVDLMKKAGKELGLSLSPNEIGCTIADLIQGQYPEIDSKL
QRGDIITKFNGDALEGLPFQV**S**YALFKGANGKVSMEVTRPKPAAAS

"PDZ45" from pET28a PDZ45

GPLGSPQEPATAEIKPNKKILIELKVEKKPMGVIVCGGKNNHVTTGCVITHVYP
EGQVAADKRLKIFDHICDINGTPIHVGSMTTLKVHQLFHTTYEKAVTLTVFRAD
PPELEKFNVDLMKKAGKELGLSLSPNEIGCTIADLIQGQYPEIDSKLQRGDIIT
KFNGDALEGLPFQVCYALFKGANGKVSMEVTRPKPTLRTEAPKA

"PDZ45 Δ3C" from pET28a PDZ45 Δ3C

GPLGSPQEPATAEIKPNKKILIELKVEKKPMGVIV**T**GGKNNHVTTG**A**VITHVYP
EGQVAADKRLKIFDHI**T**DINGTPIHVGSMTTLKVHQLFHTTYEKAVTLTVFRAD
PPELEKFNVDLMKKAGKELGLSLSPNEIGCTIADLIQGQYPEIDSKLQRGDIIT
KFNGDALEGLPFQVCYALFKGANGKVSMEVTRPKPTLRTEAPKA

"PDZ45 T553A" from pET28a PDZ45 T553A

GPLGSPQEPATAEIKPNKKILIELKVEKKPMGVIVCGGKNNHVTTGCVITHVYP
EGQVAADKRLKIFDHICDINGTPIHVGSMT**A**LKVHQLFHTTYEKAVTLTVFRAD

PPELEKFNVDLMKKAGKELGLSLSPNEIGCTIADLIQGQYPEIDSKLQRGDIIT
KFNGDALEGLPFQVCYALFKGANGKVSMEVTRPKPTLRTEAPKA

"PDZ45 F642A" from pET28a PDZ45 F642A

GPLGSPQEPATAEIKPNKKILIELKVEKKPMGVIVCGGKNNHVTTGCVITHVYP
EGQVAADKRLKIFDHICDINGTPIHVGSMTTLKVHQLFHTTYEKAVTLTVFRAD
PPELEKFNVDLMKKAGKELGLSLSPNEIGCTIADLIQGQYPEIDSKLQRGDIIT
KFNGDALEGLP**A**QVCYALFKGANGKVSMEVTRPKPTLRTEAPKA

"PDZ45 T661A" from pET28a PDZ45 T661A

GPLGSPQEPATAEIKPNKKILIELKVEKKPMGVIVCGGKNNHVTTGCVITHVYP
EGQVAADKRLKIFDHICDINGTPIHVGSMTTLKVHQLFHTTYEKAVTLTVFRAD
PPELEKFNVDLMKKAGKELGLSLSPNEIGCTIADLIQGQYPEIDSKLQRGDIIT
KFNGDALEGLPFQVCYALFKGANGKVSMEV**A**RPKPTLRTEAPKA

"PDZ45 T661E" from pET28a PDZ45 T661E

GPLGSPQEPATAEIKPNKKILIELKVEKKPMGVIVCGGKNNHVTTGCVITHVYP
EGQVAADKRLKIFDHICDINGTPIHVGSMTTLKVHQLFHTTYEKAVTLTVFRAD
PPELEKFNVDLMKKAGKELGLSLSPNEIGCTIADLIQGQYPEIDSKLQRGDIIT
KFNGDALEGLPFQVCYALFKGANGKVSMEV**E**RPKPTLRTEAPKA

"PDZ45 T666A" from pET28a PDZ45 T666A

GPLGSPQEPATAEIKPNKKILIELKVEKKPMGVIVCGGKNNHVTTGCVITHVYP
EGQVAADKRLKIFDHICDINGTPIHVGSMTTLKVHQLFHTTYEKAVTLTVFRAD
PPELEKFNVDLMKKAGKELGLSLSPNEIGCTIADLIQGQYPEIDSKLQRGDIIT
KFNGDALEGLPFQVCYALFKGANGKVSMEVTRPKP**A**LRTEAPKA

"PDZ45 T666E" from pET28a PDZ45 T666E

GPLGSPQEPATAEIKPNKKILIELKVEKKPMGVIVCGGKNNHVTTGCVITHVYP
EGQVAADKRLKIFDHICDINGTPIHVGSMTTLKVHQLFHTTYEKAVTLTVFRAD
PPELEKFNVDLMKKAGKELGLSLSPNEIGCTIADLIQGQYPEIDSKLQRGDIIT
KFNGDALEGLPFQVCYALFKGANGKVSMEVTRPKP**E**LRTEAPKA

"PDZ45 T661A/T666A" from pET28a PDZ45 T661A/T666A

GPLGSPQEPATAEIKPNKKILIELKVEKKPMGVIVCGGKNNHVTTGCVITHVYP
EGQVAADKRLKIFDHICDINGTPIHVGSMTTLKVHQLFHTTYEKAVTLTVFRAD

PPELEKFNVDLMKKAGKELGLSLSPNEIGCTIADLIQGQYPEIDSKLQRGDIIT
KFNGDALEGLPFQVCYALFKGANGKVSMEV**A**RPKP**A**LRTEAPKA

"PDZ45 T661E/T666E" from pET28a PDZ45 T661E/T666E

GPLGSPQEPATAEIKPNKKILIELKVEKKPMGVIVCGGKNNHVTTGCVITHVYP
EGQVAADKRLKIFDHICDINGTPIHVGSMTTLKVHQLFHTTYEKAVTLTVFRAD
PPELEKFNVDLMKKAGKELGLSLSPNEIGCTIADLIQGQYPEIDSKLQRGDIIT
KFNGDALEGLPFQVCYALFKGANGKVSMEV**E**RPKP**E**LRTEAPKA

"NorpA CTD" from pET28a NorpA 869-*

GSHMEPVTLESLRQEKGFQKVGKKQIKELDTLRKKHAKERTSVQKTQNAAIDKL
IKGKSKDDIRNDANIKNSINDQTKQWTDMIARHRKEEWDMLRQHVQDSQDAMKA
LMLTVQAAQIKQLEDRHARDIKDLNAKQAKMSADTAKEVQNDKTLKTKNEKDRR
LREKRQNNVKRFMEEKKQIGVKQGRAMEKLKLAHSKQIEEFSTDVQKLMDMYKI
EEEAYKTQGKTEFYA

"NorpA CTD Δ5" from pET28a NorpA 869-* Δ5

GSHMEPVTLESLRQEKGFQKVGKKQIKELDTLRKKHAKERTSVQKTQNAAIDKL
IKGKS-----
NDANIKNSINDQTKQWTDMIARHRKEEWDMLRQHAQDSQDAMKALMLTVQAAQI
KQLEDRHARDIKDLNAKQAKMSADTAKEVQNDKTLKTKNEKDRRLREKRQNNVK
RFMEEKKQIGVKQGRAMEKLKLAHSKQIEEFSTDVQKLMDMYKIEEEAYKTQGK
TEFYA

"NorpA CTD Y1094S" from pET28a NorpA 869-* Y1094S

GSHMEPVTLESLRQEKGFQKVGKKQIKELDTLRKKHAKERTSVQKTQNAAIDKL
IKGKSKDDIRNDANIKNSINDQTKQWTDMIARHRKEEWDMLRQHVQDSQDAMKA
LMLTVQAAQIKQLEDRHARDIKDLNAKQAKMSADTAKEVQNDKTLKTKNEKDRR
LREKRQNNVKRFMEEKKQIGVKQGRAMEKLKLAHSKQIEEFSTDVQKLMDMYKI
EEEAYKTQGKTEF**S**A

InaD Gene Family - PDZs 4-5

Species listed: *Ixodes scapularis* (Isca), *Pediculus humanus* (Phum), *Apis mellifera* (Amel), *Tribolium castaneum* (Tcas), *Aedes aegypti* (Aaeg), *Anopheles gambiae* (Agam), *Calliphora vicina* (Cvic), *Drosophila grimshawi* (Dgri), *Drosophila mojavensis* (Dmoj), *Drosophila virilis* (Dvir), *Drosophila willistoni* (Dwil), *Drosophila persimilis* (Dper), *Drosophila pseudoobscura* (Dpse), *Drosophila ananassae* (Dana), *Drosophila erecta* (Dere), *Drosophila yakuba* (Dyak), *Drosophila melanogaster* (Dmel), *Drosophila sechellia* (Dsec), *Drosophila simulans* (Dsim). The sequences were aligned using PROMALS3D.

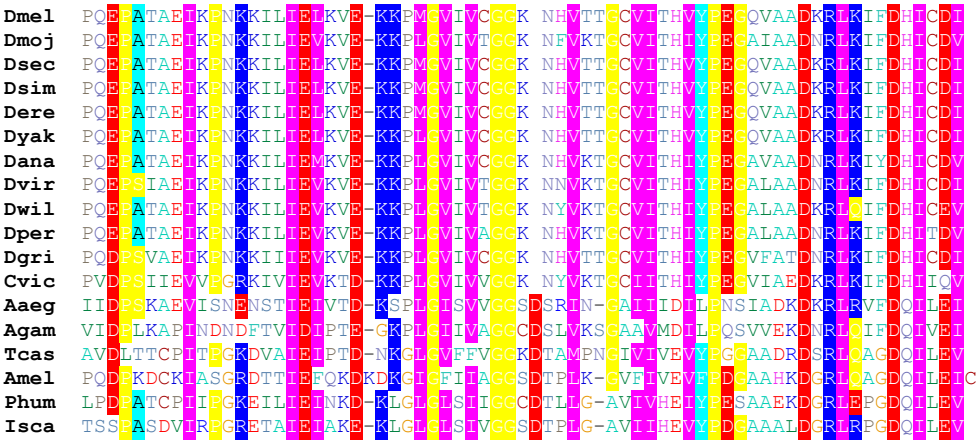

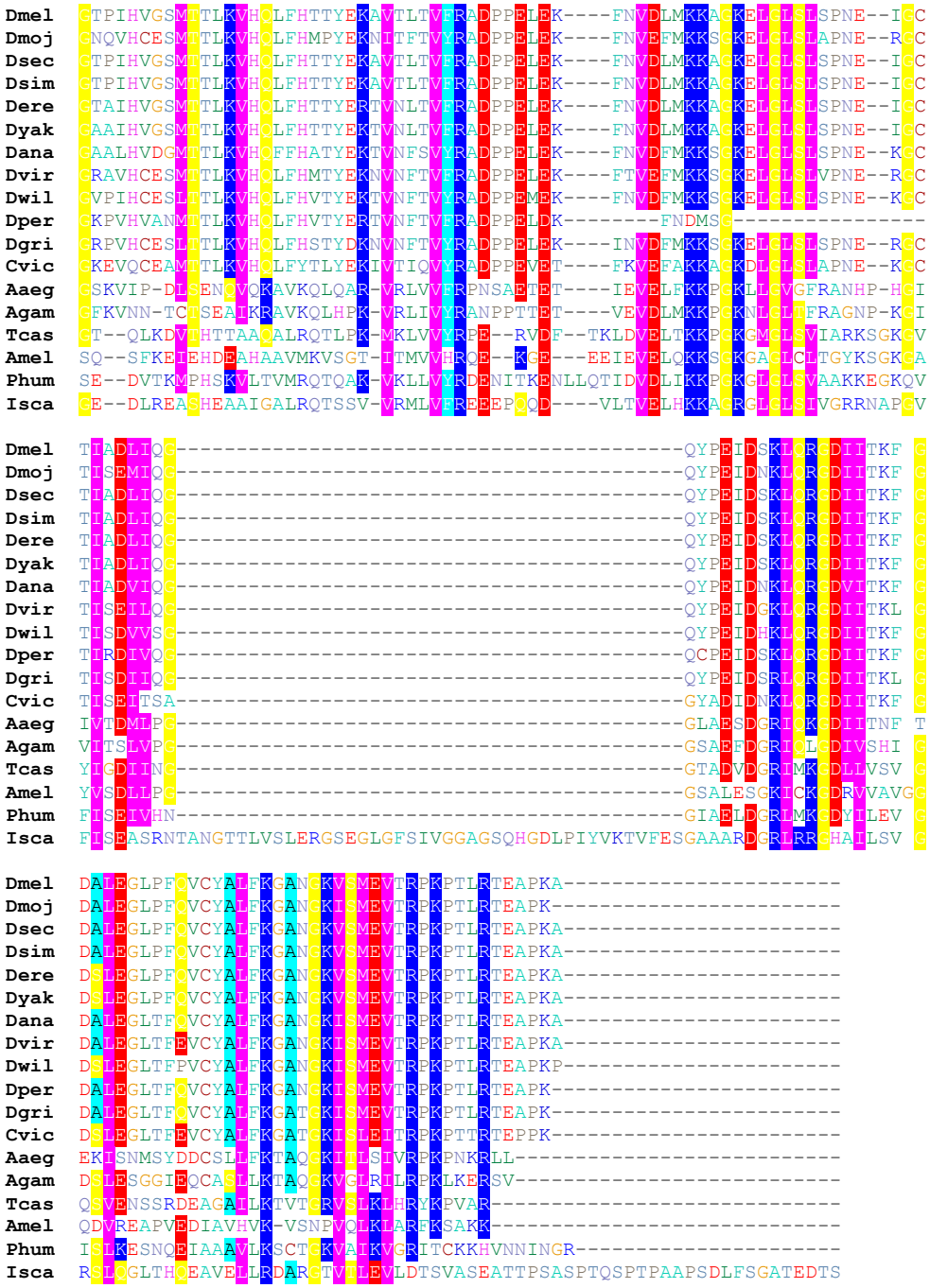
Dmel GTPIHVGSMTTLKVHQLFHTTYEKAVTLTVERADPPELEK----FNVDLMKKAQKELQLSLSPNE--IQC
Dmoj GNQVHCESMTTLKVHQLFHMPYEKNITFTVVRADPPELEK----FNVEFMKKSQKELQLSLAPNE--RQC
Dsec GTPIHVGSMTTLKVHQLFHTTYEKAVTLTVERADPPELEK----FNVDLMKKAQKELQLSLSPNE--IQC
Dsim GTPIHVGSMTTLKVHQLFHTTYEKAVTLTVERADPPELEK----FNVDLMKKAQKELQLSLSPNE--IQC
Dere GTAIHVGSMTTLKVHQLFHTTYERTVNLTVERADPPELEK----FNVDLMKKAQKELQLSLSPNE--IQC
Dyak GAAIHVGSMTTLKVHQLFHTTYEKTVNLTVERADPPELEK----FNVDLMKKAQKELQLSLSPNE--IQC
Dana GAALHVDGMTTLKVHQFFHATYEKTVNFSVVRADPPELEK----FNVDFMKKSQKELQLSLSPNE--KQC
Dvir GRAVHCESMTTLKVHQLFHMTYEKNVNFTVERADPPELEK----FTVEFMKKSQKELQLSLVPNE--RQC
Dwil GVPIHCESLTTLKVHQLFHVTYEKTVNFTVVRADPPEMEK----FNVDFMKKSQKELQLSLSPNE--KQC
Dper GKPVHVANMTTLKVHQLFHVTYERTVNFTVERADPPELDK--------FNDMSQ----------------
Dgri GRPVHCESLTTLKVHQLFHSTYDKNVNFTVVRADPPELEK----INVDFMKKSQKELQLSLSPNE--RQC
Cvic GKEVQCEAMTTLKVHQLFYTLYEKIVTIQVVRADPPEVET----FKVEFAKKAQKDLQLSLAPNE--KQC
Aaeg GSKVIP-DLSENQVQKAVKQLQAR-VRLVVERPNSAETET----IEVELFKKPQKLLQVGFRANHP-HQI
Agam GFKVNN-TCTSEAIKRAVKQLHPK-VRLIVVRANPPTTET----VEVDLMKKPQKNLQLTFRAGNP-KQI
Tcas GT--QLKDVTHTTAAQALRQTLPK-MKLVVVREE--RVDF--TKLDVELTKKPQKQMQLSVIARKSGKQV
Amel SQ--SFKEIEHDEAHAAVMKVSGT-ITMVVERQE--KGE---EEIEVELQKKSQKGAQLCLTGYKSGKQA
Phum SE--DVTKMPHSKVLTVMRQTQAK-VKLLVVRDENITKENLLQTIDVDLIKKPQKGLQLSVAAKKEGKQV
Isca GE--DLREASHEAAIGALRQTSSV-VRMLVVREEEPQQD----VLTVELHKKAQRGLQLSIVGRRNAPQV
Dmel TIADLIQG----------QYPEIDSKLQRGDIITKF G
Dmoj TISEMIQG----------QYPEIDNKLQRGDIITKF G
Dsec TIADLIQG----------QYPEIDSKLQRGDIITKF G
Dsim TIADLIQG----------QYPEIDSKLQRGDIITKF G
Dere TIADLIQG----------QYPEIDSKLQRGDIITKF G
Dyak TIADLIQG----------QYPEIDSKLQRGDIITKF G
Dana TIADVIQG----------QYPEIDNKLQRGDVITKF G
Dvir TISEILQG----------QYPEIDGKLQRGDIITKL G
Dwil TISDVVSG----------QYPEIDHKLQRGDIITKF G
Dper TIRDIVQG----------QCPEIDSKLQRGDIITKF G
Dgri TISDIIQG----------QYPEIDSRLQRGDIITKL G
Cvic TISEITSA----------GYADIDNKLQRGDIITKF G
Aaeg IVTDMLPG----------GLAESDGRIQKGDIITNF T
Agam VITSLVPG----------GSAEFDGRIQLGDIVSHI G
Tcas YIGDIING----------GTADVDGRIMKGDLIVSV G
Amel YVSDLLPG----------GSALESGKICKGDRVVAVG G
Phum FISEIVHN----------GIAELDGRLMKGDYILEV G
Isca FISEASRNTANGTTLVSLERGSEGLGFSIVGGAGSQHGDLPIYVKTVFESGAAARDGRLRRGHAILSV G
Dmel DALEGLPFQVCYALFKGANGKVSMEVTRPKPTLRTEAPKA----------
Dmoj DALEGLPFQVCYALFKGANGKISMEVTRPKPTLRTEAPK----------
Dsec DALEGLPFQVCYALFKGANGKVSMEVTRPKPTLRTEAPKA----------
Dsim DALEGLPFQVCYALFKGANGKVSMEVTRPKPTLRTEAPKA----------
Dere DSLEGLPFQVCYALFKGANGKVSMEVTRPKPTLRTEAPKA----------
Dyak DSLEGLPFQVCYALFKGANGKVSMEVTRPKPTLRTEAPKA----------
Dana DALEGLTFQVCYALFKGANGKISMEVTRPKPTLRTEAPKA----------
Dvir DALEGLTFEVCYALFKGANGKISMEVTRPKPTLRTEAPKA----------
Dwil DSLEGLTFPVCYALFKGANGKISMEVTRPKPTLRTEAPKP----------
Dper DALEGLTFQVCYALFKGANGKISMEVTRPKPTLRTEAPK----------
Dgri DALEGLTFQVCYALFKGATGKISMEVTRPKPTLRTEAPK----------
Cvic DSLEGLTFEVCYALFKGATGKISLEITRPKPTTRTEPPK----------
Aaeg EKISNMSYDDCSLLFKTAQGKILLSIVRPKPNKRLL----------
Agam DSLESGGIEQQCASLLKTAQGKVGLRILRPKLKERSV----------
Tcas QSVENSSRDEAGAILKTVTGRVSLKLHRYKPVAR----------
Amel QDVREAPVEDIAVHVK-VSNPVQLKLARFKSAKK----------
Phum ISLKESNQEIAAAVLKSCTGKVAIKVGRITCKKHVNNINGR----------
Isca RSLQGLTHQEAVELLRDARGTVILEVLDTSVASEATTPSASPTQSPTPAAPSDLFSGATEDTS

APPENDIX B
Matlab Scripts

Calcium Analysis Scripts

Calcium Simulations

Spatial Simulation Script – RunCalciumSpatialSims.m

```
function output = RunCalciumSpatialSims()

%% General stuff
t_int = linspace(0,0.1,200)/1000;

%% QB Waverforms
%Lorenzian functions
lorenzian = @(tau,n,t) 1./(gamma(n)*tau).*(t/tau).^n.*exp(-
t./tau);
tau_dark = 0.0096; n_dark = 0.5953; dark =
lorenzian(tau_dark,n_dark,t_int); dark = dark ./ max(dark);
tau_light = 0.0054; n_light = 0.2834; light =
lorenzian(tau_light,n_light,t_int); light = light ./ max(light);

%% Dark Adapted Average Waveform
nruns = 200;
ca_avg_dark = zeros(length(t_int),50);
parfor i=1:nruns
    [t,ca_free] = ca_spatial_sim6(t_int,dark,1.5e-3,1e-6,-60e-
3,1,15,1e-6);
    if i <= 10 % Keep the first ten
        dark_adapted_runs(i).t = t;
        dark_adapted_runs(i).ca_free = ca_free;
    end
    ca_avg_dark = ca_avg_dark + interp1(t,ca_free,t_int)./nruns;
end
output.dark.sims = dark_adapted_runs;
output.dark.t = t_int;
output.dark.ca_avg = ca_avg_dark;
save('dark adapted calcium sim
result.mat','t_int','ca_avg_dark','dark_adapted_runs');

%% Light Adapted Average Waveform
nruns = 200;
ca_avg_adapted = zeros(length(t_int),50);
parfor i=1:200
```

```
    [t,ca_free] = ca_spatial_sim6(t_int,light,1.5e-3,1e-6,-60e-
3,0.05,15,1e-6);
    if i < 11
        light_adapted_runs(i).t = t;
        light_adapted_runs(i).ca_free = ca_free;
    end
    ca_avg_adapted = ca_avg_adapted +
interp1(t,ca_free,t_int)./nruns;
end
output.light.sims = light_adapted_runs;
output.light.t = t_int;
output.light.ca_avg = ca_avg_adapted;
save('light adapted calcium sim
result.mat','t_int','ca_avg_adapted','light_adapted_runs');
save('calcium spatial sims.mat','output');

%% Plot results
figure;hold on;
h = axes;
for i=1:10
    i_peak =
find(mean(light_adapted_runs(i).ca_free,2)==max(mean(light_adapte
d_runs(i).ca_free,2)),1);
    plot([1:50]*1000/50,light_adapted_runs(i).ca_free(i_peak,:));
end
set(h,'FontSize',15);
xlabel('Position (nm)','FontSize',18);
ylabel('[Ca^+^+] (\muM)','FontSize',18);
plot([1:50]*1000/50,ca_avg_adapted(find(mean(ca_avg_adapted,2)==m
ax(mean(ca_avg_adapted,2)),1),:),'k','LineWidth',2);
print -depsc -tiff -r300 dark_adapted_sim_figure

figure;hold on;
h = axes;
for i=1:10
    i_peak =
find(mean(dark_adapted_runs(i).ca_free,2)==max(mean(dark_adapted_
runs(i).ca_free,2)),1);
    plot([1:50]*1000/50,dark_adapted_runs(i).ca_free(i_peak,:));
end
set(h,'FontSize',15);
plot([1:50]*1000/50,ca_avg(find(mean(ca_avg,2)==max(mean(ca_avg,2
)),1),:),'k','LineWidth',2)
xlabel('Position (nm)','FontSize',18);
ylabel('[Ca^+^+] (\muM)','FontSize',18);
print -depsc -tiff -r300 light_adapted_sim_figure

end
```

Spatial Simulation Algorithm - ca_spatial_sim6.m

```
function [t,ca_free,trp] =
ca_spatial_sim6(t_P_open_input,P_open_input,ca_ext,ca_cell,V_memb
rane,a,colocalized)
% Simulation parameters
NA = 6.02E23;
R = 8.314;
T = 298;
F = 9.65E4;
z_ca = 2;
n_trp = 15;
n_calx = 15;
P = 3.7e-15;

% Spatial parameters
D_ca = 220;
k = 50;
l_microvilli = 1.5;
r_microvilli = 0.06/2;
V_micro = pi*r_microvilli^2*l_microvilli*10^-15;
V_segment = l_microvilli/(k-1)*pi*r_microvilli^2; % um^3
V_segment_L = V_segment*10^-15; % L = 1000 mL = 1000*cm^3 = 1000
* x um^3 * (cm/um)^3
l_neck = 0.06;
r_neck = 0.035/2;
V_neck = pi*(r_neck)^2*(l_neck);
V_neck_L = V_neck*(10^-4)^3/1000;

alpha = V_membrane*F/(R*T);
p_ca = 0.85;
z_ca = 2;
b_ca = z_ca*p_ca*exp(-z_ca*alpha)/(1-exp(-z_ca*alpha))*ca_ext;

% Rate constants
sigma = a*P*alpha*b_ca/n_trp;
gamma = 7.4e3;

% Other parameters
r_calx = 3;

% Place TRP and CalX
trp = zeros(1,k);
calx = zeros(1,k);
for i=1:n_trp
   pos = 1+round(rand*(k-2));
   trp(pos) = trp(pos) + 1;
end
```

```
% Initial conditions
y0 = [ca_cell*ones(1,k)];

% Run simulation
[t,yy] = ode15s(@odefun,[t_P_open_input(1)
t_P_open_input(end)],y0);

% Generate output
ca_free = yy(1:end,1:k)*10^6; % Return uM

    function dy_dt = odefun(t,y)
        % Extract states
        ca=y(1:k);

        trp_on = P_open_input(find(t_P_open_input >= t, 1));

        dy_dt_ca = trp_on*trp'*sigma/V_segment_L - gamma.*ca;

        % Calculate spatial equations
        % Ca
        dy_dt_ca(1) = dy_dt_ca(1) + 2*D_ca/(l_microvilli/(k-
1))^2*(ca(2)-ca(1));
        for z=2:(k-2)
            dy_dt_ca(z) = dy_dt_ca(z) + D_ca/(l_microvilli/(k-
1))^2*(ca(z-1)-2*ca(z)+ca(z+1));
        end
        dy_dt_ca(k-1) = dy_dt_ca(k-1) + D_ca/(l_microvilli/(k-
1))^2*(ca(k-2)-ca(k-1)) +
(V_neck/V_segment)*D_ca/l_neck^2*(ca(k)-ca(k-1));
        dy_dt_ca(k) = dy_dt_ca(k) +
(V_segment/V_neck)*D_ca/l_neck^2*(ca(k-1)-ca(k)) +
D_ca/l_neck^2*(ca_cell-ca(k));

        % Assemble Matlab ODE vector
        % Format:
        dy_dt = [dy_dt_ca];%;dy_dt_buff];
    end
end
```

Quantum Bump Analysis

Quantum Bump Analysis – AnalyzeQBs.m

```
function output = AnalyzeQBs( input )

output = input;
```

```
for i=1:length(input)
    time = input(i).Current.t;
    values = input(i).Current.values;
    values_detrended = FilterQB(time,values,150);
    output(i).CurrentDetrended.t = time;
    output(i).CurrentDetrended.values = values_detrended;
    output(i).CurrentBaseline =
GetBaseline(time,values_detrended);
    output(i).CurrentNoise = GetNoise(time,values_detrended);
    if std(values_detrended) < 1.5 % Don't analyze really noisy
data
        possible_qbs =
FindPossibleQBs(time,values_detrended,output(i).CurrentBaseline,o
utput(i).CurrentNoise);
        output(i).IsAnalyzed = 1;
    else
        output(i).IsAnalyzed = 0;
        possible_qbs = [];
    end
    output(i).AreSuccessfulQBs = [];
    for j=1:length(possible_qbs)
        if possible_qbs(j).t(end) - possible_qbs(j).t(1) < 9
            continue;
        end
        [t_peak,J_peak,t_hr,t_hi] =
FindPeak(possible_qbs(j).t,possible_qbs(j).current,output(i).Curr
entBaseline);
        output(i).PeakTimes(j) = t_peak;
        output(i).PeakAmplitudes(j) = J_peak;
        output(i).HalfRiseTimes(j) = t_hr;
        if isempty(t_hi)
            output(i).HalfInactivationTimes(j) = NaN;
        else
            output(i).HalfInactivationTimes(j) = t_hi;
        end
        output(i).Latencies(j) = possible_qbs(j).t(1);
        output(i).TotalDurations(j) = possible_qbs(j).t(end) -
possible_qbs(j).t(1);
        valid_qb =
ValidateQB(possible_qbs(j).t,possible_qbs(j).current,output(i).La
tencies(j),output(i).PeakTimes(j),output(i).PeakAmplitudes(j),out
put(i).HalfRiseTimes(j),output(i).HalfInactivationTimes(j),output
(i).TotalDurations(j));
        if valid_qb
            output(i).ChargeIntegrals(j) =
GetCurrentIntegral(possible_qbs(j).t,possible_qbs(j).current,outp
ut(i).CurrentBaseline);
        else
            output(i).ChargeIntegrals(j) = 0;
        end
```

```
        output(i).AreSuccessfulQBs(j) = valid_qb &
output(i).ChargeIntegrals(j) > 20;
        output(i).IsAnalyzed = 1;
    end
    first_success = find(output(i).AreSuccessfulQBs,1);
    if ~isempty(first_success)
        output(i).PeakTime = output(i).PeakTimes(first_success);
        output(i).PeakAmplitude =
output(i).PeakAmplitudes(first_success);
        output(i).HalfRiseTime =
output(i).HalfRiseTimes(first_success);
        output(i).HalfInactivationTime =
output(i).HalfInactivationTimes(first_success);
        output(i).HalfWidth = output(i).HalfRiseTime +
output(i).HalfInactivationTime;
        output(i).Latency = output(i).Latencies(first_success);
        output(i).TotalDuration =
output(i).TotalDurations(first_success);
        output(i).ChargeIntegral =
output(i).ChargeIntegrals(first_success);
        output(i).IsSuccessfulQuantumBump = 1;
        output(i).NumberOfQBs =
length(find(output(i).AreSuccessfulQBs));
        output(i).MidpointPeakTime = ((output(i).Latency +
output(i).HalfRiseTime) + (output(i).Latency + output(i).PeakTime
+ output(i).HalfInactivationTime))/2;
    else
        output(i).NumberOfQBs = 0;
        output(i).IsSuccessfulQuantumBump = 0;
    end
end
    function current_fixed = RemoveTrend(t,current)
       mask = t<0|t>900; % Only fit beginning and end
       p = polyfit(t(mask),current(mask),1);
       current_fixed = current - polyval(p,t) +
GetBaseline(t,current);
    end
    function baseline = GetBaseline(t,current)
        baseline = mean(current(t<0));
    end
    function noise = GetNoise(t,current)
       noise = std(current(t<0));
    end
    function possible_qbs =
FindPossibleQBs(t,current,baseline,noise)
       noise_threshold = 2;
       threshold_crossings =  find(diff((baseline -
current)>noise_threshold*noise)~=0);
       k = 1;
       possible_qbs = [];
```

```
        while k<length(threshold_crossings)
            possible_qbs((k+1)/2).t =
t(threshold_crossings(k):threshold_crossings(k+1));
            possible_qbs((k+1)/2).current =
current(threshold_crossings(k):threshold_crossings(k+1));
            k = k+2;
        end
    end
    function [t_peak,J_peak,t_hr,t_hi] =
FindPeak(t,current,baseline)
        i_peak = find(current==min(current),1);
        t_peak = t(i_peak) - t(1);
        if (i_peak ~= 1 & i_peak ~= length(t))
         J_peak = -(mean(current(i_peak - 1: i_peak + 1)) -
baseline);
         t_hr = t(find(current-baseline<=-J_peak/2,1)) - t(1);
         t_hi = t(find(current-baseline>=-J_peak/2 & (t > t_peak +
t(1)),1)) - t_peak - t(1);
        else
            J_peak = 0;
            t_hr = 0;
            t_hi = 0;
        end
    end
    function J_int = GetCurrentIntegral(t,current,baseline)
        qb = @(ti) interp1(t,-(current - baseline),ti);
        J_int = quad(qb, t(1), t(end));
    end
    function valid =
ValidateQB(t,current,t_lat,t_peak,J_peak,t_hr,t_hi,t_dur)
        valid = J_peak>3 & t_dur>9 & t_peak>6 & t_hr < 50 & t_dur
< 150 & ~isnan(t_hi) & ~isnan(t_hr);
    end

end
```

Quantum Bump Filtering – FilterQB.m

```
function signal_filtered = FilterQB(t,signal,window)
%% FilterQB
% Filters QB traces by removing slow drift with a moving average
% filter. 25ms works well for wild-type-like QBs.

%% Determine Sampling Rate and Samples to Use for Filter
Fs = 1/mean(t(2:end)-t(1:length(t)-1));
n = Fs*window;

%% Determine baseline and final value
baseline = mean(signal(t<0));
```

```
final = mean(signal(t>t(end)*0.9)); % Use last 10% of the trace

%% Pad signal
padded = [baseline*ones(n,1);signal;final*ones(n,1)];
filtered = filter(1/n*ones(1,n),1,padded);

%% Return filtered signal
signal_filtered = signal -
filtered(round(1.5*n)+1:length(signal)+round(1.5*n));

end
```

Calculate Average Quantum Bump – GetAverageQB.m

```
function [t,average] = GetAverageQB(qbs)

%% Identify QBs to analyze
successes = [qbs.IsSuccessfulQuantumBump] & [qbs.IsAnalyzed];
alignment_point = [qbs.MidpointPeakTime];

%% Exclude QBs that occur too close to end of recording
min_final_time = 60;
for i=1:length(qbs)
    if successes(i)
        if qbs(i).Latency + min_final_time >
qbs(i).CurrentDetrended.t(end)
            successes(i) = 0;
        end
    end
end

%% Determine sample rate of each QB
for i=1:length(qbs)
    if successes(i)
        samplerate(i) =
1000/mean(qbs(i).CurrentDetrended.t(2:end) -
qbs(i).CurrentDetrended.t(1:length(qbs(i).CurrentDetrended.t)-
1));
    end
end
min_samplerate = min(samplerate(successes));

%% Adjust sample rate of QBs to minimum sampling rate
for i=1:length(qbs)
    if successes(i) & (samplerate(i) ~= min_samplerate)
        qbs(i).CurrentDetrended.values =
resample(qbs(i).CurrentDetrended.values,min_samplerate,samplerate
(i));
```

```
        qbs(i).CurrentDetrended.t =
[qbs(i).CurrentDetrended.t(1):1000/min_samplerate:qbs(i).CurrentD
etrended.t(end)];
    end
end

%% Get Minimum Overlapping Timeframe
t0 = -qbs(1).CurrentDetrended.t(end);
tf = qbs(1).CurrentDetrended.t(end);

nb = 1000000000;
na = 1000000000;
na_i = na;
for i=1:length(qbs)
    if successes(i)
        t_shifted = qbs(i).CurrentDetrended.t -
alignment_point(i);
        if t_shifted(1) > t0
            t0 = qbs(i).CurrentDetrended.t(1) -
alignment_point(i);
        end
        nb_i = length(t_shifted(t_shifted > t0 & t_shifted < 0));
        if (nb_i < nb)
            nb = nb_i;
        end
        if t_shifted(end) < tf
            tf = qbs(i).CurrentDetrended.t(end) -
alignment_point(i);
            na_i = length(t_shifted(t_shifted >= 0 & t_shifted <
tf));
        end
        if (na_i < na)
            na = na_i;
        end
    end
end

%% Calculate Average
i_first_success = find(successes==1,1);
t_shifted = qbs(i_first_success).CurrentDetrended.t -
alignment_point(i_first_success);
i_0 = find(t_shifted >= 0,1);
t = t_shifted((i_0 - nb):(i_0 + na - 1));
average = zeros(1,nb + na);
for i=1:length(qbs)
    if successes(i)
        t_shifted = qbs(i).CurrentDetrended.t -
alignment_point(i);
        i_0 = find(t_shifted >= 0,1);
```

```
        average = average + qbs(i).CurrentDetrended.values((i_0 -
nb):(i_0 + na - 1))'/qbs(i).PeakAmplitude;
    end
end
average = average ./ length(find(successes == 1));
end
```

Camgaroo Fluorescence Processing

Data Structure

The Camgaroo recordings were handled in MATLAB as a cell array with each row a different photoreceptor cell and the columns the following: (1) database identifier for the cell, (2) structure containing all the recordings for that cell, (3) the recording number corresponding to the dark control, (4) the light response, (5) ionomycin treatment, (6) EGTA treatment, (7) the processed Ca^{++} results.

Correcting for Photobleaching –

ProcessCalciumData_Photobleaching.m

```
function [cellstruct, pb_results] =
ProcessCalciumData_Photobleaching( cellstruct, rows )

for i=1:length(rows)
    fit_result =
FitPhotobleaching(cellstruct{rows(i),2}(cellstruct{rows(i),5}).Fl
uorescencePeaks);
    pb_results{rows(i)} = fit_result;
    for j=1:length(cellstruct{rows(i),2})
        [t,v] =
CorrectPhotobleaching(cellstruct{rows(i),2}(j).FluorescencePeaks,
fit_result);
        cellstruct{rows(i),2}(j).FluorescencePeaksCorrected.t =
t;

cellstruct{rows(i),2}(j).FluorescencePeaksCorrected.values = v;
    end
end
```

```
end
```

Normalize and Calculate Ca^{++} Concentrations –

ProcessCalciumData_Calcium.m

```
function [ cellstruct ] = ProcessCalciumData_Calcium( cellstruct,
t_ss )

dataToProcess = logical(zeros(1,length([cellstruct{:,1}])));
for i=1:length(dataToProcess)
    dataToProcess(i) = ~isempty(cellstruct{i,4}) &
~isempty(cellstruct{i,5});
end

for i=1:length(dataToProcess)
    if ~dataToProcess(i)
        continue;
    end
    data =
cellstruct{i,2}(cellstruct{i,4}).FluorescencePeaksCorrected;
    data_t = data.t;
    data = data.values;
    maxdata =
cellstruct{i,2}(cellstruct{i,5}).FluorescencePeaksCorrected;
    maxdata_t = maxdata.t;
    maxdata = maxdata.values;

    data_std = std(data(data_t > t_ss));
    Fmax = mean(maxdata(maxdata_t > t_ss));
    Fmax_std = std(maxdata(maxdata_t > t_ss));
    Fmin = data(1);
    Fmin_std = data_std;
    [ca,ca_low,ca_high] = GetCaConcentrations(data, [Fmin Fmax],
7, 1.3, data_std, Fmax_std, Fmin_std);
    ca_results.t = data_t;
    ca_results.ca = ca;
    ca_results.ca_low = ca_low;
    ca_results.ca_high = ca_high;
    ca_results.data_std = data_std;
    ca_results.fnorm = (data - Fmin)./(Fmax - Fmin);
    ca_results.Fmax = Fmax;
    ca_results.Fmax_std = Fmax_std;
    ca_results.Fmin = Fmin;
    ca_results.Fmin_std = Fmin_std;
    ca_results.t_ss = t_ss;
    ca_results.ca_ss = mean(ca(data_t>t_ss));
    ca_results.ca_ss_std = std(ca(data_t>t_ss));
```

```
    cellstruct{i,7} = ca_results;
end

end
```

Convert Fluorescence to Ca^{++} Concentrations –

GetCaConcentrations.m

```
function [y,low,high] = GetCaConcentrations(data, calibration,
Kd, Hill, std_F, std_Fmax, std_Fmin)

Fmin = calibration(1);
Fmax = calibration(2)-calibration(1);

F = (data - Fmin)./Fmax;
y = Kd*(-F./(F-1)).^(1/Hill);

for i = 1 : length(data)
    err(i) = f_Ca_err(data(i));
end

err = err';

low = y - err;
high = y + err;

    function conc = f_Ca(V)
        conc = Kd*(-((V-Fmin)/(Fmax-Fmin))/((V-Fmin)/(Fmax-Fmin)-
1))^(1/Hill);
    end
    function dconc = df_Ca_dF(V)
        dconc = -Kd*(-(V-Fmin)/(V-Fmax))^(1/Hill)*(-
Fmax+Fmin)/Hill/(V-Fmax)/(V-Fmin);
    end
    function dconc = df_Ca_dFmax(V)
        dconc = -(-(V-Fmin)/(V-Fmax))^(1/Hill)*Kd/(V-Fmax)/Hill;
    end
    function dconc = df_Ca_dFmin(V)
        dconc = (-(V-Fmin)/(V-Fmax))^(1/Hill)*Kd/(V-Fmin)/Hill;
    end
    function dconc = f_Ca_err(V)
        dconc =
((df_Ca_dF(V)*std_F)^2+(df_Ca_dFmax(V)*std_Fmax)^2+(df_Ca_dFmin(V
)*std_Fmin)^2)^(1/2);
    end
end
```

Camgaroo Measurement Analysis

QQ Plot Analysis Script

```
%% Do QQ comparison
output.compare_cc_ci = compareqq(output.CC_1500,output.CI_1500);
output.compare_cc_ca = compareqq(output.CC_1500,output.CA_1500);
output.compare_ci_ca = compareqq(output.CI_1500,output.CA_1500);

%% Calculate random model
plotpoints = 0:0.025:1;
nsamples = 657;
% The # of comparisons is #cells1*#cells2. There are slightly
different
% numbers of cells for each genotype, so the # of comparisons
isn't exactly
% the same. It's large enough though to not be a major source of
error.
%ntrials =
max([size(output.compare_cc_ca,1),size(output.compare_cc_ci,1),si
ze(output.compare_ci_ca,1)]);
%ntrials_mean =
mean([size(output.compare_cc_ca,1),size(output.compare_cc_ci,1),s
ize(output.compare_ci_ca,1)]);
ntrials = 500;
ntrials_mean = 500;

frescale = @(x,scale) (x - scale(1))./(scale(2) - scale(1));

% Calculate the random expectation for comparing two normal
distributions
% of equal mean and variance, sampling nsamples each time.
rndmodel_norm = zeros(ntrials,length(plotpoints));
for i=1:ntrials
    rndmodel_samples = normrnd(0,1,nsamples,2); % The two random
distributions
    % To see the effect of normalization on finite sampled
distributions,
    % plot the histogram of the two distributions normalized by
min and
    % max. It's not a perfect Gaussian due to the different
extreme values
    % sampled.

    % QQ comparison
    data1 = sort(rndmodel_samples(:,1));
    pvec = 100*((1:nsamples) - 0.5) ./ nsamples;
    data2_matched = prctile(rndmodel_samples(:,2),pvec)';
```

```
    data1_range = [min(data1),max(data1)];
    data2_range =
[min(rndmodel_samples(:,2)),max(rndmodel_samples(:,2))];
    data_dx = prctile(data1,75) - prctile(data1,25); % This is
what MATLAB says is a robust estimate of the variance
    data_dy = prctile(rndmodel_samples(:,2),75) -
prctile(rndmodel_samples(:,2),25);
    % In this case the next step is not actually necessary, but
for the
    % actual data I had to rescale distributions of different
mean and
    % variance, so I normalize by the linear fit of the second
distribution
    % (if you run matlab's normplot command you'll get a feel of
what I am
    % attempting here)
    m = data_dy / data_dx;
    b = prctile(rndmodel_samples(:,2),75) -
m*prctile(rndmodel_samples(:,1),75);
    % Interpolate the normalized data at plotpoints, this is
necessary to
    % be able to average over multiple comparisons -- the values
    % represented by the percentiles are different for each
dataset
    rndmodel_norm(i,:) = interp1(frescale(data1,data1_range), ...
        frescale(data2_matched,m*data1_range+b), plotpoints);
end

rndmodel_avg = mean(rndmodel_norm(1:ntrials_mean,:),1)-
plotpoints;

%% Plot results
figure('Position',[50 50 400 200]);
errorbar(plotpoints,mean(output.compare_cc_ci,1) -
plotpoints,std(output.compare_cc_ci,0,1)/sqrt(size(output.compare
_cc_ci,1)),'ro'); hold on;
errorbar(plotpoints,mean(output.compare_cc_ca,1) -
plotpoints,std(output.compare_cc_ca,0,1)/sqrt(size(output.compare
_cc_ca,1)),'bo'); hold on;
errorbar(plotpoints,mean(output.compare_ci_ca,1) -
plotpoints,std(output.compare_ci_ca,0,1)/sqrt(size(output.compare
_ci_ca,1)),'ko');
plot(plotpoints,rndmodel_avg,'k-','LineWidth',2);
xlabel('Normalized Data');
ylabel('Normalized Deviation');
box off
grid on
xlim([0 1]);
ylim([-0.1 0.1]);
```

```
%% Determine significance by 2-way ANOVA between measurements and
random model
temp = [output.compare_ci_ca-
ones(size(output.compare_ci_ca,1),1)*plotpoints;rndmodel_norm(1:s
ize(output.compare_ci_ca,1),:)-
ones(size(output.compare_ci_ca,1),1)*plotpoints];
[p_ci_ca,~,stats_ci_ca] =
anova2(temp,size(output.compare_ci_ca,1));
temp = [output.compare_cc_ca-
ones(size(output.compare_cc_ca,1),1)*plotpoints;rndmodel_norm(1:s
ize(output.compare_cc_ca,1),:)-
ones(size(output.compare_cc_ca,1),1)*plotpoints];
[p_cc_ca,~,stats_cc_ca] =
anova2(temp,size(output.compare_cc_ca,1));
temp = [output.compare_cc_ci-
ones(size(output.compare_cc_ci,1),1)*plotpoints;rndmodel_norm(1:s
ize(output.compare_cc_ci,1),:)-
ones(size(output.compare_cc_ci,1),1)*plotpoints];
[p_cc_ci,~,stats_cc_ci] =
anova2(temp,size(output.compare_cc_ci,1));
% couldn't figure out how to get multiple comparisons to work
correctly

%% Plot fitted distribution comparisons
ci_fits_compare = compareqq_fit(output.CI_1500);
ca_fits_compare = compareqq_fit(output.CA_1500);
figure('Position',[50 50 400 200]);
errorbar(plotpoints,mean(ci_fits_compare,1)-
plotpoints,std(ci_fits_compare,0,1)/sqrt(size(ci_fits_compare,1))
,'ro'); hold on;
errorbar(plotpoints,mean(ca_fits_compare,1)-
plotpoints,std(ca_fits_compare,0,1)/sqrt(size(ca_fits_compare,1))
,'bo'); hold on;
plot(plotpoints,rndmodel_avg,'k-','LineWidth',2);
xlabel('Normalized Data');
ylabel('Normalized Deviation in Fit');
box off
grid on
xlim([0 1]);
ylim([-0.1 0.1]);

%% Determine significance by 2-way ANOVA between fits and random
model
temp = [ci_fits_compare-
ones(size(ci_fits_compare,1),1)*plotpoints;rndmodel_norm(1:size(c
i_fits_compare,1),:)-ones(size(ci_fits_compare,1),1)*plotpoints];
[p_ci_fits,~,stats_ci_fits] =
anova2(temp,size(ci_fits_compare,1));
```

```
temp = [ca_fits_compare-
ones(size(ca_fits_compare,1),1)*plotpoints;rndmodel_norm(1:size(c
a_fits_compare,1),:)-ones(size(ca_fits_compare,1),1)*plotpoints];
[p_ca_fits,~,stats_ca_fits] =
anova2(temp,size(ca_fits_compare,1));
% couldn't figure out how to get multiple comparisons to work
correctly
```

QQ Plot for Two Distributions – compareqq.m

```
function qqcomparison = compareqq(dataset1,dataset2)

frescale = @(x,scale) (x - scale(1))./(scale(2) - scale(1));
plotpoints = 0:0.025:1;

ii = 1;
for i=1:length(dataset1.delta_smoothed)
    data1 = sort(dataset1.delta_smoothed{i}(dataset1.ss_sel{i}));
    data_dx = prctile(data1,75) - prctile(data1,25);
    pvec = 100*((1:length(data1)) - 0.5) ./ length(data1);
    data1_range = [min(data1),max(data1)];
    for j=1:length(dataset2.delta_smoothed)
        data2 = dataset2.delta_smoothed{j}(dataset2.ss_sel{j});
        data2_matched = prctile(data2,pvec)';
        data2_range = [min(data2),max(data2)];
        data_dy = prctile(data2,75) - prctile(data2,25);
        m = data_dy / data_dx;
        b = prctile(data2,75) - m*prctile(data1,75);
        qqcomparison(ii,:) = interp1(frescale(data1,data1_range),
...
            frescale(data2_matched,m*data1_range+b), plotpoints);
        ii = ii + 1;
    end
end

end
```

QQ Plot for Data and Fit – compareqq_fit.m

```
function qqcomparison = compareqq_fit(dataset)

frescale = @(x,scale) (x - scale(1))./(scale(2) - scale(1));
plotpoints = 0:0.025:1;

ii = 1;
for i=1:length(dataset.fit_output)
    data1 = sort(dataset.fit_output{i}.qqplot.data);
```

```
    data2 = dataset.fit_output{i}.qqplot.fit;
    data_dx = prctile(data1,75) - prctile(data1,25);
    pvec = 100*((1:length(data1)) - 0.5) ./ length(data1);
    data1_range = [min(data1),max(data1)];
    data2_matched = prctile(data2,pvec)';
    data2_range = [min(data2),max(data2)];
    data_dy = prctile(data2,75) - prctile(data2,25);
    m = data_dy / data_dx;
    b = prctile(data2,75) - m*prctile(data1,75);
    qqcomparison(i,:) = interp1(frescale(data1,data1_range), ...
        frescale(data2_matched,m*data1_range+b), plotpoints);
end

end
```

Fit Ca++ Measurement Distribution –

fit_ca_measurement_distribution_simple3.m

```
function [output] =
fit_ca_measurement_distribution_simple3(data,plot_results)

data = real(data);
data_mean = mean(data);
data_std = std(data);
debug = 0;
if debug
    hf = figure;
end

%% Initial Parameters
ca_basal_i = 2;
ca_peak_i = 30;
gamma_i = 7400;
sigma_i = 0.4611;
ref_lengths = GetRandomRefractoryPeriodValues(5000);

%% Waveform
t = (0:1:1.2*max(ref_lengths));
lorenzian = @(tau,n,t) 1./(gamma(n)*tau).*(t/tau).^n.*exp(-
t./tau);
tau_light = 0.0054;
n_light = 0.2834;
w = lorenzian(tau_light,n_light,t/1000);
w = w ./ max(w);

%% Data CDF and weights
[pEmp,xi] = ecdf(real(data));
```

```
sorted_data = sort(data);
data_dx = prctile(sorted_data,75) - prctile(sorted_data,25);
normal_dy = norminv(0.75,data_mean,data_std) -
norminv(0.25,data_mean,data_std);
mn = normal_dy / data_dx;
bn = norminv(0.72,data_mean,data_std) -
mn*prctile(sorted_data,75);
wgt = 1 ./ sqrt(pEmp.*(1-pEmp));
%wgt = ones(length(pEmp),1);
wgt_good = ~isnan(wgt) & ~isinf(wgt);
pvec = 100*((1:length(data)) - 0.5) ./ length(data);
wgts = sqrt(pvec/100.*(1-pvec/100));

%% Improve initial guess
% Adjust guess based on data

% Fit each parameter
options = optimset('TolX',1e-1);
ca_basal_i =
fminbnd(@(ca_basal_i)calculate_cdf_params_score(normparams([ca_ba
sal_i,ca_peak_i,gamma_i,sigma_i])),0.5,20,options);

options = optimset('TolX',1e-1);
ca_peak_i =
fminbnd(@(ca_peak_i)calculate_cdf_params_score(normparams([ca_bas
al_i,ca_peak_i,gamma_i,sigma_i])),5,1000,options);

options = optimset('TolX',10);
gamma_i =
fminbnd(@(gamma_i)calculate_cdf_params_score(normparams([ca_basal
_i,ca_peak_i,gamma_i,sigma_i])),100,10000,options);

% Refit ca_basal and ca_peak since gamma changes the shape of the
curve a lot
options = optimset('TolX',1e-1);
ca_basal_i =
fminbnd(@(ca_basal_i)calculate_cdf_params_score(normparams([ca_ba
sal_i,ca_peak_i,gamma_i,sigma_i])),0.5,20,options);

options = optimset('TolX',1e-1);
ca_peak_i =
fminbnd(@(ca_peak_i)calculate_cdf_params_score(normparams([ca_bas
al_i,ca_peak_i,gamma_i,sigma_i])),5,1000,options);

%options = optimset('TolX',1e-2);
% Don't save the optimum sigma as the new scaling factor because
you can
% account for a lot of the signaling-increased variance with a
normal
```

```
% distribution -- want to make it more likely to decrease this
parameter
%sigma_i2 =
fminbnd(@(sigma)calculate_cdf_params_score(normparams([ca_basal_i
,ca_peak_i,gamma_i,sigma_i])),0.05,0.7,options);

%options = optimset('PlotFcns',@optimplotfval,'TolFun',0.1);
%[output,fval] = fminsearch(@(in)
calculate_cdf_params_score(normparams([gamma_i2,in(1),sigma_i2,in
(2)])), [a_i,ca_cell_i],options);

% %% Least-Squares Curve Fitting to Empirical CDF
% [pEmp,xi] = ecdf(data);
% options = optimset('PlotFcns',@optimplotx);
% [fit_output,resnorm,residual] =
lsqcurvefit(@calculate_cdf_params,normparams(gamma_i,a_i,sigma_i)
,xi,pEmp,[-Inf -Inf -Inf],[Inf Inf Inf],options);
% fit_output = undo_normparams(fit_output);

%% Probability-weigthed sum of squares fit to find start point
(copied from
%% MATLAB help

options = anneal();
options.Verbosity = 2;
options.Generator = @generator;
options.StopVal = 0.01;
bounds = [normparams([0.5,ca_basal_i, 500, 0.05]); ...
          normparams([20,1000, 10000, 0.7])];
[fit_output,output.fval] = anneal(@calculate_cdf_params_score,
normparams([ca_basal_i,ca_peak_i,gamma_i,sigma_i]),options);
fit_output = undo_normparams(fit_output);
disp(['Final fit value: ', num2str(output.fval)]);
disp(['ca_basal ',num2str(fit_output(1))]);
disp(['ca_peak ',num2str(fit_output(2))]);
disp(['gamma ',num2str(fit_output(3))]);
disp(['sigma ',num2str(fit_output(4))]);

output.ca_basal = fit_output(1);
output.ca_peak = fit_output(2);
output.log_ca_peak = log10(fit_output(2));
output.k_efflux = fit_output(3);
output.log_k_efflux = log10(fit_output(3));
output.sigma = fit_output(4);

% Store qq plot data
[~,fitted_samples] =
SimulateCalciumMeasurementDistributionSimpleLorenzian(t,w,ref_len
gths, ...
```

```
        fit_output(1), fit_output(2), fit_output(3),
fit_output(4));
data_dy = prctile(fitted_samples,75) -
prctile(fitted_samples,25);
m = data_dy / data_dx;
b = prctile(fitted_samples,75) - m*prctile(sorted_data,75);

output.qqplot.pvec = pvec;
output.qqplot.data = sorted_data;
output.qqplot.normal = norminv(pvec/100,data_mean,data_std);
output.qqplot.fit = prctile(fitted_samples,pvec)';
output.qqplot.line_x = [min(sorted_data),max(sorted_data)];
output.qqplot.line_normal = mn*output.qqplot.line_x + bn;
output.qqplot.line_fit = m*output.qqplot.line_x + b;

% Store CDF data and hypothesis test results
output.fit_samples = fitted_samples;
[output.cdf.f_fit,output.cdf.x] = ecdf(fitted_samples);
[output.h_fit,output.p_fit] = kstest(data,[-100, 0;
output.cdf.x(2:end), output.cdf.f_fit(2:end); 100 1]);
[output.h_normal,output.p_normal] = jbtest(data);
output.cdf.f_normal =
normcdf(output.cdf.x(2:end),data_mean,data_std);

%% Plot final fit
if plot_results
    figure;
    scatter(sorted_data,output.qqplot.normal,'r.'); hold on;
    scatter(sorted_data,output.qqplot.fit,'bo');
    plot([min(sorted_data),max(sorted_data)],
output.qqplot.line_normal,'r-');

plot([min(sorted_data),max(sorted_data)],[min(sorted_data),max(so
rted_data)],'k-');
    plot([min(sorted_data),max(sorted_data)],
output.qqplot.line_fit,'b-');
    axis equal;
    xlabel('Data');
    ylabel('Model');
    legend('QB','Normal','Location','SouthEast');
end

%% Norm Params
    function norm = normparams(params)
        ca_basal = params(1);
        ca_peak = params(2);
        gamma = params(3);
        sigma = params(4);
```

```
        norm = ([ca_basal,log10(ca_peak),log10(gamma),sigma] -
[ca_basal_i,log10(ca_peak_i),log10(gamma_i),sigma_i])./abs([ca_ba
sal_i,log10(ca_peak_i),log10(gamma_i),sigma_i]);
    end
    function regular = undo_normparams(norm)
        ca_basal = norm(1)*abs(ca_basal_i)+ca_basal_i;
        ca_peak =
10^(norm(2)*abs(log10(ca_peak_i))+log10(ca_peak_i));
        gamma = 10^(norm(3)*abs(log10(gamma_i))+log10(gamma_i));
        sigma = norm(4)*abs(sigma_i)+sigma_i;
        regular = [ca_basal,ca_peak,gamma,sigma];
    end

function params = generator(params)
        anneal_default = @(x)
(x+(randperm(length(x))==length(x))*randn/100);
        params_new = anneal_default(params);
        if ~isempty(find(params_new < bounds(1,:) | params_new >
bounds(2,:)))
            % Try reflecting
            params_new = params + (params - params_new);
        end
        while ~isempty(find(params_new < bounds(1,:) | params_new
> bounds(2,:)))
            params_new = anneal_default(params);
        end
        params = params_new;
    end

%% CDF Function
    function score = calculate_cdf_params_score(params)
       regular = undo_normparams(params);
       [~, ca_noisy] =
SimulateCalciumMeasurementDistributionSimpleLorenzian(t, w,
ref_lengths, regular(1),regular(2),regular(3),regular(4));
       resid = (sorted_data - prctile(ca_noisy,pvec)');
       score = 500/length(sorted_data)*sum(resid.^2); %wgts'.*
       if debug
           figure(hf);
           clf;

scatter(sorted_data,norminv(pvec/100,data_mean,data_std),'r.');
hold on;
           scatter(sorted_data,prctile(ca_noisy,pvec)','bo');
           data_dy = prctile(ca_noisy,75) - prctile(ca_noisy,25);
           m = data_dy / data_dx;
           b = prctile(ca_noisy,75) - m*prctile(sorted_data,75);
           plot([min(sorted_data),max(sorted_data)],
mn*[min(sorted_data),max(sorted_data)] + bn,'r-');
```

```
plot([min(sorted_data),max(sorted_data)],[min(sorted_data),max(so
rted_data)],'k-');
            plot([min(sorted_data),max(sorted_data)],
m*[min(sorted_data),max(sorted_data)] + b,'b-');
            axis equal;
        end
        %score = sum(wgt(wgt_good).*(q_data(wgt_good) -
calculate_q(xi(wgt_good),regular(1),regular(2),regular(3),regular
(4))).^2);
    end
    function ps = calculate_cdf(xi,ca_basal,ca_peak,gamma,sigma)
        [~, ca_noisy] =
SimulateCalciumMeasurementDistributionSimpleLorenzian(t, w,
ref_lengths, ca_basal, ca_peak, gamma, sigma);
        [f,x] = ecdf(ca_noisy);
        ps = interp1([0 x(2:end)' 100],[0 f(2:end)' 1],xi);
    end
    function q = calculate_q(xi,ca_basal,ca_peak,gamma,sigma)
        [~, ca_noisy] =
SimulateCalciumMeasurementDistributionSimpleLorenzian(t, w,
ref_lengths, ca_basal, ca_peak, gamma, sigma);
        [f,x] = ecdf(ca_noisy);
        q = interp1([0 f(2:length(x)-1)' 1],[0 x(2:length(x)-1)'
100],xi);
    end

end
```

Simulate Ca^{++} Measurement Distribution –

SimulateCalciumMeasurementDistributionSimpleLorenzian.m

```
function [ ca, ca_noisy, t_c, w_conv, w_calcium ] =
SimulateCalciumMeasurementDistributionSimpleLorenzian(t, w,
ref_lengths, ca_basal, ca_peak, k_eff, sigma)
%% SimulateCalciumMeasurementDistributionSimpleLorenzian
calculates a
%% distribution of apparent average calcium values given an input
of
%% random refractory lengths by convolving a waveform of channel
activity
%% (t,w) with an exponential decay (rate = -k_eff) shifted by
ca_basal and
%% scaled by ca_peak.

%% Parameters
Kd = 7;
```

```
n = 1.3;
measurement_noise = sigma;
bump_length = 10e-3;

%% Check that t is evenly spaced at 1 ms increments
if find(diff(t) ~= 1)
    % Resample to 1 ms increments
    t_rs = 0:max(ref_lengths)*1.2;
    w_rs = interp1(t,w,t_rs);
    t = t_rs;
    w = w_rs;
end

%% Convolve the waveform with an exponential efflux process
w_eff = exp(-k_eff*t/1000);
w_conv = conv(w,w_eff);

%% Normalize by max
w_conv = w_conv/max(w_conv);
t_c = (0:length(w_conv)-1)/1000;

%% Calculate modeled calcium dynamics
w_calcium = ca_basal + ca_peak*w_conv;

%% Convert to fluorescence curve from Camgaroo binding data
w_fl = w_calcium.^n./(w_calcium.^n + Kd.^n);

%% Calculate distribution by averaging over times selected from
ref_lengths
ca_app = @(f) Kd*(f./(1-f)).^(1/n);
gauss = @(n)normrnd(0,measurement_noise,1,n);

% For performance reasons, create a log-spaced standard curve
(log b/c we
% are dealing with exp)
ref_lengths_eval =
logspace(log10(min(ref_lengths)*0.9),log10(max(ref_lengths)*1.05)
,10)/1000;
fl_integrated(1) = quad(@(ti)
interp1(t_c,w_fl,ti),0,ref_lengths_eval(1)+bump_length);
parfor i=2:length(ref_lengths_eval)
        fl_integrated(i) = quad(@(ti)
interp1(t_c,w_fl,ti),ref_lengths_eval(i-
1)+bump_length,ref_lengths_eval(i)+bump_length);
end
fl_integrated_sum = cumsum(fl_integrated);
ca_measurements_eval = ca_app(fl_integrated_sum ./
(ref_lengths_eval+bump_length)); % This is now a curve of avg ca
vs. ref length
```

```
% Calculate the distribution from the input ref times
ca =
interp1(ref_lengths_eval,ca_measurements_eval,ref_lengths/1000);
ca_noisy = ca + gauss(length(ca));

end
```

InaD Biochemistry Analysis Scripts

FRET Binding Analysis – process_fret_competition_data_nc_jp.m

```
function [f_processed, f_conc, r, rn, fitobj, gof] =
process_fret_competition_data_nc_jp(w,c,unit,f_raw,f_blank,name)

%% Process spectra
f_processed = f_raw - f_blank*ones(1,numel(c));
f_conc = f_processed([find(w > 475, 1),find(w > 528, 1)],:);

%% Plot fitted spectra
figure('Name',[name, ' Spectra']);
map = jet;
for i=1:numel(c)
    i_map = round(i/numel(c)*length(map));

plot(w,f_processed(:,i),'o','Color',map(i_map,:),'MarkerFaceColor
',map(i_map,:),'MarkerEdgeColor','none','MarkerSize',3); hold on;
end
xlabel('Wavelength (nm)','FontSize',15);
ylabel('Fluorescence (counts/s)','FontSize',15);
set(gca,'FontSize',12);
for i=1:numel(c)
    c_label{i} = [num2str(c(i)), ' ', unit];
end
legend(c_label,'Location','EastOutside');
xlim([450 600]);

%% Fit data
r = (f_conc(1,:)./f_conc(2,:))';
fitfn = fittype('(a)*x/(Kd+x)+b','Independent','x');
options =
fitoptions('Method','NonlinearLeastSquares','Robust','Bisquare','
StartPoint',[100,0.3,r(2)],'Upper',[Inf,0.4,2],'Lower',[0.5,0.05,
0.5]);
[fitobj,gof] = fit(c(2:end)',r(2:end),fitfn,options);
rn = (r - fitobj.b)./(fitobj.a);
```

```
%% Plot ratio vs concentration
figure('Name', [name, ' Titration']);
semilogx(c,r,'ko'); hold on;
plot(c,feval(fitobj,c),'k-','LineWidth',2);
legend('Data',['Fit: Kd = ',
num2str(fitobj.Kd)],'Location','SouthOutside');
xlabel(['Concentration ', unit],'FontSize',15);
ylabel('Ratio of Cerulean to Venus Fluorescence','FontSize',15);

end
```

Quasi-Equilibrated Redox Titration Simulation

Titration Script – simulate_titration.m

```
function fr =
simulate_titration(hfig,E,ref,end_time,a,K_conf,alpha_R,k_ox,k_co
nf,show_plot)

fr = zeros(numel(E),1);
for i=1:numel(E)
    [~,~,~,fr(i)] =
simulate_redox_equilibria_model_full_kinetic3(E(i),end_time,K_con
f,alpha_R,k_ox,k_conf,0);
end

if show_plot
    figure(hfig);
    clf;
    plot(E*1000,ref*100,'.'); hold on;
    plot(E*1000,a*fr*100,'o');
    xlabel('E (mV)');
    ylabel('% Reduced');
    ylim([0 100]);
end

end
```

Simulate Equilibration –

simulate_redox_equilibria_model_full_kinetic3.m

```
function [t,y,fr,fr_final] =
simulate_redox_equilibria_model_full_kinetic(Ev,end_time,K_conf,a
lpha_R,k_ox,k_conf,show_plot)
%% Constants
R = 8.314; % J/mol/K
```

```
T = 303; % K
F = 96485; % C/mol
n = 2;

%% Parameters
k_ox_O = k_ox;
kr_conf_ox = k_conf;
E0_pdz5 = -0.2846;
E0_C = E0_pdz5-R*T/(n*F)*log(alpha_R);

%% Calculate remaining kinetic constants
% Conformational dynamics:
% K_conf = C/O = k_conf/kr_conf, 0 = k_conf*O -
% kr_conf*C
kr_conf = k_conf/K_conf;
% alpha_R*K_conf = C_ox/O_ox = k_conf_ox/kr_conf_ox, 0 =
k_conf_ox*O -
% kr_conf_ox*C_ox
K_conf_ox = alpha_R*K_conf;
k_conf_ox = K_conf_ox*kr_conf_ox;

% Redox dynamics:
K_redox = exp(n*F/(R*T)*(E0_C - Ev));
K_redox_O = alpha_R*K_redox;
% K_redox = k_red/k_ox, 0 = k_ox*C - k_red*C_ox
k_red = K_redox*k_ox;
k_red_O = alpha_R*K_redox*k_ox_O;

%% Solve ODE
% K_conf = C/O, K_conf*O + O = 1, 1/(1+K_conf) = O
ic_O = 1/(1+K_conf);
ic = [0.8 0 0 0.2];
options = odeset('AbsTol',1e-8);
[t,y] = ode15s(@calculate_diffeq,[0 end_time*60*60], ic,options);
fr = y(:,1)+y(:,2);
fr_final = fr(end);

%% Output
if show_plot
    figure;
    subplot(1,2,1);
    loglog(t/60/60,y);
    legend('C','O','Cox','Oox','Location','SouthEast');
    xlabel('Time (h)');
    ylabel('Fraction of Total Protein');
    subplot(1,2,2);
    plot(t/60/60,fr);
    xlabel('Time (h)');
    ylabel('Fraction Reduced');
```

```
    ylim([0 1]);
end

%% The differential equations
    function dy = calculate_diffeq(t,y)
        dy = zeros(4,1);
        % y1: C
        dy(1) = k_conf*y(2) - kr_conf*y(1) + k_red*y(3) -
k_ox*y(1);
        % y2: O
        dy(2) = kr_conf*y(1) - k_conf*y(2) + k_red_O*y(4) -
k_ox_O*y(2);
        % y3: C_ox
        dy(3) = k_conf_ox*y(4) - kr_conf_ox*y(3) + k_ox*y(1) -
k_red*y(3);
        % y4: O_ox
        dy(4) = kr_conf_ox*y(3) - k_conf_ox*y(4) + k_ox_O*y(2) -
k_red_O*y(4);
    end
end
```

InaD Sequence Analysis

```
%% Import BLAST results
clear all;
pdz4_hits = importdata('2011-03-01_pdz4_psi3_nr.csv');
pdz5_hits = importdata('2011-03-01_pdz5_psi3_nr.csv');
pdz45_hits = importdata('2011-03-01_pdz45_psi3_nr.csv');

%% Process BLAST results
clear hits
for i=1:size(pdz4_hits.data,1)
    hits.pdz4(i).expect = pdz4_hits.data(i,10);
    hits.pdz4(i).range = [pdz4_hits.data(i,8),
pdz4_hits.data(i,9)];
    hits.pdz4(i).length = hits.pdz4(i).range(2) -
hits.pdz4(i).range(1);
    name_bytypes = regexp(pdz4_hits.textdata{i,2},'\;','split');
    for j=1:numel(name_bytypes)
        name_parts = regexp(name_bytypes{j},'\|','split');
        for k=1:floor(numel(name_parts)/2)
            hits.pdz4(i).names(j).database{k} = name_parts{(k-
1)*2+1};
            hits.pdz4(i).names(j).name{k} = name_parts{(k-
1)*2+2};
            if j == 1
                hits.pdz4(i).ginum =
str2double(hits.pdz4(i).names(j).name{1});
            end
        end
```

```
    end
end
for i=1:size(pdz5_hits.data,1)
    hits.pdz5(i).expect = pdz5_hits.data(i,10);
    hits.pdz5(i).range = [pdz5_hits.data(i,8),
pdz5_hits.data(i,9)];
    hits.pdz5(i).length = hits.pdz5(i).range(2) -
hits.pdz5(i).range(1);
    name_bytypes = regexp(pdz5_hits.textdata{i,2},'\;','split');
    for j=1:numel(name_bytypes)
        name_parts = regexp(name_bytypes{j},'\|','split');
        for k=1:floor(numel(name_parts)/2)
            hits.pdz5(i).names(j).database{k} = name_parts{(k-
1)*2+1};
            hits.pdz5(i).names(j).name{k} = name_parts{(k-
1)*2+2};
            if j == 1
                hits.pdz5(i).ginum =
str2double(hits.pdz5(i).names(j).name{1});
            end
        end
    end
end
for i=1:size(pdz45_hits.data,1)
    hits.pdz45(i).expect = pdz45_hits.data(i,10);
    hits.pdz45(i).range = [pdz45_hits.data(i,8),
pdz45_hits.data(i,9)];
    hits.pdz45(i).length = hits.pdz45(i).range(2) -
hits.pdz45(i).range(1);
    name_bytypes = regexp(pdz45_hits.textdata{i,2},'\;','split');
    for j=1:numel(name_bytypes)
        name_parts = regexp(name_bytypes{j},'\|','split');
        for k=1:floor(numel(name_parts)/2)
            hits.pdz45(i).names(j).database{k} = name_parts{(k-
1)*2+1};
            hits.pdz45(i).names(j).name{k} = name_parts{(k-
1)*2+2};
            if j == 1
                hits.pdz45(i).ginum =
str2double(hits.pdz45(i).names(j).name{1});
            end
        end
    end
end

%% Filter hits
clear remove hits_fil
% First, by expect value
% For PDZ4 and PDZ5, remove hits with E>5e-10
cutoff_single = 5e-10;
```

```
remove.pdz4 = [hits.pdz4.expect] > cutoff_single;
remove.pdz5 = [hits.pdz5.expect] > cutoff_single;
% For PDZ45, remove hits with E>5e-30
cutoff_double = 5e-40;
remove.pdz45 = [hits.pdz45.expect] > cutoff_double;
% Second, by length
% For PDZ4 and PDZ5, length > 70
cutoff_l_single = 70;
remove.pdz4 = remove.pdz4 | [hits.pdz4.length] < cutoff_l_single;
remove.pdz5 = remove.pdz5 | [hits.pdz5.length] < cutoff_l_single;
% For PDZ45, length > 160
cutoff_l_double = 160;
remove.pdz45 = remove.pdz45 | [hits.pdz45.length] <
cutoff_l_double;
% Filter
hits_fil.pdz4 = hits.pdz4(~remove.pdz4);
hits_fil.pdz5 = hits.pdz5(~remove.pdz5);
hits_fil.pdz45 = hits.pdz45(~remove.pdz45);
disp(['Removed ', num2str(sum(remove.pdz4)), ' hits from PDZ4,
leaving ', num2str(sum(~remove.pdz4)), ' hits.']);
disp(['Removed ', num2str(sum(remove.pdz5)), ' hits from PDZ5,
leaving ', num2str(sum(~remove.pdz5)), ' hits.']);
disp(['Removed ', num2str(sum(remove.pdz45)), ' hits from PDZ45,
leaving ', num2str(sum(~remove.pdz45)), ' hits.']);

%% Find genes that appear in both hit lists
hits_fil.pdz4_pdz5_common =
intersect([hits_fil.pdz4.ginum],[hits_fil.pdz5.ginum]);
hits_fil.pdz4_pdz45_common =
intersect([hits_fil.pdz4.ginum],[hits_fil.pdz45.ginum]);
hits_fil.pdz5_pdz45_common =
intersect([hits_fil.pdz5.ginum],[hits_fil.pdz45.ginum]);
hits_fil.common =
intersect(hits_fil.pdz4_pdz5_common,[hits_fil.pdz45.ginum]); %
This only tests for common genes, not hits

%% Find tandem hits
ii = 1;
N_distance = 50;
hits_fil.tandem_hits = [];
for i=1:numel(hits_fil.pdz4)
    for j=1:numel(hits_fil.pdz5)
       if hits_fil.pdz4(i).ginum == hits_fil.pdz5(j).ginum
           if (hits_fil.pdz4(i).range(2) + N_distance) >=
hits_fil.pdz5(j).range(1) && (hits_fil.pdz4(i).range(1) <
hits_fil.pdz5(j).range(1))
               hits_fil.tandem_hits(ii,1:2) = [i,j];
               ii = ii + 1;
           end
       end
```

```
    end
end
hits_fil.tandem_common_genes_pdz4_pdz5 =
unique([hits_fil.pdz4(hits_fil.tandem_hits(:,1)).ginum]);
% Find the common hits
ii = 1;
for i=1:size(hits_fil.tandem_hits,1)
    match = find([hits_fil.pdz45.ginum] ==
hits_fil.pdz4(hits_fil.tandem_hits(i,1)).ginum);
    for j=1:numel(match)
       range_domains =
[hits_fil.pdz4(hits_fil.tandem_hits(i,1)).range(1),
hits_fil.pdz5(hits_fil.tandem_hits(i,2)).range(2)];
       range_45 = hits_fil.pdz45(match(j)).range;
       % Check if the ranges overlap
       if range_domains(1) >= range_45(1) && range_domains(1) <=
range_45(2) ... % Start of range_domains contained within 45
           || range_domains(2) >= range_45(1) && range_domains(2)
<= range_45(2) ... % or End of range_domains contained within 45
           || range_domains(1) <= range_45(1) && range_domains(2)
>= range_45(2) % or 45 completely contained within range_domains
          hits_fil.tandem_common_strict(ii) =
hits_fil.pdz45(match(j)).ginum;
          hits_fil.tandem_common_strict_index(ii) = match(j);
          ii = ii + 1;
       end
    end
end
hits_fil.tandem_common_strict_index =
unique(hits_fil.tandem_common_strict_index);
hits_fil.tandem_common_strict =
unique(hits_fil.tandem_common_strict);
hits_fil.tandem_common =
unique(intersect(hits_fil.tandem_common_genes_pdz4_pdz5,[hits_fil
.pdz45.ginum]));

disp(['Found ',
num2str(length(hits_fil.tandem_common_strict_index)), ' tandem
hits in common.']);

%% Make Venn diagram of filtering
totals =
[numel(hits_fil.pdz4),numel(hits_fil.pdz5),numel(hits_fil.pdz45)]
;
overlap =
[numel(hits_fil.pdz4_pdz5_common),numel(hits_fil.pdz4_pdz45_commo
n),numel(hits_fil.pdz5_pdz45_common),numel(hits_fil.tandem_common
_strict_index)];
figure;
[h,s] = venn(totals,overlap);
```

```
%% Write gi numbers of tandem common strict hits to file for
sequence download
f = fopen('ginums.txt','w');
for i=1:numel(hits_fil.tandem_common_strict)
    fprintf(f,'%s\n',num2str(hits_fil.tandem_common_strict(i)));
end
fclose(f);
% Then use Batch Entrez to download sequences

%% Import tandem PDZ containing sequences
genes = fastaread('tandem_common_strict.fasta');

%% Process sequences
ii = 1;
clear tandem_domains
N_extend = 10;
for i=1:numel(genes) % Iterate through sequences
    header_parts = regexp(genes(i).Header,'\|','split');
    ginum = str2num(header_parts{2}); %#ok<ST2NM>
    name_parts = regexp(header_parts{end},'\[','split');
    name = strtrim(name_parts{1});
    species = '';
    if numel(name_parts) > 1
        species_parts = regexp(name_parts{2},'\]','split');
        species = strtrim(species_parts{1});
    end
    sequence = genes(i).Sequence;
    sequence_len = length(sequence);
    pdz45matches = find(ginum == [hits_fil.pdz45.ginum]);
    for j=1:numel(pdz45matches)
        if ~any(hits_fil.tandem_common_strict_index ==
pdz45matches(j))
            continue;
        end
        tandem_domains(ii).ginum = ginum;
        tandem_domains(ii).name = name;
        tandem_domains(ii).species = species;
        tandem_domains(ii).expect =
hits_fil.pdz45(pdz45matches(j)).expect;
        tandem_domains(ii).range =
hits_fil.pdz45(pdz45matches(j)).range;
        if tandem_domains(ii).range(1) > N_extend
            tandem_domains(ii).range(1) =
tandem_domains(ii).range(1) - N_extend;
        else
            tandem_domains(ii).range(1) = 1;
        end
        if tandem_domains(ii).range(2) < sequence_len - N_extend
```

```
            tandem_domains(ii).range(2) =
tandem_domains(ii).range(2) + N_extend;
        else
            tandem_domains(ii).range(2) = sequence_len;
        end
        tandem_domains(ii).Header =
[num2str(ginum),'/',num2str(tandem_domains(ii).range(1)),'-
',num2str(tandem_domains(ii).range(2))];
        tandem_domains(ii).Sequence =
sequence(tandem_domains(ii).range(1):tandem_domains(ii).range(2))
;
        ii = ii + 1;
    end
end

%% Write tandem domains to FASTA file
fastawrite('tandem_domains.fasta',tandem_domains);
% Then do promals3d alignment

%% Read PROMALS alignment
tandem_domains_aligned =
fastaread('tandem_domains_strict_aln.fasta');

%% Write species list to file
f = fopen('species.txt','w');
species = unique({tandem_domains.species});
for i=1:numel(species)
    if ~isempty(species{i})
        fprintf(f,'%s\n',species{i});
    end
end
fclose(f);

%% Filter gappy columns
gap_cutoff = 0.2;
seqs = char({tandem_domains_aligned.Sequence});
fraq_gaps=sum(isletter(seqs)==0)/numel(tandem_domains_aligned);
seqs_trunc=seqs(:,fraq_gaps<gap_cutoff);

%% Make tree
D = seqpdist(seqs_trunc,'UseParallel',true);
tree = seqneighjoin(D,'equivar',{tandem_domains.Header});
view(tree);
phytreewrite('tree.tre',tree);

%% Generate Archaeopteryx mapping table to label nodes correctly
out = [];
!del forester_mapping.txt
f = fopen('forester_mapping.txt','w');
```

```
for i=1:numel(tandem_domains)

fprintf(f,'%s\t%s\t%s\t%s\n',tandem_domains(i).Header,['SEQ_NAME:
',tandem_domains(i).name],['TAXONOMY_SN:',tandem_domains(i).speci
es],['SEQ_ACCESSION:',num2str(tandem_domains(i).ginum)]);
end
fclose(f);

%% Run decorator on tree
!del tree.xml
!del tree_decorated.xml
!java -cp forester.jar
org.forester.application.phyloxml_converter -f=nn tree.tre
tree.xml
!java -cp forester.jar org.forester.application.decorator -table
tree.xml forester_mapping.txt tree_decorated.xml

%% Define domain structure
representatives = { 'Lnx2 (Mus musculus)', 687,
[232,314;338,421;465,551;597,685], [51,89;207,210], 1,2; ...
    'MPDZ Homolog (Strongylocentrotus purpuratus)', 999,
[253,331;428,500;576,657;669,744;779,850;923,999], [], 4,5; ...
    'MPDZ Homolog (Trichoplax adhaerans)', 1926,
[129,207;267,339;376,447;550,626;708,786;869,945;1018,1100;1200,1
275;1339,1416;1498,1573;1597,1670;1725,1802;1851,1926],[],10,11;
...
    'MPDZ Homolog (Ixodes scapularis)',877,
[43,111;359,435;447,531;637,712;767,844],[],4,5; ...
    'MPDZ Homolog (Oikopleura dioica)',1781,
[18,96;137,209;233,315;401,476;546,625;797,852;853,929;991,1072;1
184,1257;1301,1373;1405,1480;1497,1568;1596,1671;1706,1780],[],11
,12; ...
    'InaD (Drosophila melanogaster)',674,
[17,106;249,332;364,448;489,577;584,664],[],4,5; ...
    'Mpz-1 (Caenorhabditis elegans)', 2166,
[20,92;290,367;426,509;593,672;800,878;1225,1312;1578,1652;1739,1
814;1840,1913;2094,2161],[],8,9; ...
    'MPDZ Homolog (Ciona intestinalis)', 2043,
[126,204;254,327;387,468;533,609;739,818;1083,1157;1234,1323;1365
,1441;1502,1573;1628,1703;1730,1803;1849,1924;1966,2043],[],10,11
; ...
    'InaDL (Homo sapiens)', 1801,
[134,221;248,328;365,453;553,639;686,772;1068,1160;1239,1322;1437
,1520;1533,1615;1676,1762],[1,65],8,9; ...
    'MPDZ (Homo sapiens)', 2070,
[137,224;257,337;377,463;553,634;700,786;1008,1089;1151,1243;1350
,1433;1483,1564;1629,1712;1725,1807;1862,1948;1987,2070], [1,63],
10, 11};

%% Plot domains
```

```
figure;
dy = 0.25;
for i=1:size(representatives,1)
    plot([1,representatives{i,2}],i*[1 1],'k'); hold on;
    for j=1:size(representatives{i,4},1)
        color = [0.5 0.5 0.5];

fill([representatives{i,4}(j,:),representatives{i,4}(j,[2,1])],i*
[1 1 1 1] + [-dy,-dy,+dy,+dy],color);
    end
    for j=1:size(representatives{i,3},1)
        color = [1 1 1];
        if j == representatives{i,5}
            color = [0 0 1];
        elseif j == representatives{i,6}
            color = [0 1 0];
        end

fill([representatives{i,3}(j,:),representatives{i,3}(j,[2,1])],i*
[1 1 1 1] + [-dy,-dy,+dy,+dy],color);
    end
end
set(gca,'YTick',1:size(representatives,1));
set(gca,'YTickLabel',representatives(:,1));
set(gca,'YDir','rev','Box','off');
ylim([0 size(representatives,1)+1]);
xlabel('Position');
```

NorpA Sensitivity Analysis Scripts

Sensitivity Analysis Script

```
%% Parameters
[param,ic] = GetPumirModelParamPublished();
mods = logspace(-2,2,40);
nrepeats = 400;
%%
wt = GenerateFittedBumps(-1, ic, param, 500);
%% PLC Phospholipase Activity
param2 = param;
for i=1:length(mods)
    param2.k_A = param.k_A*mods(i);
    output = GenerateFittedBumps(-1, ic, param2, nrepeats);
    plcpa.eff(i) = output.eff;
    plcpa.t_lat(i) = output.t_lat;
    plcpa.J(i) = output.J;
    plcpa.t_act(i) = output.t_act;
    plcpa.t_inact(i) = output.t_inact;
    plcpa.t_inact2(i) = output.t_inact2;
    plcpa.t_lat_std(i) = output.t_lat_std;
```

```
    plcpa.J_std(i) = output.J_std;
    plcpa.t_act_std(i) = output.t_act_std;
    plcpa.t_inact_std(i) = output.t_inact_std;
    plcpa.t_inact2_std(i) = output.t_inact2_std;
end
save('matlab_temp.mat');

%% PLC GAP Activity
param2 = param;
for i=1:length(mods)
    param2.gamma_P = param.gamma_P*mods(i);
    output = GenerateFittedBumps(-1, ic, param2, nrepeats);
    plcga.eff(i) = output.eff;
    plcga.t_lat(i) = output.t_lat;
    plcga.J(i) = output.J;
    plcga.t_act(i) = output.t_act;
    plcga.t_inact(i) = output.t_inact;
    plcga.t_inact2(i) = output.t_inact2;
    plcga.t_lat_std(i) = output.t_lat_std;
    plcga.J_std(i) = output.J_std;
    plcga.t_act_std(i) = output.t_act_std;
    plcga.t_inact_std(i) = output.t_inact_std;
    plcga.t_inact2_std(i) = output.t_inact2_std;
end
save('matlab_temp.mat');
```

Quantum Bump Model

Parameters – GetPumirModelParamPublished.m

```
function [param,ic] = GetPumirModelParamPublished()

ic = [0   1   0   1   0   0   0   50 0 0];

param.Ca_ext = 5000;
param.Kdn = 19.5;
param.Kdp = 6.2;
param.mp = 2;
param.mn = 3;
param.k_Bapp = 1.3E-6;
param.nd=3;
param.gamma_B= 6E-2;
param.g_Bp= 41.5;
param.g_Bn = 5.4;
param.B_t=30;
param.gamma_R= 3.7E-3;
param.g_M= 8E3;
param.k_G = 4.7E-3;
```

```
param.gamma_G = 3.5E-2;
param.G_t=50;
param.k_P = 3.9E-3;
param.gamma_P = 4.8E-2;
param.g_Pn = 11.1;
param.P_t=100;
param.gamma_A = 2.1E-2;
param.g_An = 37.8;
param.k_A = 7.4E-2;
param.k_C = 1E-2;
param.gamma_C = 5.5E-3;
param.sigma = 0.17;
param.gamma_Ca= 33;
param.Ca_0 = 0.5;

end
```

Quantum Bump Model Simulation – PumirModelPublished.m

```
function [t,yy]=PumirModelPublished(t_total,y,param)
% Adapted from code by Alain Pumir and Boris Shraiman
% Initial conditions for wt :
% 0  1  0  1  0  0  50

%%%%

%%%%%%%%%%%%%%%%%%%%%%%%%%%%%%%%%%%%%%%%%%%%%%%%%%%%%%%%%%%

%DYNAMICAL VARIABLES

%%%%%%%%%%%%%%%%%%%%%%%%%%%%%%%%%%%%%%%%%%%%%%%%%%%%%%%%%%%

% y(1)  -- TRp*

% y(2)  --- Ca

% y(3) -- G*

% y(4) -- Rh*

% y(5) ---  PLC*

% y(6) ---  DAG

% y(7)= --- B*

% y(8) --- G
```

```
% y(9)=fbn;

% y(10)=fbp

%%%%%%%%%%%%%%%%%%%%%%%%%%%%%%%%%%%%%%%%%%%%%%%%%%%%%%%%%%%%%%%%%%%%%%%

tt=0;

ii=1;

yy(ii,:)=y;
t_rh_stop = 500;
% Run until 500 ms after rhodopsin turns off if t_total = -1
while (t_total > 0 && tt<t_total) || (t_total == -1 && tt <
t_rh_stop);
    if y(4) == 0 && t_rh_stop == 500
        t_rh_stop = tt + 500;
    end
 ii=ii+1;

%% Feedback functions
fbp=(y(2)/param.Kdp)^param.mp/(1+(y(2)/param.Kdp)^param.mp);
fbn=(y(7)/param.Kdn)^param.mn/(1+(y(7)/param.Kdn)^param.mn);

%% trp
% k_Bapp is k_B/k_A^nd
z(1,1)=param.k_Bapp*((y(6))^param.nd)*(1+param.g_Bp*fbp)*(param.B
_t-y(1));
z(1,2)=y(1)*param.gamma_B*(1+param.g_Bn*fbn);

z(2,2)=0;
z(2,1)=0;

%% G-protein
z(3,1)=param.k_G*y(8)*y(4);
z(3,2)=0;
z(8,2)=0;
z(8,1)=param.gamma_G*(param.G_t-y(5)-y(3)-y(8));

%% Rh* inactivation
z(4,1)=0;
z(4,2)=y(4)*(param.g_M*fbn+param.gamma_R);

%% PLC
z(5,1)=param.k_P*(param.P_t-y(5))*y(3);
z(5,2)=param.gamma_P*y(5)*(1+param.g_Pn*fbn);
```

```
%% DAG
z(6,1)=param.k_A*y(5);
z(6,2)=param.gamma_A*y(6)*(1+param.g_An*fbn);

%%  Ca buffer which drives negative feedback
z(7,1)=param.k_C*y(2);
z(7,2)=param.gamma_C*y(7);

%% Ca
y(2)=(param.sigma*param.Ca_ext*y(1)+param.Ca_0*param.gamma_Ca+par
am.gamma_C*y(7))/(param.sigma*y(1)+param.gamma_Ca+param.k_C);

y(9)=fbn;
y(10)=fbp;

%% stochastic update
up=z(:,1);
norm_1=sum(up);
if norm_1>0
    zup=cumsum(up)/norm_1;
end
down=z(:,2);
norm_2=sum(down);
if norm_2>0
    zdown=cumsum(down)/norm_2;
end
r=rand;
if norm_1+norm_2==0
    ii=nstep+1;
else
    q=norm_1/(norm_1+norm_2);
    if r<q
        r=r/q;
        tst=find(zup>r);nn=tst(1);
        y(nn)=y(nn)+1;
        if nn==5
            y(3)=y(3)-1;
        end
        if nn==3
            y(8)=y(8)-1;
        end
    else
        r=(r-q)/(1-q);
        tst=find(zdown>r);nn=tst(1);
        y(nn)=y(nn)-1;
    end
    r2=rand;
    tt=tt+log(1/r2)/(norm_1+norm_2);
    t(ii)=tt;
    yy(ii,:)=y;
```

```
end

end



end
```

Fitting Quantum Bumps – GenerateFittedBumps.m

```
function output = GenerateFittedBumps(simtime, ic, param,
ntrials)

   parfor j=1:ntrials
       [t,yy] = PumirModelPublished(simtime,ic,param);
       trial(j).t = t;
       trial(j).yy = yy;

       ibumps = yy(:,1)>=2;
       channel_openings = diff(ibumps);
       nBumps = floor(sum(abs(channel_openings))/2);
       if nBumps == 0
           t_lat = 0;
           t_act = 0;
           J = 0;
           t_inact = 0;
           t_peak = 0;
           t_inact2 = 0;
       else
           bump_start = find(channel_openings==1,1);
           bump_end = find(channel_openings==-1,1);
           t_lat = t(bump_start);
           J = max(yy(bump_start:bump_end,1));
           i_act = find(yy(:,1)>J/2,1);
           t_act = t(i_act) - t_lat;
           i_peak = find(yy(:,1)==J,1);
           t_peak = t(i_peak);

           i_inact = find(yy(i_peak:end,1)<J/2,1);
           if isempty(i_inact)
               t_inact = NaN;
           elseif (i_inact + i_peak)>length(t)
               t_inact = Inf;
           else
               t_inact = t(i_inact + i_peak) - t_peak;
           end

           i_inact2 = find(yy((i_inact + i_peak):end,1)==0,1);
```

```
            if t_inact==NaN
                t_inact2 = NaN;
            elseif isempty(i_inact2)
                t_inact2 = NaN;
            elseif (i_inact + i_peak + i_inact2)>length(t)
                t_inact2 = Inf;
            else
                t_inact2 = t(i_inact + i_peak + i_inact2) -
(t_peak + t_inact);
            end
        end
        trial(j).t_lat = t_lat;
        trial(j).t_act = t_act;
        trial(j).t_peak = t_peak;
        trial(j).J = J;
        trial(j).t_inact = t_inact;
        trial(j).t_inact2 = t_inact2;
    end
    output.trial = trial;
    success = [output.trial.J] > 0;
    output.eff = length(find(success))/ntrials;
    output.t_lat = mean([output.trial(success).t_lat]);
    output.t_lat_std = std([output.trial(success).t_lat]);
    output.t_act = mean([output.trial(success).t_act]);
    output.t_act_std = std([output.trial(success).t_act]);
    output.J = mean([output.trial(success).J]);
    output.J_std = std([output.trial(success).J]);
    output.t_inact = mean([output.trial(success).t_inact]);
    output.t_inact_std = std([output.trial(success).t_inact]);
    output.t_inact2 = mean([output.trial(success).t_inact2]);
    output.t_inact2_std = std([output.trial(success).t_inact2]);

end
```

Bibliography

Acar, M., Pando, B. F., Arnold, F. H., Elowitz, M. B., and Oudenaarden, A. van (2010). A General Mechanism for Network-Dosage Compensation in Gene Circuits. Science 329, 1656-1660.

Adamski, F. M., Zhu, M. Y., Bahiraei, F., and Shieh, B. H. (1998). Interaction of eye protein kinase C and INAD in Drosophila. Localization of binding domains and electrophysiological characterization of a loss of association in transgenic flies. J. Biol. Chem. 273, 17713-9.

Adey, N. B., Huang, L., Ormonde, P. A., Baumgard, M. L., Pero, R., Byreddy, D. V., Tavtigian, S. V., and Bartel, P. L. (2000). Threonine phosphorylation of the MMAC1/PTEN PDZ binding domain both inhibits and stimulates PDZ binding. Cancer Res. 60, 35-7.

Alberts, B., Bray, D., Lewis, Julian, Raff, M., Roberts, K., and Walter, P. (2002). Molecular Biology of the Cell (Garland Science).

Allbritton, N. L., Meyer, T, and Sryer, L. (1992). Range of messenger action of calcium ion and inositol 1,4,5- trisphosphate. Science 258, 1812-1815.

Alloway, P. G., and Dolph, P J (1999). A role for the light-dependent phosphorylation of visual arrestin. Proc. Natl. Acad. Sci. U. S. A. 96, 6072-7.

Alon, U, Surette, M. G., Barkai, N, and Leibler, S (1999). Robustness in bacterial chemotaxis. Nature 397, 168-71.

Alon, Uri (2003). Biological networks: the tinkerer as an engineer. Science 301, 1866-7.

Alon, Uri (2007a). Simplicity in biology. Nature 446, 497.

Alon, Uri (2007b). Network motifs: theory and experimental approaches. Nat. Rev. Genet. 8, 450-61.

Altschul, S. F., Madden, T. L., Schäffer, a a, Zhang, J, Zhang, Z., Miller, W., and Lipman, D. J. (1997). Gapped BLAST and PSI-BLAST: a new generation of protein database search programs. Nucleic Acids Res. 25, 3389-402.

Alwai, A. A., Jennings, V., Grossfield, J., and Pak, W. L. (1972). Phototransduction Mutants of Drosophila melanogaster. Adv. Exp. Med. Biol. 24, 1-21.

Andrews, B. W., Yi, T.-M., and Iglesias, P. a (2006). Optimal noise filtering in the chemotactic response of Escherichia coli. PLoS Comput. Biol. 2, e154.

Andrews, B. W., and Iglesias, P. a (2007). An information-theoretic characterization of the optimal gradient sensing response of cells. PLoS Comput. Biol. 3, e153.

Angeli, D., Ferrell, J. E., and Sontag, E. D. (2004). Detection of multistability, bifurcations, and hysteresis in a large class of biological positive-feedback systems. Proc. Natl. Acad. Sci. U. S. A. 101, 1822-7.

Austin, D. W., Allen, M. S., McCollum, J. M., Dar, R. D., Wilgus, J. R., Sayler, G. S., Samatova, N. F., Cox, C. D., and Simpson, M. L. (2006). Gene network shaping of inherent noise spectra. Nature 439, 608-11.

Baird, G. S., Zacharias, D. A., and Tsien, Roger Y. (1999). Circular permutation and receptor insertion within green fluorescent proteins. Proceedings of the National Academy of Sciences of the United States of America 96, 11241-11246.

Balaban, N. Q., Merrin, J., Chait, R., Kowalik, L., and Leibler, Stanislas (2004). Bacterial persistence as a phenotypic switch. Science 305, 1622-5.

Baldwin, A. J., and Kay, L. E. (2009). NMR spectroscopy brings invisible protein states into focus. Nat. Chem. Biol. 5, 808-14.

Balázsi, G., Oudenaarden, Alexander van, and Collins, J. J. (2011). Cellular decision making and biological noise: from microbes to mammals. Cell 144, 910-25.

Barabasi, A., and Albert, R. (1999). Emergence of scaling in random networks. Science 286, 509-12.

Barkai, N, and Leibler, S (1997). Robustness in simple biochemical networks. Nature 387, 913-7.

Barton, G. M., and Kagan, J. C. (2009). A cell biological view of Toll-like receptor function: regulation through compartmentalization. Nat. Rev. Immunol. 9, 535-42.

Bashor, C. J., Helman, N. C., Yan, S., and Lim, W. A. (2008). Using engineered scaffold interactions to reshape MAP kinase pathway signaling dynamics. Science 319, 1539-43.

Ben-Zvi, D., and Barkai, Naama (2010). Scaling of morphogen gradients by an expansion-repression integral feedback control. Proc. Natl. Acad. Sci. U. S. A. 107, 6924-9.

Berg, H. C. (1993). Random Walks in Biology (Princeton University Press).

Berk, L. C. J. van den, Landi, E., Walma, T., Vuister, G. W., Dente, L., and Hendriks, W. J. a J. (2007a). An allosteric intramolecular PDZ-PDZ interaction modulates PTP-BL PDZ2 binding specificity. Biochemistry 46, 13629-37.

Berk, L. C. J. van den, Landi, E., Walma, T., Vuister, G. W., Dente, L., and Hendriks, W. J. a J. (2007b). An allosteric intramolecular PDZ-PDZ interaction modulates PTP-BL PDZ2 binding specificity. Biochemistry 46, 13629-37.

Berkefeld, H. et al. (2006). BKCa-Cav channel complexes mediate rapid and localized Ca2+-activated K+ signaling. Science 314, 615-20.

Bershtein, S., Segal, M., Bekerman, R., Tokuriki, Nobuhiko, and Tawfik, Dan S (2006). Robustness-epistasis link shapes the fitness landscape of a randomly drifting protein. Nature 444, 929-32.

Beutner, D., Voets, T., Neher, E, and Moser, T. (2001). Calcium dependence of exocytosis and endocytosis at the cochlear inner hair cell afferent synapse. Neuron 29, 681-90.

Bhattacharya, S., Dai, Z., Li, Jianquan, Baxter, S., Callaway, D. J. E., Cowburn, D., and Bu, Z. (2010). A conformational switch in the scaffolding protein NHERF1 controls autoinhibition and complex formation. J. Biol. Chem. 285, 9981-94.

Bhattacharyya, R. P., Reményi, A., Yeh, B. J., and Lim, W. A. (2006). Domains, motifs, and scaffolds: the role of modular interactions in the evolution and wiring of cell signaling circuits. Annu. Rev. Biochem. 75, 655-80.

Bleris, L., Xie, Z., Glass, D., Adadey, A., Sontag, E., and Benenson, Y. (2011). Synthetic incoherent feedforward circuits show adaptation to the amount of their genetic template. Mol. Syst. Biol. 7, 1-12.

Bloom, J. D., Romero, P. a, Lu, Z., and Arnold, F. H. (2007). Neutral genetic drift can alter promiscuous protein functions, potentially aiding functional evolution. Biol. Direct 2, 17.

Bloom, J. D., and Arnold, F. H. (2009). In the light of directed evolution: pathways of adaptive protein evolution. Proc. Natl. Acad. Sci. U. S. A. 106 Suppl , 9995-10000.

Boehr, D. D., Nussinov, Ruth, and Wright, P. E. (2009). The role of dynamic conformational ensembles in biomolecular recognition. Nat. Chem. Biol. 5, 789-96.

Bohr, C., Hasselbach, K. A., and Krogh, A. (1904). Uber einen in biologischer Beziehung wichtigen Einfluss, den die Kohlensäurespannung des Blutes auf dessen Saurstoffbindung übt. Skandinavian Archives of Physiology 16, 402-412.

Bollmann, J. H., and Sakmann, B. (2005). Control of synaptic strength and timing by the release-site Ca2+ signal. Nat. Neurosci. 8, 426-34.

Borst, A. (2009). Drosophila's view on insect vision. Curr. Biol. 19, R36-47.

Boschek, C. B. (1971). On the fine structure of the peripheral retina and lamina ganglionaris of the fly, Musca domestica. Zeitschrift für Zellforschung und mikroskopische Anatomie (Vienna, Austria : 1948) 118, 369-409.

Brandman, O., Ferrell, J. E., Li, R., and Meyer, Tobias (2005). Interlinked fast and slow positive feedback loops drive reliable cell decisions. Science 310, 496-8.

Brandman, O., and Meyer, Tobias (2008). Feedback loops shape cellular signals in space and time. Science 322, 390-5.

Bullock, T. H. (1955). Compensation for temperature in the metabolism and activity of poikilotherms. Biol. Rev. 30, 311-342.

Burton, B. G., Tatler, B. W., Laughlin, Simon B, and Tatler, B. E. N. W. (2011). Variations in Photoreceptor Response Dynamics Across the Fly Retina. J. Neurophysiol., 950-960.

Byk, T., Bar-Yaacov, M., Doza, Y. N., Minke, Baruch, and Selinger, Z. (1993). Regulatory arrestin cycle secures the fidelity and maintenance of the fly photoreceptor cell. Proc. Natl. Acad. Sci. U.S.A. 90, 1907-11.

Bähner, M, Sander, P, Paulsen, R, and Huber, a (2000). The visual G protein of fly photoreceptors interacts with the PDZ domain assembled INAD signaling complex via direct binding of activated Galpha(q) to phospholipase cbeta. J. Biol. Chem. 275, 2901-4.

Bähner, Monika, Frechter, S., Silva, N. Da, Minke, Baruch, Paulsen, Reinhard, and Huber, Armin (2002). Light-Regulated Subcellular Translocation of Drosophila TRPL Channels Induces Long-Term Adaptation and Modifies the Light-Induced Current. Neuron 34, 83-93.

Carnegie, G. K., and Scott, John D (2003). A-kinase anchoring proteins and neuronal signaling mechanisms. Genes Dev. 17, 1557-68.

Cavanaugh, J., Fairbrother, W. J., Palmer, A. G. I., Rance, M., and Skelton, N. J. (2007). Protein NMR Spectroscopy: Principles and Practice 2nd ed. (Burlington, MA: Elsevier).

Chang, D.-E., Leung, S., Atkinson, M. R., Reifler, A., Forger, D., and Ninfa, A. J. (2010). Building biological memory by linking positive feedback loops. Proc. Natl. Acad. Sci. U. S. A. 107, 175-80.

Chapman, S. A., and Asthagiri, A. R. (2009). Quantitative effect of scaffold abundance on signal propagation. Mol. Syst. Biol. 5, 313.

Cheng, H., and Lederer, W. J. (2008). Calcium sparks. Physiol. Rev. 88, 1491-545.

Cheverud, J. M., Ehrich, T. H., Vaughn, T. T., Koreishi, S. F., Linsey, R. B., and Pletscher, L. S. (2004). Pleiotropic effects on mandibular morphology II: differential epistasis and genetic variation in morphological integration. J. Exp. Zool., Part B 302, 424-35.

Chevesich, J., Kreuz, A. J., and Montell, C. (1997). Requirement for the PDZ domain protein, INAD, for localization of the TRP store-operated channel to a signaling complex. Neuron 18, 95-105.

Chidiac, P., and Ross, E. M. (1999). Phospholipase C-beta 1 Directly Accelerates GTP Hydrolysis by Galpha q and Acceleration Is Inhibited by Gbeta gamma Subunits. J. Biol. Chem. 274, 19639-19643.

Choi, J., Ko, J., Park, E., Lee, J.-R., Yoon, J., Lim, S., and Kim, Eunjoon (2002). Phosphorylation of stargazin by protein kinase A regulates its interaction with PSD-95. J. Biol. Chem. 277, 12359-63.

Choi, K. Y., Satterberg, B., Lyons, D. M., and Elion, E. a (1994). Ste5 tethers multiple protein kinases in the MAP kinase cascade required for mating in S. cerevisiae. Cell 78, 499-512.
Chou, H.-H., Chiu, H.-C., Delaney, N. F., Segre, D., and Marx, C. J. (2011). Diminishing Returns Epistasis Among Beneficial Mutations Decelerates Adaptation. Science 332, 1190-1192.
Chung, H J, Xia, J., Scannevin, R. H., Zhang, X, and Huganir, R L (2000). Phosphorylation of the AMPA receptor subunit GluR2 differentially regulates its interaction with PDZ domain-containing proteins. J. Neurosci. 20, 7258-67.
Chung, Hee Jung, Huang, Y. H., Lau, L.-F., and Huganir, Richard L (2004). Regulation of the NMDA receptor complex and trafficking by activity-dependent phosphorylation of the NR2B subunit PDZ ligand. J. Neurosci. 24, 10248-59.
Clackson, T., and Wells, J. a (1995). A hot spot of binding energy in a hormone-receptor interface. Science 267, 383-6.
Cook, B., Bar-Yaacov, Margalit, Cohen Ben-Ami, H., Goldstein, R. E., Paroush, Z., Selinger, Zvi, and Minke, Baruch (2000). Phospholipase C and termination of G-protein-mediated signalling in vivo. Nat. Cell Biol. 2, 296-301.
Cooper, A., and Dryden, D. (1984). Allostery without conformational change. Eur. Biophys. J. 11, 103–109.
Costanzo, M. et al. (2010). The genetic landscape of a cell. Science 327, 425-31.
Cowman, A. F., Zuker, C. S., and Rubin, G. M. (1986). An opsin gene expressed in only one photoreceptor cell type of the Drosophila eye. Cell 44, 705-10.
Creighton, T. E. (1993). Proteins: Structures and Molecular Properties 2nd ed. (New York, NY: W.H. Freeman and Company).
Cronin, M. A., Diao, F., and Tsunoda, Susan (2004). Light-dependent subcellular translocation of Gq{alpha} in Drosophila photoreceptors is facilitated by the photoreceptor-specific myosin III NINAC. J. Cell. Sci. 117, 4797-4806.
Cui, Q., and Karplus, M. (2008). Allostery and cooperativity revisited. Protein Sci. 17, 1295-307.
Cunningham, B. C., and Wells, J. A. (1993). Comparison of a structural and a functional epitope. J. Mol. Biol. 234, 554-63.
DePristo, M. a, Weinreich, D. M., and Hartl, D. L. (2005). Missense meanderings in sequence space: a biophysical view of protein evolution. Nat. Rev. Genet. 6, 678-87.
Dear, P. (2006). The Intelligibility of Nature: How Science Makes Sense of the World (University of Chicago Press).
Dekel, E., and Alon, Uri (2005). Optimality and evolutionary tuning of the expression level of a protein. Nature 436, 588-92.

Dessauer, C. W. (2009). Adenylyl cyclase--A-kinase anchoring protein complexes: the next dimension in cAMP signaling. Mol. Pharmacol. 76, 935-41.

Devary, O., Heichal, O., Blumenfeld, a, Cassel, D., Suss, E., Barash, S., Rubinstein, C. T., Minke, B, and Selinger, Z (1987). Coupling of photoexcited rhodopsin to inositol phospholipid hydrolysis in fly photoreceptors. Proc. Natl. Acad. Sci. U. S. A. 84, 6939-43.

Dickens, M. (1997). A Cytoplasmic Inhibitor of the JNK Signal Transduction Pathway. Science 277, 693-696.

Dill, K. A., and Chan, H. S. (1997). From Levinthal to pathways to funnels. Nat. Struct. Biol. 4, 10-19.

Dima, R. I., and Thirumalai, D. (2006). Determination of network of residues that regulate allostery in protein families using sequence analysis. Protein Sci. 15, 258-268.

Dobzhansky, T. (1964). Biology, molecular and organismic. Am. Zool. 4, 443-452.

Dodge, F. A., Knight, B. W., and Toyoda, J. (1968). Voltage noise in Limulus visual cells. Science 160, 88-90.

Dolph, P. J., Man-Son-Hing, H., Yarfitz, S., Colley, N. J., Deer, J. R., Spencer, M., Hurley, J. B., and Zuker, C. S. (1994). An eye-specific G beta subunit essential for termination of the phototransduction cascade. Nature 370, 59-61.

Dolph, PJ J., Ranganathan, Rama, Colley, NJ J., Hardy, R. W. R., Socolich, M., and Zuker, C. S. (1993). Arrestin function in inactivation of G protein-coupled receptor rhodopsin in vivo. Science 260, 1910-6.

Doyle, D. A., Lee, A., Lewis, J., Kim, E., Sheng, M., and MacKinnon, R. (1996). Crystal structures of a complexed and peptide-free membrane protein-binding domain: molecular basis of peptide recognition by PDZ. Cell 85, 1067-76.

Doza, Y N, Minke, B, Chorev, M., and Selinger, Z (1992). Characterization of fly rhodopsin kinase. Eur. J. Biochem. 209, 1035-40.

Dublanche, Y., Michalodimitrakis, K., Kümmerer, N., Foglierini, M., and Serrano, L. (2006). Noise in transcription negative feedback loops: simulation and experimental analysis. Mol. Syst. Biol. 2, 41.

Eldar, A., Dorfman, R., Weiss, D., Ashe, H., Shilo, B.-zion, and Barkai, Naama (2002). Robustness of the BMP morphogen gradient in Drosophila embryonic patterning. Nature 419.

Eldar, A., and Elowitz, M. B. (2010). Functional roles for noise in genetic circuits. Nature 467, 167-73.

Elia, N., Frechter, S., Gedi, Y., Minke, Baruch, and Selinger, Zvi (2005). Excess of Gbetae over Gqalphae in vivo prevents dark, spontaneous activity of Drosophila photoreceptors. J. Cell. Biol. 171, 517-26.
Elowitz, M. B., Levine, A. J., Siggia, E. D., and Swain, P. S. (2002). Stochastic gene expression in a single cell. Science 297, 1183-6.
Fain, G. L., Hardie, R., and Laughlin, Simon B (2010). Phototransduction and the evolution of photoreceptors. Curr. Biol. 20, R114-24.
Fall, C. P., Marland, E. S., Wagner, J. M., and Tyson, J. J. (2002). Computational Cell Biology (New York, NY: Springer).
Feng, W., Shi, Yawei, Li, Ming, and Zhang, Mingjie (2003). Tandem PDZ repeats in glutamate receptor-interacting proteins have a novel mode of PDZ domain-mediated target binding. Nat. Struct. Biol. 10, 972-8.
Ferrell, J. E. (2008). Feedback regulation of opposing enzymes generates robust, all-or-none bistable responses. Curr. Biol. 18, R244-5.
Fersht, A. (1999). Structure and Mechanism in Protein Science (WH Freeman).
Fisher, R. (1918). The correlation between relatives on the supposition of Mendelian inheritance. Trans. - R. Soc. Edinburgh 52, 399-433.
Flint, J., and Mackay, T. F. C. (2009). Genetic architecture of quantitative traits in mice, flies, and humans. Genome Res. 19, 723-33.
Force, A., Cresko, W. a, Pickett, F. B., Proulx, S. R., Amemiya, C., and Lynch, M. (2005). The origin of subfunctions and modular gene regulation. Genetics 170, 433-46.
Franceschini, N., and Kirschfeld, K (1971). Pseudopupil phenomena in the compound eye of drosophila. Kybernetik 9, 159-82.
Frechter, S., Elia, N., Tzarfaty, V., Selinger, Zvi, and Minke, Baruch (2007). Translocation of Gq alpha mediates long-term adaptation in Drosophila photoreceptors. J. Neurosci. 27, 5571-83.
Fuentes, E. J., Der, C. J., and Lee, A. L. (2004). Ligand-dependent dynamics and intramolecular signaling in a PDZ domain. J. Mol. Biol. 335, 1105-15.
Garrard, S. M., Capaldo, C. T., Gao, L., Rosen, M. K., Macara, I. G., and Tomchick, D. R. (2003). Structure of Cdc42 in a complex with the GTPase-binding domain of the cell polarity protein, Par6. EMBO J. 22, 1125-33.
Gerhart, J., and Kirschner, M. (2007). The theory of facilitated variation. Proc. Natl. Acad. Sci. U. S. A. 104 Suppl , 8582-9.
Gianni, S. et al. (2006). Demonstration of long-range interactions in a PDZ domain by NMR, kinetics, and protein engineering. Structure 14, 1801-9.
Gillespie, D. T. (1976). A general method for numerically simulating the stochastic time evolution of coupled chemical reactions. J. Comput. Phys. 22, 403-434.

Goentoro, L., Shoval, O., Kirschner, M. W., and Alon, Uri (2009). The incoherent feedforward loop can provide fold-change detection in gene regulation. Mol. Cell 36, 894-9.
Gonzalez-Bellido, P. T., Wardill, T. J., and Juusola, Mikko (2011). Compound eyes and retinal information processing in miniature dipteran species match their specific ecological demands. Proc. Natl. Acad. Sci. U. S. A. 108, 4224-9.
Good, M. C., Zalatan, J. G., and Lim, W. A. (2011). Scaffold proteins: hubs for controlling the flow of cellular information. Science 332, 680-6.
Green, R. A. et al. (2011). A high-resolution C. elegans essential gene network based on phenotypic profiling of a complex tissue. Cell 145, 470-82.
Grootjans, J. J., Reekmans, G, Ceulemans, H., and David, G (2000). Syntenin-syndecan binding requires syndecan-synteny and the co-operation of both PDZ domains of syntenin. J. Biol. Chem. 275, 19933-41.
Gu, Y., Oberwinkler, Johannes, Postma, M., and Hardie, Roger C. (2005). Mechanisms of light adaptation in Drosophila photoreceptors. Curr. Biol. 15, 1228-34.
Gunasekaran, K., Ma, Buyong, and Nussinov, Ruth (2004). Is allostery an intrinsic property of all dynamic proteins? Proteins 57, 433-43.
Gupta, P. B., Fillmore, C. M., Jiang, G., Shapira, S. D., Tao, K., Kuperwasser, C., and Lander, E. S. (2011). Stochastic State Transitions Give Rise to Phenotypic Equilibrium in Populations of Cancer Cells. Cell 146, 633-644.
Gutenkunst, R. N., Waterfall, J. J., Casey, F. P., Brown, K. S., Myers, C. R., and Sethna, J. P. (2007). Universally Sloppy Parameter Sensitivities in Systems Biology Models. PLoS Comput. Biol. 3, 8.
Hahn, A. R. (2004). The Role of the Scaffolding Protein InaD in Localization of Signalign Complexes to the Rhabdomeres of Drosophila Photoreceptors. 161.
Halabi, N., Rivoire, O., Leibler, Stanislas, and Ranganathan, Rama (2009). Protein sectors: evolutionary units of three-dimensional structure. Cell 138, 774-86.
Hammes, G. G., Chang, Y.-C., and Oas, T. G. (2009). Conformational selection or induced fit: a flux description of reaction mechanism. Proc. Natl. Acad. Sci. U. S. A. 106, 13737-41.
Han, J.-dong J. et al. (2004). Evidence for dynamically organized modularity in the yeast protein-protein interaction network. Nature 430, 88-93.
Hardie, R C, and Minke, B (1994). Calcium-dependent inactivation of light-sensitive channels in Drosophila photoreceptors. J. Gen. Physiol. 103, 409-27.
Hardie, Roger C. (1996a). Calcium signalling: setting store by calcium channels. Curr Biol 6, 1371-3.

Hardie, Roger C. (1985). Functional organization of the fly retina. In Progress in Sensory Physiology, Vol. 5 D. Ottoson, ed. (Berlin, Heidelberg, New York, Tokyo: Springer), pp. 1-79.

Hardie, Roger C. (1996b). INDO-1 measurements of absolute resting and light-induced Ca2+ concentration in Drosophila photoreceptors. J. Neurosci. 16, 2924-33.

Hardie, Roger C., Gu, Y., Martin, Fernando, Sweeney, Sean T., and Raghu, Padinjat (2004). In vivo light-induced and basal phospholipase C activity in Drosophila photoreceptors measured with genetically targeted phosphatidylinositol 4,5-bisphosphate-sensitive ion channels (Kir2.1). J. Biol. Chem. 279, 47773-82.

Hardie, Roger C., Martin, F., Cochrane, G. W., Juusola, Mikko, Georgiev, P., and Raghu, P. (2002). Molecular Basis of Amplification in Drosophila Phototransduction: Roles for G Protein, Phospholipase C, and Diacylglycerol Kinase. Neuron 36, 689-701.

Hardie, Roger C., Martin, Fernando, Chyb, Sylwester, and Raghu, Padinjat (2003). Rescue of light responses in the Drosophila "null" phospholipase C mutant, norpAP24, by the diacylglycerol kinase mutant, rdgA, and by metabolic inhibition. J. Biol. Chem. 278, 18851-8.

Hardie, Roger C., Raghu, P., Moore, S., Juusola, Mikko, Baines, R. A., and Sweeney, S. T. (2001). Calcium influx via TRP channels is required to maintain PIP2 levels in Drosophila photoreceptors. Neuron 30, 149-59.

Hardie, Roger C., and Minke, Baruch (1992). The trp gene is essential for a light-activated Ca2+ channel in Drosophila photoreceptors. Neuron 8, 643-51.

Hardie, Roger C., and Raghu, P. (2001). Visual transduction in Drosophila. Nature 413, 186-93.

Hardie, Roger C. (1995). Photolysis of caged Ca2+ facilitates and inactivates but does not directly excite light-sensitive channels in Drosophila photoreceptors. J. Neurosci. 15, 889-902.

Hardie, Roger C., Peretz, A., Pollock, J. A., and Minke, Baruch (1993). Ca2+ limits the development of the light response in Drosophila photoreceptors. Proc. R. Soc. Lond. B Biol. Sci. 252, 223-9.

Harris, W. a, Stark, W. S., and Walker, J. a (1976). Genetic dissection of the photoreceptor system in the compound eye of Drosophila melanogaster. The Journal of physiology 256, 415-39.

Hartwell, L. H., Hopfield, J. J., Leibler, S, and Murray, a W. (1999). From molecular to modular cell biology. Nature 402, C47-52.

Hastings, J. W., and Sweeney, B. M. (1957). On the Mechanism of Temperature Independence in a Biological Clock. Proc. Natl. Acad. Sci. U. S. A. 43, 804-11.

Heidelberger, R., Heinemann, C., Neher, E, and Matthews, G. (1994). Calcium dependence of the rate of exocytosis in a synaptic terminal. Nature 371, 513-5.
Henderson, S. R., Reuss, Helmut, and Hardie, Roger C. (2000). Single photon responses in Drosophila photoreceptors and their regulation by Ca2+. J. Physiol. 524, 179-194.
Hill, A. (1910). The possible effects of the aggregation of the molecules of haemoglobin on its dissociation curves. J Physiol 40.
Hille, B. (2001). Ionic channels of excitable membranes 3rd ed. B Hille, ed. (Sunderland, MA: Sinauer).
Hillier, B. J., Christopherson, K. S., Prehoda, K E, Bredt, D. S., and Lim, W. A. (1999). Unexpected Modes of PDZ Domain Scaffolding Revealed by Structure of nNOS-Syntrophin Complex. Science 284, 812-815.
Hochstrate, P., and Hamdorf, K. (1990). Microvillar components of light adaptation in blowflies. J. Gen. Physiol. 95, 891-910.
Hofstee, C. A., Henderson, S., Hardie, Roger C., and Stavenga, D. G. (1996). Differential effects of ninaC proteins (p132 and p174) on light-activated currents and pupil mechanism in Drosophila photoreceptors. Vis. Neurosci. 13, 897-906.
Hogenesch, J. B., and Ueda, H. R. (2011). Understanding systems-level properties: timely stories from the study of clocks. Nat. Rev. Genet. 12, 407-16.
Hopfield, J. J. (1974). Kinetic proofreading: a new mechanism for reducing errors in biosynthetic processes requiring high specificity. Proc. Natl. Acad. Sci. U. S. A. 71, 4135-9.
Hornung, G., and Barkai, Naama (2008). Noise propagation and signaling sensitivity in biological networks: a role for positive feedback. PLoS Comput. Biol. 4, e8.
Houchmandzadeh, B., Wieschaus, E., and Leibler, Stanislas (2002). Establishment of developmental precision and proportions in the early Drosophila embryo. Nature 415, 798-802.
Howard, J., Blakeslee, B., and Laughlin, S. B. (1987). The intracellular pupil mechanism and photoreceptor signal: noise ratios in the fly Lucilia cuprina. Proc. R. Soc. Lond. B Biol. Sci. 231, 415-35.
Huang, J., Liu, C.-H., Hughes, S. A., Postma, M., Schwiening, C. J., and Hardie, Roger C. (2010). Activation of TRP channels by protons and phosphoinositide depletion in Drosophila photoreceptors. Curr. Biol. 20, 189-97.
Huber, A., Sander, P., Bahner, M., and Paulsen, R. (1998). The TRP Ca2+ channel assembled in a signaling complex by the PDZ domain protein INAD

is phosphorylated through the interaction with protein kinase C (ePKC). FEBS Lett. 425, 317-22.
Huber, A., Sander, P., Gobert, A., Bähner, M, Hermann, R., and Paulsen, R. (1996). The transient receptor potential protein (Trp), a putative store-operated Ca2+ channel essential for phosphoinositide-mediated photoreception, forms a signaling complex with NorpA, InaC and InaD. EMBO J. 15, 7036-45.
Huber, A., Sander, P., and Paulsen, R. (1996). Phosphorylation of the InaD gene product, a photoreceptor membrane protein required for recovery of visual excitation. J. Biol. Chem. 271, 11710-7.
Huber, Armin, Sander, Philipp, and Paulsen, Reinhard (1996). Phosphorylation of the InaD gene product, a photoreceptor membrane protein required for recovery of visual excitation. J. Biol. Chem. 271, 11710-7.
Huizen, R. van, Miller, K., Chen, D. M., Li, Y., Lai, Z. C., Raab, R. W., Stark, W. S., Shortridge, R. D., and Li, M (1998). Two distantly positioned PDZ domains mediate multivalent INAD-phospholipase C interactions essential for G protein-coupled signaling. EMBO J. 17, 2285-97.
Hung, A. Y., and Sheng, Morgan (2002). PDZ domains: structural modules for protein complex assembly. J. Biol. Chem. 277, 5699-702.
Inoue, H., Yoshioka, T., and Hotta, Y. (1988). Membrane-associated phospholipase C of Drosophila retina. J. Biochem. (Tokyo) 103, 91-4.
Jackson, C. J., Foo, J.-L., Tokuriki, N, Afriat, L., Carr, P. D., Kim, H.-K., Schenk, G., Tawfik, D S, and Ollis, D. L. (2009). Conformational sampling, catalysis, and evolution of the bacterial phosphotriesterase. Proc. Natl. Acad. Sci. U. S. A. 106, 21631-6.
Jackson, C. L., and Hartwell, L. H. (1990). Courtship in S. cerevisiae: both cell types choose mating partners by responding to the strongest pheromone signal. Cell 63, 1039-51.
Jacob, F. (1977). Evolution and tinkering. Science 196, 1161-1166.
James, L. C., Roversi, P., and Tawfik, Dan S (2003). Antibody multispecificity mediated by conformational diversity. Science 299, 1362-7.
Jarosz, D. F., Taipale, M., and Lindquist, S. (2010). Protein homeostasis and the phenotypic manifestation of genetic diversity: principles and mechanisms. Annu. Rev. Genet. 44, 189-216.
Jarosz, D. F., and Lindquist, S. (2010). Hsp90 and environmental stress transform the adaptive value of natural genetic variation. Science 330, 1820-4.
Jensen, R. a (1976). Enzyme recruitment in evolution of new function. Annu. Rev. Microbiol. 30, 409-25.
Johnson, E. C., and Pak, W L (1986). Electrophysiological study of Drosophila rhodopsin mutants. J. Gen. Physiol. 88, 651-73.

Juusola, M., and Hardie, Roger C. (2001). Light adaptation in Drosophila photoreceptors: I. Response dynamics and signaling efficiency at 25 degrees C. J. Gen. Physiol. 117, 3-25.
Kalisky, T., Dekel, E., and Alon, Uri (2007). Cost-benefit theory and optimal design of gene regulation functions. Phys. Biol. 4, 229-45.
Kashtan, Nadav, and Alon, Uri (2005). Spontaneous evolution of modularity and network motifs. Proc. Natl. Acad. Sci. U. S. A. 102, 13773-8.
Kemp, M., Go, Y.-M., and Jones, D. P. (2008). Nonequilibrium thermodynamics of thiol/disulfide redox systems: a perspective on redox systems biology. Free Radical Biol. Med. 44, 921-37.
Kennedy, M. B. (1995). Origin of PDZ (DHR, GLGF) domains. Trends in Biochem. Sci. 20, 350.
Khersonsky, O., and Tawfik, Dan S (2010). Enzyme promiscuity: a mechanistic and evolutionary perspective. Annu. Rev. Biochem. 79, 471-505.
Kimura, M. (1991). Recent development of the neutral theory viewed from the Wrightian tradition of theoretical population genetics. Proc. Natl. Acad. Sci. U. S. A. 88, 5969-73.
Kirschfeld, K (1967). Die projektion der optischen Umwelt auf das Raster der Rhabdomere im Komplexauge von MUSCA. Exp. Brain Res. 3, 248-70.
Kirschner, M., and Gerhart, J. (1998). Evolvability. Proc. Natl. Acad. Sci. U. S. A. 95, 8420-7.
Kiselev, A., Socolich, M., Vinós, J., Hardy, R. W., Zuker, C. S., and Ranganathan, Rama (2000). A molecular pathway for light-dependent photoreceptor apoptosis in Drosophila. Neuron 28, 139-52.
Kollmann, M., Løvdok, L., Bartholomé, K., Timmer, J., and Sourjik, V. (2005). Design principles of a bacterial signalling network. Nature 438, 504-7.
Koshland, D. E., Némethy, G., and Filmer, D. (1966). Comparison of experimental binding data and theoretical models in proteins containing subunits. Biochemistry 5, 365-85.
Kosloff, M., Elia, N., Joel-Almagor, T., Timberg, R., Zars, T. D., Hyde, D. R., Minke, Baruch, and Selinger, Zvi (2003). Regulation of light-dependent Gqalpha translocation and morphological changes in fly photoreceptors. EMBO J. 22, 459-68.
Kranz, J. E., Satterberg, B., and Elion, E. a (1994). The MAP kinase Fus3 associates with and phosphorylates the upstream signaling component Ste5. Genes Dev. 8, 313-27.
Krogan, N. J. et al. (2006). Global landscape of protein complexes in the yeast Saccharomyces cerevisiae. Nature 440, 637-43.
Kumar, S., Ma, B, Tsai, C. J., Sinha, N., and Nussinov, R (2000). Folding and binding cascades: dynamic landscapes and population shifts. Protein Sci. 9, 10-9.

Kunkel, T. A., and Bebenek, K. (2000). DNA replication fidelity. Annu. Rev. Biochem. 69, 497-529.
Kurakin, A. (2007). Self-organization versus Watchmaker : ambiguity of molecular recognition and design charts of cellular circuitry. J. Mol. Recognit., 205-214.
Kussell, E., and Leibler, Stanislas (2005). Phenotypic diversity, population growth, and information in fluctuating environments. Science 309, 2075-8.
Land, M. F., and Fernald, R. D. (1992). The evolution of eyes. Annu. Rev. Neurosci. 15, 1-29.
Lander, A. D. (2011). Pattern, growth, and control. Cell 144, 955-69.
Lander, A. D., Gokoffski, K. K., Wan, F. Y. M., Nie, Q., and Calof, A. L. (2009). Cell Lineages and the Logic of Proliferative Control. PLoS Biol. 7, e15 EP -.
Laughlin, Simon B, Ruyter van Steveninck, R. R. de, and Anderson, J. C. (1998). The metabolic cost of neural information. Nat. Neurosci. 1, 36-41.
Lee, H. H., Molla, M. N., Cantor, C. R., and Collins, J. J. (2010). Bacterial charity work leads to population-wide resistance. Nature 467, 82-85.
Lee, H.-J., and Zheng, J. J. (2010). PDZ domains and their binding partners: structure, specificity, and modification. Cell Commun. Signaling 8, 8.
Lee, Y J, Dobbs, M. B., Verardi, M. L., and Hyde, D. R. (1990). dgq: a drosophila gene encoding a visual system-specific G alpha molecule. Neuron 5, 889-98.
Lee, Y. J., Shah, S., Suzuki, Emiko, Zars, T., O'Day, P. M., and Hyde, D. R. (1994). The Drosophila dgq gene encodes a G alpha protein that mediates phototransduction. Neuron 13, 1143-57.
Lehner, B. (2011). Molecular mechanisms of epistasis within and between genes. Trends in Genet., 1-9.
Lestas, I., Vinnicombe, G., and Paulsson, J. (2010). Fundamental limits on the suppression of molecular fluctuations. Nature 467, 174-8.
Levchenko, a, Bruck, J., and Sternberg, P. W. (2000). Scaffold proteins may biphasically affect the levels of mitogen-activated protein kinase signaling and reduce its threshold properties. Proc. Natl. Acad. Sci. U. S. A. 97, 5818-23.
Li, H. S., and Montell, C. (2000). TRP and the PDZ protein, INAD, form the core complex required for retention of the signalplex in Drosophila photoreceptor cells. J. Cell. Biol. 150, 1411-22.
Lin, D.-T., and Huganir, Richard L (2007). PICK1 and phosphorylation of the glutamate receptor 2 (GluR2) AMPA receptor subunit regulates GluR2 recycling after NMDA receptor-induced internalization. J. Neurosci. 27, 13903-8.
Lipson, H., Pollack, J. B., and Suh, N. P. (2002). On the origin of modular variation. Evolution 56, 1549-56.

Liu, C.-H., Satoh, A. K., Postma, M., Huang, J., Ready, Donald F., and Hardie, Roger C. (2008). Ca2+-dependent metarhodopsin inactivation mediated by calmodulin and NINAC myosin III. Neuron 59, 778-89.

Liu, J. D., and Parkinson, J. S. (1989). Role of CheW protein in coupling membrane receptors to the intracellular signaling system of bacterial chemotaxis. Proc. Natl. Acad. Sci. U.S.A. 86, 8703-7.

Liu, Mingya, Parker, L. L., Wadzinski, B. E., and Shieh, B.-H. (2000). Reversible Phosphorylation of the Signal Transduction Complex in Drosophila Photoreceptors. J. Biol. Chem. 275, 12194-12199.

Liu, W., Wen, W., Wei, Z., Yu, J., Ye, F., Liu, C.-hsiung, Hardie, Roger C, and Zhang, Mingjie (2011). The INAD Scaffold Is a Dynamic, Redox-Regulated Modulator of Signaling in the Drosophila Eye. Cell 145, 1088-101.

Lo, W.-cheong, Chou, C.-shan, Gokoffski, K. K., Wan, F. Y.-M., Lander, A. D., Calof, A. L., and Nie, Q. (2009). Feedback regulation in multistage cell lineages. Math. Biosci. Eng. 6, 59-82.

Locasale, J. W., Shaw, A. S., and Chakraborty, A. K. (2007). Scaffold proteins confer diverse regulatory properties to protein kinase cascades. Proc. Natl. Acad. Sci. U. S. A. 104, 13307-12.

Lockless, S. W., and Ranganathan, R (1999). Evolutionarily conserved pathways of energetic connectivity in protein families. Science 286, 295-9.

Long, J., Wei, Z., Feng, W., Yu, C., Zhao, Y.-xiang, and Zhang, Mingjie (2008). Supramodular nature of GRIP1 revealed by the structure of its PDZ12 tandem in complex with the carboxyl tail of Fras1. J. Mol. Biol. 375, 1457-68.

Ma, Buyong, and Nussinov, Ruth (2010). Enzyme dynamics point to stepwise conformational selection in catalysis. Curr. Opin. Chem. Biol. 14, 652-9.

Ma, L., and Iglesias, P. a (2002). Quantifying robustness of biochemical network models. BMC Bioinf. 3, 38.

Ma, W., Lai, L., Ouyang, Q., and Tang, C. (2006). Robustness and modular design of the Drosophila segment polarity network. Mol. Syst. Biol. 2, 70.

Ma, W., Trusina, A., El-Samad, H., Lim, W. a, and Tang, C. (2009). Defining network topologies that can achieve biochemical adaptation. Cell 138, 760-73.

Maciag, K., Altschuler, S. J., Slack, M. D., Krogan, N. J., Emili, A., Greenblatt, J. F., Maniatis, T., and Wu, L. F. (2006). Systems-level analyses identify extensive coupling among gene expression machines. Mol. Syst. Biol. 2, 2006.0003.

Mangan, S, and Alon, U (2003). Structure and function of the feed-forward loop network motif. Proc. Natl. Acad. Sci. U. S. A. 100, 11980-5.

Marcus, S., Polverino, A., Barr, M., and Wigler, M. (1994). Complexes between STE5 and components of the pheromone-responsive mitogen-activated protein kinase module. Proc. Natl. Acad. Sci. U.S.A. 91, 7762-6.
Matsuda, S., Mikawa, S., and Hirai, H. (1999). Phosphorylation of serine-880 in GluR2 by protein kinase C prevents its C terminus from binding with glutamate receptor-interacting protein. J. Neurochem. 73, 1765-8.
Matsumoto, H. et al. (1994). Phosrestin I undergoes the earliest light-induced phosphorylation by a calcium/calmodulin-dependent protein kinase in Drosophila photoreceptors. Neuron 12, 997-1010.
Matsumoto, Hiroyuki, O'Tousa, J. E., Pak, William L., Tousa, J. E. O., and Url, S. (1982). Light-induced modification of Drosophila retinal polypeptides in vivo. Science 217, 839-41.
Matsumoto, Hiroyuki, and Pak, William L. (1984). Light-induced phosphorylation of retina-specific polypeptides of Drosophila in vivo. Science 223, 184-6.
Mauceri, D., Gardoni, F., Marcello, E., and Luca, M. Di (2007). Dual role of CaMKII-dependent SAP97 phosphorylation in mediating trafficking and insertion of NMDA receptor subunit NR2A. J. Neurochem. 100, 1032-46.
McAdams, H. H., and Arkin, a (1999). It's a noisy business! Genetic regulation at the nanomolar scale. Trends in Genet. 15, 65-9.
Meier, S., and Ozbek, S. (2007). A biological cosmos of parallel universes: does protein structural plasticity facilitate evolution? BioEssays 29, 1095-104.
Melen, G. J., Levy, S., Barkai, Naama, and Shilo, B.-Z. (2005). Threshold responses to morphogen gradients by zero-order ultrasensitivity. Mol. Syst. Biol. 1, 2005.0028.
Milo, R, Shen-Orr, S., Itzkovitz, S., Kashtan, N, Chklovskii, D., and Alon, U (2002). Network motifs: simple building blocks of complex networks. Science 298, 824-7.
Minke, B, and Armon, E. (1984). Activation of electrogenic Na-Ca exchange by light in fly photoreceptors. Vision Res. 24, 109-15.
Mishra, P., Socolich, Michael, Wall, M. A., Graves, J., Wang, Z., and Ranganathan, Rama (2007). Dynamic Scaffolding in a G Protein-Coupled Signaling System. Cell 131, 80-92.
Mitchell, J., Gutierrez, J., and Northup, J. K. (1995). Purification, characterization, and partial amino acid sequence of a G protein-activated phospholipase C from squid photoreceptors. J. Biol. Chem. 270, 854-9.
Monod, J., Wyman, J., and Changeux, J.-P. J. (1965). On the Nature of Allosteric Transitions: A Plausible Model. J. Mol. Biol. 12, 88-118.
Montell, C., Jones, K., Zuker, C. S., and Rubin, G. (1987). A second opsin gene expressed in the ultraviolet-sensitive R7 photoreceptor cells of Drosophila melanogaster. J. Neurosci. 7, 1558-66.

Morais Cabral, J. H., Petosa, C., Sutcliffe, M. J., Raza, S., Byron, O., Poy, F., Marfatia, S. M., Chishti, A. H., and Liddington, R. C. (1996). Crystal structure of a PDZ domain. Nature 382, 649-52.

Moriya, H., Shimizu-Yoshida, Y., and Kitano, H. (2006). In vivo robustness analysis of cell division cycle genes in Saccharomyces cerevisiae. PLoS Genet. 2, e111.

Morohashi, M., Winn, A. E., Borisuk, M. T., Bolouri, H., Doyle, John, and Kitano, H. (2002). Robustness as a measure of plausibility in models of biochemical networks. J. Theor. Biol. 216, 19-30.

Mousseau, T. A., and Roff, D. A. (1987). Natural selection and the heritability of fitness components. Heredity 59 (Pt 2), 181-97.

Murakoshi, H., Wang, Hong, and Yasuda, R. (2011). Local, persistent activation of Rho GTPases during plasticity of single dendritic spines. Nature 472, 100-104.

Nagai, T., Ibata, K., Park, E. S., Kubota, M., Mikoshiba, K., and Miyawaki, A. (2002). A variant of yellow fluorescent protein with fast and efficient maturation for cell-biological applications. Nat. Biotechnol. 20, 87-90.

Nandelstadh, P. von, Ismail, M., Gardin, C., Suila, H., Zara, I., Belgrano, A., Valle, G., Carpen, O., and Faulkner, G. (2009). A class III PDZ binding motif in the myotilin and FATZ families binds enigma family proteins: a common link for Z-disc myopathies. Mol. Cell. Biol. 29, 822-34.

Neckers, L. (2007). Heat shock protein 90: the cancer chaperone. J. Biosci. 32, 517-30.

Neher, Erwin (1998). Vesicle pools and Ca2+ microdomains: new tools for understanding their roles in neurotransmitter release. Neuron 20, 389-99.

Nevozhay, D., Adams, R. M., Murphy, K. F., Josic, K., and Balázsi, G. (2009). Negative autoregulation linearizes the dose-response and suppresses the heterogeneity of gene expression. Proc. Natl. Acad. Sci. U. S. A. 106, 5123-8.

Niemeyer, B. A., Suzuki, E., Scott, K., Jalink, K., and Zuker, C. S. (1996). The Drosophila light-activated conductance is composed of the two channels TRP and TRPL. Cell 85, 651-9.

Ninio, J. (1975). Kinetic amplification of enzyme discrimination. Biochimie 57, 587-95.

Nise, N. S. (2000). Control Systems Engineering 3rd ed. (New York, NY: John Wiley & Sons, Inc.).

Niu, X., Chen, Q., Zhang, Jiahai, Shen, W., Shi, Yunyu, and Wu, J. (2007). Interesting structural and dynamical behaviors exhibited by the AF-6 PDZ domain upon Bcr peptide binding. Biochemistry 46, 15042-53.

Nourry, C., Grant, S. G. N., and Borg, J.-P. (2003). PDZ domain proteins: plug and play! Sci. STKE 2003, RE7.

Novák, B., and Tyson, J. J. (2008). Design principles of biochemical oscillators. Nat. Rev. Mol. Cell Biol. 9, 981-91.
Oberwinkler, J., and Stavenga, D. G. (2000). Calcium transients in the rhabdomeres of dark- and light-adapted fly photoreceptor cells. J. Neurosci. 20, 1701-9.
Oberwinkler, Johannes, and Stavenga, D. G. (2000). Calcium imaging demonstrates colocalization of calcium influx and extrusion in fly photoreceptors. Proc. Natl. Acad. Sci. U. S. A. 97, 8578-83.
Oberwinkler, Johannes, and Stavenga, D. G. (1998). Light Dependence of Calcium and Membrane Potential Measured in Blowfly Photoreceptors In Vivo. J. Gen. Physiol. 112, 113-124.
Oleksiuk, O. et al. (2011). Thermal robustness of signaling in bacterial chemotaxis. Cell 145, 312-21.
Onuchic, J. N., Luthey-Schulten, Z., and Wolynes, P. G. (1997). Theory of protein folding: the energy landscape perspective. Annu. Rev. Phys. Chem. 48, 545-600.
Ostroy, S. E., Wilson, M., and Pak, William L (1974). Drosophila rhodopsin: photochemistry, extraction and differences in the norp AP12 phototransduction mutant. Biochem. Biophys. Res. Commun. 59, 960-6.
Page, M. I., and Jencks, W. P. (1971). Entropic contributions to rate accelerations in enzymic and intramolecular reactions and the chelate effect. Proc. Natl. Acad. Sci. U. S. A. 68, 1678-83.
Paj, W. K., Istrit, S. E., Deland, M. C., and Wu, C F (1976). Photoreceptor mutant of Drosophia: is protein involved in intermediate steps of phototransduction? Science 194, 956-9.
Pak, William L, and Lidington, K. J. (1974). Fast electrical potential from a long-lived, long-wavelength photoproduct of fly visual pigment. J. Gen. Physiol. 63, 740-56.
Palani, S., and Sarkar, C. a (2011). Synthetic conversion of a graded receptor signal into a tunable, reversible switch. Mol. Syst. Biol. 7, 480.
Park, S.-H., Zarrinpar, A., and Lim, W. A. (2003). Rewiring MAP kinase pathways using alternative scaffold assembly mechanisms. Science 299, 1061-4.
Penkert, R. R., DiVittorio, H. M., and Prehoda, K. E. (2004). Internal recognition through PDZ domain plasticity in the Par-6-Pals1 complex. Nat. Struct. Mol. Biol. 11, 1122-7.
Peretz, A, Suss-Toby, E., Rom-Glas, A., Arnon, A., Payne, R., and Minke, B (1994). The light response of Drosophila photoreceptors is accompanied by an increase in cellular calcium: effects of specific mutations. Neuron 12, 1257-67.

Peretz, Asher, Sandler, C., Kirschfeld, Kuno, Hardie, Roger C., and Minke, Baruch (1994). Genetic dissection of light-induced Ca2+ influx into Drosophila photoreceptors. J. Gen. Physiol. 104, 1057-77.
Peterson, F. C., Penkert, R. R., Volkman, B. F., and Prehoda, K. E. (2004). Cdc42 regulates the Par-6 PDZ domain through an allosteric CRIB-PDZ transition. Mol. Cell 13, 665-76.
Petit, C. M., Zhang, Jun, Sapienza, P. J., Fuentes, E. J., and Lee, A. L. (2009). Hidden dynamic allostery in a PDZ domain. Proc. Natl. Acad. Sci. U.S.A. 106, 18249-54.
Phillips, A. M., Bull, A., and Kelly, L. E. (1992). Identification of a Drosophila gene encoding a calmodulin-binding protein with homology to the trp phototransduction gene. Neuron 8, 631-42.
Poelwijk, F. J., Vos, M. G. J. de, and Tans, S. J. (2011). Tradeoffs and Optimality in the Evolution of Gene Regulation. Cell 146, 462-470.
Ponting, C. P. (1997). Evidence for PDZ domains in bacteria, yeast, and plants. Protein Sci 6, 464-8.
Popescu, D. C., Ham, A.-J. L., and Shieh, B.-H. (2006). Scaffolding Protein INAD Regulates Deactivation of Vision by Promoting Phosphorylation of Transient Receptor Potential by Eye Protein Kinase C in Drosophila. J. Neurosci. 26, 8570-8577.
Popovych, N., Sun, S., Ebright, R. H., and Kalodimos, C. G. (2006). Dynamically driven protein allostery. Nat. Struct. Mol. Biol. 13, 831-8.
Postma, M., Oberwinkler, Johannes, and Stavenga, D. G. (1999). Does Ca2+ reach millimolar concentrations after single photon absorption in Drosophila photoreceptor microvilli? Biophys. J. 77, 1811-23.
Printen, J. A., and Sprague, G. F. (1994). Protein-protein interactions in the yeast pheromone response pathway: Ste5p interacts with all members of the MAP kinase cascade. Genetics 138, 609-19.
Pumir, A., Graves, J., Ranganathan, Rama, and Shraiman, B. I. (2008). Systems analysis of the single photon response in invertebrate photoreceptors. Proc. Natl. Acad. Sci. U. S. A. 105, 10354-9.
Raghu, P., Colley, N. J., Webel, R., James, T., Hasan, G., Danin, M., Selinger, Z., and Hardie, Roger C. (2000). Normal phototransduction in Drosophila photoreceptors lacking an InsP(3) receptor gene. Mol. Cell Neurosci. 15, 429-45.
Raghu, P., Usher, K., Jonas, S., Chyb, S., Polyanovsky, A., and Hardie, Roger C. (2000). Constitutive activity of the light-sensitive channels TRP and TRPL in the Drosophila diacylglycerol kinase mutant, rdgA. Neuron 26, 169-79.
Raghuram, V., Hormuth, H., and Foskett, J. K. (2003). A kinase-regulated mechanism controls CFTR channel gating by disrupting bivalent PDZ domain interactions. Proc. Natl. Acad. Sci. U. S. A. 100, 9620-5.

Ranganathan, R, and Stevens, C. F. (1995). Arrestin binding determines the rate of inactivation of the G protein-coupled receptor rhodopsin in vivo. Cell 81, 841-8.
Ranganathan, Rama, Harris, G. L., Stevens, C. F., and Zuker, C. S. (1991). A Drosophila mutant defective in extracellular calcium-dependent photoreceptor deactivation and rapid desensitization. Nature 354, 230-2.
Ranganathan, Rama, Bacskai, B. J., Tsien, R. Y., and Zuker, C. S. (1994). Cytosolic calcium transients: spatial localization and role in Drosophila photoreceptor cell function. Neuron 13, 837-48.
Ready, D F, Hanson, T. E., and Benzer, S. (1976). Development of the Drosophila retina, a neurocrystalline lattice. Dev. Biol. 53, 217-40.
Reuss, H., Mojet, M. H., Chyb, S., and Hardie, Roger C. (1997). In vivo analysis of the drosophila light-sensitive channels, TRP and TRPL. Neuron 19, 1249-59.
Richter, D., Katz, B., Oberacker, T., Tzarfaty, V., Belusic, G., Minke, Baruch, and Huber, Armin (2011). Translocation of the Drosophila transient receptor potential-like (TRPL) channel requires both the N- and C-terminal regions together with sustained Ca2+ entry. J. Biol. Chem. 286, 34234 -34243.
Rizzo, M. A., Springer, G. H., Granada, B., and Piston, D. W. (2004). An improved cyan fluorescent protein variant useful for FRET. Nat. Biotechnol. 22, 445-9.
Roff, D. A., and Mousseau, T. A. (1987). Quantitative genetics and fitness: lessons from Drosophila. Heredity 58 (Pt 1), 103-18.
Roguev, A. et al. (2008). Conservation and rewiring of functional modules revealed by an epistasis map in fission yeast. Science 322, 405-10.
Running Deer, J. L., Hurley, J B, and Yarfitz, S. L. (1995). G protein control of Drosophila photoreceptor phospholipase C. J. Biol. Chem. 270, 12623-8.
Sako, Y., Nagafuchi, a, Tsukita, S., Takeichi, M., and Kusumi, a (1998). Cytoplasmic regulation of the movement of E-cadherin on the free cell surface as studied by optical tweezers and single particle tracking: corralling and tethering by the membrane skeleton. J. Cell. Biol. 140, 1227-40.
Sando, J. J., and Beals, J. K. (2003). Enzyme assays for protein kinase C activity. Methods In Molecular Biology Clifton Nj 233, 63-76.
Satoh, A. K., Xia, H., Yan, L., Liu, C.-H., Hardie, Roger C, and Ready, Donald F (2010). Arrestin translocation is stoichiometric to rhodopsin isomerization and accelerated by phototransduction in Drosophila photoreceptors. Neuron 67, 997-1008.
Satoh, A. K., and Ready, Donald F. (2005). Arrestin1 mediates light-dependent rhodopsin endocytosis and cell survival. Curr. Biol. 15, 1722-33.
Schneggenburger, R., and Neher, E (2000). Intracellular calcium dependence of transmitter release rates at a fast central synapse. Nature 406, 889-93.

Schwarz, E. M., and Benzer, S. (1997). Calx, a Na-Ca exchanger gene of Drosophila melanogaster. Proc. Natl. Acad. Sci. U. S. A. 94, 10249-54.
Scott, K., Becker, A., Sun, Y., Hardy, R., and Zuker, C. S. (1995). Gq alpha protein function in vivo: genetic dissection of its role in photoreceptor cell physiology. Neuron 15, 919-27.
Scott, K., Sun, Y., Beckingham, K., and Zuker, C. S. (1997). Calmodulin regulation of Drosophila light-activated channels and receptor function mediates termination of the light response in vivo. Cell 91, 375-83.
Scott, Kristin, and Zuker, C. S. (1998). Assembly of the Drosophila phototransduction cascade into a signalling complex shapes elementary responses. Nature 395, 805-8.
Shah, N. a, and Sarkar, C. a (2011). Robust Network Topologies for Generating Switch-Like Cellular Responses. PLoS Comput. Biol. 7, e1002085.
Sheetz, M. P., Schindler, M., and Koppel, D. E. (1980). Lateral mobility of integral membrane proteins is increased in spherocytic erythrocytes. Nature 285, 510-1.
Shen-Orr, S. S., Milo, Ron, Mangan, Shmoolik, and Alon, Uri (2002). Network motifs in the transcriptional regulation network of Escherichia coli. Nature genetics 31, 64-8.
Shepherd, G. M. (1996). The dendritic spine: a multifunctional integrative unit. Journal of neurophysiology 75, 2197-210.
Shieh, B. H., and Zhu, M. Y. (1996). Regulation of the TRP Ca2+ channel by INAD in Drosophila photoreceptors. Neuron 16, 991-8.
Shieh, B.-H. H., Zhu, M.-Y. Y., Lee, J. K., Kelly, I. M., and Bahiraei, Frohar (1997). Association of INAD with NORPA is essential for controlled activation and deactivation of Drosophila phototransduction in vivo. Proc. Natl. Acad. Sci. U.S.A. 94, 12682-7.
Shinar, G., and Feinberg, M. (2010). Structural sources of robustness in biochemical reaction networks. Science 327, 1389-91.
Shulman, A. I., Larson, C., Mangelsdorf, D. J., and Ranganathan, Rama (2004). Structural determinants of allosteric ligand activation in RXR heterodimers. Cell 116, 417-29.
Singer, A. U., Waldo, G. L., Harden, T. K., and Sondek, J. (2002). A unique fold of phospholipase C-beta mediates dimerization and interaction with G alpha q. Nat. Struct. Biol. 9, 32-6.
Skerker, J. M., Prasol, M. S., Perchuk, B. S., Biondi, E. G., and Laub, M. T. (2005). Two-component signal transduction pathways regulating growth and cell cycle progression in a bacterium: a system-level analysis. PLoS Biol. 3, e334.
Smith, D. P., Ranganathan, Rama, Hardy, Robert W., Marx, J., Tsuchida, T., and Zuker, C. S. (1991). Photoreceptor deactivation and retinal degeneration

mediated by a photoreceptor-specific protein kinase C. Science 254, 1478-84.
Smock, R. G., Rivoire, O., Russ, W. P., Swain, J. F., Leibler, Stanislas, Ranganathan, Rama, and Gierasch, L. M. (2010). An interdomain sector mediating allostery in Hsp70 molecular chaperones. Molecular Systems Biology 6, 1-10.
Sole, R. V., and Fernandez, P. (2003). Modularity "for free" in genome architecture? 1-9.
Songyang, Z. et al. (1997). Recognition of unique carboxyl-terminal motifs by distinct PDZ domains. Science 275, 73-7.
Songyang, Zhou, and Cantley, L.C. (1995). Recognition and specificity in protein tyrosine kinase-mediated signalling. Trends in Biochem. Sci. 20, 470–475.
Sorger, P. K. (2005). A reductionist's systems biology: opinion. Curr. Opin. Cell Biol. 17, 9-11.
Sprinzak, D., Lakhanpal, A., Lebon, L., Garcia-Ojalvo, J., and Elowitz, M. B. (2011). Mutual inactivation of notch receptors and ligands facilitates developmental patterning. PLoS Comput. Biol. 7, e1002069.
Stiffler, M. A., Chen, J. R., Grantcharova, V. P., Lei, Y., Fuchs, D., Allen, J. E., Zaslavskaia, L. A., and MacBeath, G. (2007). PDZ domain binding selectivity is optimized across the mouse proteome. Science 317, 364-9.
Strogatz, S. H. (1994). Nonlinear Dynamics and Chaos 1st ed. (Cambridge, MA: Perseus Books Publishing).
Sun, X. J., Rothenberg, P., Kahn, C. R., Backer, J. M., Araki, E., Wilden, P. A., Cahill, D. A., Goldstein, B. J., and White, M. F. (1991). Structure of the insulin receptor substrate IRS-1 defines a unique signal transduction protein. Nature 352, 73-7.
Suzuki, E, Katayama, E., and Hirosawa, K. (1993). Structure of photoreceptive membranes of Drosophila compound eyes as studied by quick-freezing electron microscopy. J. Electron Microsc. 42, 178-184.
Szajewski, R. P., and Whitesides, G. M. (1980). Rate constants and equilibrium constants for thiol-disulfide interchange reactions involving oxidized glutathione. Journal of the American Chemical Society 102, 2011-2026.
Süel, G. M., Garcia-Ojalvo, J., Liberman, L. M., and Elowitz, M. B. (2006). An excitable gene regulatory circuit induces transient cellular differentiation. Nature 440, 545-50.
Süel, G. M., Lockless, Steve W., Wall, M. A., and Ranganathan, Rama (2003). Evolutionarily conserved networks of residues mediate allosteric communication in proteins. Nat. Struct. Biol. 10, 59-69.
Tadross, M. R., Dick, I. E., and Yue, D. T. (2008). Mechanism of Local and Global Ca2+ Sensing by Calmodulin in Complex with a Ca2+ Channel. Cell 133, 1228-1240.

Threadgill, D. W. et al. (1995). Targeted disruption of mouse EGF receptor: effect of genetic background on mutant phenotype. Science 269, 230-4.
Tian, Q.-B. et al. (2006). Interaction of LDL receptor-related protein 4 (LRP4) with postsynaptic scaffold proteins via its C-terminal PDZ domain-binding motif, and its regulation by Ca/calmodulin-dependent protein kinase II. Eur. J. Neurosci. 23, 2864-76.
Tkacik, G., Walczak, A. M., and Bialek, W. (2009). Optimizing information flow in small genetic networks. I.
Tokuriki, Nobuhiko, and Tawfik, Dan S (2009). Protein dynamism and evolvability. Science 324, 203-7.
Tonikian, R. et al. (2008). A specificity map for the PDZ domain family. PLoS Biol. 6, e239.
Toyoshima, S., Matsumoto, N., Wang, P., Inoue, H., Yoshioka, T., Hotta, Y., and Osawa, T. (1990). Purification and partial amino acid sequences of phosphoinositide-specific phospholipase C of Drosophila eye. J. Biol. Chem. 265, 14842-8.
Tremblay, L. W., Dunaway-Mariano, D., and Allen, K. N. (2006). Structure and activity analyses of Escherichia coli K-12 NagD provide insight into the evolution of biochemical function in the haloalkanoic acid dehalogenase superfamily. Biochemistry 45, 1183-93.
Tsai, T. Y.-C., Choi, Y. S., Ma, W., Pomerening, J. R., Tang, C., and Ferrell, J. E. (2008). Robust, tunable biological oscillations from interlinked positive and negative feedback loops. Science 321, 126-9.
Tsunoda, S, Sun, Y., Suzuki, E, and Zuker, C. S. (2001). Independent anchoring and assembly mechanisms of INAD signaling complexes in Drosophila photoreceptors. J. Neurosci. 21, 150-8.
Tsunoda, Susan, Sierralta, J., Sun, Y., Bodner, R., Suzuki, E., Becker, A., Socolich, M., and Zuker, C. S. (1997). A multivalent PDZ-domain protein assembles signalling complexes in a G-protein-coupled cascade. Nature 388, 243-9.
Tsunoda, Susan, and Zuker, C. S. (1999). The organization of INAD-signaling complexes by a multivalent PDZ domain protein in Drosophila photoreceptor cells ensures sensitivity and speed of signaling. Cell Calcium 26, 165-71.
Villiers, B. R. M., and Hollfelder, F. (2009). Mapping the limits of substrate specificity of the adenylation domain of TycA. Chembiochem 10, 671-82.
Vinós, J., Jalink, K., Hardy, R. W., Britt, S. G., and Zuker, C. S. (1997). A G protein-coupled receptor phosphatase required for rhodopsin function. Science 277, 687-90.

Voltz, J. W., Brush, M., Sikes, S., Steplock, D., Weinman, E. J., and Shenolikar, S. (2007). Phosphorylation of PDZ1 domain attenuates NHERF-1 binding to cellular targets. J. Biol. Chem. 282, 33879-87.

Waddington, C. H. (1942). Canalization of development and the inheritance of acquired characters. Nature 150, 563.

Wagner, Günter P, Pavlicev, M., and Cheverud, J. M. (2007). The road to modularity. Nat. Rev. Genet. 8, 921-31.

Wagner, G.P., and Altenberg, L. (1996). Perspective: Complex adaptations and the evolution of evolvability. Evolution 50, 967–976.

Waldo, G. L. et al. (2010). Kinetic scaffolding mediated by a phospholipase C-beta and Gq signaling complex. Science 330, 974-80.

Wang, C. K., Pan, L., Chen, J., and Zhang, Mingjie (2010). Extensions of PDZ domains as important structural and functional elements. Protein & Cell 1, 737-51.

Wang, T., Wang, X., Xie, Q., and Montell, C. (2008). The SOCS box protein STOPS is required for phototransduction through its effects on phospholipase C. Neuron 57, 56-68.

Wang, T., Xu, H., Oberwinkler, Johannes, Gu, Y., Hardie, Roger C., and Montell, C. (2005). Light activation, adaptation, and cell survival functions of the Na+/Ca2+ exchanger CalX. Neuron 45, 367-78.

Wang, W., Weng, J., Zhang, Xu, Liu, Maili, and Zhang, Mingjie (2009). Creating conformational entropy by increasing interdomain mobility in ligand binding regulation: a revisit to N-terminal tandem PDZ domains of PSD-95. J. Am. Chem. Soc. 131, 787-96.

Weinman, E. J. et al. (2007). Parathyroid hormone inhibits renal phosphate transport by phosphorylation of serine 77 of sodium-hydrogen exchanger regulatory factor-1. J. Clin. Invest. 117, 3412-20.

Weinreich, D. M., Delaney, Nigel F, Depristo, M. a, and Hartl, D. L. (2006). Darwinian evolution can follow only very few mutational paths to fitter proteins. Science 312, 111-4.

Wes, P. D., Xu, X. Z., Li, H. S., Chien, F., Doberstein, S. K., and Montell, C. (1999). Termination of phototransduction requires binding of the NINAC myosin III and the PDZ protein INAD. Nat. Neurosci. 2, 447-53.

Wilk, M. B., and Gnanadesikan, R. (1968). Probability plotting methods for the analysis of data. Biometrika 55, 1-17.

Williamson, W. R., and Hiesinger, P. R. (2010). Preparation of developing and adult Drosophila brains and retinae for live imaging. J. Visualized Exp.

Wong, H.-C., Bourdelas, A., Krauss, A., Lee, H.-J., Shao, Y., Wu, D., Mlodzik, M., Shi, D.-L., and Zheng, J. (2003). Direct binding of the PDZ domain of Dishevelled to a conserved internal sequence in the C-terminal region of Frizzled. Mol. Cell 12, 1251-60.

Wong, W., and Scott, J. D. (2004). AKAP signalling complexes: focal points in space and time. Nat Rev Mol Cell Biol 5, 959-70.
Woods, R. J., Barrick, J. E., Cooper, T. F., Shrestha, U., Kauth, M. R., and Lenski, R. E. (2011). Second-Order Selection for Evolvability in a Large Escherichia coli Population. Science 331, 1433-1436.
Wu, C. F., and Pak, W L (1975). Quantal basis of photoreceptor spectral sensitivity of Drosophila melanogaster. J. Gen. Physiol. 66, 149-68.
Wu, C. F., and Pak, W. L. (1978). Light-induced voltage noise in the photoreceptor of Drosophila melanogaster. J. Gen. Physiol. 71, 249-68.
Wu, H., Feng, W., Chen, J., Chan, L.-N., Huang, S., and Zhang, Mingjie (2007). PDZ domains of Par-3 as potential phosphoinositide signaling integrators. Mol. Cell 28, 886-98.
Wu, L., Niemeyer, B., Colley, N., Socolich, M., and Zuker, C. S. (1995). Regulation of PLC-mediated signalling in vivo by CDP-diacylglycerol synthase. Nature 373, 216-22.
Xiong, W., and Ferrell, J. E. (2003). A positive-feedback-based bistable "memory module" that governs a cell fate decision. Nature 426, 460-5.
Xu, X. Z., Chien, F., Butler, A., Salkoff, L., and Montell, C. (2000). TRPgamma, a drosophila TRP-related subunit, forms a regulated cation channel with TRPL. Neuron 26, 647-57.
Xu, X. Z., Li, H. S., Guggino, W. B., and Montell, C. (1997). Coassembly of TRP and TRPL produces a distinct store-operated conductance. Cell 89, 1155-64.
Yamada, T., Takeuchi, Y., Komori, N., Kobayashi, H., Sakai, Y., Hotta, Y., and Matsumoto, H (1990). A 49-kilodalton phosphoprotein in the Drosophila photoreceptor is an arrestin homolog. Science 248, 483-6.
Yi, T. M., Huang, Y., Simon, M. I., and Doyle, J (2000). Robust perfect adaptation in bacterial chemotaxis through integral feedback control. Proc. Natl. Acad. Sci. U. S. A. 97, 4649-53.
Yoshioka, T., Inoue, H., and Hotta, Y. (1985). Absence of phosphatidylinositol phosphodiesterase in the head of a Drosophila visual mutant, norpA (no receptor potential A). J. Biochem. 97, 1251-4.
Yoshioka, T., Inoue, H., and Hotta, Y. (1983). Defective phospholipid metabolism in the retinular cell membrane of norpA (no receptor potential) visual transduction mutants of Drosophila. Biochem. Biophys. Res. Commun. 111, 567-73.
Young, N. M., and Hallgrímsson, B. (2005). Serial homology and the evolution of mammalian limb covariation structure. Evolution 59, 2691-704.
Yu, R. C. et al. (2008). Negative feedback that improves information transmission in yeast signalling. Nature 456, 755-61.
Yuste, R, Majewska, a, and Holthoff, K. (2000). From form to function: calcium compartmentalization in dendritic spines. Nat. Neurosci. 3, 653-9.

Yuste, Rafael (2011). Dendritic Spines and Distributed Circuits. Neuron 71, 772-781.

Zaccolo, M., and Pozzan, T. (2002). Discrete microdomains with high concentration of cAMP in stimulated rat neonatal cardiac myocytes. Science 295, 1711-5.

Zarrinpar, A., Park, S.-H., and Lim, W. A. (2003). Optimization of specificity in a cellular protein interaction network by negative selection. Nature 426, 676-80.

Zhang, Jun, Sapienza, P. J., Ke, H., Chang, A., Hengel, S. R., Wang, Huanchen, Phillips, G. N., and Lee, A. L. (2010). Crystallographic and nuclear magnetic resonance evaluation of the impact of peptide binding to the second PDZ domain of protein tyrosine phosphatase 1E. Biochemistry 49, 9280-91.

Zhang, Q., Fan, J. S., and Zhang, M (2001). Interdomain chaperoning between PSD-95, Dlg, and Zo-1 (PDZ) domains of glutamate receptor-interacting proteins. J. Biol. Chem. 276, 43216-20.

Zimmerman, S. B. (1993). Macromolecular crowding effects on macromolecular interactions: some implications for genome structure and function. Biochimica et biophysica acta 1216, 175-85.

Zimmermann, P., Meerschaert, K., Reekmans, Gunter, Leenaerts, I., Small, J. V., Vandekerckhove, J., David, Guido, and Gettemans, J. (2002). PIP(2)-PDZ domain binding controls the association of syntenin with the plasma membrane. Mol. Cell 9, 1215-25.

Zuker, C. S., Cowman, Alan F., and Rubin, Gerald M. (1985). Isolation and structure of a rhodopsin gene from D. melanogaster. Cell 40, 851-8.

Zuker, C. S., Montell, C., Jones, K., Laverty, T., and Rubin, G. M. (1987). A rhodopsin gene expressed in photoreceptor cell R7 of the Drosophila eye: homologies with other signal-transducing molecules. J. Neurosci. 7, 1550-7.